

**Clastic injection:
process to product**

Jessica Amy Ross

Submitted in accordance with the requirements for the degree of
Doctor of Philosophy

The University of Leeds
School of Earth and Environment

October 2013

Declaration of authorship

The candidate confirms that the work submitted is her own, except where work which has formed part of jointly-authored publications has been included. The contribution of the candidate and the other authors to this work has been explicitly indicated below. The candidate confirms that appropriate credit has been given within the thesis where reference has been made to the work of others.

The work in **Chapter 5** reproduces a manuscript that was published in *Sedimentology* in 2011.

Ross, J.A., Peakall, J. and Keevil, G.M. (2011) An integrated model of extrusive sand injectites in cohesionless sediments. *Sedimentology*, **58**, 1693-1715.

Data were collected in the laboratory by Jessica Ross. All data were processed, interpreted, presented and the conceptual model designed by Jessica Ross. Ideas were shaped during discussion with co-authors.

The work in **Chapter 7** reproduces a manuscript that was published in the *Journal of the Geological Society* in 2013.

Ross, J.A., Peakall, J. and Keevil, G.M. (2013) Sub-aqueous sand extrusion dynamics, *Journal of the Geological Society*, **170**, 593-602.

Fieldwork was completed by Jessica Ross. All presented data were collected and interpreted and the model designed by Jessica Ross. Ideas were shaped during discussion with co-authors.

Chapter 8 reproduces a manuscript that has been accepted for publication in *Sedimentology*.

Ross, J.A., Peakall, J. and Keevil, G.M. DOI: 10.1111/sed.12115. Facies and fluid flow of sandstone-hosted columnar intrusion: the pipes of Kodachrome Basin State Park.

Fieldwork was completed by Jessica Ross. All presented data were collected, analysed and interpreted by Jessica Ross. Ideas were shaped and developed through discussion with co-authors.

This copy has been supplied on the understanding that it is copyright material and that no quotation from the thesis may be published without proper acknowledgement.

© 2013 The University of Leeds and Jessica Amy Ross

The right of Jessica Amy Ross to be identified as Author of this work has been asserted by her in accordance with the Copyright, Designs and Patents Act 1988.

Acknowledgments

My most sincere thanks go to my supervisors Jeff Peakall and Gareth Keevil who have unfailingly supported me and provided invaluable guidance from the inception of the research project, through to the final thesis. I would also like to thank Russell Dixon for his technical support during the experimental phases of this project and Eric Condcliffe for his exhaustive knowledge of all things SEM. Gareth Keevil and Rachael Dale provided important support in the field in Ireland and the USA respectively. Mads Huuse acted as external examiner for this thesis who, along with Dave Hodgson is thanked for a rigorous and enjoyable viva. Also, for providing comments which have challenged me to improve this thesis.

There are some people without whom I would, quite literally have gone insane, firstly Rich who has been my constant anchor to reality through his love and unfailing support. I have been lucky enough to share office 7.131 with fellow troglodytes; Alan, Hollie, Jo, Rachael, Sarah and Steve who have managed to make me laugh when I never thought I could. I couldn't have done it without you. Finally, my parents, brother and sisters never allowed me to believe that I couldn't do it, so I got on and did it.

Funding for this research has come from the Natural Environment Research Council PhD studentship number NE/H524673/1 with additional financial support gratefully received from the Earth Surface Science Institute at the University of Leeds and the 2011 Gill Harwood Memorial Award from the British Sedimentological Research Group.

Abstract

Subsurface sediment remobilisation and subsequent extrusion records the release of overpressure through a sealing lithology by an injecting slurry. This investigation focuses upon injections occurring in the shallow-subsurface and utilises a multidisciplinary approach to reappraise the dynamics of sand injections across a variety of scales. The study provides detailed analysis from the laboratory and field on three scale of form: centimetre-scale fluidisation pipes, metre-scale extrusions and decimetre-scale fluidisation pipes. The investigation has helped bridge the knowledge-gap and converge ideas between traditional geologically-derived interpretations of sand injections and fluidisation pipes considered in chemical engineering. Laboratory modelling of fluidisation pipes provides the first process-based model of shallow sub-aqueous sand injection and extrusion in cohesionless sediments and recognises a series of processes hitherto unlinked to previously described internal sedimentary structures in fluidisation pipes. Fluidisation is shown to occur through a series of discrete phases and critically, the style, stability and temporal evolution of piping, along with flow velocity and concentration, are shown to exhibit considerable variability. The novel application of particle tracking velocimetry to active sand injections suggests that this technique could be invaluable in unravelling the flow dynamics in active injections. A process-based mechanism of sand extrusion formation is proposed through investigation of the internal architecture of seismically-induced sub-aqueous sandstone extrusions. Sand sheets are shown to form through deposition from gravity currents when multiple vents extrude coevally, whereas sand mounds or volcanoes will form from a single vent unless bypassing mechanisms such as channelisation influence sediment deposition. Previous estimate of flow velocity in sandstone intrusions and Reynolds numbers are shown to be inaccurate by up to two orders of magnitude. The investigation also demonstrates that sandstone-hosted intrusions exert control on basinal fluid flow in a manner previously identified only in mudstone-hosted intrusions and proposes a new model of the formation of the sandstone intrusions in Kodachrome Basin State Park.

Thesis Structure

Title:.....	i
Declaration of authorship.....	ii
Acknowledgments	iv
Abstract	v
Thesis Structure	vi
Table of Contents.....	vi
List of Figures	xii
List of Tables.....	xxi
Nomenclature.....	xxii

Table of Contents

1. Thesis context, significance and structure.....	1
1.1. Thesis rationale and objectives.....	1
1.2. Thesis structure	2
2. Outcrop and seismic based studies of sandstone intrusions.....	4
2.1. Fluidisation inferred from geological systems.....	4
2.2. Elements of a sandstone intrusion complex.....	5
2.2.1. Parent beds.....	6
2.2.2. Dykes and Sills	8
2.2.3. Sandstone extrusions	9
2.3. Injection in coarse grained environments.....	10
3. Clastic injection: liquefaction, fluidisation and injection processes	11
3.1. Introduction	11

3.2.	Seepage & liquefaction	11
3.3.	Transition from liquefaction to fluidisation	14
3.4.	Fluidisation	16
3.5.	Injection processes	17
3.5.1.	Overpressure	17
3.5.2.	Triggering	17
3.5.3.	Emplacement mechanisms	18
3.5.4.	Fluid types	19
3.6.	Post-intrusion fluid flow	19
3.7.	Summary	20
4.	Fluidisation Theory	21
4.1.	Introduction to liquid-solid fluidisation	21
4.2.	Binary Fluidisation	23
4.3.	Heterogeneous behaviour in solid-liquid suspensions.	24
4.3.1.	Channelling	24
4.3.2.	Wavy to bubbling regimes	25
4.3.3	Parvoids	26
4.4.	Phase changes in fluidisation regimes	27
4.5.	Grain size / shape effects on fluidisation	28
4.6.	Expansion characteristics of homogenous fluidisation	29
4.7.	Binary-solid fluidisation	32
4.7.1.	Inversion	33
4.8.	Bulk density effects	35
4.9.	Settling velocity effects	35
4.9.1.	Balancing the forces	36
4.9.1.	Segregation velocities	36

4.10.	Summary	37
5.	Experimental modelling of sand injection.....	38
5.1.	Introduction	38
5.1.1.	Fluidisation	40
5.2.	Experimental methodology	41
5.3.	Results.....	45
5.3.1.	Experimental parameters.....	47
5.3.2.	Void Formation and Infiltration.....	48
5.3.3.	Rupture.....	50
5.3.4.	Pipe Morphology	51
5.4.4.	Pipe Dynamics.....	57
5.5.	Discussion	63
5.5.1.	Infiltration and Void Formation.....	64
5.5.2.	Rupture.....	65
5.5.3.	Piping.....	66
5.5.4.	Venting	68
5.5.5.	Wall effects	73
5.5.6.	An integrated model of extrusive sand injectites	74
5.6.	Conclusions.....	77
6.	Pipe flow processes in sand injectites.....	79
6.1.	Introduction	79
6.1.1.	Flow conditions in active injections.....	80
6.1.2.	Evidence from erosive-type structures	81
6.1.3.	Laminations at pipe margins.....	83
6.1.4.	Experimental evidence	83
6.1.5.	Theoretical considerations of flow regimes in fluidisation pipes.	84

6.1.6.1.	Previous estimates of flow Reynolds number	86
6.2.	Experimental Methodology	90
6.2.1.	Tank setup.....	90
6.3	Data collection	92
6.3.1.	Particle tracking velocimetry.....	94
6.4.	Experimental results.....	98
6.4.1.	Pressure data.....	98
6.4.2.	Particle movement prior to pipe arrival	99
6.4.3.	Particle and fluid movement during fluidisation.....	102
6.5.	Discussion	113
6.5.1.	Pressure	113
6.5.2.	Particle concentration	113
6.5.3.	Calculation of flow regime in experimental pipes	114
6.5.4.	Flow structures.....	117
6.5.5.	Future work	121
6.6.	Conclusions.....	121
6.7.	Appendix: PTV code.....	123
7.	Sub-aqueous sand extrusion dynamics	131
7.1.	Introduction	131
7.1.1.	Sand volcanoes and mounds.....	132
7.1.2.	Sand sheets.....	132
7.2.	Geological Setting	134
7.2.1.	Soft-sediment deformation in the Shannon Basin.....	135
7.2.3.	Methods.....	136
7.3.	Results – Facies.....	137
7.3.1.	A – Undisturbed facies.....	141

7.3.2.	B - Deformed facies	143
7.3.3.	C – Remobilised facies	145
7.4.	Discussion	150
7.4.1.	Depositional mechanism.....	150
7.4.2.	Preservation of the sandstone sheet	152
7.4.3.	Existing models of sand sheet formation.....	153
7.4.4.	A process-based model of extrudite formation	155
7.4.5.	Identification of extruded sand sheets	157
7.5.	Conclusions.....	159
8.	Facies and fluid flow of sandstone-hosted columnar intrusions.....	160
8.1.	Introduction	160
8.1.2.	Intrusion Facies.....	163
8.1.3.	Methods.....	163
8.2.	Geological Background	164
8.2.1.	Stratigraphy	166
8.3.	Results.....	168
8.3.1.	Intrusion Facies.....	168
8.3.2.	Intrusion Morphology	173
8.3.3.	Internal Structures.....	175
8.3.4.	Intrusion and host relationships	178
8.3.5.	SEM data.....	179
8.4.	Discussion	184
8.4.1.	Palaeogeography.....	184
8.4.2.	Origin of the intruded material & timing	187
8.4.3.	Particle segregation in fluidization pipes	190
8.4.4.	Initial intrusion and microfracturing	191

8.4.5.	Flow regimes in pipes.....	192
8.4.6.	Flow regime and velocity during sand injection	194
8.4.7.	Flow Reynolds numbers	198
8.4.8.	Energy release and triggering mechanism	201
8.4.9.	Post Intrusion Fluid Flow	203
8.4.10.	Implications for petroleum exploration.....	205
8.5.	Conclusions.....	206
8.6.	Appendix.....	207
9.	Sandstone- and mudstone-hosted intrusions, a comparative analysis: geometry, facies, processes, and fluid flow.	210
9.1.	Introduction	210
9.2.	Architectural elements of clastic intrusions.	211
9.3.	Distribution of sandstone intrusions.....	214
9.4.	Extrudites	216
9.5.	Intrusion and host rock relationships.	219
9.6.	Internal processes in injectites.....	221
9.7.	Facies in clastic intrusions.....	222
9.8.	Intrusions as long-term fluid conduits.....	223
9.9.	Ease of recognition in core and seismic data.....	224
9.10.	Suggestions for future work	225
10.	References.....	228

List of Figures

- Figure 2.2.** Schematic block diagram showing the elements of a sandstone injection complex. Parent sand body geometry is marked by dashed line. Modified from Hurst *et al.* (2011). 6
- Figure 2.3.** Conical sandstone intrusions from the Faroe-Shetland basin showing characteristic discordance. Arrows denote the tops of the intrusions. From Cartwright *et al.* (2008). 8
- Figure 3.1.** Compressibility of mixed particle systems; (a) as deposited; (b) effects of compression and shearing. Redrawn from Yamamuro and Lade (1999). 13
- Figure 4.1.** Basic set-up for a fluidised bed. (1) water inlet, (2) inlet section, (3) homogenising section, (4) distributor plate, (5) column containing particulate bed. Adapted from Asif *et al.* (1992). 22
- Figure 4.2.** Determination of the minimum fluidisation velocity from the pressure drop across a bed (left) and the bed height (right). A-B region is where particles are in a fixed bed, at the base of a column. Fluidisation begins at point B, flow rate decreases from point C. Incipient fluidisation is point D. Redrawn from Couderc (1985). 22
- Figure 4.3.** Richardson-Zaki plot of dimensionless fluidisation velocity against time-averaged mean voidage to demonstrate discontinuous bed expansion. From Didwania and Homsy (1981). 26
- Figure 4.4.** Classification of fluidisation behaviour of solids (horizontal axis) by ambient water (left, vertical dimensional axis) or by any fluid (right, vertical dimensional axis). p_p is particle pressure, d_p grain diameter and De is a dimensionless density number ($\rho p p$) (Redrawn from Di Felice (1995). 28
- Figure 4.5.** (A) The disparity in slope between experimental settling velocities (symbols) and Richardson-Zaki predictions (lines). Whereas when wall effects are ignored (B), experimental values of n as a function of Re (symbols) are in good agreement with Richardson-Zaki predictions (line). Adapted from Di Felice and Kehlenbeck (2000). 32
- Figure 4.6.** Bed inversion phenomenon. Black filled circles represent type 1 (smaller, denser) particles, large open circles denote type 2 (large, less dense)

particles. From Di Felice (1995), based on experimental observations of Moritomi *et al.* (1986)..... 34

Figure 5.1. **(A)** Schematic illustration of experimental set up, **(B)** Details of inlet pipe configurations. (Run 6 middle configuration, Run 7, bottom configuration, all others as top)..... 42

Figure 5.2. A series of video stills demonstrating the most significant periods in the structural evolution of a run (here *Run 4*). **(A)** Starting 3-layer stratigraphy. Apparent slight doming on the upper surface of the sediment and in the middle layer is due to barrel distortion. **(B)** Initiation of void. **(C)** Rupture occurs and pipe propagates to surface. Infiltration horizon can be seen above the dish-shaped fine layer following fluidisation. **(D)** Venting at surface and initiation of secondary pipe. **(E)** Piping has stabilised and fine material can be seen lining the inner edges of the pipes. **(F)** Final geometry showing pipes and sand volcanoes. Much of the fine layer has been elutriated and redeposited on top of the sediment column. The times at which these stills were taken are as follows (in minutes and seconds): **A** – 0.00, **B** – 2.22, **C** – 8.30, **D** – 8.33, **E** – 9.43, **F** – 11.05. Scales shown are in centimetres (lower) and inches (upper). 46

Figure 5.3. **(A)** Diagram of the inclined pipe in *Run 4* demonstrating stress pipes in the infiltration horizon above the pipe. Scale bar 1 cm. **(B)** Red arrows highlight stress pipes aligned at a high angle to the walls of a clastic sill. Coin for scale is 3 cm diameter (adapted from Diggs (2007))..... 49

Figure 5.4. Preservation of initial rupture zone results in fine sediment swirls preserved in surrounding coarse sediment. From *Run 2*, at 0.42 minutes (upper) and 1.57 minutes (lower). Key features have been outlined in **B** to enhance clarity. Scales shown are in centimetres (lower) and inches (upper). 51

Figure 5.5. Pipe morphologies from 2 runs. Video frames have been interpreted for clarity. **(A)** From *Run 5* at 0.59 minutes. The main pipe is migrating to the left whilst the pipe to the right stays stationary, both maintaining a vertical morphology. A poorly defined zone of fluidised, convecting sediment exists to the right of the main pipe. Sand ball morphology is seen to the right of the right-hand pipe. **(B)** From *Run 7* at 1.52 minutes. There are eight, clearly defined pipes venting water and fluidised

sediment, each separated by unfluidised sediment from the original top layer or clasts of incorporated top-layer material. Black dots are 1 cm spaced..... 53

Figure 5.6. Series of stills from Run 10 demonstrating the development of dyke and sill style piping. A) Following rupture and piping onset, a new pipe begins to migrate upwards and horizontally from a deformed sediment boundary. B) Horizontal migration is abandoned in favour of vertical migration. C) Fluidised sediment “ponds” and migrates laterally beneath an impermeable heterogeneity, either pre-existing in the upper sediment layer or due to fine sediment amalgamating on the upper edge of the sill. D) The pipe reaches the sediment surface and begins venting sediment. This morphology remains stable for the duration of this run. Black dots are 1 cm spaced..... 56

Figure 5.7. Effects of pipe migration on layering. The pipe has migrated to the left from out of view on the right of the photo. The original fine ballotini layer has been completely removed and the boundary between the coarse ballotini and overlying silica sand is difficult to discern due to fluidisation. Aggregates of fine ballotini that were originally in the middle layer are left suspended in the silica sand layer, which also contains coarse ballotini. This is evident from the colour difference on the right and left of the pipe. From *Run 9* at 6.23 minutes. Black dots are 1 cm spaced..... 58

Figure 5.8. Photograph of an excavated sand volcano orientated with the sediment surface at the top. The topographic feature has relief of 4 mm and has a clear vent. Dashed lines denote the region where a pipe would be expected if it were present. Scale in mm..... 60

Figure 5.9. Topographic relief created through venting. Important features are labelled and topography marked by the dashed lines. **A)** *Run 4* at 10.22 minutes. The sand volcano is approximately 2 cm high and has two vents fed by separate pipes. The pipe to the right is venting sediment at a faster rate than the left hand pipe. Horizontal scale is 30 cm. **B)** *Run 11* at 7.30 minutes. Pipe is migrating to the left of the picture and relict topography of oviform sand mounds is visible to the right of the picture. **C)** *Run 7* at 5.30 minutes. Multiple pipes have produced an undulating topography, with an extinct pipe (centre, marked by thick arrow) in the depression between two active sand volcanoes and an active vent on the far right

with negative topographic relief. Black dots are 1 cm spaced. **D)** *Run 4* post-experiment vent, millimetre scale visible. **E)** *Run 9* at 1.47 minutes, post-experiment. Fine sediment can be seen draped over an asymmetric vent. To the right of the vent sediment flows comprising the sand volcano flanks are clearly visible. **F)** Internal structure of sand volcano in *Run 4*. 61

Figure 5.10. Schematic representation of a new model of pipe formation in cohesionless sediments. **A)** Starting conditions with a fine sediment layer between two, thick, coarse sediment layers. When overpressure is generated heterogeneities in the upper layer determine whether the system develops into **B)** (homogeneous upper layer) An even void forms beneath the fine sediment layer immediately followed by infiltration of fine sediment into the top layer and stress pipe formation (partial fluidisation) or **C)** (heterogeneous upper layer) An uneven void is formed with an inverted conical shape. Infiltration into the upper layer occurs with localised absence of infiltration horizon at void apex. From these initial stages the following occurs: **B1)** Rupture and initial pipe formation. Failed rupture zones may be preserved and a fluidised zone develops at the base of the pipe which is now elutriating fluidised sediment. This configuration is not stable. **C1)** In this scenario, one or two rupture zones may have occurred resulting in two pipes elutriating sediment and water. Most of the fine sediment has been removed, although a small amount remains between pipes. **C2)** here multiple ruptures have occurred, leading to multiple pipes. Most fine sediment has been elutriated and a zone of fluidised sediment exists below the base of pipes. An unstable configuration which will lead to one of the pipes becoming dominant and others shutting down. **D1)** A dominant pipe has stabilised and the rim is lined with fine sediment; preventing pipe migration. A localised zone of fluidised sediment exists around the vent with down bending of all layers orientated towards the base of the pipe. **D2)** Unconfined pipe migrates laterally. Original stratification is undisturbed on the leading side of the pipe whereas where the pipe has passed, sediment is homogenous and relict topography is preserved on the surface. A zone of circulating fluidised sediment is associated with the rear of the migrating pipe. **E)** Schematic demonstrating gravity currents flowing down the sides of a sand volcano to develop sand sheets and fine-

grained sediment is held in suspension before settling and draping sand volcano. This model does not take into account atypical features such as double void apex formation, dyke and sill intrusions, unusual topography and infiltration associated with sub-vertical pipes.	76
Figure 6.1. Diagram showing the range of outcrop evidence for low regime in injections. Heavy arrows denote flow direction in each example. Flow in G is into the page.	82
Figure 6.2. Velocity as a function of sand fraction; r is conduit radius. From (Gallo and Woods (2004)).	85
Figure 6.3. Velocity (u) as a function of conduit radius (r) for a given overpressure at the base of the fracture (s) is sand fraction. From Gallo and Woods (2004).	86
Figure 6.4. Schematic showing the experimental set up. Dotted area is the gravel and mesh baffle. All input pipes are shown in blue. Those from the manifold to the test tank are all the same length (1 m).	92
Figure 6.5. Photograph of the upper sediment layers to demonstrate stratigraphy. Apparent curve of fine layer is due to barrel distortion arising from tank curvature. The fine Ballotini layer is 1 cm thick.	92
Figure 6.6. (A,B) Frames extracted from video files to demonstrate the very fine-detail achievable using a commercially available digital video camera (Nikon 3100) when the particles are stationary (right of image) compared to streaking and lack of detail when particles are in motion (left of image). (C) Sample frame from the Phantom camera. Flow in the pipe is from the base left to the top right; and black “seeding” particles are visible in the centre of the pipe.	93
Figure 6.7. Schematic to show particle tracking between frame-pairs.	95
Figure 6.8. Photographs to demonstrate how the high speed camera and LED lights are mounted relative to the tank. A – Led lights, B – Tank wall.	96
Following a successful experimental run in which a fluidisation pipe passed through the field of view, the following steps were undertaken to process the images ready for particle tracking: (i) isolation of the area of interest in the image sequence using image masking in order to minimise noise; (ii) application of a Sobel operator to increase individual particle visibility (see details below); (iii) calculation	

of the arithmetic mean of all 100 images in the stack by computing the average values of the pixels' intensity in pre-defined interrogation areas; (iv) subtraction of the calculated image mean from each subsequent image in the stack to remove any stationary features in the image; (v) subtraction of a duplicate of the first image from the stack (this further reduces/removes stationary features); (vi) subtraction of a duplicate of the last image from the stack (this further reduces/removes stationary features); and, (vii) conversion to double images as required for the particle tracking steps outlined in section 6.3.1. Note that the Sobel operator is an edge detection filter that performs a 2-D spatial gradient measurement on an image and thus highlights the particle edges, having the overall effect of increasing the contrast of the seeding particles. 96

Figure 6.10. Close-up of the infiltration horizon that commonly develops above the fine-grained layer. 100

Figure 6.9. Pressure trends from runs 1-5. Left hand images are the pressure trends for the complete duration of each experimental run with the exception of the end of run 4 (D) and the beginning of run 5 (E). The vertical grey bars highlight the time period shown in the right-hand graph ('). Red arrows 1 and 2 denote consecutive rupture events. A 20-point moving average has been applied to the 20 s intervals (black line) to remove noise and improve visualisation of the pressure trends. 101

Figure 6.11. Inclined infiltration of fine-grained sediment prior to the arrival of a migrating fluidisation pipe (light coloured zone to left of images). Secondary grain (white arrow) shows sub-horizontal path. Initial and final grain locations denoted by black circles. Total time elapsed is 1 second. 102

Manually measured flow velocities of particles at various points across the pipe diameter are presented below (Table 6.2). These measurements capture individual particles that the code is, as yet, unable to track. All particles were tracked over a 100ms period to ensure that the same particle remained in field of view. 105

Figure 6.12. From experiment 5. Time-series of interpreted video frames over a 20 s period (every 10th frame) demonstrating particle trajectories and the variety of morphologies at any given time. Frames run from top left to bottom right. Frames are 16 mm wide. 106

Figure 6.13. (Left) From Experiment 4, showing every-other frame extracted over 2 seconds of video (left) to demonstrate the spatial and temporal variation in pipe morphology. (Right) Interpretation of the video frames showing particle trajectories (arrows) and flow zones. The pipe is migrating from left to right. Frames are 16 mm wide. Key is the same as Figure 6.12.	107
Figure 6.14. The horizontal and vertical components of the flow across the whole field of view, as derived by the PTV code. Red box denotes area shown in Figure 6.15.	108
Figure 6.15. Horizontal and vertical velocity vectors below $1 \times 10^{-2} \text{ ms}^{-1}$	109
Figure 6.17. Series of consecutive images demonstrating the trajectory of a particle suspended in the main flow over 40 milliseconds. Image is $23.57 \times 17.33 \text{ mm}$	112
Figure 6.18. The pressure field at the pipe wall associated with travelling waves. m_0 = number of eigenvalues in the plane. Dark red corresponds to negative values, white to positive values. From Wedin and Kerswell (2004).	119
Figure 6.19. Axial section of a pipe at different downstream positions showing three-fold azimuthal symmetry in a travelling wave at $\text{Re} = 1250$. High speed streaks in the downstream flow component at the pipe wall (red) are more stable than low speed streaks (blue) near the centre of the pipe. Velocity components are shown by arrows, negative values are red and positive values are blue. From Faisst and Eckhardt (2003).	119
Figure 7.1. Location map of the study area.	135
Figure 7.2. Photomontage of the outcrop at Freagh Point, facing West. Faults are marked and sand volcano vents are shown by white dots along with facies distribution in the underlying interpretation. Yellow 1 m scale bar to centre-left. See text for facies codes.	138
Figure 7.3. Detailed sedimentary log of the study area with units and facies codes.	139
Figure 7.4. Photographs demonstrating the facies present (A) sand volcanoes with sandstone sheet comprising facies C1. (B) View facing NE, of units 4, 5 and 6. Yellow notebook sits on unit 4. Red arrow denotes thickness of facies A1. (C) Photomontage of units 1 and 2 showing deformation in facies B1. (D) View	

perpendicular to (E) to demonstrate large-scale dewatering structures and lack of directional indicators within this facies. Red arrow denotes extent of facies *A1*. (E) Bedding plane view of top of unit 3, showing mud diapir (*B2*) within *B1*. Person is standing above one edge of diapir. 140

Figure 7.5. 3D schematic model of Freagh Point idealised along the plane of a major growth fault which cross-cuts the outcrop, demonstrating the relationships between and within the facies present. Facies labels and stratigraphic units are shown on the left of the figure. 141

Figure 7.6. Photomontage of facies *C1* where it is cross-cut by a major growth fault. Continuous laminations within the sand-sheet are well preserved and have been interpreted (white lines) for clarity. Images flow from top-left to bottom-right. ... 146

Figure 7.7. Scatter diagram of flank angles from representative sand volcanoes. The data demonstrates the decrease in sand volcano flank angles with increased distance from vent, up to 30 cm. A minor increase in flank angle is seen at 40 cm, or equidistant between vents. 147

Figure 7.8. Cross-sectional view through the extruded sandstone sheet highlighting a sand volcano and positions of back-scattered electron diffraction images of the sandstone sheet demonstrating the decrease in grain-size away from vents. Quartz grains are black. Lens-cap for scale in upper image. 148

Figure 7.9. Photomontage demonstrating the relationship between facies *C2* (individual sand volcanoes outlined in red) and *A1* (white laminations). Scale bar (yellow) 1 m. 149

Figure 7.10. Process-based model of extrudite formation. (A) Where multiple, closely-spaced vents are present, the interaction of gravity currents will produce a sand-sheet with continuous laminations between vents. (B) A single vent will produce a discrete feature, such as a mound due to radial gravity flows. Long term extrusion events will result in channelling, redirecting the radial gravity flows, resulting in deposition away from the extrusion-site as shown to the right of the cartoon. 156

Figure 8.2. Geological Map of the study area with pipes. All pipes occur within the Carmel Formation or Gunsight Butte Member of the Entrada Sandstone. Modified after Doelling <i>et al.</i> (2000).....	165
Figure 8.12. Model depicting injection complex architecture and processes. (A) Fluid Flow from Navajo sandstone. (B) Fluidisation and pipe intrusion with preferential exploitation of conglomeratic channels in Carmel Formation. (C) Laminated Rind facies with placer-style accumulation of heavy minerals in concentric laminations. (D) Hydro-fractured clast breccia in silty facies of the Gunsight Butte Member. (E) Normal and reverse grading in sills. (F) - Extrusion (max. pressure gradient). (G) Exotic lithologies suspended in pipes (Page Sandstone, Carmel Formation, chert pebbles from J-2 unconformity). (H) Fluidisation zones possibly representing vents at the palaeosurface.	186
Figure 9.1 Synthesis of the key similarities and differences between mudstone-hosted, sandstone-hosted and shallow sandstone intrusions based on experimental and field observations combined with those from the literature.....	213
Figure 9.2 Tripartite architecture of mudstone-hosted intrusions (left, from Hurst <i>et al.</i> , 2011) and bipartite architecture of sandstone-hosted intrusions.....	211
Figure 9.3 Summary of the relationship between host strata and the architecture of sandstone intrusions in the Panoche Giant Injectite Complex. The “sill zone” is marked by the red box. From Hurst <i>et al.</i> (2011) based on Vigorito and Hurst (2010).....	214
Figure 9.4. Intrusion margins at a range of scales. Curvilinear intrusion margins with thick, fine-grained lining. From experiments in Chapter 7. B. Interpreted sketch of a sandstone sill, host rock is white and margin is curvilinear. Flow is from left to right in image. Adapted from Kawakami and Kawamura (2002). C. Undulous margin between injected banded sandstone (SC) and host mudstone (HC) interpreted as a scallop. Adapted from Scott <i>et al.</i> , (2009).....	220

List of Tables

Table 4.1. Values of the dimensionless parameter n as a function of the terminal Reynolds number. From Richardson and Zaki (1954) and Di Felice and Kehlenbeck (2000).	32
Table 5.1. Summary of parameters used in the experiments. Glass bead and silica sand densities were 2.6 g cm^{-3} . Hydraulic head was 105 cm in all experiments. Water velocities were assumed to be approximately 0.3 cm sec^{-1} , the lower detection limit of the flow meter. All experiments had a 1 cm thick middle layer, composed of fine Ballotini ($0\text{-}44 \text{ }\mu\text{m}$) with $<10\%$ Poly V [®] ($1.1\text{-}1.2 \text{ g cm}^{-3}$) as a tracer. See Figure 5.1 for details of inlet configuration.	45
Table 5.2. Wall effect numbers for this and previously published studies.....	74
Table 6.1. Calculated volumetric flow rates for each experimental run	99
Table 6.2. Particle flow velocities at a range of pints across the pipe diameter.....	106
Table 6.3. Calculated pseudo-fluid density (ρ_{pf}) and viscosities (μ_{pf}) from experimental observations.....	116
Table 6.4. Calculated maximum and minimum flow Reynolds numbers for measured velocities in an active fluidisation pipe (experiment 3) based on pseudofluid values.....	116
Table 6.5. Calculated flow Reynolds numbers with density and dynamic viscosity values for pure water.	117
Table 8.1. Facies present within the injections.	170
Table 8.2. Mean porosities for each facies averaged over 5 samples. Porosity calculated by point counting.....	181
Table 8.3. Minimum settling velocities for a clast diameter of 0.7 m as a function of grain concentration in the pseudo-fluid, for the example in Scott <i>et al.</i> (2009).....	198
Table 8.4. Minimum settling velocities for a clast diameter of 3 m through a pseudo-fluid of varying particle concentrations, for a pipe in the Kodachrome Basin.	199
Table 8.5. Recalculated minimum flow velocities and flow Reynolds numbers for the data in Scott <i>et al.</i> (2009) showing that values have dropped by up to 2 orders of magnitude.	200
Table 8.6. Calculated Reynolds numbers (Re) for grain concentrations of $\phi = 0.54$, $\phi = 0.35$ and $\phi = 0.15$ for a pipe in the Kodachrome Basin.....	202

Nomenclature

A	Aperture (m)
Ar	Archimedes number
C	Cohesive strength
C_D	Drag coefficient for a particle in relative motion with a fluid (non-dimensional)
$C_{D,o}$	Drag coefficient for a solitary particle in relative motion with an infinite fluid (non-dimensional)
d	Clast diameter (m)
d_s	the diameter of a sphere with the same volume as the particle
d_c	the diameter of a circle of the same area as the projected profile of the particle in its most stable orientation
ε	Voidage
e	Void ratio
E_{pot}	Potential energy
F_k	Drag force
η	Porosity
G	Specific gravity
g	Acceleration due to gravity
$H_{(c)}$	Pipe height / 3
i_c	Critical hydraulic gradient
k	Volumetric shape factor
n	an exponent, a function of particle shape
φ	Solid volume fraction
φ_s^*	Pseudofluid in contact with the larger particle phase
ρ	Density (kg m^{-3})

Ψ	Sphericity / grain shape
σ_n	Normal stress
ϱ	Internal friction coefficient
τ	Shear stress
T	Tensile strength
μ	Kinematic viscosity (Pa s)
U	Velocity (ms ⁻¹)
V_d	Volume of the injected sand grains

Subscripts

s,p	solid
f	fluid
pf	pseudo fluid
q	quartz
L	larger particle
S	smaller particle
i	single sphere
mf	minimum fluidisation

This page is intentionally left blank

1. Thesis context, significance and structure

1.1. Thesis rationale and objectives

The recognition of sandstone intrusions as an important component in hydrocarbon plays within the last 18 years has promoted a period of intensive research focussed on the subsurface remobilisation of sediment. (e.g. Dixon *et al.*, 1995; Molyneux *et al.*, 2002; Huuse *et al.*, 2004; Hurst *et al.*, 2005; Lonergan *et al.*, 2007) Prior to their recognition in hydrocarbon plays, sandstone intrusions have been recognised in a range of geological settings for nearly 200 years (Murchison, 1827) and ancient examples of extrusions were described in the mid 20th century (Gill and Kuenen, 1957). Although it is widely accepted that sand injection results from the fluidised flow of sand into fractures, driven by overpressured fluids, there remains a lack of process understanding regarding the nature of the flow during active injections and direct observations of the impact on surrounding sediments. Transport and subsequent sedimentation of grains from parent sand bodies has, until now, remained poorly understood and the dynamics of the intrusion process itself have been largely ignored. Given the inability of field and core-based studies to shed light upon the sedimentary processes in active injection, physical modelling offers considerable potential for constraining the flow conditions during injection. As sand injection occurs in a wide variety of sedimentological settings and at a range of scales (e.g. Saucier, 1989; Purvis *et al.*, 2002; Strachan, 2002; Davies *et al.*, 2003; Moreau *et al.*, 2011), it may be assumed that the processes remain largely similar throughout. The modelling component of this project sets out to recreate sand injections in a laboratory environment, building upon previous conceptual ideas, with the aim of understanding the dynamics of clastic injection, from process to product.

The field-based aspect of this project is framed by a gap in the knowledge surrounding both the dynamics of sand extrusion in subaqueous settings and the nature of injection in coarse-grained successions. Extruded sandstones are known to form stratigraphic traps for hydrocarbon accumulations as sheets or mounds with 4-way dip closure (Hurst *et al.*, 2006; Andresen *et al.*, 2009). As oilfields such as the Eocene Chestnut reservoir in the North Sea may already be producing from extruded sandstones (Huuse *et al.*, 2005), there exists a need to further the understanding of their formation dynamics and geometries in order to aid their recognition in the future.

Although many of the studies in the recent surge of literature have been focussed on the nature of injections in deep-water, or at least, fine-grained successions, there remained a lack of investigations into injections in continental strata. Aeolian plays can comprise vast reservoirs such as the Argyll/Ardmore field in the Central North Sea (Gluyas, 2005) and injections have been recognised in such successions in outcrop (Netoff, 2002; Chan *et al.*, 2007; Loope *et al.*, 2013; Rowe, 2013). It must be considered however, that such intrusion will be practically invisible in 3-D seismic data and the identification of facies may prove enigmatic in core. Therefore a systematic investigation of the geometries and facies of sandstone injections hosted in the aeolian Entrada Sandstone of the Colorado Plateau is undertaken with the aim of highlighting their significance in coarse-grained strata and shedding light on the complex relationships between injection and host strata from a new perspective.

1.2. Thesis structure

This thesis begins with an introduction to the concept of fluidisation and the conditions required for inducing sand injection. This is followed by a theoretical review of fluidisation which discusses relevant literature from a chemical engineering point of view to support the inferences made in later chapters. This leads into a review of fluidisation in geological systems in the form of sand

injection. Results in the form of four independent research chapters are presented, each with their own rationale, discussion and conclusions, two of which are published, one is in review and the fourth is in preparation for publication. The thesis is concluded with a synthesis of the key advances made in relation to the existing knowledge of mudstone-hosted sandstone intrusions.

2. Outcrop and seismic based studies of sandstone intrusions

2.1. Fluidisation inferred from geological systems

Fluidisation is known to be important for the formation of a wide range of geological features, including: i) *en masse* dewatering structures, ii) clastic dykes and sills, and, iii) sand volcanoes, sand sheets and other extrudites (e.g., Maltman, 1994; Jolly and Lonergan, 2002; van Rensbergen *et al.*, 2003; Gallo and Woods, 2004; Hurst *et al.*, 2006; Vigorito *et al.*, 2008; Rodrigues *et al.*, 2009). Sandstone intrusions are the product of the remobilisation of unconsolidated sediments in the subsurface by the flow of fluids, most often basinal waters produced during consolidation and dewatering of underlying sediments (Jonk *et al.*, 2005). At low fluid velocities, pore fluid is able to percolate through sediment without creating a local difference in velocities between fluid and sediment grains (liquefaction) or suspending the sediment (fluidisation), this is termed seepage (Lowe, 1975).

The most detailed description of classical fluidisation in nature from the so-called boiling sand springs in Nebraska (Guhman and Pederson, 1992) where the upwards flow of groundwater through cylindrical conduits acts to suspend sand grains, although no net-flow of sand occurs. Guhman and Pederson (1992) report this phenomenon in a series of springs close to the Dismal River and attribute the localised flow of water to secondary permeability in buried cohesive units. Springs are up to 10 m in diameter and have been plumbed to depths of 44 m revealing circular cross-sections and defined walls. The “boiling” sand layer consists of a mixture of sand grains and water, where the sand grains are held in suspension and are overlain by clear water, with a distinct interface separating them. In this case the

sand is fluidised by the upward-flowing water, and as the authors report a “churning action” in the suspended sand, it is possible that the fluidised column is exhibiting heterogeneous behaviour (*Section 3.3*). During measurement of spring depth using a 9 kg weight on the end of a line, sharp tugging was felt at 26 m depth, this could possibly be due to “necking” of the conduit causing increased turbulence (Guhman and Pederson, 1992).

2.2. Elements of a sandstone intrusion complex

A comprehensive review by Hurst *et al.*, (2011) has provided an elegant classification of the elements of an intrusive complex and these are summarised in Figure 2.2. An intrusion complex can generally be subdivided in four components; (i) a parent sand body; (ii) dykes; (iii) sills; and, (iv) extrusions. Sandstone sills are approximately concordant with the fabric of the host strata and are generally considered to be tabular bodies but are known to exhibit “stepping” with minor discordance connecting adjacent sills. Dykes are generally discordant and cross-cut stratigraphy and are termed low-angle dykes up to 20° and high-angle above 20°. Although the review of Hurst *et al.*, (2011) is inclusive of most aspects of sand injection, owing to bias in the pre-existing literature towards injection in mudstone-dominated successions, much of the review therein refers to injections in deep-marine environments. This section aims to briefly appraise the current understanding and introduce additional elements that have previously been overlooked due to their small scale or recent identification.

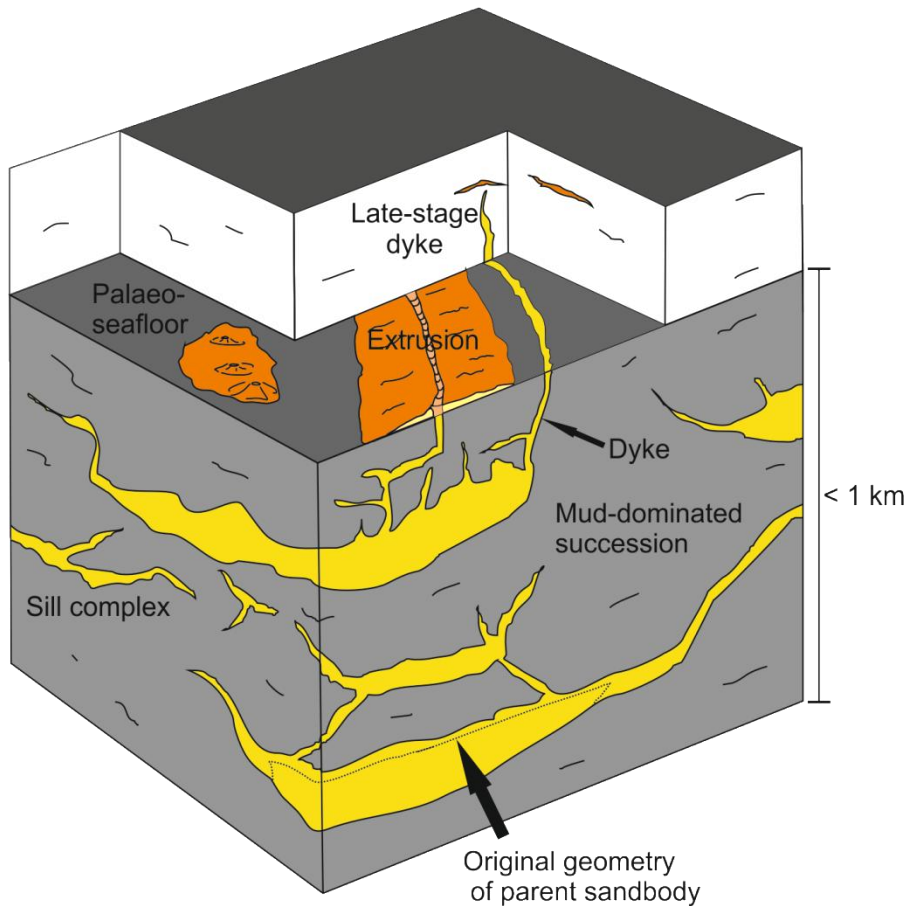


Figure 2.2. Schematic block diagram showing the elements of a sandstone injection complex. Parent sand body geometry is marked by dashed line. Modified from Hurst *et al.* (2011).

2.2.1. Parent beds

A non-exhaustive list of parent sand-bodies for injection complexes has been compiled by Hurst *et al.*, (2011) with 11 out of the 15 studies based on deep-marine depositional elements (Dixon *et al.*, 1995; Surlyk and Noe-Nygaard, 2001; Hillier and Cosgrove, 2002), Purvis *et al.*, 2002; Strachan, 2002; Duranti and Hurst, 2004; Briedis *et al.*, 2007; Hamberg *et al.*, 2007; Hubbard *et al.*, 2007; Lonergan *et al.*, 2007; Satur and Hurst, 2007) and two studies being based on shallow-marine systems (Obermeier, 1996; Hildebrandt and Egenhoff, 2007), demonstrating the bias in recognition from deep-marine successions. This may in part be due to differential erosion of mudstone and sandstone enabling their enhanced recognition in outcrop,

but is primarily due to the density difference between mudstone and clearly discordant sandstone bodies which is so easily discernible in seismic data (Fig. 2.3).

In all cases however, the parent unit shows extensive dewatering in the form of; (i) dish and pillar structures (e.g. Surlyk and Noe-Nygaard, 2001; Duranti and Hurst, 2004), (ii) inclined laminae (e.g. Dixon *et al.*, 1995); Purvis *et al.*, 1992) and/or, (iii), a degree of homogenisation and loss of depositional fabric (e.g. Obermeier, 1996; Hamberg *et al.*, 2007). As suggested in Figure 2.1, the external geometry of a parent unit is often heavily modified by remobilisation and subsequent injection and is often transformed from lenticular channels to lenses with mounded tops (e.g. Duranti and Hurst, 2004; Wild and Briedis, 2010) and “wing-like” margins (e.g. Huuse *et al.*, 2007; Jackson, 2007; Cartwright, 2010). Many of these examples are limited to remobilisation at depth (> 100 m) and little research has been conducted into the effects of fluidisation on shallow-buried sandstone bodies with the exception of Hildebrandt and Egenhoff (2007) and Oliveira *et al.*, (2009). The model of Hildebrandt and Egenhoff (2007) is scrutinised in detail in section 7.6 with regard to the proposed seafloor extrusion above shallow-marine massive sands, however, the internal structures reported from shallowly buried remobilised bodies are consistent with their deep-water counterparts with pervasive dish structures, flame structures and structureless zones (Hildebrandt and Egenhoff, 2007; Oliveira *et al.*, 2009; 2011)

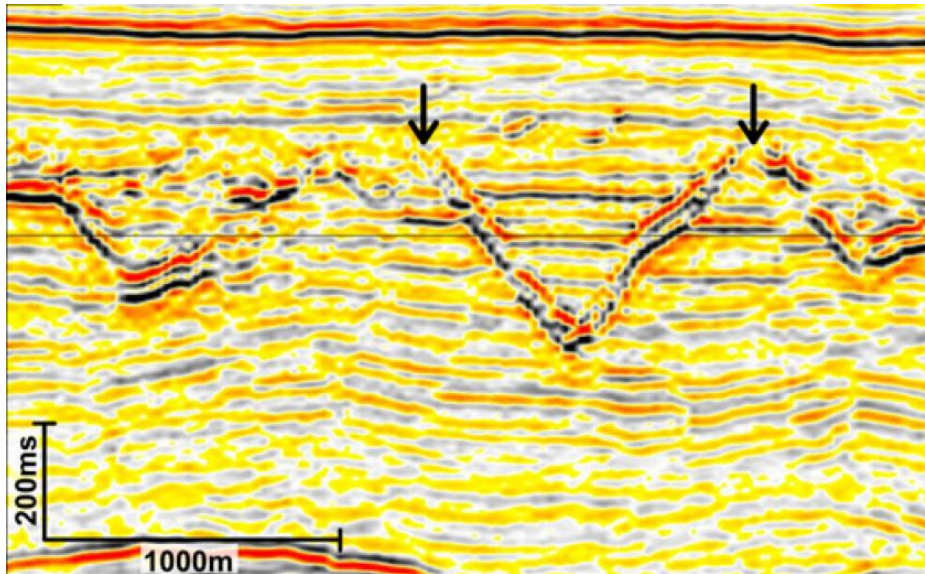


Figure 2.3. Conical sandstone intrusions from the Faroe-Shetland basin showing characteristic discordance. Arrows denote the tops of the intrusions. From Cartwright et al. (2008).

2.2.2. Dykes and Sills

Sandstone dykes and sills form the intrusive element of mudstone-hosted injection complexes and their dimensions, external geometries and internal sedimentological textures have been studied extensively in core and outcrop (e.g. Peterson, 1968; Taylor, 1982; Duranti and Hurst, 2004; Diggs, 2007; Parize et al., 2007; Thompson et al., 2007; Scott et al., 2009; Sherry et al., 2012). Tabular or saucer-shaped sills can extend laterally for kilometres and dykes can cross-cut over 100 m of stratigraphy (Huuse et al., 2005b; Vigorito et al., 2008). It is thought that the macro-scale (m to km) geometry of these intrusive elements is controlled primarily by the process of hydrofracturing (Levi et al., 2011) with the immediate (< 1m) relationship between the intrusion and host strata being dominated by erosive processes such as corrasion and abrasion (e.g. Kawakami and Kawamura, 2002; Diggs, 2007; Scott et al., 2009; Kane, 2010). Erosion is not observed along the entire margins of sandstone injections and much of the eroded material consists of clasts of mudstone or host-rock which is then suspended in the sandstone intrusion (e.g. Scott et al., 2009). The nature of injectite margins and how they relate to flow conditions during

emplacement is discussed in more detail in Chapter 6. Very little is known about the grain-scale processes that are involved in the incorporation of host strata into the active injection; corrosion is believed to be a dominant process along with hydrofracturing and subsequent spalling of the host (Scott *et al.*, 2009). Evidence providing the basis of the corrosion theory includes sand grains (from the injecting slurry) being embedded in (host) mudstone clasts (Scott *et al.*, 2009), however, there is no way to discern at what point in the intrusion process the grains became imbedded, thus highlighting the need for further experimental study of injection processes.

Dykes are not always linear features and geometries include; tapering (Strachan, 2002); bulbous and curved (Parize *et al.*, 2007); bifurcating (Hubbard *et al.*, 2007); and planar features (Duranti and Hurst, 2004). Outcrop and core-based studies are inherently limited in terms of spatial analysis unless comprehensive 3-D exposure of an injection complex in outcrop occurs. Sills are generally tabular features but have been reported as showing bifurcation (Truswell, 1972) and stepping (Parize *et al.*, 2007) although their geometry is likely to be inherently linked to the stratigraphic architecture of the horizontal strata into which they intrude.

2.2.3. Sandstone extrusions

Extrudites or sandstone extrusions are bodies of sand that have been vented following the intersection of a sand injection with the surface and have been described from a wide-variety of stratigraphic settings and on a range of scales from centimetres to kilometres (Chapter 7.1). Often strongly associated with seismic activity (Obermeier, 1996; Quigley *et al.*, 2013), extrusions can take the form of sand volcanoes, such as the well-known examples up to 1.5 m in diameter from the Carboniferous of County Clare, Ireland (Gill and Kuenen, 1957; Strachan, 2002) but can also produce extruded “sheets” of sand covering up to 250 km³, as in the North Sea subsurface (Løseth *et al.*, 2012). These large-scale examples are described from seismic data and the extruded sand purportedly displays features such a wedging-out radially and gently dipping internal reflectors (Løseth *et al.*, 2012), similar

characteristics to outcrop-observed counterparts (Hurst *et al.*, 2006). Analogue experiments have been conducted which investigate the distribution of fluidised sediment once erupted through a fracture (Rodrigues *et al.*, 2009; Ross *et al.*, 2011). The experimental observations of Rodrigues *et al.* (2009), although heavily cited by Løseth *et al.* (2012), could be called into question as air is utilized therein as the ambient medium into which sediment was ejected. The implications of this ambiguity and the dynamics of extruded material and how extrudites are formed are discussed in detail in Chapter 7.

2.3. Injection in coarse grained environments

Studies investigating the remobilisation of sand and subsequent injection into a coarse-grained host remain somewhat behind the level of research into mudstone-hosted injections. The numerous examples of sand injected into mud in the literature highlight their increasing recognition as a key component of deep-water clastic systems (e.g. Parize and Friès 2003; Huuse and Mickelson 2004; Jackson, 2007; Shoulders *et al.*, 2007; Vigorito *et al.*, 2008; Cartwright 2010). However it is clear that remobilisation and injection do occur in coarse-grained clastic systems, and on a variety of scale, ranging from cm-scale dykes and sills (Glennie and Hurst, 2007; Hurst and Glennie, 2008) to decimetre-scale “mega-pipes” and columnar intrusions (Hannum, 1979; Netoff, 2002; Huuse *et al.*, 2005b; Chan *et al.*, 2007). As the fine-grained sealing mudstone inherent to deep-water systems is mostly absent in these coarse-grained settings, other strata such as evaporites and carbonates with low vertical permeabilities (Chan *et al.*, 2007) can prevent early dewatering and subsequent overpressuring of pore fluid in the parent bed. The aim of Chapter 8 is to investigate how the injection processes in aeolian strata, may differ from those in fine-grained hosts in terms of initiation and development. Chapters 5 and 6 detail experimental modelling of sand injection in coarse-grained strata.

3. Clastic injection: liquefaction, fluidisation and injection processes

3.1. Introduction

Soft-sediment deformation (ssd) is considered to occur in unlithified sediments or sedimentary rocks that are not entirely lithified as a result of intergranular movement in response to an applied stress. A combination of forces acting on an unstable sediment is often responsible for the genesis of ssd structures, the most ubiquitous being gravity, which results in Rayleigh-Taylor instabilities, downslope-movement and compaction (Maltman, 1994). If sediment has not undergone sufficient compaction and remains underconsolidated with high porosity, low-cohesion and inter-granular bonds, it will be susceptible to remobilisation. This requires grains to be mobilised by the fluid flow through the sediment (the most prevalent source of fluid being water lost from consolidation of surrounding sediments) and subsequent upwards transport of those grains to a new locus as an injection. Subsurface fluid migration is driven by a pressure differential between the pore fluid and either a shallow aquifer or the surface/seabed.

3.2. Seepage & liquefaction

Grains of non-cohesive sediment are acted upon by three forces; (i) the tractive force of the cumulative flow driven for example by the hydraulic head; (ii) the local seepage force, and; (iii) gravity. If the flow of fluid through the sediment exerts no net force upon the grains and results in little to no grain reorganisation, it can be termed seepage. The phenomenon of liquefaction occurs when an external factor, such as cyclic loading from seismic shock pressurises pore fluid in sediment and destroys a metastable particle configuration (Hird and Hassona, 1990). If pore

pressure is increased to equal that of the burial pressure, the effective stress on the sediment / pore water mixture is therefore zero and the sediment acts as a viscous fluid, showing no shear strength (Maltman, 1994). Rounded grains have been shown to liquefy more easily than angular grains or sediments containing significant amounts of platy minerals, which increase the compressibility and cohesion of sediment (Hird and Hassona, 1990).

Yamamuro and Lade (1999) tested natural sands for their liquefaction potential using undrained triaxial compression testing. This technique determines the shear strength of a material by the deviation from the measured compressive strength. They show that most earthquake-induced liquefaction occurs in loose, silt rich sands, although most laboratory studies on liquefaction have been performed on clean sand and that there is a strong correlation between the liquefaction potential of a soil and its fines content (Yamamuro and Lade 1999). Isotropic compression was conducted to create confining pressures (25 – 500 k Pa) and shear tests were commenced immediately before creep could occur in the test sample. At low confining pressures (< 125 k Pa), complete static liquefaction occurs whereas at higher confining pressures the sample underwent temporary liquefaction and showed dilatant behaviour. Liquefaction potential was also tested by increasing the fines content, from zero to 50% and it was found that liquefaction potential increased with increased fines content. When compression tests with no fines were carried out, the sample did not undergo static liquefaction. Yamamuro and Lade (1999) suggest that increasing the percentage of fine grained material in a sample results in the effective stress paths being depressed, with smaller differences in initial peak stress. The authors also studied the axial strain in the sample and noted that it decreases as the fines content is increased. They concluded that despite the increase in sample density through increased fines content, the liquefaction potential increased and therefore neither void ratio, or density of sand should be used as an indicator of liquefaction potential. These findings are confirmed by Shapiro and Yamamuro (2003) who showed through laboratory testing that the

presence of silt greatly increased the compressibility of otherwise clean sand. In order to explain this behaviour, Yamamuro and Lade (1999) put forward a hypothesis regarding the structure of sediments with liquefaction potential; if silty-sand is deposited under low-energy conditions the particle-structure is highly compressible. The fabric has a loose structure with fine grains occupying the void space between larger particles. Most of the load placed on test sediment with this type of structure is supported by the larger grains, with fine grains merely acting to increase the overall density of the sediment, without affecting overall behaviour. Nevertheless, some of the fine grains will be present at the contacts of the larger grains, sometimes holding them apart; it is these particle interactions that are responsible for the compressive behaviour of the sediment. When the system is compressed and sheared, these fine-particles are forced from between the grain contacts and into the void spaces, thus decreasing the overall volume of the sediment (Figure 3.1.)

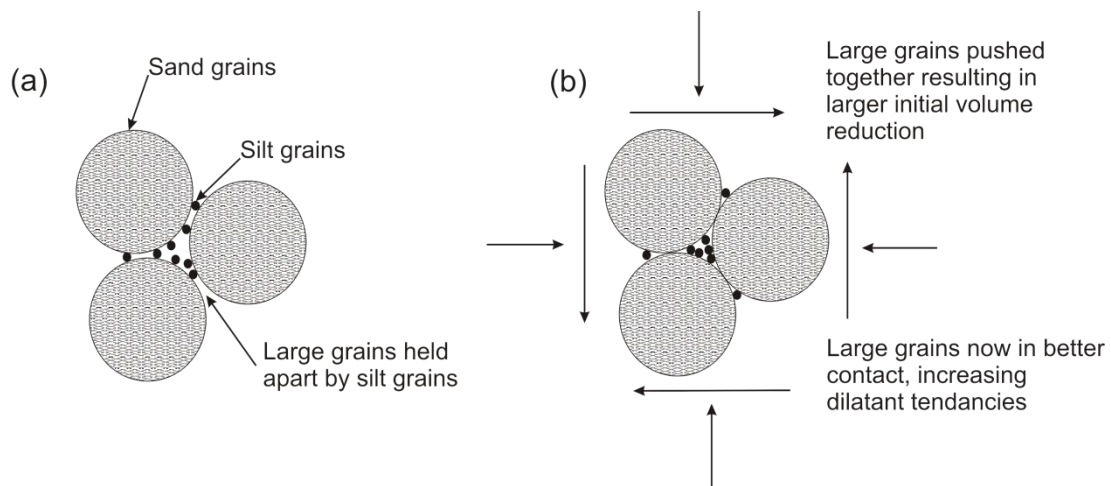


Figure 3.1. Compressibility of mixed particle systems; (a) as deposited; (b) effects of compression and shearing. Redrawn from Yamamuro and Lade (1999).

Experimental triaxial testing of silty sediments found that increasing fines content from 0-44% decreased the liquefaction resistance of fine to medium sand, with this trend being reversed for fine fractions above 44% (Xenaki and Athanasopoulos, 2003). This is known as the transition fines content, and up to this fines content,

compressive behaviour is mainly controlled by the larger grains. Beyond this critical threshold, compression behaviour is controlled by the fine grains. This threshold can be anywhere between 20% and 44% depending on the fine fraction, volume fraction and stress conditions (Monkul and Ozden, 2007). It was found that in mixed sediment, shear strength decreases with a corresponding increase in silt content whereas for a layered sample with the same amount of silt, shear strength is unaffected (Naeini and Baziar, 2004). If the mean grain diameter ratio ($D_{50\text{-sand}}/d_{50\text{-silt}}$) also influences liquefaction potential with small ratio resulting in increasing liquefaction potential corresponding with increasing fines content. As $D_{50\text{-sand}}/d_{50\text{-silt}}$ increases, liquefaction potential of the silty sand becomes close to that of clean sand (Monkul and Yamamuro, 2011)

Under undrained conditions, when pore-water is still present in a sample, pore pressure will increase and the potential for liquefaction becomes obvious (Yamamuro and Lade 1999); this situation is most applicable to sediments at the surface where compaction has not occurred. It is this uncompacted structure proposed by Yamamuro and Lade (1999) that may also be responsible for increased dilatancy with increased confining pressures, as well as decreasing compressibility of the sediment and increasing the “stiffness” of the sediment structure.

3.3. Transition from liquefaction to fluidisation

Seepage is unlikely to create sedimentary structures unless the system becomes liquefied, by seismic shock for example, or an increase in fluid velocity fluidises the system. According to Lowe (1975), the term seepage can also be applied when pore-fluid flow rates are above the minimum fluidisation velocity, but the sediment is either highly compact or confined by an overlying permeable layer as drag on the sediment particles is negated by compaction. This scenario can be represented graphically (Figure 2.1) where the area below the dashed line represents a fixed bed of particles, where contacts between the particles negate the difference between

weight and particle-fluid interaction forces. Between the two curves, particles are suspended and fully supported by the fluid. Above the solid curve, drag force exceeds particle weight, but only in a system with an overlying confining layer, restraining particle movement (Di Felice, 2010). This would be termed seepage by the classification of Lowe (1975).

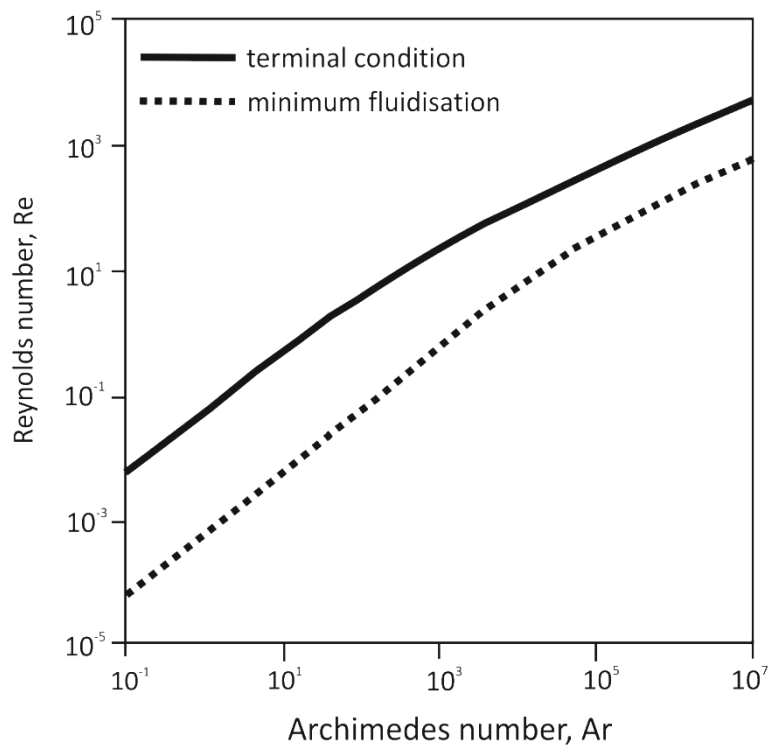


Figure 2.1. Minimum fluidisation and terminal Reynolds number as a function of Archimedes number. The area above terminal condition denotes seepage at high fluid velocities where the drag force exceeds particle weight. Adapted from Di Felice (2010).

The upper, “seepage” zone is probably very common in natural geological systems, but most fluidisation features form when the confining overlying layer is impermeable and pore pressure builds up in the saturated bed. In order to fluidise grains in a sealed system, there must be a differential pressure gradient across the

bed (Jolly and Lonergan, 2002). If a saturated, overpressurised bed is capped by an impermeable unit, the overburden pressure is partially supported by the pore fluid, and partially by grain-grain contacts. Overpressure occurs when the pore fluid pressure in a sealed bed is greater than the surrounding, or hydrostatic pressure (Maltman, 1994). Sudden hydraulic fracture of the sealing unit occurs when overpressure in the sealed bed reaches a critical threshold and would create the required pressure gradient, fluidising the grains and entraining them. Once excess pressure has been released, fracture propagation stops, and the grain-water mixture freezes as a clastic intrusion or sand injection (Jolly and Lonergan, 2002). If the overlying strata are cohesive, fracture occurs as planar dykes orientated parallel to the least compressive strength (Jolly and Lonergan, 2002) and where overlying sediments are non-cohesive, intrusions occur as pipes (Nichols, 1995, Ross *et al.*, 2011). Flow regimes in fluidisation pipes have yet to be determined although theoretical estimates have been calculated based upon grain-size and textural relationships in sand injections (Duranti and Hurst, 2004; Scott *et al.*, 2009; Sherry *et al.*, 2012). It has been suggested that flow in liquefied systems is dominantly laminar and fluidisation is characterised by a turbulent flow regime (Duranti and Hurst, 2004; Hurst *et al.*, 2011) although Di Felice (2010) clarifies this as systems with $Ar < 10$ are dominated by viscous forces and are therefore laminar, and those with $Ar > 10^5$ are dominated by inertial forces and are therefore turbulent.

3.4. Fluidisation

Once sediment has been liquefied it is primed for fluidisation and will remain in this state until pore pressure is reduced below the burial load (Maltman, 1994). Fluidised sediment injection can only occur if fluid migration through the sediment driven by a pressure gradient is of a sufficient velocity to overcome any resistance the grains have to mobilise due to friction thus entraining the grains as a slurry which continues to flow until the pressure gradient has been equalised.

3.5. Injection processes

3.5.1. Overpressure

In order to initiate fluidisation and sand injection, a parent bed must be overpressured, in that pore-fluid pressure must be elevated, and will build as a function of the sealing capacity of the host and the rate of fluid charge into the parent bed (Hurst *et al.*, 2011). The change in the sealing capacity of the host rock can be related to the mechanical compaction rate of mudstone, or diagenesis and subsequent cementation of sandstone. The development of overpressure can also be driven by the reduction in pore volume within the parent bed due to disequilibrium compaction and may also be driven by tectonic compression on a basinal scale, a relatively rapid method of building overpressure (Osborne and Swarbrick, 1997). On a smaller scale, overpressure can be driven by a hydraulic head difference over a river channel levee for example (Li *et al.*, 1996; Singh *et al.*, 2001) or due to artesian flow in an aquifer (Dragantis and Janda, 2003) provided a sealing lithology is present above the aquifer. Diagenetic phase transitions such as the opal A to CT can release water within a buried parent sand body (Davies *et al.*, 2006), and provided a seal is present, can produce overpressure and prime the reservoir for fluidisation when triggered.

3.5.2. Triggering

It is the catastrophic release of overpressure in the parent sand body and fracturing of the sealing lithology that ultimately results in sand injection and the mechanism that triggers this release is varied. The most cited cause of fluidisation and sand injection is seismic activity (e.g. Saucier, 1989; Obermeier, 1996; Moretti, 2000; Boehm and Moore, 2002; González de Vallejo *et al.*, 2005; Huuse *et al.*, 2005b; Hildebrandt and Egenhoff, 2007; Moretti and Sabato, 2007; Alfaro *et al.*, 2010) due to the cyclic loading imparted into the overpressured reservoir, although until recently, evidence for earthquake induced sand injection was only available from the shallow subsurface (e.g. Saucier 1989; Obermeier, 1996). Cyclic stresses can also

be imparted by storm waves and result in sand injection (Hildebrant and Egenhoff, 2007) and tsunamis are known to cause sand injection (Le Roux *et al.*, 2008) and subsequent extrusion (Martin and Bourgeois, 2011). Load induced overpressuring may result from the rapid deceleration of a slump above an overpressured reservoir for example (Strachan, 2002). Bolide impact has even been suggested as a trigger for large-scale sand injection (Alvarez *et al.*, 1998). The rapid migration of brines or hydrocarbon fluids into a sand body can initiate fluidisation and perhaps sand injection (Cartwright *et al.*, 2003; Jonk *et al.*, 2005). The migration of fluids from deep within a basin is attributed to the formation of the largest sandstone intrusion complexes in the North Sea Basin (e.g. Løseth *et al.*, 2013; Huuse *et al.*, 2005b).

3.5.3. Emplacement mechanisms

3.5.3.1. Hydrofracturing

The failure or rupture of any sealing strata is assumed to be by hydraulic fracture that occurs when the pore pressure in the parent sand body exceeds the fracture gradient of the seal (Jolly and Lonergan, 2002). Two processes are involved; firstly a fracture will initiate and propagate through the surrounding lithology and secondly, due to a pressure gradient between the parent sand-body and the fracture tip, fluid will migrate out of the parent sand-body, and if the velocity of that fluid is above the minimum fluidisation velocity for the sediment, be filled by fluidised slurry of sand and fluid. At depth, the initiation of the hydrofracture is thought to be reliant on the on the intersection of the differential stress with the Griffith extensional failure envelope of the host strata. For example when the internal fluid pressure in a sedimentary succession or parent sand body acts against the principle stresses within the host.

Near-surface propagation of clastic dykes has also been analysed as a coupled fluid and elastic-fracturing process where the flow rate for the fluid has been solved simultaneously with the elastic deformation of the host (Levi *et al.*, 2011). This

approach is based upon solving equations for a fracture driven by a fluid and on the stress intensity criterion for propagation.

3.5.4. Fluid types

Formation fluids are generally assumed to be the fluidising medium in most cases of sand injection (Hurst *et al.*, 2011) with hydrocarbons sometimes acting as a contributing agent (Duranti and Mazzini, 2006; Sherry *et al.*, 2012) Significant volumes of fluid are inferred to have been involved in the process of sand injection (Duranti, 2007). In some cases, hydrocarbons are thought to have partially driven the injection process (Jonk *et al.*, 2005; Sherry *et al.*, 2012) though not solely due to the increased relative buoyancy of the fluids (Jonk, 2010). The presence of gas raises interesting questions certainly with regard, not only to the hydrodynamics of fluidisation (see *section 3.2*), but the energy and potential explosiveness of the injection process due to the high buoyancy of hydrocarbon gases such as methane as a driving fluid as suggested by Hubbard *et al.* (2007). This may counteract the low viscosity of the gas and thus lower capacity to support grains and large clasts in a flow.

3.6. Post-intrusion fluid flow

Numerous examples exist of hydrocarbon-stained sandstone injections in the subsurface (Mazzini *et al.*, 2003), and outcrop (e.g. Jenkins, 1930; Sherry *et al.*, 2012), and their importance as hydrocarbon reservoirs (Dixon *et al.*, 1995; Duranti *et al.*, 2002; Huuse *et al.*, 2005; de Boer *et al.*, 2007; Briedis *et al.*, 2007) merely highlights their role as long-term fluid conduits following their emplacement. Multiple stages of cementation revealed through cathodoluminescence have been utilized to show injections may act as single-phase fluid flow conduits (Mazzini *et al.*, 2003). Petrographic and microthermometric fluid-inclusion analysis has revealed a complex fluid-flow history from the Kimmeridgian of NE Scotland involving fluidisation by fluids other than the ambient pore-fluid and subsequent migration

of host basinal fluids (Jonk *et al.*, 2003). It would seem obvious that the relatively high permeability and porosity of sandstone injected into mudstone would make them conduits for fluid-flow long after their emplacement, but no study to date has investigated the effects of sandstone intrusion on fluid-flow in coarse-grained successions. *Section 8.4.9* forms the first study to address this question.

3.7. Summary

Sudden release of overpressure from saturated, unconsolidated sand through hydraulic fracturing of an overlying, sealing lithology, results in injection of a sand-fluid slurry into the fracture. Once the excess pressure has been released, the fracture closes onto the intruded grains as a sand injection. Planar sandstone injections are common features of deep marine environments and form once element of injection complexes which also incorporate; parent sand beds; sills and, extrusions and are recognised on a range of scales from mm to seismic-scale.

Suggested triggers for the release of overpressure include, but are not limited to, seismic shock, tsunamis and rapid loading and although aqueous fluids are a common fluidising medium, hydrocarbons have been shown to emplace some injection

4. Fluidisation Theory

4.1. Introduction to liquid-solid fluidisation

Where solid particles lie on top of one another in a bed, they are said to be in a fixed state. It is not until they come into contact with a flow, which in geological applications may be water, gas or brine that they can become fluidised and the bed becomes a two-phase system. Fluidisation occurs when each individual particle becomes suspended in the flow and the bed as a whole remains static (Couderc, 1985). Figure 4.1 shows the set-up required for fluidisation in a circular or rectangular column. A homogenising manifold (3 in Figure 4.1) is required to ensure even water flow across the whole column and prevent deviations for ideal behaviour (see *section 4.2.1.*) (Couderc, 1985).

In an idealised situation, a pressure drop on the base of the bed occurs at incipient fluidisation where individual particles are suspended in the flow and increases with flow rate until the bed becomes completely fluidised, with the particles able to move freely within the bed (Couderc, 1985; Di Felice, 1995). The total volume of the bed also increases during fluidisation as the particulate framework is no longer grain-supported and becomes fluid-supported. As demonstrated in Figure 4.2 the incipient, or minimum fluidisation velocity is determined using the decreasing flow rate (Point D, Figure 4.2.) and is the shift between the fluidised and fixed state. The fundamental fluidisation condition is defined by the equality between the fluid pressure drop across a fluidised bed and the buoyant weight of the solid particles per unit area of a cross-section of the bed.

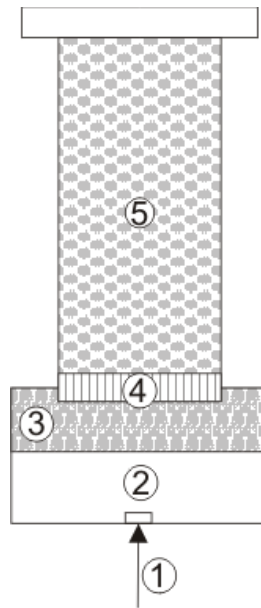


Figure 4.1. Basic set-up for a fluidised bed. (1) water inlet, (2) inlet section, (3) homogenising section, (4) distributor plate, (5) column containing particulate bed. Adapted from Asif *et al.* (1992).

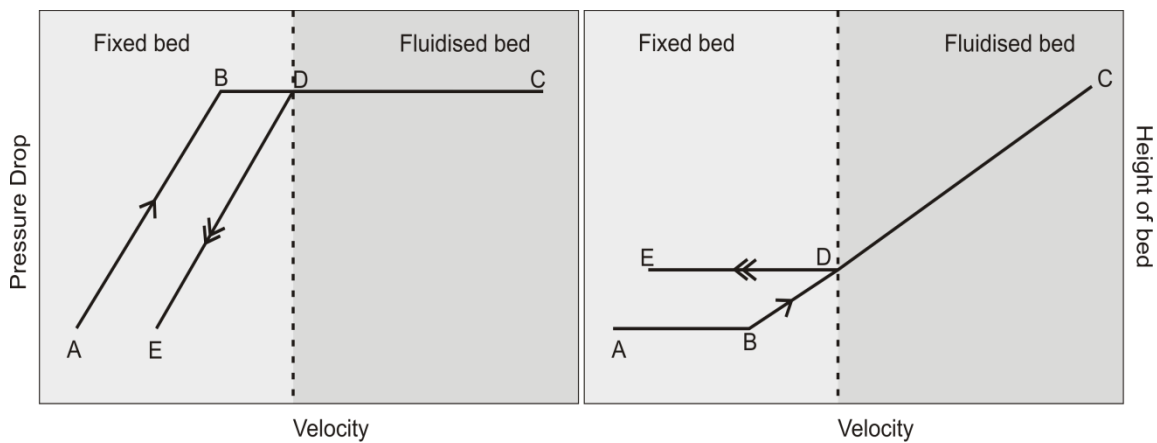


Figure 4.2. Determination of the minimum fluidisation velocity from the pressure drop across a bed (left) and the bed height (right). A-B region is where particles are in a fixed bed, at the base of a column. Fluidisation begins at point B, flow rate decreases from point C. Incipient fluidisation is point D. Redrawn from Couderc (1985).

The minimum or incipient fluidisation velocity can be empirically derived into *Equation 4.1*. Using the following conditions:

U_{mf}	Minimum fluidisation velocity
d	Grain size
ϕ	Grain shape
ρ_s	Grain density
ρ_f	Fluid density
μ	Fluid viscosity
ε_{mf}	Intergranular porosity (voidage) at minimum fluidisation velocity
g	Acceleration due to gravity

The following equation is valid for the minimum fluidisation velocity of a bed of spheres at a low Reynolds number (< 20) (Stanley-Wood *et al.* (1990):

$$U_{mf} = \frac{\varepsilon_{mf}^3 (\rho_s - \rho_f) g (\phi d)^2}{s (1 - \varepsilon_{mf}) \mu 36} \quad (4.1)$$

4.2. Binary Fluidisation

There are key differences between idealised liquid-solid (particulate) and gas-solid fluidisation systems, the most important to note is that in liquid-solid systems the bed will expand homogenously with the particles moving apart steadily. Whereas in a gas-solid system, where the density contrast between the particles and the fluidising medium is high, bubbles form at the base of a fluidised bed and rise up through it; this type of system is said to be aggregative and not particulate (Di Felice, 1995). The above behaviours describe idealised systems in a steady state.

Liquid – fluidised suspensions also demonstrate unsteady state behaviour as outlined below.

4.3. Heterogeneous behaviour in solid-liquid suspensions.

4.3.1. Channelling

Channelling is a deviation from the idealised homogenous behaviour of fluidised beds and is characterised by locally organised solid movements often in the form of two vertical conduits, one channelling upwards where liquid velocities are high and one downwards within the bed where liquid velocities are lower. These vertical channels are connected by horizontal flows and can be recognised by an uneven pressure drop across the bed at minimum fluidisation in an initially homogenous sediment. It is thought that channelling behaviour develops as a result of the uneven distribution of water at the base of the fluidising bed (Handley *et al.*, 1966; Couderc and Angelino, 1970 *in Couderc, 1985*) and may be avoidable with the use of a homogenizing section at the base of the bed either in the form of a distributor plate or a fixed section just below the fluidised bed comprised of solid particles (Couderc, 1985).

4.3.2. Wavy to bubbling regimes

Didwania and Homsy (1981) identified four discrete flow regimes in water-fluidised beds of glass beads from photographic analysis and optical light transmission measurements through the bed. They conclude that the boundaries between the regimes are distinct and in order of increasing U/U_{mf} : wavy flow, wavy flow with transverse structure, fine-scale bubbling flow; and bubbling. This was the first report of a bubbling state in low-density particulate fluidisation, a

regime usually observed in gas-fluidised systems. For the particles used in their experiment *Set A*, $U_{mf} = 0.73 \text{ cm s}^{-1}$, voidage waves begin to form in the upper part of the bed when $U/U_{mf} = 1$ to 1.4 and develop a transverse structure as they propagate upwards through the bed. These waves begin to form further down the bed as U/U_{mf} increases, until $U/U_{mf} = 3.4$. Above this value, a turbulent regime develops and no bubbles form until $U/U_{mf} = 4.4$, above which occasional bubbles develop until a threshold is reached at $U/U_{mf} = 6.5$ when a bubbling regime appears (Didwania and Homsy, 1981). Changes in the expansion behaviour of the bed were also noted during regime changes, notably that the bed expanded uniformly during wavy and turbulent regimes, but fluctuations in the height of the bed were seen during the bubbly regime and sharp transition in bed behaviour were observed as demonstrated by Figure 4.3. Other studies have noted similar inhomogenities, such as bubbles and high voidage waves and are comprehensively listed in Di Felice (1995).

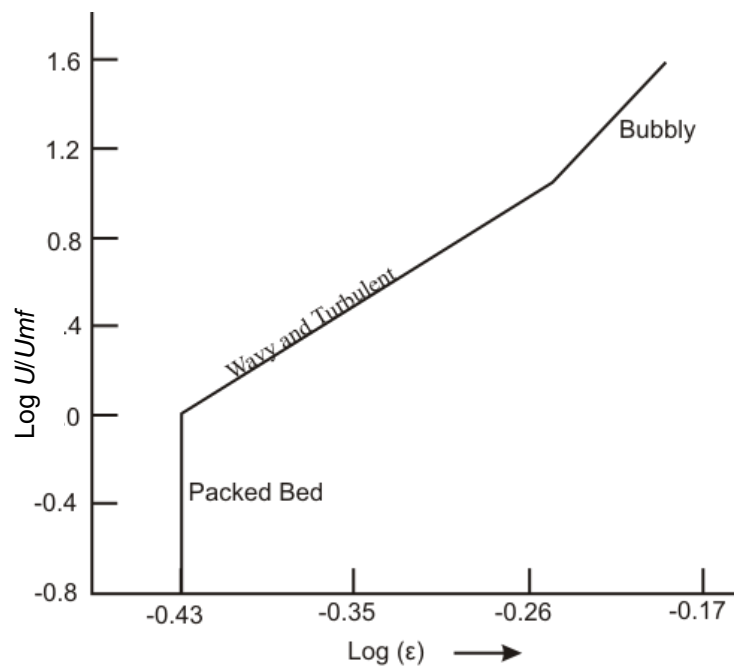


Figure 4.3. Richardson-Zaki plot of dimensionless fluidisation velocity against time-averaged mean voidage to demonstrate discontinuous bed expansion. From Didwania and Homsy (1981).

4.3.3 Parvoids

These are high-voidage horizontal bands that form at the base of a fluidised bed, just above the distributor. They are approximately 1 cm deep, can occupy all or part of the cross-section of the bed and propagate upwards through the bed through the raining of particles from the top to the bottom until they break through at the bed surface. Unlike channelling, parvoids do not form as a result of uneven distribution of fluids, but are natural instability phenomena of fluidised beds (Couderc, 1985). They were first noted by Hassett (1961) in fluidised beds of glass ballotini as horizontal bands of low density or completely void bubbles (Hassett, 1961). Rising bands of low density regions have also been reported for systems employing viscous liquids such as glycerin as a fluidising medium (Volpicelli *et al.*, 1966) and high-density particles (Singh and Joseph, 1991).

4.4. Phase changes in fluidisation regimes

Although no systematic study into bubbling phenomena has been carried out (Di Felice, 1995) it has been put forward that the maximum size of a bubble is reached when its rising velocity equals the single-particle settling velocity (Didwania and Homsy, 1981). The size, shape and upwards velocity of the bubble is heavily dependant on the viscosity of the fluid (e.g. glycerin, paraffin, water) and the density of the solid (Harrison *et al.*, 1961). Equations derived in Di Felice (1995) and Gibilaro *et al.*, (1990) are able to predict the minimum bubbling voidage for copper-water or lead-glycerin beds as particle size or fluid properties are changed, and the phase changes during fluidisation by any fluid as a function of the dimensionless Archimedes number (Ar) (Figure 4.4).

$$Ar = \frac{d^3 \rho_f (\rho_p - \rho_f) g}{\mu_f^2}$$

(4.2)

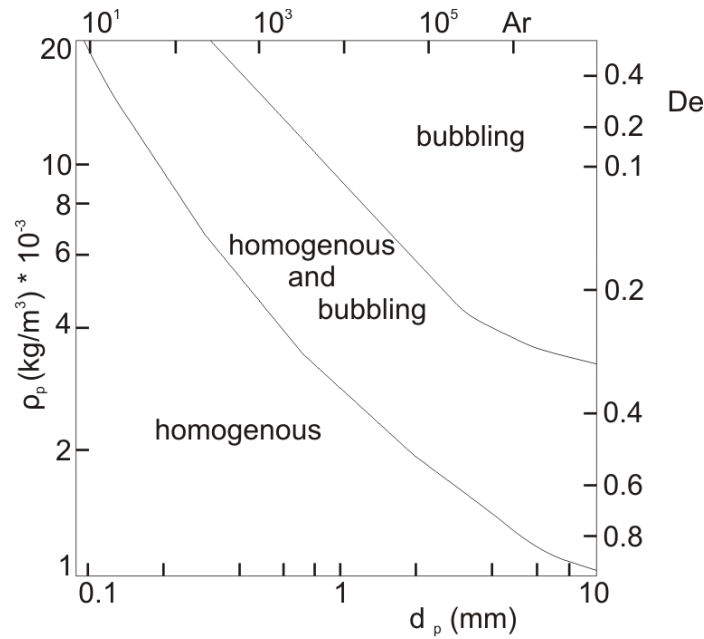


Figure 4.4. Classification of fluidisation behaviour of solids (horizontal axis) by ambient water (left, vertical dimensional axis) or by any fluid (right, vertical dimensional axis). p_p is particle pressure, d_p grain diameter and De is a dimensionless density number $(\frac{\rho}{\rho_p})$ (Redrawn from Di Felice (1995)).

4.5. Grain size / shape effects on fluidisation

The minimum fluidisation velocity is affected by particle shape, size and density and therefore is relevant only when all the particles in a bed are uniform. As noted above, beds expand when they become fluidised and equations have been devised from experimental results to analyse the relationship between velocity within the fluidised bed (u) to the settling velocity of a single sphere in the column (u_i) to the void fraction within the bed (Couderc, 1985). Other results have been derived using the drag force (F_k) on a particle within a fluidised bed and the drag force (F_{ks}) acting on a single sphere and how the ratio between these values is affected by the bed voidage, thus determining a voidage function (Equation 4.3).

$$f(\varepsilon) = \frac{F_k}{F_{ks}} \quad (4.3)$$

Particle shape can also have a significant effect on the expansion behaviour of fluidised beds and further equations have been devised by Limas-Ballesteros *et al.*, (1982) to incorporate the sphericity (ψ) of a solitary particle (*Equation 4.4*) and a particle in a fluidised bed (*Equation 4.5*).

$$F_k/F_{ks} = f(\varepsilon, \psi) \quad (4.4)$$

$$F_k = V(\rho_p - \rho_L)g \quad (4.5)$$

These estimations show a good correlation with experimental results, having a mean deviation of 4.3% for spheres and 3.7% for non-spherical particles (Limas-Ballesteros *et al.* 1982). Also, when studying the expansion properties of beds of mixed solids, it is important to determine the variation of void fraction with height, not solely the void fraction (Couderc, 1985).

4.6. Expansion characteristics of homogenous fluidisation

When a liquid solid bed is fluidised, the contact between the upper surface of the bed and the freeboard (the zone just above the particle bed surface) remains smooth and sharp unless the particle suspension has a particularly low concentration or particle sizes are disparate (Di Felice, 1995). The expansion characteristics of a bed can be affected by physical boundaries such as the distributor plate at the base of the system or the walls of the column. It has been shown by Asif *et al.* (1992) that the distributor plate only affects the homogeneity of fluidisation if the particle density is low. They found that low density plastic beads (1.61 g/cm^3) were significantly and easily affected by jets of fluid issuing from the outlets in the distributor plate, causing stirring effects. High density (2.46 g/cm^3), 2 mm diameter glass beads are not affected in this manner, even over a wide range of liquid superficial velocities ($4 - 16 \text{ cm s}^{-1}$) and bed pressure drops (0.5 – 22 kPa). Asif *et al.* (1992) propose that this

is due to the movement of the dense particles dissipating jets of water emerging from the distributor plate, thus negating any distortion of the flow. The effect of the particle diameter / column diameter ratio (d / D) on bed expansion characteristics is less well investigated, although it has been recognised that in heterogeneous fluidisation, d / D and more particularly, the column diameter can have a significant effect on the shift between wavy and bubbling regimes for example (Di Felice, 1995). Loeffler and Ruth (1959) carried out experiments to determine whether d / D has any discernible effects on homogenous fluidisation and it was found that fluidisation characteristics are only affected when the column diameter is of the same order of magnitude to the particle diameter.

Richardson and Zaki (1954) were the first to summarise the relationship between bed voidage and the superficial fluid velocity in a fluidised bed and relate this to the terminal settling velocity of a single particle in the system. Through an extensive series of experiments in a range of flow regimes, they investigated the sedimentation behaviour of liquid-solid suspensions and the effect the void fraction has on the settling velocity of a particle. The culmination of these results was what is now known as the Richardson-Zaki correlation, valid for a bed of spheres of a specific size (*Equation 4.6*), and shows that the ratio of the superficial liquid velocity to the settling velocity of a single particle is a function of the overall voidage in a fluidised system:

$$u = u_i \varepsilon^n \quad (4.6)$$

Richardson and Zaki (1954) also demonstrated that n is a function of the flow regime (from viscous to inertial) shown by the terminal Reynolds number (Re_t) and the d/D ratio (where Re_t is $d_p \rho u_i / \mu$ (dimensionless) d_p is the particle diameter and D the tube diameter). Therefore, for example in a viscous flow regime, where $Re_t < 0.2$: $n = 4.65 + 19.5 d/D$ (Richardson and Zaki, 1954). Table 4.1 summarises the following correlations from Richardson and Zaki (1954) which have also been summarised by Di Felice (1995) and Di Felice and Kehlenbeck (2000).

$Re_t < 0.2$	$n = 4.65 + (19.5 * d/D)$
$0.2 < Re_t < 1$	$n = 4.35 + (17.5 * d/D)^{-0.03}$
$1 < Re_t < 200$	$n = 4.45 + (18 * d/D)Re_t^{-0.1}$
$200 < Re_t < 500$	$n = 4.45 Re_t^{-0.1}$
$Re_t > 500$	$n = 2.39$

Table 4.1. Values of the dimensionless parameter n as a function of the terminal Reynolds number. From Richardson and Zaki (1954) and Di Felice and Kehlenbeck (2000).

Taking into account the wall effects of the column, Di Felice and Kehlenbeck (2000) suggested that; according to the Richardson-Zaki correlation, the wall-effect becomes more pronounced as a suspension becomes more concentrated, which does not agree with experimental results. Once the wall-effect is removed however, the Richardson-Zaki correlation agrees well with experimental data (Figure 4.5)

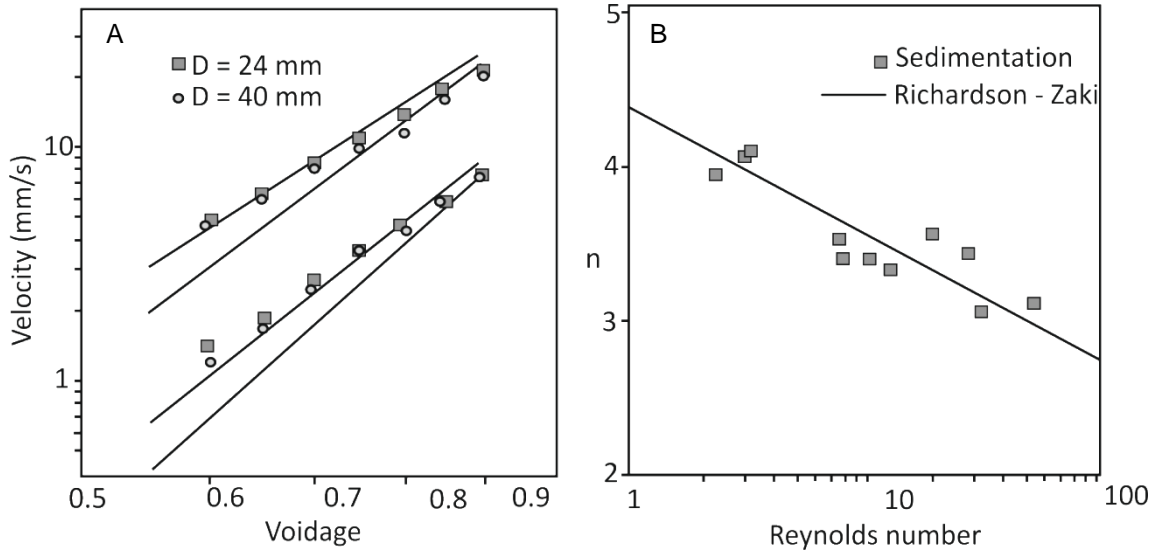


Figure 4.5. (A) The disparity in slope between experimental settling velocities (symbols) and Richardson-Zaki predictions (lines). Whereas when wall effects are ignored (B), experimental values of n as a function of Re (symbols) are in good agreement with Richardson-Zaki predictions (line). Adapted from Di Felice and Kehlenbeck (2000).

4.7. Binary-solid fluidisation

Binary mixtures are those where the particles differ in either size and/or density for example small, dense particles and large, less-dense particles in a fluidised system, It is important to determine the interactions between the particles and the fluid during fluidisation. Under steady-state conditions, when all particles are suspended in the fluidising medium one must be able to determine the effects of each individual particle on the fluid. Particles of differing sizes will have different effects on the fluid as they will have different velocities relative to the fluid, mostly owing to their settling velocity (Di Felice, 1995). In terms of sedimentation velocities, Batchelor (1982) derived expressions for both small and large particles in a low-concentration binary system and showed that the settling velocity of small particles is substantially affected by the concentration of large particles. The converse is true for large particles, whose settling velocity is less affected by the concentration of smaller particles. In order to determine the particle-fluid interactive forces, a

number of workers (Richardson and Shabi, 1960; Kennedy and Bretton, 1966; Lockett and Al-Habbooby, 1973, 1974; Masliyah, 1979; Moritomi *et al.*, 1986) used empirical approaches, for example the “overall voidage model” which assumes the forces between the fluid and particles are exclusively a function of the void surrounding a particle. Di Felice (1995) provides a comprehensive argument for why this should not be the case; simply modifying void fraction in the Richardson-Zaki equation is insufficient, instead the unhindered particle settling velocity must also be altered. This leads to the assumption that, in a binary system a large particle settles in a fluid which has a cumulative density of the fluid and small particles and a viscosity equal to that of the fluid (Selim *et al.*, 1983). More recent studies however, demonstrate that both the density and the viscosity of the cumulative fluid and small particles should be considered (Di Felice, 2010).

4.7.1. Inversion

Fluidisation of a binary mixture of solids differing in size or density results in the generation of a two-layer bed. At low fluid velocities, this occurs as the larger or denser particles settle at the base of the bed with the smaller or less dense particles on top. If the particle size distribution is distinctly bimodal, then there will be a distinct contact between the two layers, whereas with a spread of particle sizes (or densities) the boundary between the layers will be less easy to discern and some mixing will occur at the interface (Di Felice, 1995). Interestingly, the converse is true at high fluid velocities if the larger particles are also the less dense species (Escudié *et al.*, 2006) when the layers are inverted. This inversion phenomenon was neatly summarised by Di Felice (1995) after experimental observations by Moritomi *et al.* (1986) and is reproduced in Figure 4.6. The smaller, denser particles (type 1) are at the base of the column at slow fluid velocities and as this is increased, the smaller particles begin to enter the upper layer of large, type 2 particles. This process results in a 3 layer scenario with a pure layer of type 1 particles at the base, a layer of mixed size particles and an upper layer composed purely of type 2 particles. As the fluid velocity is increased the amount of type 1 particles in the mixed layer increases until

the entire fluidised column is a homogenous binary mixture; this is known as the inversion point (Di Felice, 1995; Escudié *et al.*, 2006). Beyond this, a pure layer of type 2 particles will be present at the top of the system with a mixed zone underneath until the final type 2 particle has moved into the upper zone and a sharp contact once again separates type 1 and type 2 particles (Figure 4.6).

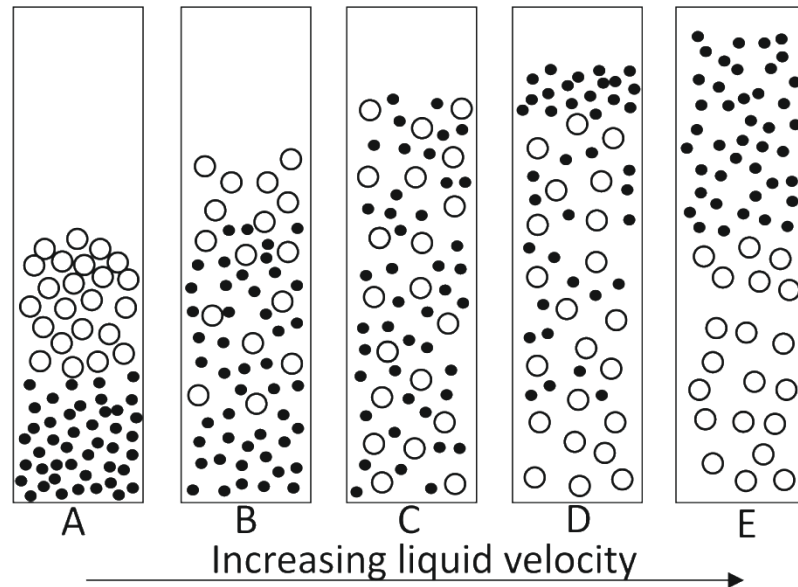


Figure 4.6. Bed inversion phenomenon. Black filled circles represent type 1 (smaller, denser) particles, large open circles denote type 2 (large, less dense) particles. From Di Felice (1995), based on experimental observations of Moritomi *et al.* (1986).

Different models have been applied to predict and describe the inversion phenomenon. These are dealt with comprehensively in Escudié *et al.* (2006) and are summarised here. Five theoretical methods have been proposed: (i) evaluating the bulk densities of the monocomponent beds of type 1 or type 2 particles; (ii) the settling velocities of the particle types; (iii) balancing the forces that act on the particles; (iv) the segregation velocity of one species (*i.e.* the segregation velocity of type 1 particles from a pseudo-fluid comprised of a mixture of the fluid and type 2 particles); (v) bed expansion properties of the binary mixture of type 1 and 2 particles (Escudié *et al.*, 2006). Inversion phenomena have implications relevant to

geological fluidisation and the transport of large particles in a slurry composed of smaller particles + fluid (see *Section 8.4.6.*)

4.8. Bulk density effects

These models are based on the bulk densities of a bed of either type 1 or type 2 particles fluidised under the same conditions (liquid type and superficial fluid velocity) as a binary bed. The difference between the bulk densities determines the degree of mixing between the beds. These models assume that there is either a defined segregation between the two beds or that they are fully mixed (at the inversion point), at which point the bulk densities of a type 1 monocomponent bed is equal to the bulk density of a type 2 monocomponent bed. Epstein and Leclair (1985) estimated the total voidage of a monocomponent bed (ε_j) from the Richardson-Zaki correlation and Hu (2002) approximated ε_j for a monocomponent bed via the balance of forces acting on a single particle. This approach requires the gravitational force, the drag force and the buoyancy force as exerted by the suspension of liquid and particles. Unfortunately these models are lacking in that they only take into account the properties of the particle and the liquid and therefore do not incorporate how the overall composition of a suspension can affect the point of inversion in a binary mixture.

4.9. Settling velocity effects

An approach taken by various workers invokes the settling velocity of the particle types and assumes an envelope of liquid or liquid and solids surrounding a “test” particle to determine interaction between the fluid and particle-particle interactions (Escudié *et al.*, 2006). The apparent porosity model of Patwardhan and Tien (1985) used an average particle diameter in a bed of different sized particles to estimate the porosity in the bed at the point of inversion. The effective voidage model (Bhattacharya and Dutta, 2002) determines the settling velocity of a particle in much the same way, but the “test” particle diameter remains unchanged, only the

diameters of surrounding particles are averaged. Stratification in a fluidised binary bed is thought to be a result of the difference in settling velocities of the two particle types, and at the inversion point the settling velocity of the particles is equal and the voidage can then be calculated.

4.9.1. Balancing the forces

Two models have been proposed to balance the forces acting on the particles, the unit cell model (Moritomi *et al.*, 1986) and the force balance model (Funamizu and Takakuwa, 1995). The unit cell model envisages that a fluidised suspension consists of spherical cells, each with a spherical particle, surrounded concentrically by fluid which flows symmetrically around the particle in an upwards direction as a creeping flow (Escudié *et al.*, 2000). The presence of other particles in the model then acts to alter the buoyant weight of the particle but not the laminar flow field surrounding it. The force balance model applies the drag force on a particle in a monocomponent bed and applies it to a binary bed whilst taking into account particle-particle interaction (Funamizu and Takakuwa, 1995) although Escudié *et al.* (2006) point out that this model would benefit from incorporating the size-ratios of the particles.

4.9.1. Segregation velocities

Once the voidage in a mixed bed and the fluid density has been calculated, it is possible to determine the segregation velocity of a single particle type. Inversion is assumed to occur when the segregation velocity of a type 1 particle in a pseudo-fluid is zero. At this point the bed is homogenous with regular voidages and concentrations of solids (Escudié *et al.* 2006).

4.10. Summary

This section has introduced the concept of whole bed fluidisation with respect to the fluidising medium and grain size and shape variations, and provides background for some of the concepts introduced in later sections of the thesis. Fluidisation is shown to be dependent on the balance between the fluid pressure across the bed and the weight of the particles per area of the bed. The fluidisation medium is shown to exert a strong influence on fluidisation behaviour with gas-solid fluidisation prone to heterogeneous behaviour and liquid-solid suspensions. The transition from homogenous to bubbling regime is dependent on the fluid properties relative to the Archimedes number and the upper limit of the bubbling regime is dependent on the size of the particles. Grain size and shape will constrain fluidisation behaviour as a function of the drag force acting on a particle along with the initial voidage of a bed. The Richardson-Zaki correlation predicts the expansion behaviour of a monocomponent bed, albeit without consideration of wall effects. In a binary system, the settling behaviour of large particles is largely unaffected by the smaller particles and the converse relationship is also demonstrated. Although dealing primarily with whole-bed fluidisation from a chemical engineering perspective, this approach is necessary due to the paucity of geologically relevant literature and warranted by the validity of the concepts when applied to geological systems as demonstrated by the study of Di Felice (2010).

5. Experimental modelling of sand injection

5.1. Introduction

Fluidisation is known to be important for the formation of a wide range of geological features, including: i) *en masse* dewatering structures, ii) clastic dykes and sills, and, iii) sand volcanoes, sandstone sheets and other extrudites (e.g., Maltman, 1994; Jolly and Lonergan, 2002; van Rensbergen *et al.*, 2003; Gallo and Woods, 2004; Hurst *et al.*, 2006; Vigorito *et al.*, 2008; Rodrigues *et al.*, 2009). Such fluidisation features form in a wide array of sedimentological settings, including: i) aeolian sand seas (e.g., Netoff, 2002; Huuse *et al.*, 2005b; Glennie and Hurst, 2007; Hurst and Glennie, 2008), ii) lacustrine lakes (e.g., Moretti and Sabato, 2007; Alfaro *et al.*, 2010), iii) alluvial floodplains (e.g. Saucier, 1989; Guhman and Pederson, 1992; Audemard *et al.*, 2005; Bezerra *et al.*, 2005), iv) at the base of river channel levees (e.g., Li *et al.*, 1996; Singh *et al.*, 2001; Obermeier *et al.*, 2005), v) glacio-fluvial deposits (van der Meer *et al.*, 1999, 2009), vi) beaches and barrier islands (e.g., Draganits *et al.*, 2003; González de Vallejo *et al.*, 2005; Le Roux *et al.*, 2008), vii) sub-tidal sands (e.g., Massari *et al.*, 2001), viii) estuarine deposits (e.g., Plint, 1983), ix) shallow-marine deposits (e.g., Boehm and Moore 2002; Thompson *et al.*, 2007; Scott *et al.*, 2009), x) deep-marine settings (e.g., Parize and Fries 2003; Hurst *et al.*, 2005; de Boer *et al.*, 2007; Jackson 2007; Huuse, 2008), and, xi) potentially on other planets (e.g., Mahaney *et al.*, 2004).

Despite increased recognition of the scale and importance of fluidisation related structures the understanding of the processes controlling sand injection remains poor, with mechanisms being inferred predominantly from outcrop and core studies (e.g., Massari *et al.*, 2001; Duranti *et al.*, 2002; Dragantis *et al.*, 2003; Parize

and Friés, 2003; Duranti and Hurst, 2004; Hubbard *et al.*, 2007; Scott *et al.*, 2009; van der Meer *et al.*, 2009). A large amount of work has been undertaken in the field of fluidisation theory particularly with respect to fluidised beds (see overview in Di Felice, 1995, Chapter 4 examines this in more detail); however the interaction with sedimentary strata is much less well studied. A key limitation is the relative paucity of direct field observations of fluidisation and injection in natural systems (Guhman and Pederson, 1992). Given the limited direct field observations physical modelling offers considerable potential for studying both sedimentary processes and products (e.g., Owen, 1996; Peakall *et al.*, 1996; Paola *et al.*, 2009), yet relatively few studies have been undertaken on geological fluidisation processes (Lowe, 1975; Nichols *et al.*, 1994; Nichols, 1995; Pralle *et al.*, 2003; Mörz *et al.*, 2007; Frey *et al.*, 2009; Rodrigues *et al.*, 2009). Lowe's (1975) initial study of fluidisation provides interesting descriptions of experimental fluidisation but does not outline the experimental regime under which work was carried out, nor provides documentary evidence. More recent laboratory studies have focused on flow regimes in single layered materials (Mörz *et al.*, 2007), variations in fluidisation thresholds in two-layers (Nichols *et al.*, 1994), comparison between water and gas-escape structures in laminated sediments (Frey *et al.*, 2009), and on purely gas-driven fluidisation (Pralle *et al.*, 2003; Rodrigues *et al.*, 2009).

In order to better elucidate the processes of sand injection and extrusion in geological materials, this study examines water driven fluidisation through multi-layered stratigraphy. To simplify the problem cohesionless materials were utilised, with a fine-grained layer between two coarser-grained layers. Such an experimental set-up is a good analogue for many of the environments where sand intrusion occurs, in particular those where thin silt, silty-sand or finer sand layers are present between thicker coarser cleaner sands (e.g., Netoff, 2002; González de Vallejo *et al.*, 2005; Fernandes *et al.*, 2007; Glennie and Hurst, 2007; Hurst and Glennie, 2008; Rodríguez-López *et al.*, 2008) or where sands or silty-sands are present between coarser sometimes gravelly layers (e.g., Bezerra *et al.*, 2005; van der Meer *et al.*,

2009). The experiments are also in part analogous to sand intrusions produced in sequences with cohesive seals such as many lacustrine (e.g., Moretti and Sabato, 2007), shallow marine (e.g., Boehm and Moore, 2002, Thompson *et al.*, 2007) and deep-marine settings (e.g., Gill and Kuenen, 1957; Hiscott, 1979; Hurst *et al.*, 2003; Huuse *et al.*, 2004, 2007). Whilst the nature of hydraulic fracturing in cohesionless and cohesive materials differs (e.g., Cosgrove, 1995, 2001), once fracturing has occurred many of the flow processes associated with these structures can be expected to show similarities.

5.1.1. Fluidisation

Fluidisation is a process where solids transform into fluids through an increase in pore pressure and an accompanying loss of interparticle friction, with the fluid velocities sufficient to transport grains within the fluid (see Di Felice, 1995). The minimum fluidisation velocity (U_{mf}) of a single layer for particles of a uniform grain size, with a Reynolds number of <20 can be expressed by the following equation (Stanley-Wood *et al.*, 1990; Nichols *et al.*, 1994):

$$U_{mf} = \frac{\varepsilon_{mf}^3 (\rho_p - \rho_f) g (\phi d)^2}{5(1 - \varepsilon_{mf}) \mu 36} \quad (5.1)$$

where U_{mf} is a function of intergranular porosity at minimum fluidisation (ε_{mf}), ρ_p grain density, ρ_f fluid density, g acceleration due to gravity, d grain size, ϕ grain shape and μ fluid viscosity. Fluidisation where water is the fluidising medium is known as homogenous or particulate fluidisation (Di Felice, 1995). Elutriation occurs as u (superficial fluid velocity) exceeds U_{mf} and particles are entrained in the flow and carried up to the free surface of the particulate bed. At U_{mf} , effective stress and shear strength of the bed disappear and as bed expansion occurs and pore-space increases, the pressure gradient across the system increases. The hydraulic

gradient (dimensionless) at the point of hydraulic failure (occurrence of fluidisation structures) is termed the critical hydraulic gradient and expressed as (Craig, 2004):

$$i_c = \frac{G_s - 1}{1 + e} \quad (5.2)$$

Where G_s is the specific gravity of the particles and e is the void ratio, which is defined as (Craig, 2004):

$$e = \frac{\eta}{\eta - 1} \quad (5.3)$$

Where η equals porosity.

These equations are either based around single grain-sizes or contain properties such as porosity which are best estimated when grain-size is uniform. Consequently, the experiments in this study make use of artificial sediments (glass spheres), or well-sorted clean silica sands used for glass manufacture, that have much tighter grain-size distributions than typical cohesionless sediments.

5.2. Experimental methodology

A series of experiments were conducted within a vertical clear Perspex cylindrical tank (1.2 m high x 0.3 m diameter) (Fig. 5.1) with ten inlet pipes at the base (1 m length, 0.01 m diameter). A manifold controlled water flow through the inlet pipes maintaining an even flow across each of the input pipes (Fig. 5.1 A). Water supply to the manifold was via a 2 cm diameter flexible pipe, fitted with a Cole-Parmer ultrasonic flow meter (model 32986-00), capable of measuring water velocities greater than 0.3 cm sec⁻¹. In each experiment water flowed through the inlet pipes into the Perspex tank. Each inlet pipe was removable and had a self-sealing valve fitted to ensure that flow was directed to connected pipes when inlet configurations were changed (Fig. 5.1 B). A 20 cm deep coarse sand layer was placed at the base of

the tank and acted as a baffle, providing even flow distribution across the tank diameter.

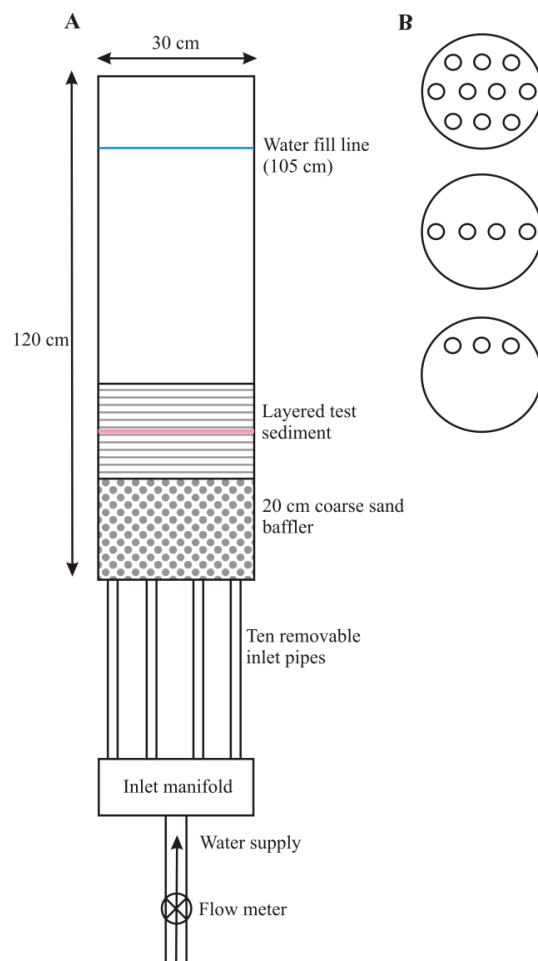


Figure 5.1. A) Schematic illustration of experimental set up, B) Details of inlet pipe configurations. (Run 6 middle configuration, Run 7, bottom configuration, all others as top).

In order to examine the mechanics of fluidisation, a simple 3-layer stratigraphy was utilised with a finer layer separating two coarser layers. These layered test materials were introduced above the baffle, and in the majority of experiments the lower and upper layers consisted of near-spherical 2.6 g cm^{-3} glass beads ($150\text{-}300 \text{ }\mu\text{m}$ coarse glass beads) separated by a layer consisting of $0\text{-}44 \text{ }\mu\text{m}$ fine glass beads, mixed with $<10\%$ low-density red plastic granules (Poly V[®] $1.1\text{-}1.2 \text{ g cm}^{-3}$) as a tracer. This mixture of grain sizes in the middle layer would lower the overall porosity and

permeability of the layer (Beard and Weyl, 1973; Nagtegaal, 1978; Nichols *et al.*, 1994). A number of experiments (*Runs 8-11*) instead used 150-170 μm silica sand as the top layer, and *Run 11* had silica sand as the top and base layers. The middle layer was always 1 cm thick. Glass beads were chosen as the primary test material as they have the same density as quartz sand, a relatively tight particle distribution, and do not have the intra- and inter-batch variability in grain-size distributions and particle shape inherent in natural sands. Poly V[®] was chosen as the tracer for the finer-grained layer as this is a brightly coloured material that makes for excellent visualisation, does not suffer the intra- and inter-batch variability of natural materials, and its low density allows it to be coarse enough not to exhibit cohesion-like forces, yet mimic much smaller particles in terms of erosion, transport and deposition (Peakall *et al.*, 1996; 2007; Amos *et al.*, 2010). The grain-size distributions of the sediments were measured with a Malvern Mastersizer 2000e particle size analyser. The tank was filled with water to 105 cm above the base and dry sediment was added to form the layers. The layer directly overlying the baffle was always 6 cm of fine glass beads with the exception of *Run 1*, where the base layer was 2 cm thick and *Run 11* where both the base and upper layers were silica sand. The colour contrast between brown silica sand and the colourless glass beads which appear white, allowed for easier observation. A deep water column during sediment addition and settling allowed even deposition across the tank diameter. Poly V[®] and fine glass beads were wetted before adding to the tank to prevent separation. A 30 minute settling time following addition of fine glass beads and Poly V[®] was allowed to avoid fine material being incorporated into the upper layer. After the upper coarse sediment layer was added, water was pumped out of the tank to the starting 105 cm mark. Experiments examined the influence of three main variables on the structures formed during fluidisation: i) the thickness of the overlying coarse sediment layer, ii) the configuration of inlet pipes and iii) water velocity. Where inlet pipes and water velocity parameters were varied, the thickness of the layers was kept constant (Table 5.1).

Run No.	Base layer thickness (cm)	Base layer material	Base layer grain size (μm)	Top layer thickness (cm)	Top layer material	Top layer grain size (μm)	Water velocity (cm sec^{-1})	Inlet configuration	Total discharge ($\text{cm}^3 \text{sec}^{-1}$)
1	2	Glass beads	150-300	2	Glass beads	150-300	0.3*	All	1.52
2	6	Glass beads	150-300	5	Glass beads	150-300	0.3	All	1.52
3	6	Glass beads	150-300	3	Glass beads	150-300	0.6	All	3.0
4	6	Glass beads	150-300	9	Glass beads	150-300	0.3*	All	1.52
5	6	Glass beads	150-300	2	Glass beads	150-300	0.3	All	1.52
6	6	Glass beads	150-300	6	Glass beads	150-300	0.3*	4 middle only	0.6
7	6	Glass beads	150-300	6	Glass beads	150-300	0.6	1 line only	0.3
8	6	Glass beads	150-300	6	Silica sand	150-170	0.3*	All	1.52
9	6	Glass beads	150-300	4	Silica sand	150-170	0.3	All	1.52
10	6	Glass beads	150-300	10	Silica sand	150-170	0.3*	All	1.52
11	6	Silica sand	150-170	6	Silica sand	150-170	0.3*	All	1.52

Table 5.1. Summary of parameters used in the experiments. Glass bead and silica sand densities were 2.6 g cm^{-3} . Hydraulic head was 105 cm in all experiments. * Water velocities were assumed to be approximately 0.3 cm sec^{-1} , the lower detection limit of the flow meter. All experiments had a 1 cm thick middle layer, composed of fine ballotini (0-44 μm) with <10% Poly V® ($1.1\text{-}1.2 \text{ g cm}^{-3}$) as a tracer. See **Figure 5.1** for details of inlet configuration.

Run 6 utilised the four central inlet pipes, whilst *Run 7* used a single line of pipes to produce asymmetrical flow (see Fig 5.1). Before each run the sediment was allowed to settle and a clear water column developed. Two Sony digital video cameras (25 frames per second) were mounted on the angle iron supporting the tank at 90° to each other, aligned with the test sediment to accurately record the development of features. Video recording was started approximately 5 seconds before the water supply was turned on and the water velocity remained constant throughout each experiment. Each experiment lasted between 1 and 15 minutes; recording was stopped when new fluidisation features were no longer observed to form.

5.3. Results

In the course of the experiments, a consistent pattern of feature development was noted, i) development of a water-filled void or voids and infiltration of fine sediment in the overlying bed), ii) progressive void growth, iii) rupture which occurred at either single or multiple sites, iv) piping, v) extrusion of sediment, vi) closure of pipes. This pattern is broadly repeatable with changes in the dynamics of developing water escape pipes affecting the duration of developmental stages. Each of these phases is briefly described and illustrated below (Fig. 5.2) and then discussed in subsequent sections. Prior to this a brief analysis is undertaken of the conditions under which fluidization in the experiments took place.

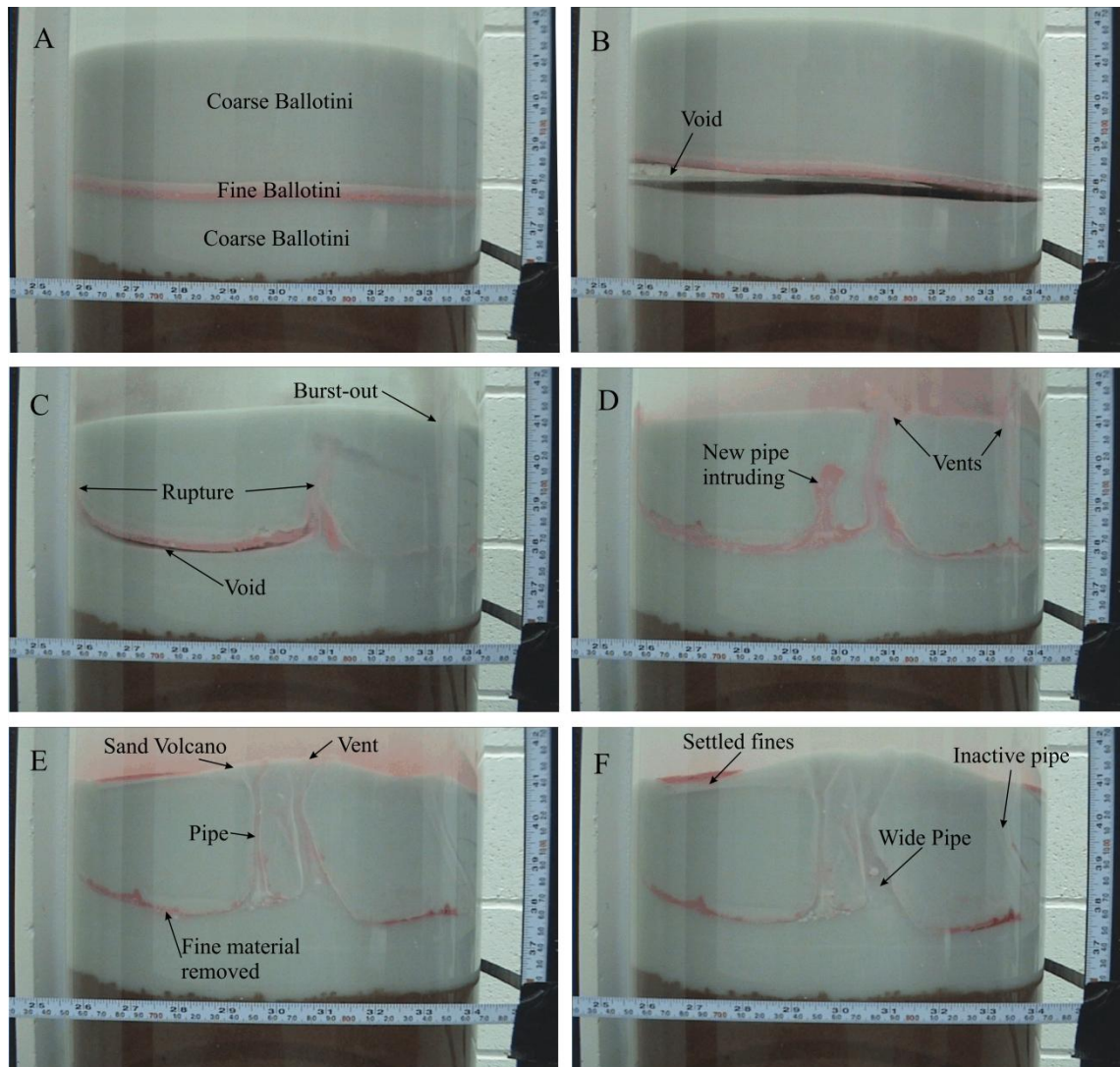


Figure 5.2. A series of video stills demonstrating the most significant periods in the structural evolution of a run (here *Run 4*). (A) Starting 3-layer stratigraphy. Apparent slight doming on the upper surface of the sediment and in the middle layer is due to barrel distortion. (B) Initiation of void. (C) Rupture occurs and pipe propagates to surface. Infiltration horizon can be seen above the dish-shaped fine layer following fluidisation. (D) Venting at surface and initiation of secondary pipe. (E) Piping has stabilised and fine material can be seen lining the inner edges of the pipes. (F) Final geometry showing pipes and sand volcanoes. Much of the fine layer has been elutriated and redeposited on top of the sediment column. The times at which these stills were taken are as follows (in minutes and seconds): **A** – 0.00, **B** – 2.22, **C** – 8.30, **D** – 8.33, **E** – 9.43, **F** – 11.05. Scales shown are in centimetres (lower) and inches (upper).

5.3.1. Experimental parameters

All of the experiments reported here reached a point at which the sediments underwent a transformation to a state of fluidisation. An idealized hydraulic gradient at the point of fluidisation can be calculated for these experiments using Equation 5. The following values were used: specific gravity of the grains (G_s) = 2.6, porosity (η) = 0.47 (cubic packing assumed), and void packing ratio of 0.89. This gives a critical hydraulic gradient (i_c) of 0.85. Pressure gradients were not measured in these experiments (cf. Mörz *et al.*, 2007; Frey *et al.*, 2009) so it is not possible to independently assess the accuracy of these idealized values. However, given that the particles are not perfectly unimodal, that they do vary slightly at an intra- and inter-batch level, and that the middle finer-grained stratigraphic layer contained small amounts of low-density tracer particles, then such estimates likely contain substantial error (>20%) (cf. Frey *et al.*, 2009). As a result of these complexities, and in particular the grain-size distribution, the minimum fluidisation velocity (equation 1) is not estimated since this will be unrepresentative of actual behaviour. Another factor that complicates attempts at estimating flow conditions is the fact that flow discharge is not constant in a given experiment but rather varies as a function of pressure, for instance increasing slightly once breakthrough occurs. Vigorito *et al.*, (2008) suggest that in natural fluidised systems, the potential pressure gradient reaches a peak as intruded sediment breaches the surface, thus maximising the energy driving intrusion.

Given the limitations inherent in estimating the flow hydraulics in these simulations, then the experiments can only be considered as analogue models (Hooke, 1968; Peakall *et al.*, 1996). The experiments demonstrate the array of fluidisation processes and sedimentation that are possible within simple layered stratigraphy, but do not elucidate the detailed hydraulic conditions responsible for each of these. Such analogue models have been very successfully used in a wide range of sedimentological fields to improve physical understanding (e.g., Schumm *et al.*, 1987; van Heijst *et al.*, 2001; Keevil *et al.*, 2007), and Paola *et al.* (2009) have

argued for the 'unreasonable effectiveness' of such models, despite the absence of scaling and detailed local hydraulic measurement.

5.3.2. Void Formation and Infiltration

Voids form beneath the fine layer as a function of the build up of pressure below the low permeability horizon and the gravitational effective stress of the overlying sediment package. Experiments showed that the formation of voids (Fig. 5.2B) is dependent on; the thickness of the overlying strata; the permeability contrast between the base and middle layers, and the volume of water discharged into the sediment column. In the Runs 1-7 void formation took no longer than 13 seconds, with an average of 8 seconds following flow initiation. The void generally took the form of a single apex, although in *Run 4*, two apices formed on opposing sides of the tank. Water in the void was quiescent allowing fine sediment to "rain-out" through the void and settle on the surface of the base layer, as previously described by Nichols *et al.* (1994). Water within the void was observed to become turbulent if rupture was imminent or occurring.

An infiltration horizon, easily identified from the red coloured fine-grained particles, was often observed forming at the interface between the fine and upper coarse layers as fine sediment particles infiltrated the pores in the overlying coarse material due to the upwards water pressure (See Fig. 5.2 B). An infiltration horizon was not always observed, most likely due to tight packing of the overlying sediment preventing the fine material from entering pores. Furthermore, where it occurred and the void formed an apex, the infiltration horizon disappeared. This is thought to be due to overpressure widening pores, enabling fine material to migrate further into the overlying layer and dissipate, although no observation was made of it reaching the sediment surface. The development of millimetre-scale sub-vertical water-escape structures within the infiltration horizon provides further evidence of overpressure (see Fig. 5.3;), although they were frequently destroyed during late-stage fluidisation. However, where the locus of fluidisation switches during the process these features can be preserved. Similar structures, termed stress-pillars

have been described previously (Lowe, 1975) and are the result of partial fluidisation along developing flow paths within sediment. Within these experiments, stress pillars were observed on the upper side of a dipping pipe, which showed its own infiltration horizon (Fig. 5.3).

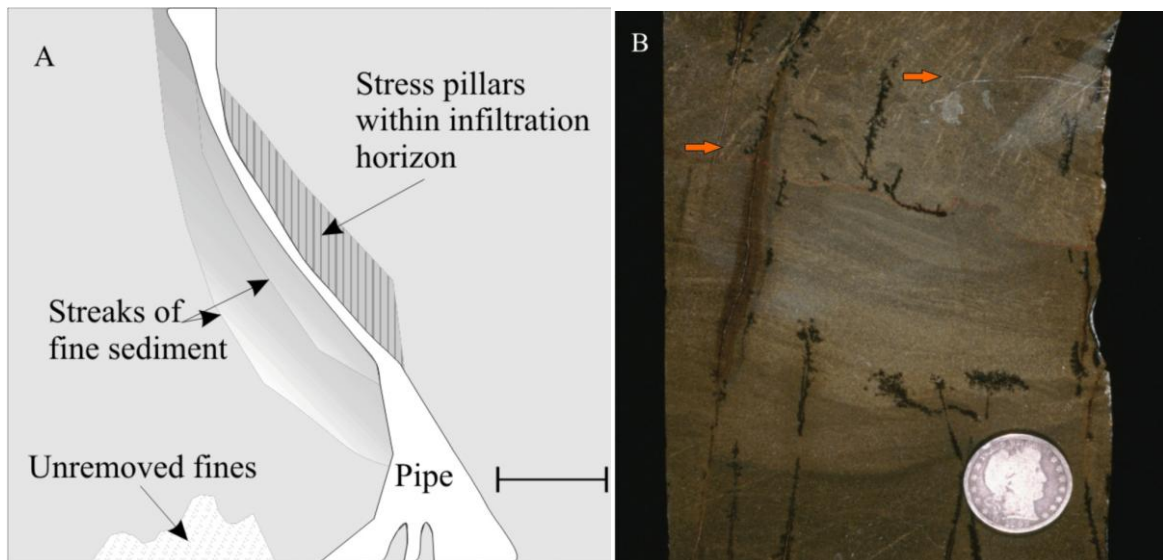


Figure 5.3. (A) Diagram of the inclined pipe in *Run 4* demonstrating stress pipes in the infiltration horizon above the pipe. Scale bar 1 cm. (B) Red arrows highlight stress pipes aligned at a high angle to the walls of a clastic sill. Coin for scale is 3 cm diameter (adapted from Diggs (2007)).

This provides evidence that not all the overpressurised fluid within the pipe is being channelled and some may be escaping vertically as a response to the angle of the pipe versus the pressure from beneath. The infiltration horizon began to grow when the void thickness reached as little as 5 mm, but never permeated more than 10 mm into the overlying sediment. However, there is not a clear correlation between void thickness and the thickness of the infiltration horizon.

5.3.3. Rupture

Water pressure beneath the upper sediment layer increased during void formation and rupture occurred when a critical threshold was reached (Fig. 5.2 C); in the experiments the overpressurised water rapidly moved upwards, fluidising any sediment it came into contact with. As the overpressurised water was forced upwards, fractures opened in the overlying sediment which were rapidly exploited by fluidised material and piping was initiated. The mode of rupture can take various forms, from occurring in an isolated zone from 1 cm to 10 cm diameter, via multiple zones forming synchronously or by complete overturning of the upper sediment column. No correlation between void geometry and rupture style was seen. Rupture is a swift process and remnants of such an event are rarely preserved once piping begins. Failed rupture zones may be preserved however if rupture occurs at more than one location. This results in the initial rupture site being shut down and the secondary rupture point becoming dominant. During this process, water involved in the initial rupture is rapidly diverted to the second locus, the change in direction entraining sediment and creating convolute features. These unsuccessful ruptures, or failed zones, can be preserved providing they are not removed by subsequent pipe migration as seen in Fig. 5.4, where the secondary pipe migrates away from the initial rupture zone. The preserved rupture zone is isolated from any source and is completely encompassed by coarse sediment, bearing resemblance to load structures (Fig. 5.4 B)

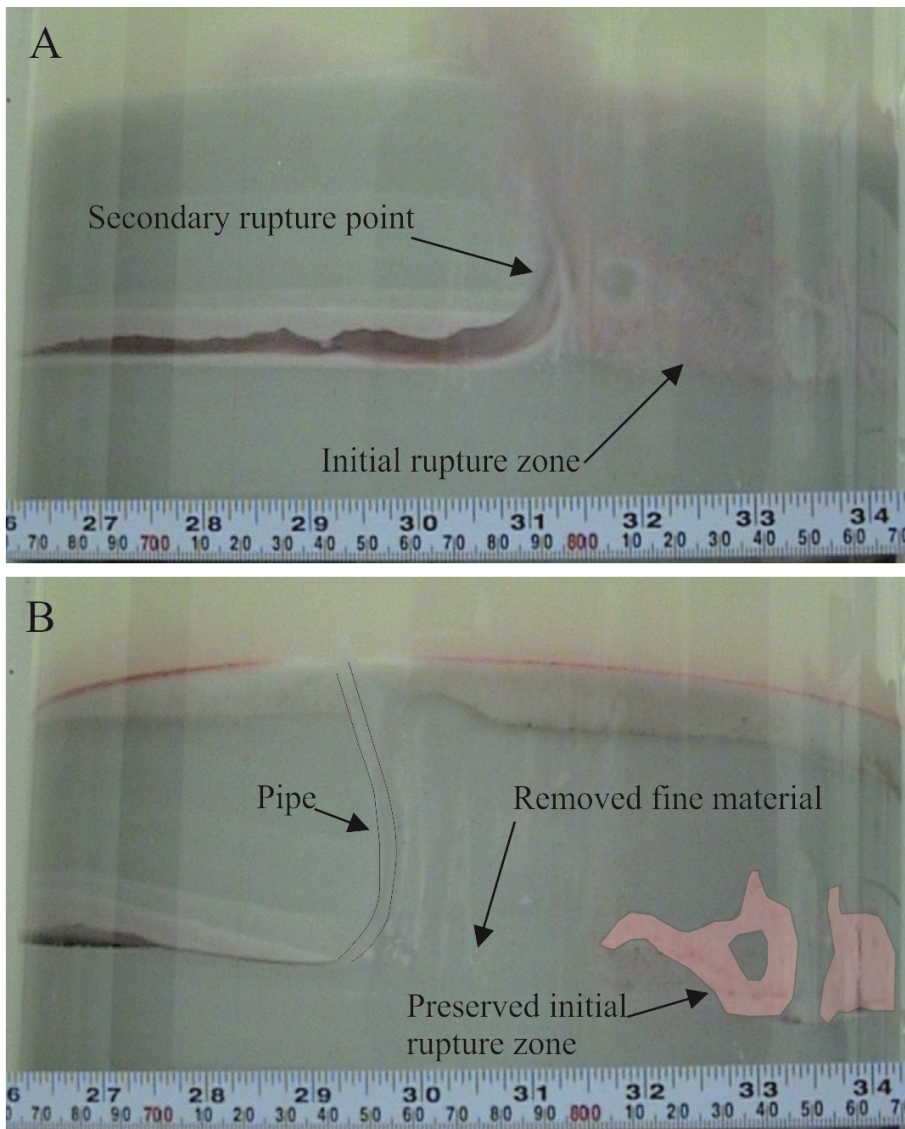


Figure 5.4. Preservation of initial rupture zone results in fine sediment swirls preserved in surrounding coarse sediment. From *Run 2*, at 0.42 minutes (upper) and 1.57 minutes (lower). Key features have been outlined in **B** to enhance clarity. Scales shown are in centimetres (lower) and inches (upper).

5.3.4. Pipe Morphology

Piping occurred as overpressurised water was vented from the void, fluidising sediment along its path and around it; elutriated sediment was transported above the sediment surface into the overlying water-column. The geometry of the pipes observed in the experiments was varied producing a number of distinct styles: *i*) vertical and narrow, *ii*) vertical and wide, *iii*) a funnel shape that widens towards

the top, *iv*) sub-vertical, *v*) sinuous showing a dyke and sill, or stepped morphology, or *vi*) a poorly defined, yet wide zone of fluidised sediment. Pipes were expressed at the surface as a singular vent as opposed to fissure-style venting and it was clear that once a pipe began to vent at the surface, flow rate within the pipe increased. Experiments often showed more than one style of piping, either because pipes formed independently, or because the pipe morphology evolved throughout the duration of the experiment. Each of these styles of piping will be discussed separately.

5.3.4.1 *Thin Vertical Pipes*

These pipes are less than 1 cm wide and vary little between the source and the sediment surface, although pipe morphology is not always consistent even within this subset as shown in Figure 5.5 A (a single pipe of this type to the right of the picture) and B (three pipes of this type are present in the centre of the figure). These pipes often have a thin (< 2 mm) lining of fine sediment (glass beads), which is preserved once flow has stopped. This lining accumulates as water flows radially out of the pipe due to the flow velocity gradient between the pipe and the ambient velocity in the surrounding sediment, carrying fine sediment with it.

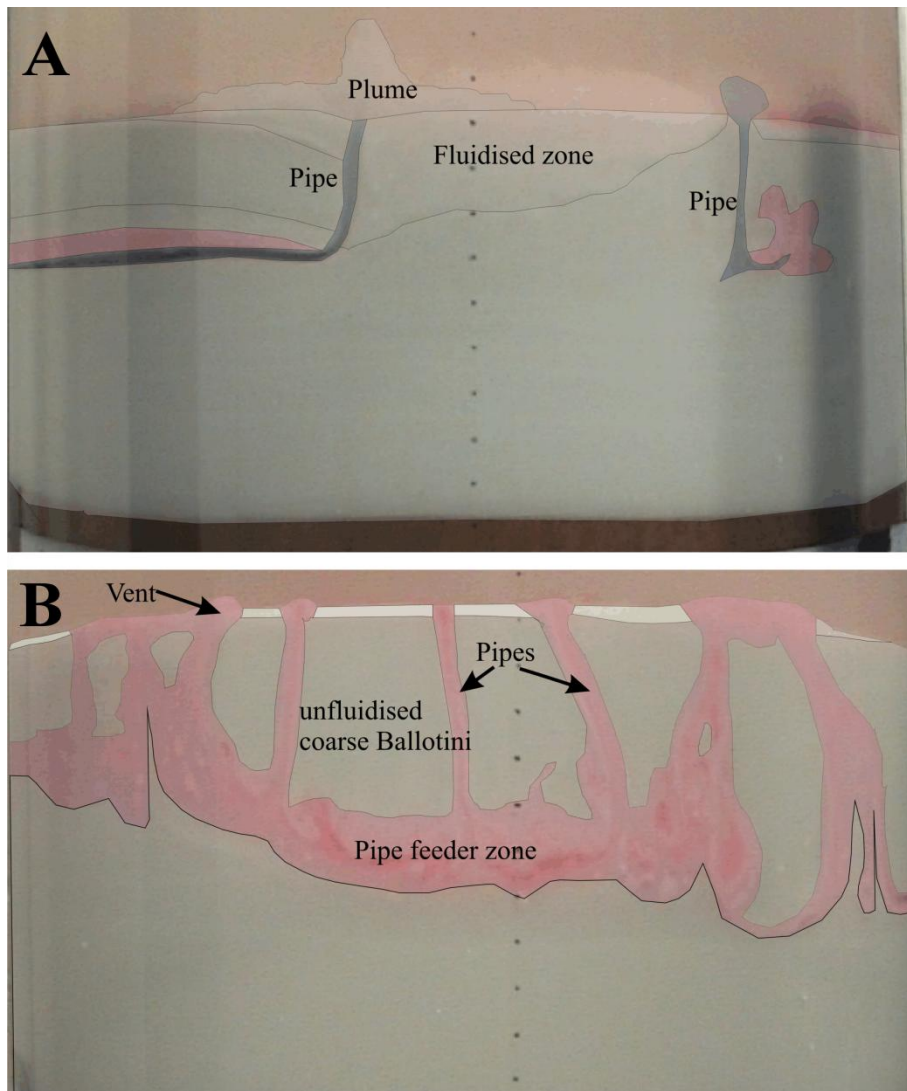


Figure 5.5. Pipe morphologies from 2 runs. Video frames have been interpreted for clarity. **A)** From *Run 5* at 0.59 minutes. The main pipe is migrating to the left whilst the pipe to the right stays stationary, both maintaining a vertical morphology. A poorly defined zone of fluidised, convecting sediment exists to the right of the main pipe. Sand ball morphology is seen to the right of the right-hand pipe. **B)** From *Run 7* at 1.52 minutes. There are eight, clearly defined pipes venting water and fluidised sediment, each separated by unfluidised sediment from the original top layer or clasts of incorporated top-layer material. Black dots are 1 cm spaced.

This accretion of fine sediment blocks pores and prevents radial flow through the sides of the pipes, stabilising the vertical morphology. In the present study, once most of the fine material was elutriated from the middle layer, a sharp contact existed between the base of the pipes and the lower sediment layer (Fig 5.2 E).

5.3.4.2. Wide Vertical Pipes and Fluidised Zones

These two styles of fluidisation have been combined, as they are often strongly associated. Wide pipes often had a defined contact with host sediment during fluidisation, whereas fluidised zones had a gradational boundary with host sediment. Wide pipes often migrated and disrupted the grain packing of sediment they disturbed, thus facilitating fluidisation and creating wide zones of fluidisation that formed in the wake of a migrating pipe. This effect was also observed in runs where the top layer thickness was only 2 cm; negating any effect overlying sediment thickness may have on this process. Observations suggest that it is the nature of the ruptures occurring in the fine layer that control how focused the initial piping is. Therefore, if the fine layer had been removed by infiltration, or by a broad rupture, fluidisation occurred in wide zones, only disrupted by an amorphous amalgamation of fine sediment trapped during collapse (Fig. 5.4 A). This structure is easily eroded and thus removed during subsequent stages of fluidisation.

Conversely, wide fluidisation pipes were observed bifurcating and splitting apart to form two smaller pipes (a supplementary .avi (5stress_pipes.avi) of this process in *Run 8* is available on the accompanying DVD). This is thought to be due to the lack of a fine sediment rim on the pipe, as this stabilises the circumference of the pipe; without it water can escape from the pipe radially due to the high water pressure, subsequently fluidising sediment surrounding the pipe, creating a fluidised halo. The wide fluidisation zones formed when rupture occurred in one place, suggesting flow rate is a factor in formation. If rupture subsequently occurred in another area of the tank, the flow rate through the original pipe was reduced, allowing the pipe to stabilise and accumulate fine material on its edges due to slower elutriation rates.

5.4.3.3. *Sub-Vertical and Stepped*

Sub-vertical and vertical pipes were observed simultaneously from multiple rupture sites, demonstrating that starting conditions may not entirely dictate the nature of the end-product of fluidisation. However, in *Run 4*, where two ruptures occurred very close together one occurred slightly before the other; water from the original rupture escaped upward faster than the second, although the dominant pipe actually originated from the second rupture. From this point it migrated upwards at a 70° angle until it connected with the fluidised sediment from the first rupture (Fig. 5.3, *Run 4*). At this point water no longer flowed upwards from the primary rupture, but migrated laterally to the base of the pipe and flowed upwards through it. The underside of the pipe became lined with fine sediment and thus stabilised.

Dyke and sill style, or stepped piping is most common in the earliest stages of fluidisation as the pipe propagated upward through overlying sediment (Fig. 5.6). The morphology of this style of piping is similar to that seen in igneous dyke and sill complexes and has short (2 cm) sills linked by pipes (up to 3 cm). Pipes do not always originate from the end of the small lateral intrusions, but more often from a mid-point, possibly due to propagation from the end of sills being prevented by a permeability decrease. In *Run 10* the “stepped” morphology (Fig. 5.6) was associated with an amalgamation of fine sediment on the upper side of the sill; fluidised sediment subsequently reached the surface via exploitation of hydraulic fractures in the overlying cohesionless sediment.

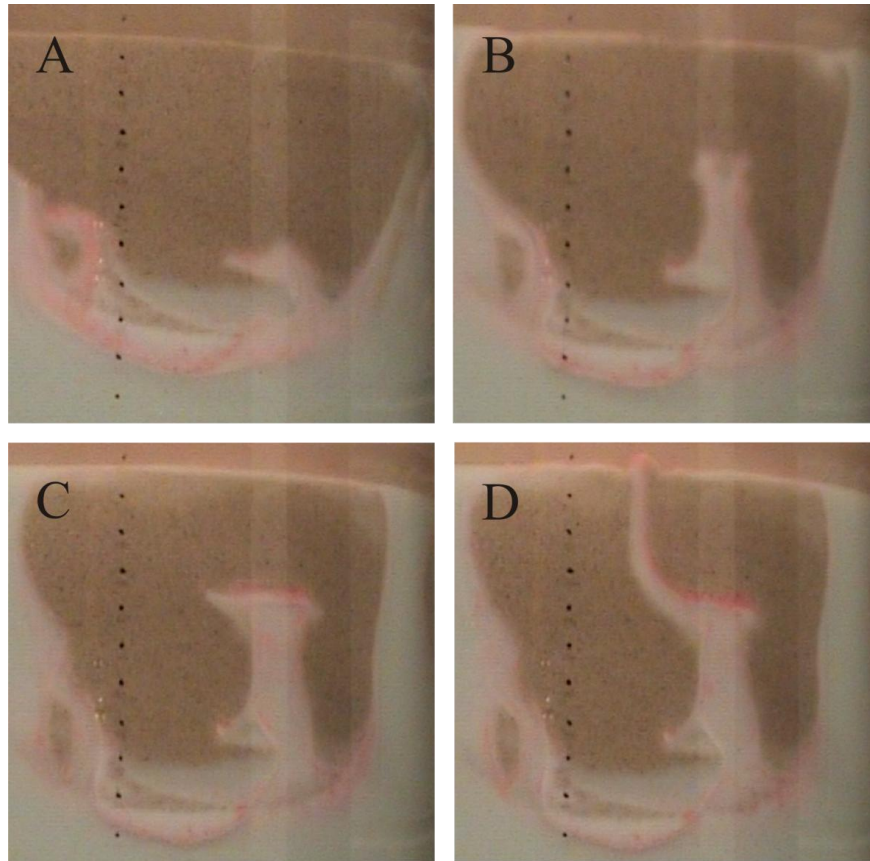


Figure 5.6. Series of stills from Run 10 demonstrating the development of dyke and sill style piping. A) Following rupture and piping onset, a new pipe begins to migrate upwards and horizontally from a deformed sediment boundary. B) Horizontal migration is abandoned in favour of vertical migration. C) Fluidised sediment “ponds” and migrates laterally beneath an impermeable heterogeneity, either pre-existing in the upper sediment layer or due to fine sediment amalgamating on the upper edge of the sill. D) The pipe reaches the sediment surface and begins venting sediment. This morphology remains stable for the duration of this run. Black dots are 1 cm spaced.

Where an atypical, quiescent rupture occurred, pipes formed at a slower rate, being less able to breach the overlying sediment resulting in dyke and sill morphology as the pipe migrated towards the sediment surface. Sills formed when fluidised material pools between what may be a low permeability horizon. Any permeability contrast within the silica sand is most likely a result of mild grain sorting during

settling prior to the experiment or a hiatus in adding the sediment creating a pseudo-bedding plane. In *Run 3*, this morphology developed as a vertical pipe formed and subsequently became inactive as another pipe became dominant and migrated away from the original pipe. During this process sediment surrounding the early pipe subsided unevenly as material from beneath it was fluidised and vented causing the pipe to deform in a ductile manner, possibly facilitated by the fine material within the pipe.

5.4.4. Pipe Dynamics

Migration of pipes is often inherently linked to their morphological evolution but some experiments show other effects of pipe dynamics. One of the most striking observations was that of lateral pipe migration observed both from the edge of the experiment and above the sediment surface, some pipes travelling almost the entire circumference of the test vessel (94 cm). These pipes showed a conical morphology with a narrow base originating at the base of the fine sediment layer. The direction of pipe migration was often dependent on the rupture conditions, as rupture following an asymmetric void resulted in water migrating towards the breakthrough point travelling at different speeds. As pipes migrated towards the side from which most water moved, they erased the stratigraphy through erosion on the leading edge, elutriating fines and leaving behind characteristic structureless sediment. Amalgamations of fine material were left suspended in the coarse sediment and once the pipe has migrated away, there is no evidence regarding their origin other than this heterogeneous incorporation of finer-grained material. Figure 5.7 illustrates this and the colour difference between the glass beads, which appear white, and brown silica sand highlights the disturbed boundary between the bottom layer and the overlying fluidised sediment. Amalgamations of fine sediment were present throughout the upper sediment layer, showing the pervasiveness of fluidisation and the circulating zone of fluidisation on the stoss side of the pipe. The fluidised deposit can most accurately be described as structureless sand with aggregates of fine sediment showing no orientation. The migration of the pipe also

had effects on the infiltration horizon and fine sediment layer, as the pipe encroached; these layers simultaneously dipped towards the base of the pipe.

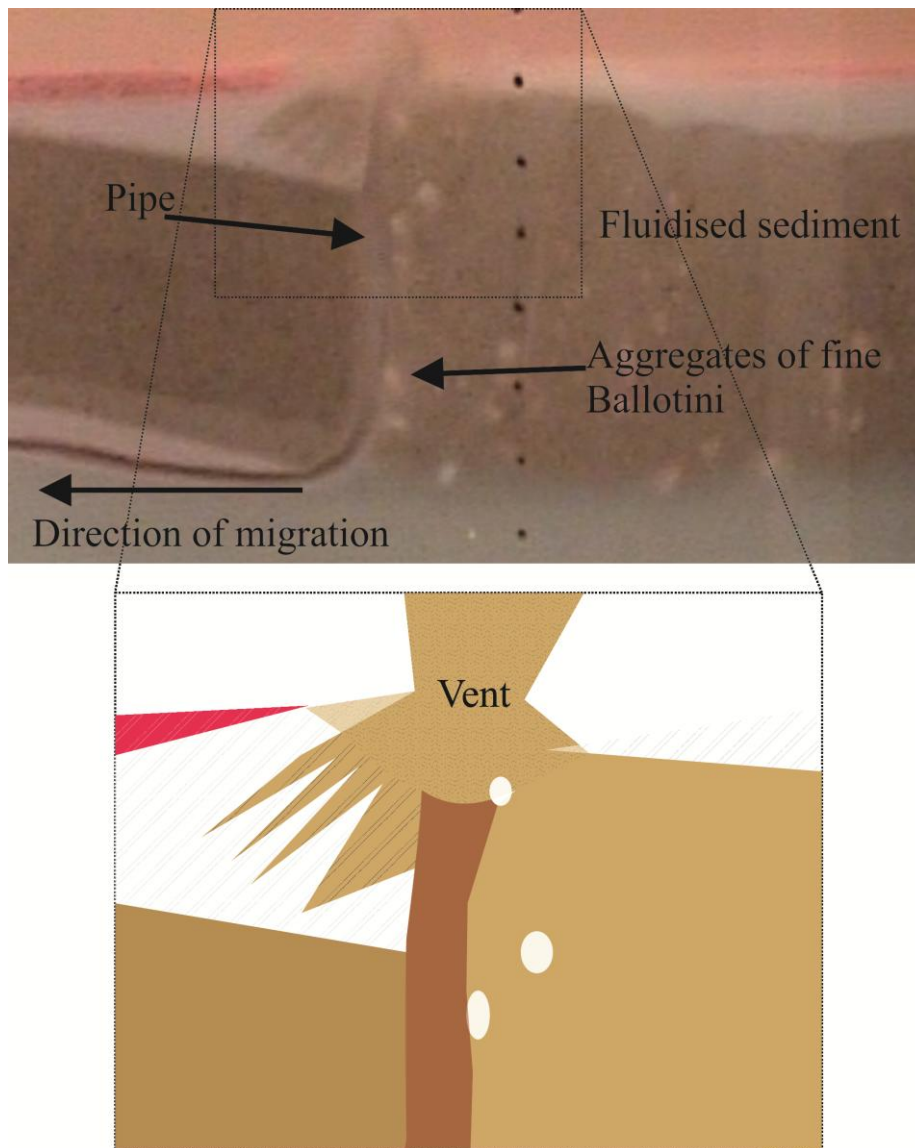


Figure 5.7. Effects of pipe migration on layering. The pipe has migrated to the left from out of view on the right of the photo. The original fine ballotini layer has been completely removed and the boundary between the coarse ballotini and overlying silica sand is difficult to discern due to fluidisation. Aggregates of fine ballotini that were originally in the middle layer are left suspended in the silica sand layer, which also contains coarse ballotini. This is evident from the colour difference on the right and left of the pipe. From *Run 9* at 6.23 minutes. Black dots are 1 cm spaced.

The formation of extrusive features such as sand volcanoes and the likelihood of their preservation are heavily dependent on the phenomena of pipe migration. When pipes remained stationary for more than a few seconds, and if the ejection rate was not too high, the sediment they extruded was deposited as a sand volcano on the surface around the vent where the pipe meets the sediment surface. In some cases, the pipe began to migrate after topography was formed and subsequently removed it, re-fluidising and re-distributing the sediment. Pipe migration away from vent sites was investigated further in one experiment: after the experiment was complete and water drained from the test vessel, a single sand volcano, observed to have formed from a migrating vent was carefully removed from the centre of the test vessel. This feature was carefully split apart down the centre, but no distinct feeder pipe was observed below the vent as would be expected (Fig. 5.8) even when the sample was repeatedly sectioned. This is thought to be due to lateral migration of an underlying feeder pipe away from the vent site, therefore a discrete feeder system is not seen. Amalgamation of pipes was also observed when one of two adjacent pipes became dominant; this has previously been documented occurring in studies of seepage (Wilhelm and Wilmański, 2002) as smaller pipes are reoriented towards the dominant pipe.

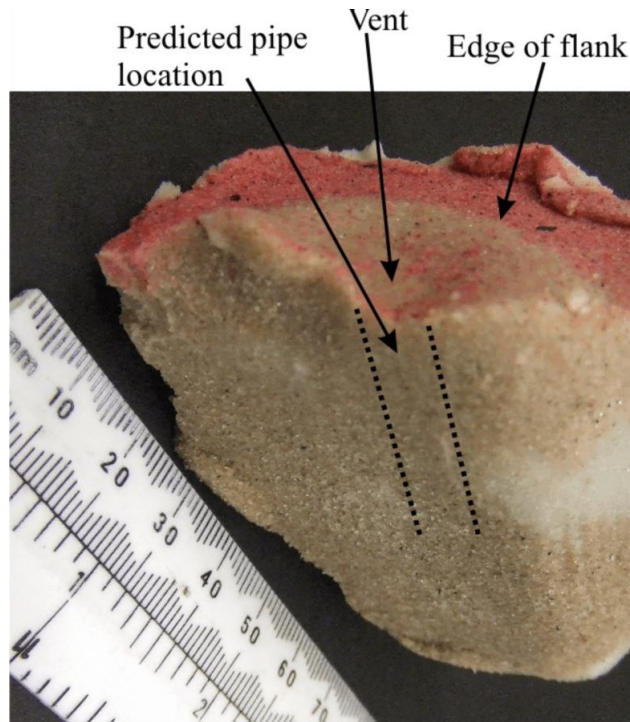


Figure 5.8. Photograph of an excavated sand volcano orientated with the sediment surface at the top. The topographic feature has relief of 4 mm and has a clear vent. Dashed lines denote the region where a pipe would be expected if it were present. Scale in mm.

5.4.5. Vents

The point or zone where a pipe intersects the sediment surface is termed the vent and a number of different venting styles were observed in these experiments. Extrusion of sediment ranged from violent, producing a high plume of fluidised sediment and water up to 5 cm high, to relatively quiescent venting of sediment and water. This quiescent style of venting was often responsible for building topography around the vent (Fig. 5.9 A). Despite this, vents creating topographic features were not always associated with fluidisation induced at low fluid velocities. Figure 5.9 B shows a series of undulating sand mounds that have formed in response to a migrating pipe; evidence that surface topography is not necessarily completely destroyed by fluidisation during lateral pipe migration.

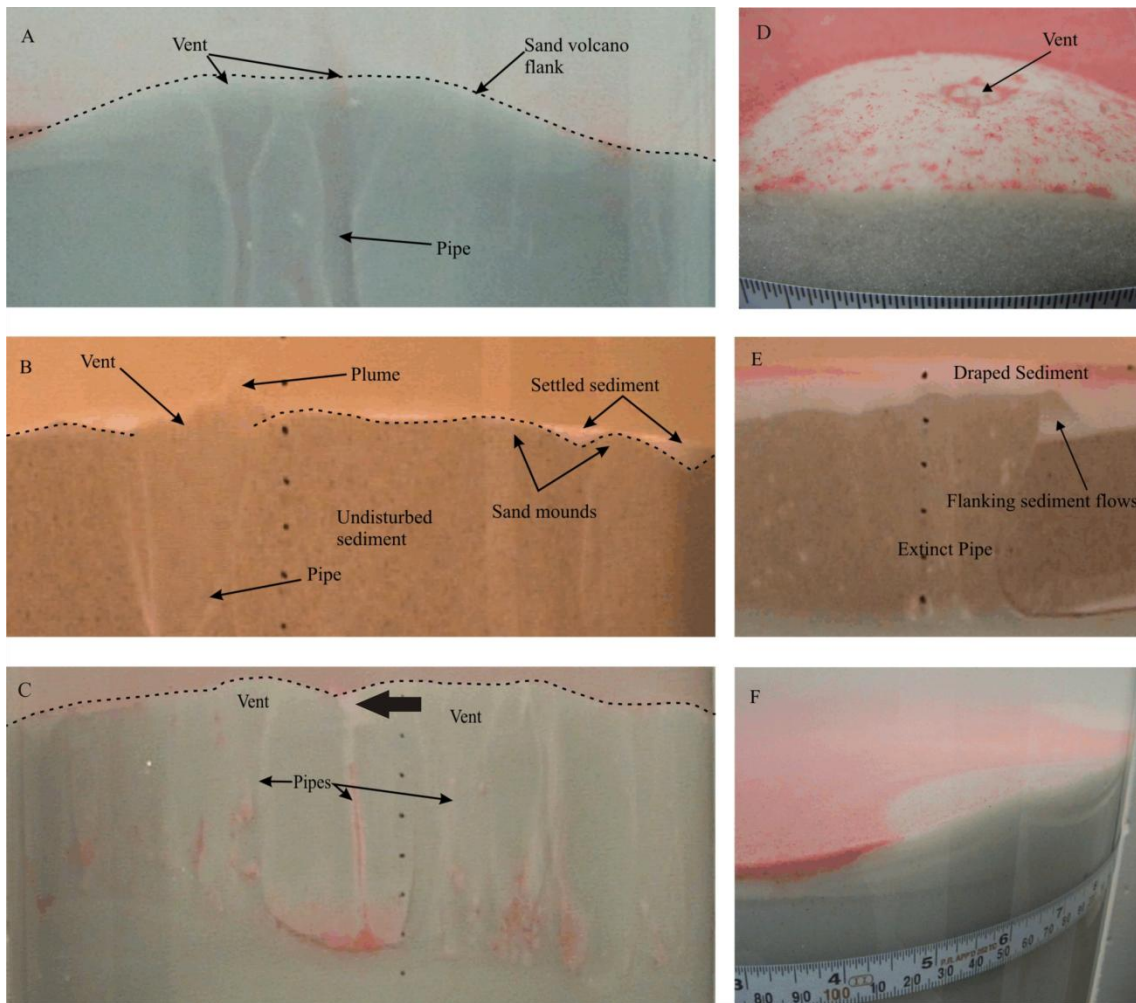


Figure 5.9. Topographic relief created through venting. Important features are labelled and topography marked by the dashed lines. **A)** *Run 4* at 10.22 minutes. The sand volcano is approximately 2 cm high and has two vents fed by separate pipes. The pipe to the right is venting sediment at a faster rate than the left hand pipe. Horizontal scale is 30 cm. **B)** *Run 11* at 7.30 minutes. Pipe is migrating to the left of the picture and relict topography of oviform sand mounds is visible to the right of the picture. **C)** *Run 7* at 5.30 minutes. Multiple pipes have produced an undulating topography, with an extinct pipe (centre, marked by thick arrow) in the depression between two active sand volcanoes and an active vent on the far right with negative topographic relief. Black dots are 1 cm spaced. **D)** *Run 4* post-experiment vent, millimetre scale visible. **E)** *Run 9* at 1.47 minutes, post-experiment. Fine sediment can be seen draped over an asymmetric vent. To the right of the vent

sediment flows comprising the sand volcano flanks are clearly visible. F) Internal structure of sand volcano in *Run 4*.

These undulating sand mounds may be a response to coeval deposition of elutriated sediment and pipe migration; they have subsequently been draped by settled fine sediment (white). This interpretation is supported by their asymmetric shape, as the mounds verge towards the direction in which the pipe migrated. Eruption of fluidised sediment did not always result in the formation of typical sand volcano morphology. Slow discharge rates had one of two effects on vent style during and after fluidisation. If water discharge rate was sufficiently slow, no elutriated material was carried higher than the sediment surface, therefore no distinct vent deposits were formed. When water input rates were higher, extinct vents were seen to be filled with coarse sediment as the rapid settling rate of this material post-fluidisation did not allow for grading to occur and fine sediment remains suspended in the water column above the sediment surface for longer periods, subsequently draping the vent following settling.

Detailed observations of vents yield two end-member scenarios, that of positive relief being generated on the sediment surface and that of sediment surrounding the vent subsiding and a lens-shaped deposit of fluidised sediment forming as shown in Fig. 5.9 A and D (positive vent relief) and Fig. 5.9 C (sediment subsidence around vent due to elutriation of underlying sediment, marked by thick arrow). The dipping of layers towards the vent is not limited to the uppermost layer of sediment as the unfluidised fine layer and infiltration horizon often deformed towards the base of the pipe. This process is potentially due to subsidence of all the sediment overlying the void due to elutriation of material. The accommodation generated on the sediment surface during this process is filled with settling sediment (Fig. 5.9 B). Active sand volcano growth is achieved through sustained flow of grains away from the vent as the water that supported them during fluidisation escapes into the water column, allowing grains to fall either side of the vent. Once a sand volcano

has formed, a central crater can be seen with clear slopes, these features developed in a number of experiments (Fig. 5.9 D and F).

The internal structure of a vent can be seen in Fig. 5.9 F. The sediment comprising the flanks is reversely graded (fine sediment at the bottom) as the fine sediment was vented first, immediately following rupture, then the pipe began to source coarse sediment and vented it, these sediments subsequently settle into alternating layers. In *Run 8*, the vent of a migrating pipe was surrounded by re-sedimented fine material. As silica sand was vented, it settled on top of the fine grained material and within seconds, slumped into the underlying unconsolidated layer, creating laminations dipping away from the vent. Abandonment of flanks surrounding the vent through pipe migration (Fig. 5.9 B as sand mounds) resulted in cusped structures on the sediment surface and oviform sand volcanoes and sand sheets. In Fig. 5.9 E successive layers of silica sand can be seen interleaved with the fine sediment that comprises much of the sand volcano flanks. Fine grained sediment that was vented and not incorporated into volcanoes remained suspended in the water column and subsequently settled under gravity. This blanketed any surface features with 1 – 2 mm of fine sediment and can be seen in Figs. 5.9 E, F and D.

5.5. Discussion

The experiments comprising this study have shown that a range of fluidisation features analogous to those observed in the field can be simulated in the laboratory. In light of the observations made during these experimental runs, further deductions could be made from a number of documented and previously studied field examples of fluidisation products (e.g., Gill, 1979; Plint, 1983; Draganits *et al.*, 1993; Mount, 1993; Collinson, 1994; Obermeier, 1996; Massari *et al.*, 2001; Netoff, 2002; Parize and Friès, 2003; Bezerra *et al.*, 2005; Diggs, 2007; van der Meer *et al.*, 2009). These features include: sand balls, load casts, stress pipes and sand volcanoes. The main findings of the study will be discussed in the order in which the results were presented.

5.5.1. Infiltration and Void Formation

Mörz *et al.* (2007) do not mention the development of infiltration horizons or voids prior to piping in their study of fluid venting, merely that lateral voids develop sub-horizontally to bedding, occurring simultaneously with the widening of micro-channels. This study has demonstrated that infiltration above voids is not uniform, especially where the void is not of a uniform thickness, therefore leading to local variations in pore-pressure due to infiltration. Intriguingly, rupture does not always occur at the apex of the void (see Fig. 2 B, C) contrary to the findings of Nichols *et al.*, (1994). The disparity between this study and Nichols *et al.*, (1994) is probably related to the uneven formation of the infiltration horizon, as it locally blocks pores, creating an uneven void and localised thinning of the overlying strata. These factors can cause initiation of rupture and breakthrough at sites other than the void apex. Variations in infiltration horizon behaviour above voids are most likely related to minor heterogeneities (such as the presence of fine – grained material) in the overlying layer which were likely present herein but may not have been present in the experiments of Nichols *et al.*, (1994) who liquefied their sediment prior to each experiment. The presence of an infiltration horizon on the upper-edge of a steeply dipping pipe has not been recognised in the field, or previous experimental studies. It is interpreted to represent flow of water vertically out of the pipe due to a strong vertical hydraulic gradient, facilitated by the absence of a fine sediment lining on the upper side of the pipe, thus leaving pores open. The lack of infiltration horizons on pipes that are not inclined, suggests this process is limited to sub-vertical pipes. The appearance of stress pipes (with similarities to the micro-channels of Mörz *et al.*, 2007) in the infiltration horizons of all experiments suggests that partial fluidisation in the form of stress pipes, is closely associated with full fluidisation, or piping.

Stress pipes have been documented in the field in Oklahoma (Lowe, 1975) and are associated with highly deformed laminations, often below them. Stress pipes can be seen in Fig. 5.3 B, taken from Diggs (2007); they are present on the margin of a chaotically bedded sandstone sill, supporting the experimental observation from

this study that stress pipes can be closely associated with sand injection. Diggs (2007) speculates that stress pipes seen in outcrop form post-fluidisation, however, this study demonstrates that their formation can be synchronous with primary fluidisation. Furthermore, there are marked similarities in morphology and spatial relationship of the main pipes and stress pipes observed in both the field and the laboratory. Using the assumptions of Diggs (2007), in order to form stress pipes (post-major pipe emplacement); a second period of partial fluidisation would be required. In this scenario, primary fluid flow would re-utilise the previously emplaced dykes as fluid conduits. Despite the apparent morphological similarity between the phenomena described by Diggs (2007) and those produced in our experimental runs, it is important to note that there may be multiple origins for these structures. There is evidence of multiphase fluidisation in the rock record (Massari *et al.*, 2001; Hurst *et al.*, 2003) and these pulses of injection may be invoked as a mechanism for creating an intrusion with features that are difficult to place in a chronological order. Despite this, these experiments demonstrate that synchronous formation of stress pipes and major pipes can be incorporated into current models and that existing field observations can be re-interpreted in the light of these findings.

5.5.2. Rupture

It is thought that rupture occurs when the infiltration horizon reaches a critical thickness, blocking pores in the overlying coarse sediment, therefore blocking any minor water-escape routes, such as stress-pipes, causing a relative increase in water pressure, regardless of the discharge rate. No correlation is seen between the thickness of the infiltration horizon and time until rupture although larger voids result in more violent rupture.

The preservation of failed rupture zones provides an interesting alternative to common explanations of sand loading features, such as static liquefaction of

sediments. Features similar to overturned bedding, as produced in *Run 2* (Fig. 4), are an example of fluidisation features, preserved in fortuitous conditions and have not previously been described from experimental results. Although load structures are commonly thought to be produced by sand sinking into an underlying mud layer, forming load casts and ultimately sand balls, and expelling flame structures from the mud (Collinson, 1994), it may be possible that fluidisation is responsible for some more complex convolute structures that are otherwise difficult to explain as load structures (Lowe, 1975, Frey *et al.*, 2009), or that a continuum exists between structures formed from loading and from fluidisation, as proposed by Owen (1996). The concept of localised failed rupture zones, which will create a gravitationally unstable density contrast between the fluidised and non-fluidised sediments (Owen, 1996), has not previously been addressed and could be a valuable addition to models regarding the relationship between loading and fluidisation.

5.5.3. Piping

The varieties of pipe morphologies described in this study are all documented in outcrop (e.g., Mount, 1993; Netoff, 2002; Duranti and Hurst, 2004) but have never before been produced in experiments. In many studies of sand injection, the feeder conduits are tabular, sheet-like dykes (e.g., Jolly and Lonergan, 2002; Duranti and Hurst, 2004; Hurst *et al.*, 2007) but cylindrical, elliptical and funnel-shaped pipes have been described in outcrop and attributed to water-table fluctuations (Massari *et al.*, 2001; Netoff and Shroba, 2001; Draganits *et al.*, 2003) and seismic shock (Plint, 1983; Netoff, 2002; González *et al.*, 2005). Also, zones of liquefaction surrounding fluidisation pipes similar to those produced in our experiments have been reported from outcrop (Draganits *et al.*, 2003). Specifically, the occurrence of two or more styles of piping within a single experiment is novel. This behaviour shows that, although parameters such as bed thickness were varied, multiple piping styles occur in experiments regardless of whether bed thickness was 3 cm or 10 cm. Stepped-pipe morphology was however, limited to experiments in which the overburden was thickest, or comprised of silica sand, as a response to high

overburden pressure and grain-size differences. These observations of stepped morphology are consistent with those from field studies (e.g., Hiscott, 1979; Obermeier, 1996; Parize and Friès, 2003; Bezerra *et al.*, 2005; van der Meer *et al.*, 2009), especially that of van der Meer *et al.*, (1999) where thin clay laminae are seen to change the orientation of water escape structures. Stepped injection is also seen in core from the Alba Formation in the North Sea (Duranti and Hurst, 2004), although it is important to recognise that many of these intrusions are mudstone hosted and were created at considerably higher confining pressures.

The production of fluidisation pipes with a fine-sediment lining is unique as this behaviour has not been documented in previous experimental studies (Nichols *et al.*, 1994; Nichols, 1995) but lined pipes have been observed in outcrop. Mount (1993), observed fine sediment lining the inner edge of fluidisation pipes, where water escaping outwards from a central pipe has partially fluidised surrounding sediment, removing most of the fines. These haloes were observed to grade gradually into non-fluidised sediment further away from the central pipe. This is supported by observations in this study, as once flow has ceased, the boundary between fluidised and undisturbed sediment is difficult to discern. Similarly, sand volcanoes formed in modern environments can show vents with a clay lining (Neumann-Mahlkau, 1976) and pipes underlying sand volcanoes in Japan are lined with goethite (Okada and Whitaker, 1979). Field studies of fluidisation pipes in Utah show them to have distinct walls enriched with a calcite cement (Netoff and Shroba, 2001; Netoff, 2002) (Chapter 8). It is feasible that grain-size differences between the pipe and the host rock facilitated this enrichment by focusing the flow of diagenetic fluid. However, pipes that are emplaced during upwelling of overpressurised groundwater, and thought to have formed less explosively do not show lining with fine sediment, instead displaying internal slumping of laminae (Massari *et al.*, 2001) or concentric cylindrical laminae (Draganits *et al.*, 2003). It is thought that the fine-grained sediment that lines the inner-edges of these thin,

vertical pipes is a strong factor in their stable behaviour; without this lining, the pipe may begin to migrate.

Lateral pipe migration in experimental fluidisation has been documented in seepage studies in single sediment layers (Mörz *et al.*, 2007), and has been reported by Lowe (1975) who suggested that the sediment remained structured after the pipe had migrated through it. Experimental parameters in these studies are either undefined (Lowe, 1975) or have only a single-layer stratigraphy (Mörz, *et al.*, 2007) and no discussion has been made on the effects and implications of pipe dynamics. However, here for the first time pipe migration in layered sediment has been documented, along with associated disturbance of sediment layers. Lovell (1974) alludes to such vent migration during extended periods of sediment extrusion based on a study of sand volcanoes in Kirkcudbrightshire, Scotland. Large areas of sand that show water escape features are usually interpreted as the product of *en masse* liquefaction or fluidisation (e.g., Jolly and Lonergan, 2002) whilst this work suggests the possibility that they may have been only locally fluidised, with pipe migration creating the broad, spatial extent of fluidised sediment. If this type of deposit were to be encountered in outcrop or core it may be difficult to determine its origin due to the absence of evidence for pipe-migration, perhaps classing it as an unstratified sand resulting from liquefaction rather than the result of lateral migration of a fluidisation pipe; although scaling must be taken into account.

5.5.4. Venting

These experiments have produced novel surface expressions of piping including; asymmetric and flat-topped vents (Fig. 5.9). These styles have not been described previously and these atypical vent features, characterised by little or no vertical relief, may have direct implications for outcrop studies. For example, a vent that did not produce topography at the time of formation may not be easily recognisable as a fluidisation feature in outcrop and could be misinterpreted as an erosional surface,

or as a liquefaction feature. Additionally, much of the material extruded from vents (at least those that are subaqueous) does not form sand volcanoes, but instead flows away from the vent site as gravity currents, thus covering the surrounding areas with elutriated sediment, creating sand sheets on the surface (Fig. 5.9 F, 5sand_sheets.avi – see DVD). None-the-less where flow rates to the surface are relatively low then classical sand volcanoes did form in these experiments, producing prominent vents with dipping laminations on the flanks. These dipping laminations were formed as a result of spontaneous segregation of different size particles (Makse *et al.*, 1997) and through slumping of coarse material into underlying fine sediment. Lateral transport of grain flows across the sand volcano flanks may have been aided by fluid flow emanating from the flanks of the sand volcanoes, as a result of the surrounding halo of circulating water around the vent; although fluid velocities were not high enough to liquefy the flank sediment.

Sandstone volcanoes have been reported from a variety of sedimentary settings: i) shelf environments (e.g., Burne, 1970; Higgs, 1998), ii) deep-water turbidites (e.g., Gill and Keunen, 1957; Gill, 1979; Pringle, *et al.*, 2007), iv) deltaic environments (Johnson, 1977; Okada and Whitaker, 1979), iv) fluvial (e.g., Allen, 1961; Williams and Rust, 1969) and v) shallow ponds following vibration-induced fluidisation (e.g., Neumann-Mahlkau, 1976). Analogous sub-aerial features are termed ‘sand boils’ or ‘sand blows’ and have been frequently observed after earthquakes (e.g., Saucier, 1989; Obermeier, 1996; Audemard *et al.*, 2005; Reddy *et al.*, 2009), and also along river levees during flood conditions (e.g., Singh *et al.*, 2001; Obermeier *et al.*, 2005; Li *et al.*, 2009). In the latter case the sand boils occur due to a hydraulic head difference across levees causing focused seepage away from the flooding river (Li *et al.*, 2009). They have a similar internal structure to the sub-aqueous sand volcanoes described in this study, with a well-defined pipe, vent and steeply dipping laminated flanks. There are a number of key discrepancies between sub-aqueous and sub-aerial sand extrusions linked to the behaviour of elutriated and extruded sediment:

5.5.4.1. *Extruded sand sheets*

Sediment that is violently ejected sub-aqueously was observed to form lateral gravity currents that transported the sediment away from the side of the vent and formed extruded sand sheets over large areas of the tank (see 5sand_sheets.avi on accompanying DVD). Such extruded sandstone sheets have been detailed from sub-aqueous systems above slumps (Gill and Keunen, 1957; Strachan, 2002; Jonk *et al.*, 2007; Vigorito *et al.*, 2008), described as flowing considerable distances on the palaeosurface above massive pipes (Netoff, 2002) and are often triggered by seismic activity (Hesse and Reading, 1978; Collinson, 1994), but their formative mechanisms have not previously been described. Boehm and Moore (2002) described extruded sandstone sheets that extend hundreds of metres from feeder dykes at the Majors Creek site in Santa Cruz County, California where the extruded material has a slightly coarser grain size than the underlying conduits. Similarly, large sandstone mounds interpreted as extrudites that merge laterally into sheets have been reported from the Panoche Giant Injection Complex, California where continued sediment extrusion is attributed to the maximum potential pressure gradient being achieved between the source bed at depth and the point of extrusion, thus maximising the energy driving the intrusion process (Vigorito *et al.*, 2008). This study provides the first experimental observations of sub-aqueous sand sheet formation; however sub-aerial sand sheets have previously been reported from experiments using air as the fluidising agent (Rodrigues *et al.*, 2009). Natural sub-aerial extruded sand sheets have also been noted (e.g. Saucier, 1989; Obermeier, 1996). Differences between sub-aerial and sub-aqueous extruded sand sheets might be expected based on their formative processes. Sub-aerial sheets form through air fall during ejections, and laterally extensive sand sheets form; i) the most violent venting events or ii) from the coalescing of closely spaced sand blow mounds (Saucier, 1989). In contrast, sub-aqueous examples have the added transport mechanism of gravity currents to distribute the material over much larger areas. These differences in process mechanics reflect those observed experimentally.

5.5.4.2. *Sand volcanoes*

Sand volcanoes were observed experimentally to form either as isolated features or on top of extruded sand sheets. In both cases, sand volcano development represents a dominance of local deposition of extruded material over lateral sediment transport, indicative of less violent eruption of material. Furthermore, the experiments show that sand volcanoes can form in the same events as extruded sand sheets, as the magnitude of the ejection decreases and sedimentation becomes progressively more confined around the vent. In contrast, some previous field studies have suggested that sheets and sand volcanoes form in separate events (Jonk *et al.*, 2007). Whilst this is possible, through experiments, it is shown here that sand volcanoes can form during the late stages of fluidisation and often overlie extruded sand from earlier stages of venting. Slope angles of subaqueous volcano flanks reflect both the grain-size and shape characteristics that control subaerial volcano flanks, but also the relative importance of laterally driven gravity current transport which will act to lower flank gradients.

The internal geometry of sand volcanoes showing steeply dipping, alternating laminae has been documented in the field, (Neumann-Mahlkau, 1976; Okada and Whitaker, 1979) especially in the Namurian of County Clare, Ireland (Gill and Kuenen 1957; Gill, 1979), most recently using ground-penetrating radar to study the region directly underlying sandstone volcanoes on the Ross Slump (Pringle *et al.*, 2007). This study supports field observations by Pringle *et al.*, (2007) and Gill and Kuenen (1957) that sand volcano flanks may be composed of alternating fine and coarse laminae due to grain flows and show a composite morphology where multiple sand volcanoes occupy the same area over a period of time. Internally, differences might be expected between sub-aerial and sub-aqueous sand volcanoes. In a sub-aerial environment both fine-grained and coarse material compose the flanks of the volcano, with fine grained material trapped in alternating laminations, whereas in sub-aqueous settings, more of the expelled mud and other fine grained material will be held in suspension in the water column before undergoing gravity

settling. Jonk *et al.*, (2007) also note the coarse-grained texture of sand volcanoes and invoke a mechanism for this whereby only the coarse fraction of the source sand was fluidised and vented, thus leaving behind fine-grained material and clay particles. There is no evidence of this mechanism in these experiments, instead the evidence suggests that the fine-fraction is in fact preferentially fluidised and, in the case of any sub-aqueous sediment extrusion, the fine-fraction remains suspended in the water-column before gravity settling. Field data supports such a model of mud being transported and placed into suspension, since sandstone dykes in County Clare, Ireland showed a 25% mud matrix, whilst the sand volcanoes only had about 10% mud matrix (Strachan, 2002).

5.5.4.3. *Self-preservation of sand volcanoes*

In the experiments fine-grained material was observed to drape the sand volcanoes and associated sand sheets (Fig. 5.9E). Such material is derived from slower settling of the finest-grained component that has been ejected into the water-column. This allows time for coarse-grained sediment extrusions to accumulate before effectively being sealed by the settling of fine-grained material from the water column. Similar caps of remobilised sediment were observed in the experiments of Frey *et al.*, (2009). Field examples can show sandstone volcanoes and sheets covered by thin-layers of fine-grained material (Gill and Keunen, 1957; Strachan, 2002). It can be inferred that the fine-grained cap on these sand volcanoes is a form of self-sealing, or self-preservation by the mechanism described above and is one of the reasons why preservation of sand volcanoes can in many cases be so exquisite. Sub-aerial systems will not exhibit this form of self-sealing and coupled with their presence on the land surface, gives sub-aerial sand volcanoes very low preservation potential.

5.5.5. Wall effects

Most of the observations in the present experiments have been obtained through analysis of the sediments immediately adjacent to the side-walls. Such an approach is in keeping with previous experimental work in the field (Nichols *et al.*, 1994; Nichols, 1995; Mörz *et al.*, 2007; Frey *et al.*, 2009). Nonetheless it is important to consider whether this approach is fully representative of the processes and deposits. The side wall interface will exhibit reduced friction due to the smooth inner wall, and thus sediment failure is more likely to take place at this boundary. It may also be the case that this reduced friction at the wall may increase the migration rate of features such as mobile pipes, and locally enhance the size of voids. However, the present experiments demonstrate from observation of the upper surface and cross-section analysis, that i) fluidisation features are not limited to the sidewalls, ii) pipes migrate internally within the sediment mass, and iii) sediment architecture internal to the tank can exhibit the same features as those observed adjacent to the sidewalls. Thus the influence of the sidewalls does not appear to be leading to observations of features or processes that are unrepresentative of the bulk mass of sediment. The correspondence between features internal to the tank and those viewed at the sidewalls, may reflect the relatively large tank used in these experiments. The cross-sectional area in this study was 651 cm², giving a cross-sectional area / sidewall circumference ratio of 7.2, compared with 3.5 for the small circular tank of Nichols *et al.* (1994) and 1.4 for the rectangular tank of Frey *et al.* (2009 (Table 5.2).

	This Study	Nichols <i>et al.</i> , (1994)	Mörz <i>et al.</i> , (2007)	Frey <i>et al.</i> , (2009)
Area (cm ²)	651.4	153.9	380	171
Circumference (cm)	90	43.9	69	120
Wall effect number	7.2	3.5	5.5	1.4

Table 5.2. Wall effect numbers for this and previously published studies.

High wall effect numbers reflect a lack of interaction between the walls of the tank and centre. It is also important to note that apparent doming of the upper surface and middle layer of the sediment is an effect of perspective enhancing the already present barrel distortion in the images. A more detailed assessment of sidewall effects is contingent on the development of non-invasive techniques for observing away from tank walls.

5.5.6. An integrated model of extrusive sand injectites

The array of features observed in these experiments can be incorporated into a new model of pipe formation in cohesionless sediments during fluidisation (Fig. 5.10). This model integrates the typical features observed during the fluidisation experiments including void formation, pipe initiation and failed rupture zones (Fig. 5.10 B, C), multiple rupture sites (Fig. 5.10 B1), pipe migration and homogenisation of sediment (Fig. 5.10 D2) and vent formation and stabilisation (Fig. 5.10 D). The model concentrates on pipe dynamics, sand volcano formation and subsequent draping. However, in all cases extruded sand sheets can also form in the initial stages, with the subsequent development and self-sealing of sand volcanoes (Fig. 5.10 E). Atypical features such as: double void apex development, pipes showing stepping morphology, infiltration and stress pipes associated with sub-vertical pipes and vents showing unusual morphology have been omitted from the model for clarity.

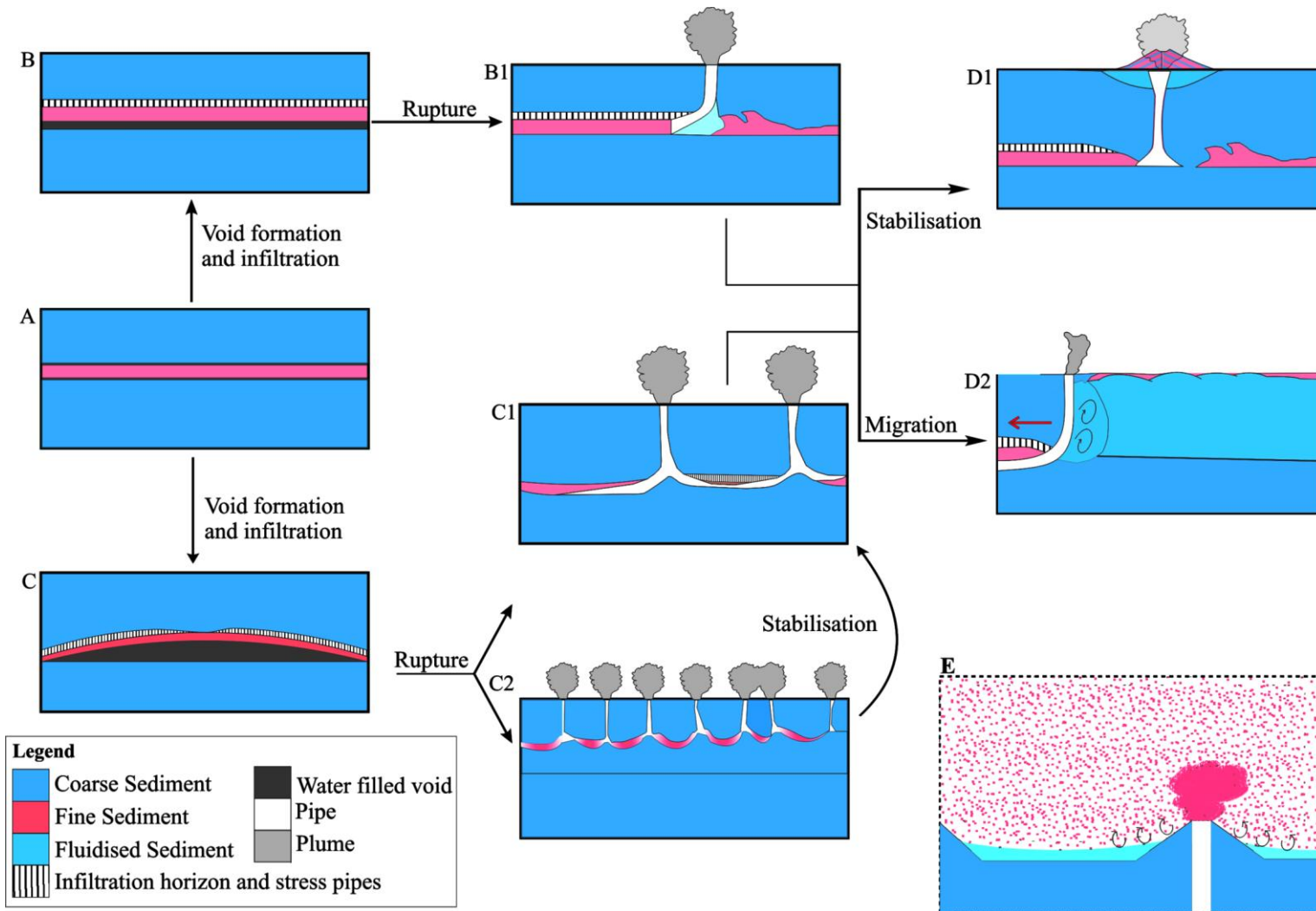


Figure 5.10. Schematic representation of a new model of pipe formation in cohesionless sediments. **A)** Starting conditions with a fine sediment layer between two, thick, coarse sediment layers. When overpressure is generated heterogeneities in the upper layer determine whether the system develops into **B)** (homogeneous upper layer) An even void forms beneath the fine sediment layer immediately followed by infiltration of fine sediment into the top layer and stress pipe formation (partial fluidisation) or **C)** (heterogeneous upper layer) An uneven void is formed with an inverted conical shape. Infiltration into the upper layer occurs with localised absence of infiltration horizon at void apex. From these initial stages the following occurs: **B1)** Rupture and initial pipe formation. Failed rupture zones may be preserved and a fluidised zone develops at the base of the pipe which is now elutriating fluidised sediment. This configuration is not stable. **C1)** In this scenario, one or two rupture zones may have occurred resulting in two pipes elutriating sediment and water. Most of the fine sediment has been removed, although a small amount remains between pipes. **C2)** here multiple ruptures have occurred, leading to multiple pipes. Most fine sediment has been elutriated and a zone of fluidised sediment exists below the base of pipes. An unstable configuration which will lead to one of the pipes becoming dominant and others shutting down. **D1)** A dominant pipe has stabilised and the rim is lined with fine sediment; preventing pipe migration. A localised zone of fluidised sediment exists around the vent with down bending of all layers orientated towards the base of the pipe. **D2)** Unconfined pipe migrates laterally. Original stratification is undisturbed on the leading side of the pipe whereas where the pipe has passed, sediment is homogenous and relict topography is preserved on the surface. A zone of circulating fluidised sediment is associated with the rear of the migrating pipe. **E)** Schematic demonstrating gravity currents flowing down the sides of a sand volcano to develop sand sheets and fine-grained sediment is held in suspension before settling and draping sand volcano. This model does not take into account atypical features such as double void apex formation, dyke and sill intrusions, unusual topography and infiltration associated with sub-vertical pipes.

5.6. Conclusions

The experiments undertaken within this study have produced an array of fluidisation features, many never before observed experimentally, and have shown for the very first time the dependency of fluidisation features on a number of factors such as uneven rupture or lining of pipes, often regardless of controlled parameters. Key findings include the production of features analogous to convolute structures which were preserved and are supportive of existing theories on the continuum of features between liquefaction and fluidisation (Lowe, 1975; Collinson, 1994; Owen, 1996). Sub-aqueous systems have been shown to form extruded sand sheets across the entire experimental surface, driven in large part by gravity currents. These sheets are overlain by sand-volcanoes that have been shown to exhibit self-preserving behaviour, as a result of the settling of fine-grained material on and around the sand volcano, contrary to the behaviour of extruded material from sub-aerial sand volcanoes or sand-boils.

The experimental results have enabled the construction of an integrated model (Fig. 5.10) of pipe initiation and evolution in cohesionless sediments to be proposed for the first time. The model provides a first attempt at assimilating the processes and effects of: sediment heterogeneities, infiltration of fines, void formation and subsequent rupture. These phenomena have been found to affect the formation and behaviour of pipes during clastic injection.

Small ruptures evolve into vertical pipes, which stabilise easily, providing fluid flow rate is low enough to allow lining of the pipes internal circumference with fine sediment. Without this accumulation of fines, pipes evolve further and migrate laterally, homogenising and elutriating sediment, thus showing that relatively large volumes of sediment can be fluidised by a small, yet dynamic, pipe. Wide or multiple rupture zones have been shown to produce migrating pipes and broad zones of fluidisation without confined piping. Such features would normally be

interpreted as the products of *en masse* liquefaction rather than complex fluidisation. This is the first time stress pipes have been observed associated with infiltration horizons, and the first documentation of their simultaneous formation. This study has produced an initial indication that the migration of fluidisation pipes may isolate sand volcanoes or extrudites from an underlying fluidisation system and physically demonstrates that pipe stabilisation can occur through lining of pipes with fine sediment.

6. Pipe flow processes in sand injectites

6.1. Introduction

Sand injections form when fluidised sand, as a slurry of sand and water, is forcibly injected into fractures in over or underlying sediment as a response to overpressure in a parent sand unit. Sand injections form high-permeability networks of sandstone dykes and sills through relatively low-permeability host strata and have been reported from, but are not limited to mudstone host rocks (e.g. Hurst *et al.*, 2005; Jackson, 2007; Sherry *et al.*, 2012), with pipes and columns forming when injections occurs in a coarse-grained host (e.g. Netoff, 2002; Huuse *et al.*, 2005). Despite the significant interest in the genesis of sandstone intrusions, the majority of our understanding regarding flow processes during injection comes from field observations of the margins of exposed sandstone intrusions (e.g. Duranti *et al.*, 2002; Parize and Friès, 2003; Scott *et al.*, 2003; Sherry *et al.*, 2012), and core-based studies (Duranti and Hurst, 2004). Although this evidence may appear robust, only the products of fluidisation, such as the final geometry and structure, are considered (e.g. Duranti, 2007; Hurst and Glennie, 2008; Vigorito and Hurst, 2010), with particular attention paid to grain-size variations (Peterson, 1968; Hubbard *et al.*, 2007), and erosional features at intrusion margins (Vigorito *et al.*, 2008; Scott *et al.*, 2009; Kane, 2010).

Some studies recognise the distinction between structures formed during the peak-flow of the injection, and lamination created by internal shear during waning flow (Kane, 2010; Sherry *et al.*, 2012); an important consideration when estimating flow conditions during emplacement of intrusions. Physical modelling studies of geological fluidisation have highlighted processes such as, hydraulic fracture

propagation in cohesive sediments (Rodrigues *et al.*, 2009), the initiation of fluidisation pipes, and production of sand volcanoes in single-layer (Mörz *et al.*, 2007) and multi-layer sediments (Nichols *et al.*, 2004; Nichols, 2005; Ross *et al.*, 2011). However, no attempt has been made to quantify the nature of granular flow during sand injection experimentally, which is the focus of this chapter.

6.1.1. Flow conditions in active injections

There is much variation and consequently uncertainty in the interpretation of the flow regimes required to create sand injectites. Several interpretations of intrusions have relied on the assumption that all fluidisation is turbulent without specific evidence in support of the notion (Lowe, 1975; Duranti and Hurst, 2004; Chan *et al.*, 2007). Lowe (1975) suggested that although fluidisation is associated with turbulent flow, there is a probable continuum of flow states ranging from slow, laminar, hydroplastic shear, to rapid, fully turbulent fluidised flow. Scott *et al.*, (2009) put forward an equally speculative range of flow regimes, from low-velocity viscous, hydroplastic laminar to high-velocity turbulent flow. In addition, it has been suggested that spatial and temporal variations in these differing flow dynamics create the variety of geometries and internal structures in injectites (Scott *et al.*, 2009). Linear margins on a dyke are easy to interpret as injections along a planar fracture (Hurst *et al.*, 2011) however, bulbous (Keighley and Pickerill, 1994; Hubbard *et al.*, 2007) and rounded margins (Surlyk *et al.*, 2001) fit fracture models less easily. Furthermore, these deviations from expected fracture patterns have been interpreted as due to anisotropy in the host sediment or rheoplastic moulding (Keighley and Pickerill, 1994). Structures similar to flute marks found on the base of turbidites are described from intrusion margins, and are attributed to erosion on injectite margins, and taken as direct evidence of turbulent flow (Hurst *et al.*, 2011).

6.1.2. Evidence from erosive-type structures

Several studies have attributed non-linear contacts between injected sand and surrounding sediment to non-specific erosive or turbulent flow (Massari *et al.*, 2001; Hurst and Glennie, 2008; Vigorito *et al.*, 2010). Other studies have identified specific erosive structures on pipe edges and termed them: (i) flute-like marks (Kane, 2010) (Fig. 6.1 B); (ii) flutes (Jonk, 2010; Moreau *et al.*, 2012) (Fig. 6.1 C); (iii) flute and groove casts (Peterson, 1968); and, (iv) erosional scours and scallops (Scott *et al.*, 2009) (Fig. 6.1 D), all concluding that the formative flows were turbulent. A few studies are distinct in claiming flow during injection was laminar despite irregular intrusion margins. Diggs (2007) describes intrusion margins as displaying “low-relief linear structures” (Fig. 6.1 G) and attributes their formation to frictional drag as it is unclear whether they are orientated parallel or perpendicular to flow and also identifies “structures resembling flute and groove casts” ascribed to stopping of host sediment at the pipe margin (Diggs, 2007). Where previous workers concluded that flow in active injection is laminar, the nature of the injectite-host contact was not taken as evidence for flow regime and interpretations were generally based on the interior structure of the intrusion (Dott, 1966; Peterson, 1968; Taylor, 1982). Taylor (1982) attributes linear pipe walls to the cohesive nature of the host sediment and where “flutes” occur on pipe walls their origin is interpreted to be due to a sudden change in the viscosity or velocity of the intruding sediment as opposed to scouring.

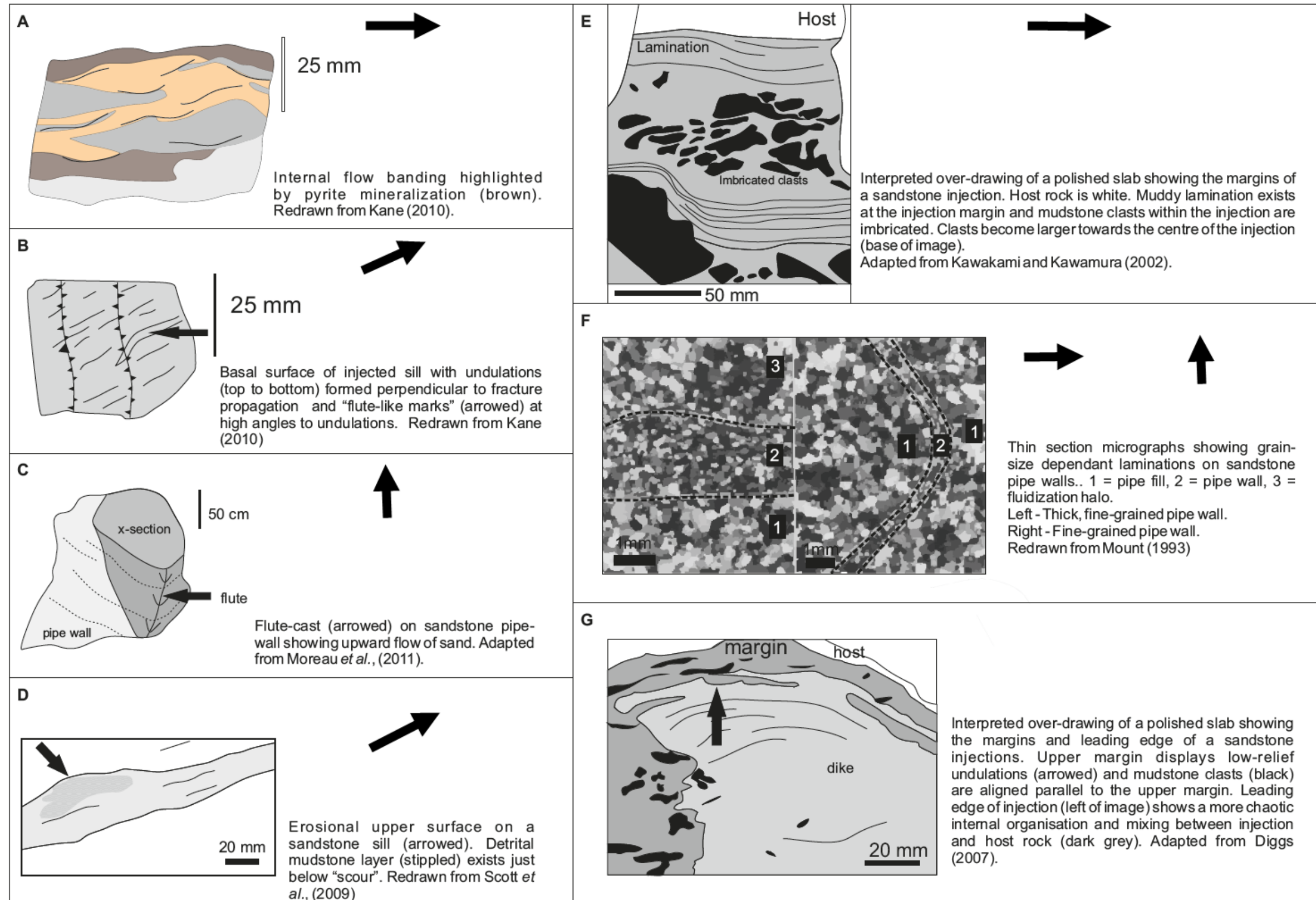


Figure 6.1. Diagram showing the range of outcrop evidence for low regime in injections. Heavy arrows denote flow direction in each example. Flow in G is into the page.

6.1.3. Laminations at pipe margins

Three types of lamination are reported from pipe margins: (i) the alignment of tabular grains (Peterson, 1968; Dixon *et al.*, 1995; Diggs, 2007); (ii) the alignment of clast long-axes (Dixon *et al.*, 1996; Kawakami and Kawamura, 2002; Diggs, 2007; Levi *et al.*, 2007) (Fig. 6.1.E); and, (iii) the presence of laminations at, or adjacent to fine-grained injection margins (Peterson 1968; Taylor, 1982; Mount, 1993) (Fig. 6.1 F). Grading, or laminations, are developed in both single and multiple layers; grading occurring as both normal and reverse perpendicular to pipe margins (Peterson, 1968). The origin of these laminations is not fully understood and putative mechanisms include: (i) repeated pulses of injection through the same conduit (Diggs, 2007); (ii) flow-banding preserved during flow deceleration due to shearing of grains (Kane, 2010) (Fig. 6.1 A); or, (iii) reorganisation of grains in a jammed granular network by percolating pore-water following fluidisation (Sherry *et al.*, 2012). Previous studies have interpreted lamination and tabular grain alignment at injection margins to be evidence of laminar flow during injection (Dott 1966; Peterson 1968; Taylor 1982; Dixon 1995; Diggs 2007). In all cases presented in this section, with the exception of Levi *et al.* (2007) who based their flow regime estimate on theoretical modelling, the flow in the active injection is assumed to be laminar.

6.1.4. Experimental evidence

Experimental studies into the nature of fluidisation in geological materials began with Lowe (1975), who describes some interesting results, but without providing experimental parameters required to understand the true implications of the work. Although the work of Nichols (1994) and Nichols *et al.* (1995) provides excellent constraints on the nature on rupture and relationships between piping and overburden thickness, there is little description of the nature of the flow in active fluidisation pipes. Only the study of Ross *et al.* (2011) (Chapter 5) has attempted to make detailed morphological observations of the pipes, and no effort has been

made to quantify flow velocity and particle trajectories in fluidisation pipes through experimental modelling.

One of the limitations of past experiments is that pressure records, where present, lack sufficient resolution to monitor the detailed flow dynamics. In particular, no previous study has recorded digital pressure readings throughout fluidisation experiments (Ross *et al.*, 2011), instead relying on manometers which have inherent delays as it takes a finite time for the magnitude of a pressure change to register along the tube (Nichols, 1994). It has been shown that manometers consisting of tube length as small as 2 m will have delays of 2 seconds in recording the pressure change (Sinclair and Robbins, 1953). Therefore, although general pressure trends can be recorded, it would not be possible to record rapidly fluctuating pressure or, for example, the pressure drop in the system at the moment of rupture and the onset of piping.

6.1.5. Theoretical considerations of flow regimes in fluidisation pipes.

The outcrop-based study of Diggs (2007) invokes a “probable” laminar flow regime as being responsible for alignment of tabular grains parallel to the edge of sandstone dykes whereas the more theoretical approach of Gallo and Woods (2004) attributes alignment of grains on pipes walls to turbulent drag effects. They propose that the average velocity of fluidised slurry in a pipe is at its highest at low sand concentrations as demonstrated in Figure 6.2. In this regime, turbulent drag in the flow balances the overpressure whereas at sand fractions higher than $\phi = 0.2$, grain-grain interactions become progressively more dominant and the flow less homogenous. At higher sand concentrations, the effective viscosity of the slurry increases (Gallo and Woods, 2004). Pipe diameter also has a significant effect on flow velocity, as flow velocity is highest at the centre of a conduit, and retarded at pipe walls due to frictional effects (Gallo and Woods, 2004). Therefore, larger diameter pipes will exhibit commensurately smaller frictional losses (Fig. 6.2).

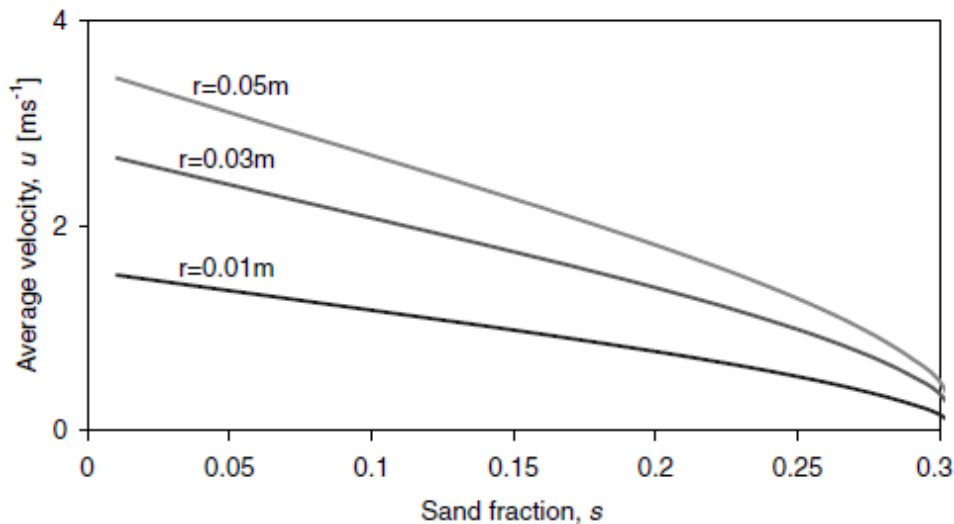


Figure 6.2. Velocity as a function of sand fraction; r is conduit radius. From (Gallo and Woods (2004).

Gallo and Woods (2004) showed through a theoretical approach, that fluidised flows are dominated by turbulence, however their model assumed a connection to the surface with no mass being lost from the conduit and a steady, homogenous and well-mixed flow. Therefore, the properties of the slurry such as viscosity and density are averaged across the conduit diameter and based upon the concentration of sand in the fluid (Gallo and Woods, 2004). Figure 6.3 shows the relationship between the radius of a pipe and the average velocity of a fluidised flow. The arc of the curve demonstrating that for a pipe with a small radius (< 0.002 m), viscous effects are negligible and in the smallest pipes, the closeness of the walls alters the viscous effects (Gallo and Woods, 2004).

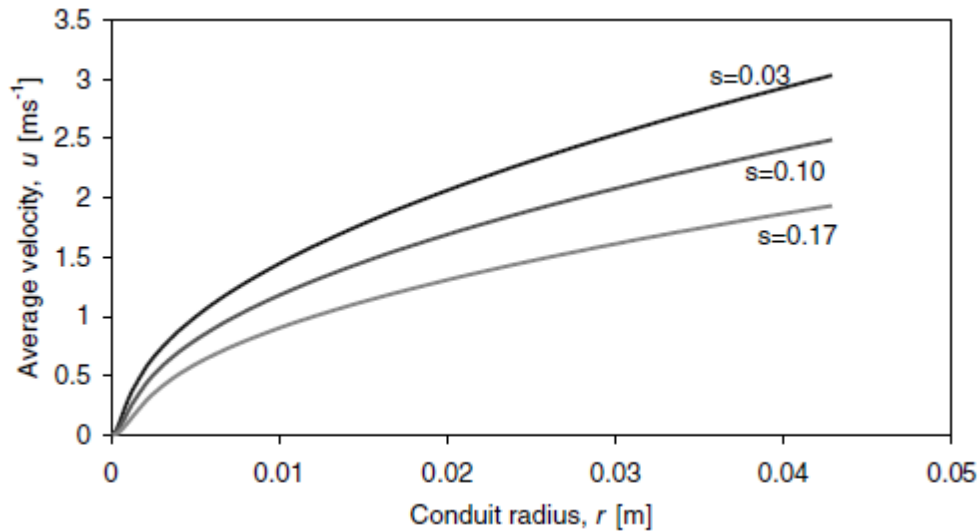


Figure 6.3. Velocity (u) as a function of conduit radius (r) for a given overpressure at the base of the fracture (s) is sand fraction. From Gallo and Woods (2004).

6.1.6.1. Previous estimates of flow Reynolds number

Calculation of the flow Reynolds number in an active injectite was first attempted by Duranti and Hurst (2004) with their method being replicated by Scott *et al.*, (2009) and Sherry *et al.*, (2012). In order for the flow regime to be determined, the velocity of the fluidised sand-water suspension must first be calculated. As this is not directly obtainable from an outcrop or core-based study, the minimum fluid velocity required to hold the largest clast in the system in suspension is considered the overall fluid velocity. The minimum fluid velocity corresponds to the fall velocity of the particle. The approach of Duranti and Hurst (2004) follows Allen (1985) in utilising the square root law for determining the fall velocity since the application of Stokes' law would be unacceptable as it is valid only for particles up to 100 μm (Allen, 1985).

Calculation of flow velocity using clast terminal-fall-velocity

The square root law of Allen (1985) implemented by Duranti and Hurst (2004) and Scott *et al.*, (2009) for the calculation of the terminal fall velocity of a clast assumes

perfectly spherical grains in clear, stagnant fluid with no edge friction (Equation 6.1).

$$U = k \left(\frac{\rho_s - \rho_f}{\rho_f} gD \right)^{0.5} \quad (6.1)$$

where ρ_f is the ambient fluid density, ρ_s is the particle density, g is gravity, D is the particle diameter, and k is given by:

$$k = \frac{4}{3} C_{D,0} \quad (6.2)$$

where $C_{D,0}$ is the drag coefficient for a solitary sphere in a fluid with a particulate concentration of zero, taken as a constant of 0.45 (Allen, 1985), and ρ_{pf} is taken as the density of the ambient fluid, in this case that of the pseudo-fluid; the average fluid-particulate density (Duranti and Hurst, 2004; Scott *et al.*, 2009; Sherry *et al.*, 2012). However, despite implementation of an arbitrary drag coefficient, ($C_{D,0} = 0.45$) which incidentally, is valid only for small spheres, whereas $C_{D,0}$ for coarse, natural particles is approximately 1.4 (Gregory, 2010), Equation 6.1 still does not account for drag on the particle imparted from the surrounding (pseudo)fluid and thus is flawed. A more suitable formulation of the problem is presented in Equation 6.3 (Allen, 1985) which accounts for the effects of a particle-laden fluid on the settling velocity of a clast.

$$U = \left(\frac{4(1-\phi)^{2n}(\rho_s - \rho_{pf})gD}{3 C_D \rho_{pf}} \right)^{0.5} \quad (6.3)$$

Where ϕ_s is the solid volume concentration and C_D in the fluidised system is given by (Allen, 1985):

$$C_D = C_{D,0} / (1 - \phi_s)^{2n-2} \quad (6.4)$$

The exponent n is a function of particle shape (Richardson and Zaki, 1954):

$$n = 2.7k_s^{0.16} \quad (6.5)$$

Where k_s is a volumetric shape factor which must be calculated from the particle dimensions (Richardson and Zaki, 1954).

Calculation of flow Reynolds number

Once the terminal fall velocity of the largest clast in a given system has been established through implementation of Equation 6.3, the flow Reynolds number can be calculated as it is a function of flow velocity, pseudo-fluid density, pseudo-fluid viscosity and the diameter (d) of the fracture or pipe (Equation 6.6).

$$Re = \frac{(U*d*\rho_{pf})}{\mu_{pf}} \quad (6.6)$$

The previous estimates of Reynolds number by Duranti and Hurst (2004) and Scott *et al.* (2009) did not account for the true viscosity of a sediment-water mixture, and relied on an averaged density of the particles and water based upon the particle concentration, and a viscosity close to that of water to calculate “overwhelmingly turbulent” flow in active injections (Scott *et al.*, 2009). This omission was noted by Sherry *et al.* (2012) who calculated flow Reynolds numbers based upon a range of fluid viscosities from 1-30 PaS, derived from studies of debris flow rheology (Major and Pierson, 1992). However, it is possible to quantify the fluid density and viscosity based upon the particle concentration using the following approach (Di Felice, 2010).

$$\rho_{pf} = \phi\rho_s + (1 - \phi)\rho_f \quad (6.7)$$

$$\mu_{pf} = \mu_f(1 - \phi)^{-2.8} \quad (6.8)$$

The calculations of Scott *et al.*, (2009) are reappraised in Chapter 8, sections 8.4.6. and 8.4.7.

Calculation of flow velocity as a function of energy loss during injection.

An alternative approach was utilized by Duranti (2007) and is based upon the concept of energy transfer into the injection system. By calculating the total volume

of sediment in an injection complex, it is possible to calculate the amount of energy that must be imparted into a slurry (e.g. as overpressure in the form of seismic shock) to cause the grains and fluidising medium to be lifted. The flow velocity is then calculated as in Equation 6.8 and is treated as a function of the pseudo-fluid density relative to the density of the overlying lithostatic column:

$$U = \sqrt{2gH \left(\frac{\rho_r}{\rho_f} - 1 \right) \frac{T}{fL+T}} \quad (6.8)$$

Where T is the maximum dyke thickness and fL the fracture length. A range of Reynolds values are then calculated ($14,778 < Re < 147,778$) which are based upon a range of fluid viscosities (0.1 – 1 PaS). The approach implemented by Duranti (2007) is novel, but does not truly account for frictional losses in the fluid. Energy losses due to friction and shear at the dyke wall are explored but disregarded due to their negligible value in comparison to the total amount of energy in the system, since the hydraulic radius of the system is small. The friction coefficient utilized in the approach of Duranti (2007) is valid for turbulent channel flow in rivers (Allen, 1985) where a value for flow in a pipe would be more suitable, and also disregards the increased effects of the wall as the hydraulic radius decreases. It is noted that variations in fracture aperture between the tip and any arbitrary point along its length will vastly change the flow velocity at that point, due to increased loss of energy due to friction at smaller apertures.

No previous study has attempted to quantify the flow regime in active sand injections through experimental techniques, instead relying on theoretical approaches. This chapter presents the first attempt to track individual sand particles in active fluidisation pipes in order to further understanding of grain-scale processes in pipe formation. The experiments assess

- (i) the effect of migrating fluidisation pipes on host sediment heterogeneity;

- (ii) the trajectories of fluidised grains in pipes;
- (iii) spatial and temporal changes in flow within fluidisation pipes;
- (iv) the effect of fluidisation pipes on the surrounding sediment and production of features analogous to natural examples.
- (v) the Reynolds number and flow regimes within the pipes.

6.2. Experimental Methodology

The experiments presented herein were conducted in the Sorby Environmental Fluid Dynamics Laboratory at the University of Leeds. The tank used is a modified version of that utilised in **Chapter 5** (Figure 5.1). The addition of a header tank allows the experiments to be run at constant head via a fixed-speed pump and a Keller PR33X/0-3bar pressure transducer was fitted to the manifold in place of a flow meter to enable collection of pressure measurements at 16 ms intervals during each experiment via a piezoresistive strain gauge and 16-bit analogue output (Figure 6.4.).

6.2.1. Tank setup

The 3-layer stratigraphy established in **Chapter 5** has been largely retained as it provides an excellent reproduction of natural overpressure building up beneath an impermeable layer and then rupturing at loci to produce fluidisation pipes. In order to reduce grain-size variation, lower and upper layers (6 cm each) consisted of near-spherical 2.6 g/cm³ 150-300 µm coarse glass beads separated by a 1 cm layer consisting of 0-44 µm fine glass beads. Plastic granules were not used in these experiments, instead to improve visualization of granular movement 150-300 µm coarse glass beads were dyed using blue engineering layout ink (Figure 6.5). This ink is not water-soluble and thus did not interfere with the results. These dyed grains were mixed with the un-dyed glass beads forming approximately 10% of the

upper coarse-grained layer volume and periodically added to the upper coarse-grained layer during building of the sediment column to create highly visible layers to enable visualisation and particle tracking. The tank was fitted with a baffle 30 cm high containing gravel to homogenise the flow across the cross-section and topped with a 100 μm stainless steel mesh to prevent the test sediment from entering the baffle and possibly blocking the pipes during tank emptying. The tank was filled with water before the addition of sediment to ensure that no air bubbles were present in the water column or the manifold. As air is compressible, any changes in pressure may not be recorded accurately if it is present.

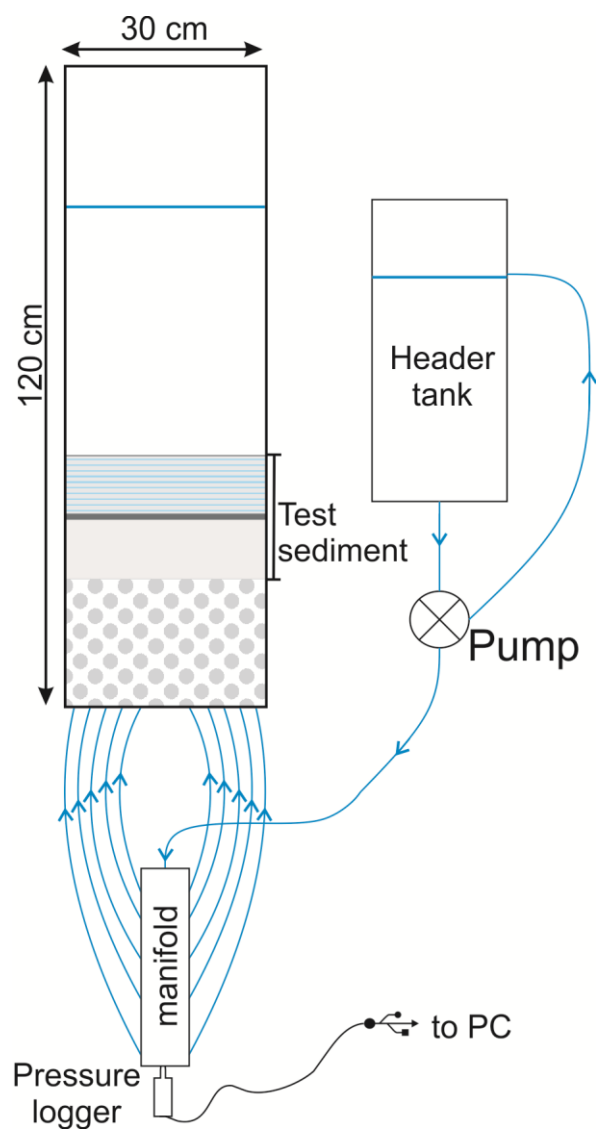


Figure 6.4. Schematic showing the experimental set up. Dotted area is the gravel and mesh baffle. All input pipes are shown in blue. Those from the manifold to the test tank are all the same length (1 m).

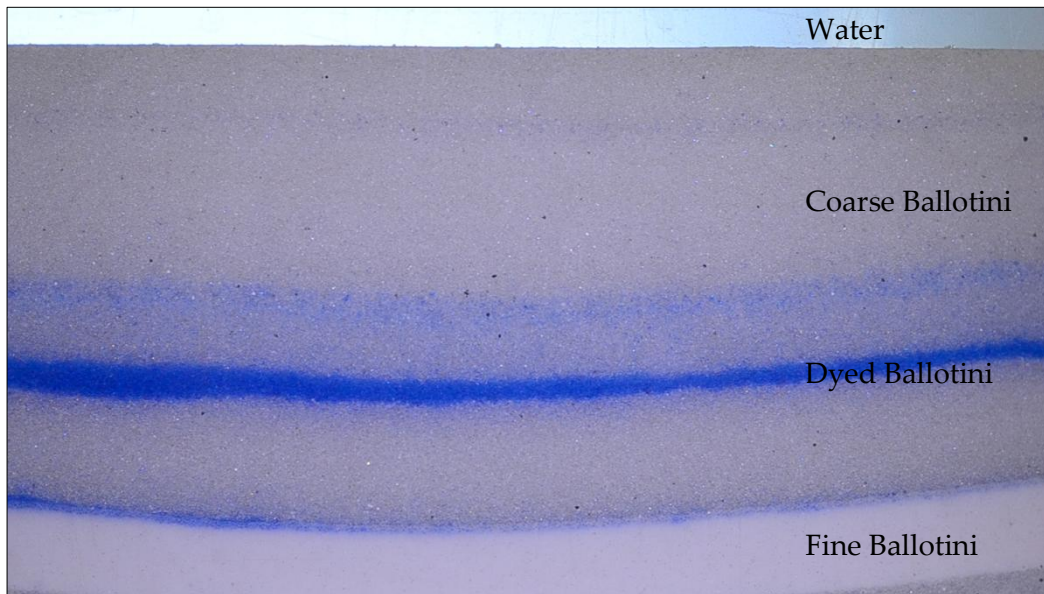


Figure 6.5. Photograph of the upper sediment layers to demonstrate stratigraphy. Apparent curve of fine layer is due to barrel distortion arising from tank curvature. The fine Ballotini layer is 1 cm thick.

6.3 Data collection

Primary data collection was via video recording of fluidisation pipes at macro-scale using a Nikon 3100 DSLR. Although this provided excellent visualization of individual grains (Figure 6.6a), it was impossible to achieve the frame-rate required for clear visualization of fluidised grains (Figure 6.6a) due to the limited shutter-speed and rolling-shutter. This technique does however provide good visualization of the movement of fine-grained particles through the pore-spaces of the coarse-grained layer. Recording of frames was initiated once a migrating fluidisation pipe was about to enter the field of view and continued until the camera recording limit (10 minutes) or the pipe migrated out of the frame. In order to accurately track the

trajectory of fluidised particles in the pipe it was necessary to upgrade the capture equipment to a Vision Research® Phantom v9.1 high-speed camera capable of 1000 frames per second (fps) at 2 megapixels with a 2 microsecond shutter-speed. This prevents the “streaking-out” of particles between frames and thus enables particle tracking. Due to limited data storage on the Phantom camera, frame-rate was manually set at 100 fps in order to allow continuous recording for 12000 frames (2 minutes) The Phantom camera is enabled with continuous video stream output to PC meaning that recording could be initiated as a migrating fluidisation pipe entered the frame.

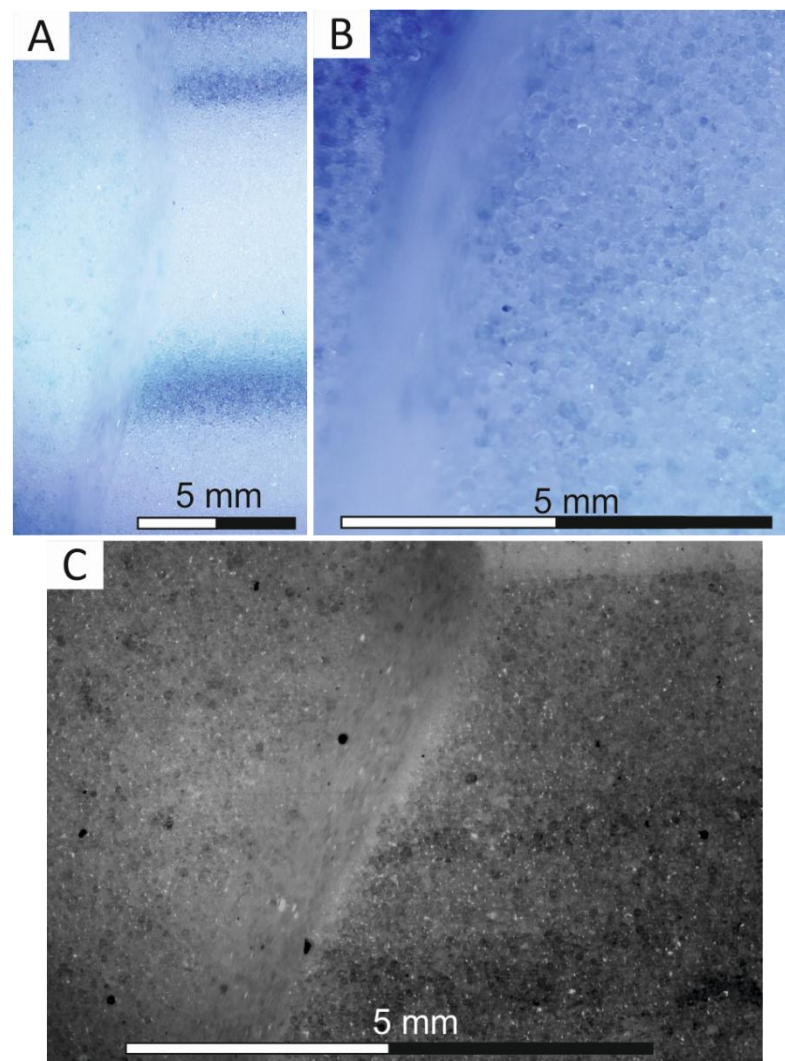


Figure 6.6. (A,B) Frames extracted from video files to demonstrate the very fine-detail achievable using a commercially available digital video camera (Nikon 3100) when the particles are stationary (right of image) compared to streaking and lack of

detail when particles are in motion (left of image). (C) Sample frame from the Phantom camera. Flow in the pipe is from the base left to the top right; and black “seeding” particles are visible in the centre of the pipe.

Following a successful experimental run in which a migrating fluidisation pipe entered the field of view, data was uploaded in Dantec Dynamics® software DynamicStudio for particle tracking velocimetry.

6.3.1. Particle tracking velocimetry

Particle tracking velocimetry (PTV) is a technique for measuring two components of velocity in a flow. PTV is an extension of the more commonly used particle imaging velocimetry. PTV involves tracking the displacement of discrete particles between a pair of images (image A and image B). The locations of the particles are identified via areas of maximum intensity, a Gaussian function is fitted to map all the discrete particles on each image, this allows for the identification of the centre of each particle via a model of each image. Pattern matching identifies particles pairs that are present on the derived model from both images A and B (Fig, 6.7). The spatial offset between the particles between image A and B gives the velocity of each particle pair (pixels per second), once each image has been corrected for scale the velocity is converted to metric units. The results presented herein were calculated using Dantec DynamicStudio, this is a proprietary software package widely used for both PIV and PTV analysis. The particle tracking technique within DynamicStudio is an adaption of the Kanade-Lucas-Tomasi (KLT) feature tracking code (see appendix). The algorithm identifies suitable features to track by examining the minimum eigenvalues (the change in magnitude of a vector that does not change direction during applied shear) of each interrogation area and the features therein are then tracked using a Newton-Raphson method of minimising the difference between them (Tomasi and Kanade, 1991; Shi and Tomasi, 1994; Birchfield, 1997).

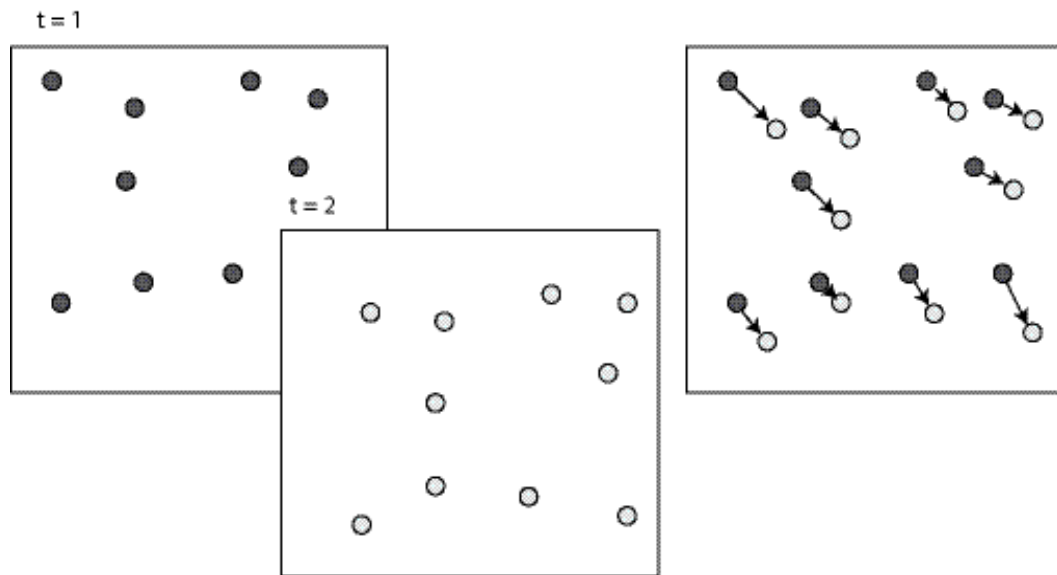


Figure 6.7. Schematic to show particle tracking between frame-pairs.

6.3.1.1. Experimental application of PTV

As it is impossible to illuminate an arbitrary plane within the fluid flow with a laser pulse, it was not possible to use PIV to analyse the flow within the tank. The particle motion is only visible through the clear bounding wall of the tank, which was illuminated using high-strength LED lights (Figure 6.8). The high-speed camera records 100fps at 1632 x 1200 pixels at 14-bit image depth (16,000 shades of grey). The relatively small number of painted seeding particles present within the area of interest complimented PTV, as this technique is optimised for systems with low density seeding. This limits the potential problem of ambiguity when identifying pixel pairs that occurs when the seeding density is too high.



Figure 6.8. Photographs to demonstrate how the high speed camera and LED lights are mounted relative to the tank. **A** – Led lights, **B** – Tank wall.

Following a successful experimental run in which a fluidisation pipe passed through the field of view, the following steps were undertaken to process the images ready for particle tracking: (i) isolation of the area of interest in the image sequence using image masking in order to minimise noise; (ii) application of a Sobel operator to increase individual particle visibility (see details below); (iii) calculation of the arithmetic mean of all 100 images in the stack by computing the average values of the pixels' intensity in pre-defined interrogation areas; (iv) subtraction of the calculated image mean from each subsequent image in the stack to remove any stationary features in the image; (v) subtraction of a duplicate of the first image from the stack (this further reduces/removes stationary features); (vi) subtraction of a duplicate of the last image from the stack (this further reduces/removes stationary

features); and, (vii) conversion to double images as required for the particle tracking steps outlined in section 6.3.1. Note that the Sobel operator is an edge detection filter that performs a 2-D spatial gradient measurement on an image and thus highlights the particle edges, having the overall effect of increasing the contrast of the seeding particles.

The particle tracking algorithm within DynamicStudio is set up to use interrogation areas of 64 x 64 pixels with 25% image field overlap and 79% noise reduction. This minimises the production of incorrect vectors. These settings have been determined by iteration through the settings available in DynamicStudio to produce the most valid vectors. All vectors are verified by superimposing the calculated vectors over the raw images in MatLab and visually confirming that the vectors are representing the true particle trajectories.

6.4. Experimental results

Due to the manual operation of the valve that directed flow toward the experimental tank, that also re-circulated flow back into the header tank (Figure 6.2), the flow rate between each experiment was variable. As the pressure transducer logged the exact duration of each experiment, and the cross-sectional area of the tank is known, a volumetric flow rate of between 11 and 19 cm³ s⁻¹ for each experiment can be calculated (Table 6.1).

Run	Water in (cm ³)	Time (s)	Flow rate (cm ³ s ⁻¹)	PTV images
1	6517	326	19	✓
2	6834	425	16	✓
3	3871	300	12.9	✓
4	6256	551	11.4	✗
5	8326	680	12.2	✗

Table 6.1. Calculated volumetric flow rates for each experimental run.

Pressure data was logged during each experimental run and shown in real-time on a linked PC. This provided an immediate association between visual observations of the fine-grained layer rupturing and the related change in pressure signature

6.4.1. Pressure data

Data from 5 experimental runs are presented in Figure 6.9 for the entirety of each run and the rupture period (*Chapter 5.3.3*) during which the overpressure which has built-up beneath the fine-grained layer is released. Each run demonstrates a steady increase in pressure following the onset of flow, which is visualised as a sharp increase in pressure as the pump is switched-on and valve opened. As this operation was completed manually, there are variations in the beginning of the pressure-logs apart from Figure 6.9A where the beginning of the experiment is not shown due to its length. Pressure continues to increase steadily as a function of the

increasing hydraulic head in the experimental tank. The area highlighted by a grey bar represents a 20 s period around the rupture of the fine-grained layer. Twenty second intervals have been highlighted to demonstrate the varying pressure responses to rupture. A 20-point moving average has been applied to remove noise from the signal. There is no correlation between rupture style (wide or narrow pipes 5.4.2) although a secondary rupture zone is recorded in Figure 6.9 B' (arrow 2) as the initial rupture zone fails and therefore pipe breakthrough occurs at a new locus following a rapid increase in pressure of 0.0004 bar (see Section 5.3.3.). Figure 6.9A' shows excessive noise likely due to air bubbles in the manifold but only a small decrease in pressure is recorded over the rupture period (01:02 – 01:07 mm:ss). In almost all cases (B' – D') there is an initially rapid decrease in pressure as rupture occurs followed by a brief period where pressure increases, then drops and then begins to climb again according to the hydraulic head increase. This is illustrated well in Figure 6.9 C' as pressure drops at 00:35.8, increases at 00:36.9 and reaches a minimum between 00:39.6 and 00:43.8 before trending upwards.

6.4.2. Particle movement prior to pipe arrival

Lateral pipe migration is a dominant feature during the experiments and a phenomenon described in Chapter 5. In all experiments, the character of the sediment column was altered prior to the arrival of a fluidisation pipe in the vicinity. The main method was by infiltration of the fine-grains through the pore spaces of coarse Ballotini. Background seepage and transport of fine-grained material occurred in almost all cases via vertical permeability conduits through the coarse sediment. High-resolution images of the infiltration horizon described in Section 5.3.2 are shown in Figure 6.10.

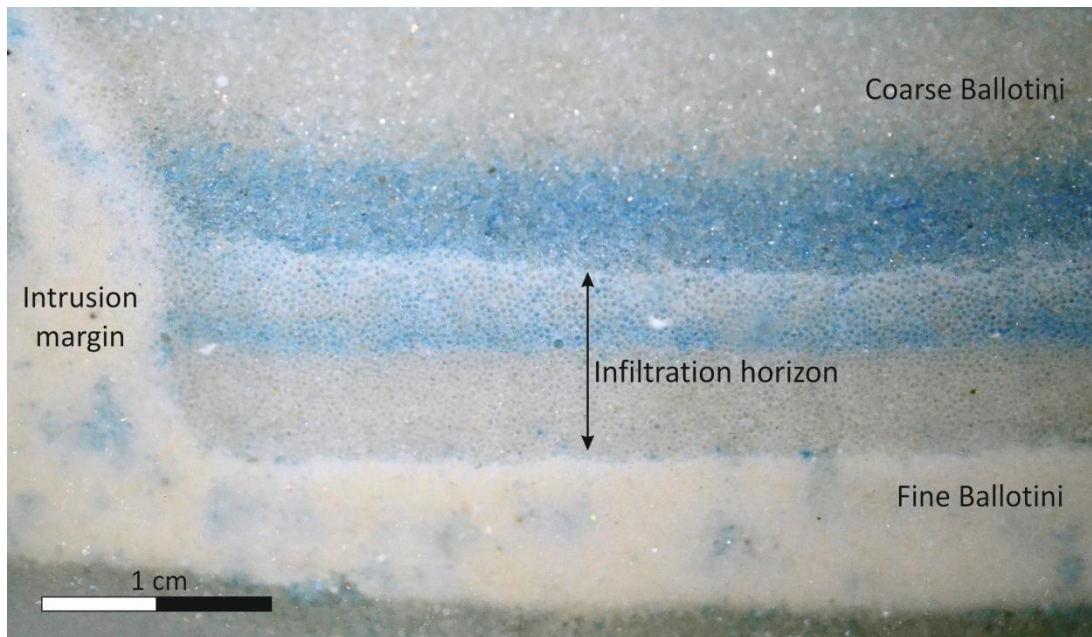


Figure 6.10. Close-up of the infiltration horizon that commonly develops above the fine-grained layer.

Migration of the fine-grained material was not limited to the creation of an infiltration horizon however, and as pipes migrated towards the study section (field of view), these conduits change direction, becoming inclined and sometimes horizontal. Figure 6.11 shows the paths of two grains through the pore-spaces at a velocity around 2 mm sec^{-1} . As the coarse grains are not yet being fluidised, the fine grains are creating a fabric between the coarse grains according to the migration direction.

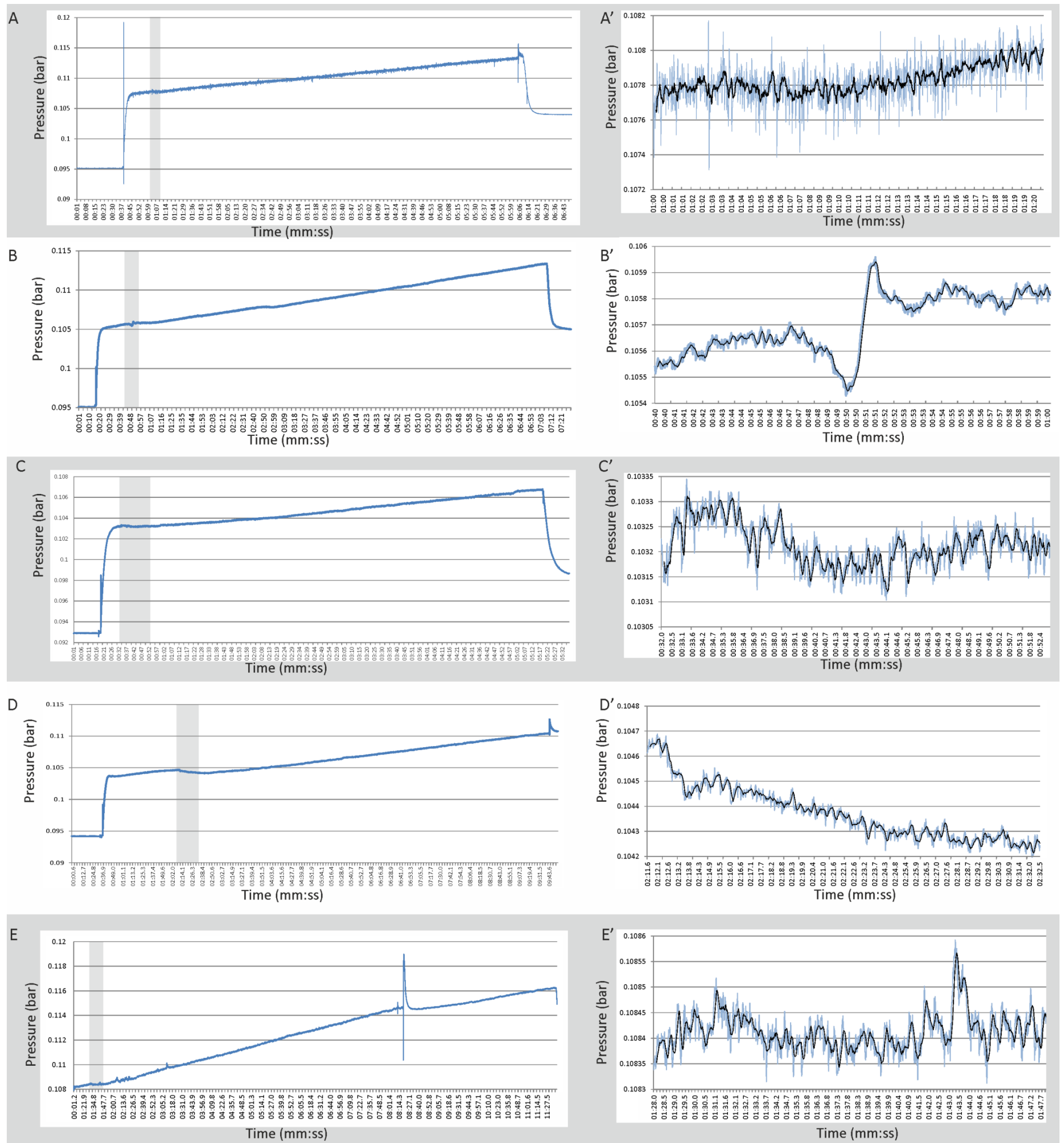


Figure 6.9. Pressure trends from runs 1-5. Left hand images are the pressure trends for the complete duration of each experimental run with the exception of the end of run 4 (D) and the beginning of run 5 (E). The vertical grey bars highlight the time period shown in the right-hand graph ('). Red arrows 1 and 2 denote consecutive rupture events. A 20-point moving average has been applied to the 20 s intervals (black line) to remove noise and improve visualisation of the pressure trends.

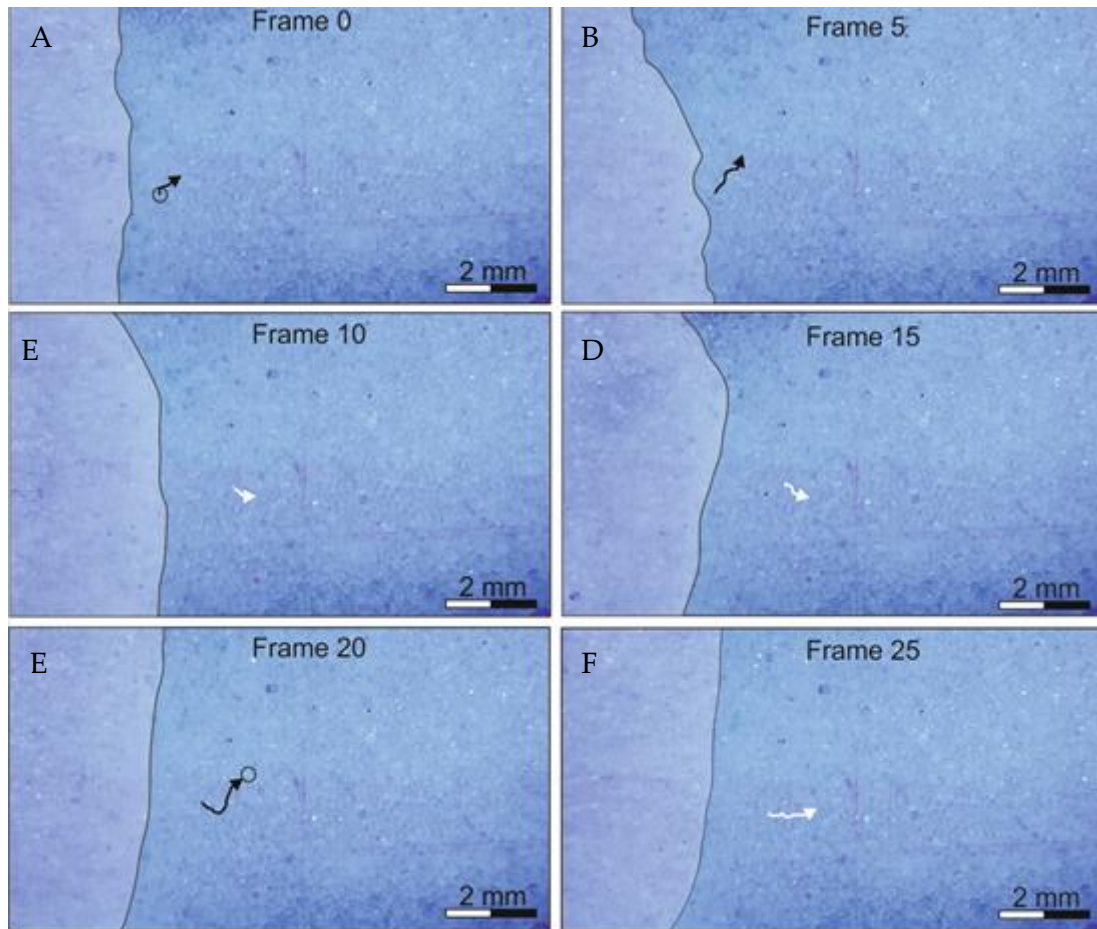


Figure 6.11. Inclined infiltration of fine-grained sediment prior to the arrival of a migrating fluidisation pipe (light coloured zone to left of images). Secondary grain (white arrow) shows sub-horizontal path. Initial and final grain locations denoted by black circles. Total time elapsed is 1 second.

6.4.3. Particle and fluid movement during fluidisation

Lateral infiltration horizons up to 1 cm thick develop at the margins of fluidisation pipes. These margins always develop on the leading edge of a pipe if it is stationary for more than 1-2 seconds. The development of this horizon is a precursor to pipe stabilization and often to the subsequent production of an infiltration horizon on the opposing margin. This margin is then destroyed if the pipe later migrates. By manually tracking the approximate trajectories of particles, the production and destruction of this margins can be observed. Relict infiltration horizons are often left

in the wake of a migrating pipe and are seen as sub-vertical light streaks (Figure 6.11). The morphology of the pipes show considerable temporal and spatial variation (Figure 6.12) displaying the following range of morphologies within a 20 second interval; (i) straight pipe with linear margins (Fig. 6.12 1); (ii) pipe with an apparently bulbous top (Fig 6.12 8); (iii) pipe with “scour-like” trailing-margin (Fig. 6.12 11); (iv) sinuous pipe with single bend (Fig. 6.12 15) (i; (v) sinuous pipe with double bend (Fig. 6.12 22; 30); (vi) pipe with wide base (Fig. 6.12 35) and (vii) sinuous pipe with “scour-like” margins (Fig. 6.12 35; 46). The rapid change in morphology is caused by eddies migrating upstream (vertically) and by re-sedimentation of fluidised sediment both on the leading and trailing edges of the pipe (6.4.3.2).

6.4.3.1. Concentration variation in pipes

The concentration (ϕ) is seen to vary considerably both temporally and spatially in fluidisation pipes. In Fig. 6.13, the dark areas in the video frames are areas of low particle concentration as the pipe is composed of mostly water, allowing light to be absorbed rather than reflected back towards the camera, whereas higher concentrations are visible as white areas in the pipes. Low concentration areas are strongly associated with the upward-migrating eddies and maximum particle concentration occurs just above the eddies.

6.4.3.2. Slumping and re-sedimentation around pipes

Slumping of the fluidised sediment occurred in every experiment on the trailing edge of a pipe and manually tracked particles showing these downward trajectories are shown on Fig. 6.13. This phenomenon was touched upon in section 5.4.4 as part of the venting process. The slumping of fluidised sediment can be seen to occur to the base (lower edge) of pipes and sediment can be recirculated multiple times if a pipe is migrating. There is significant internal reorganisation of the coarse-grains via avalanching and rolling of grains. As these coarse grains slump downwards,

fine grains are completely elutriated through the dynamic grain framework. Grains are seen to recirculate up to a dozen times before being ejected from the vent at the surface. Large particles (aggregates of painted sediment for example) are observed recirculating in the pipe. This effect will be even more dominant where pipes approach the surface, since the exit velocities of the spreading flows is insufficient to transport these particles, and as a consequence they repeatedly fall into the main conduit. Over time, at surface points or other zones of where widening occurs, large particles may accumulate, and ultimately these may act to block the pipe. Thus, these clasts fall into the conduit multiple times, remaining suspended below the vent without being transferred above the sediment-water interface.

Avalanching of coarse grains also develops on the leading edge of a pipe if it remains stationary for any period. This process is seen as high-angle downward motion of the particles that often erodes an infiltration horizon on the pipe's leading-margin resulting in the pipe back-stepping due to the influx of sediment, and then the pipe becoming sinuous (Fig. 6.12 38 and 39). The slumped grains are then plucked away from the pipe margin and re-fluidised. This traction-dominated zone is up to 10 grain-diameters thick and leads to the creation of high-angle lineations parallel to the infiltration horizon.

6.4.3.3. Grain entrainment mechanism

The leading edge of a pipe is responsible for the majority of sediment erosion and incorporation into the fluidised flow and develops in a broadly repeatable pattern where grains are rolled up the pipe margin against the infiltration horizon and due to the temporal changes in flow velocity and therefore pressure within the pipe, grains are plucked away from the pipe margin and fluidised. If obstacles are present in the pipe (an amalgamation sediment that occurred during the painting process for example), flow is diverted around the obstacle and scouring of the pipe margin occurs by abrasion. The three-dimensional scale of these scours is not known

although they are oriented parallel to flow. These processes mimics the vertically migrating eddies that also suspend grains by plucking and abrasion. However, abrasion is not a dominant process in grain suspension at the pipe margins.

6.4.5. Flow velocities in fluidisation pipes

Manually measured flow velocities of particles at various points across the pipe diameter are presented below (Table 6.2). These measurements capture individual particles that the code is, as yet, unable to track. All particles were tracked over a 100ms period to ensure that the same particle remained in field of view.

Area of flow	Flow velocity (cm s ⁻¹)
Leading wall	4.6
Leading wall	3.0
Flow centre	11.23
Flow centre	10.86
Flow centre	5.23
Trailing wall	8.05
Trailing wall to centre	9.77

Table 6.2. Particle flow velocities at a range of points across the pipe diameter.

Particle velocities are notably lower along the leading edge of the pipe and greatest along the centre of the pipe. Particles suspended from the trailing edge often migrate into the centre of a pipe after a short period of suspension.

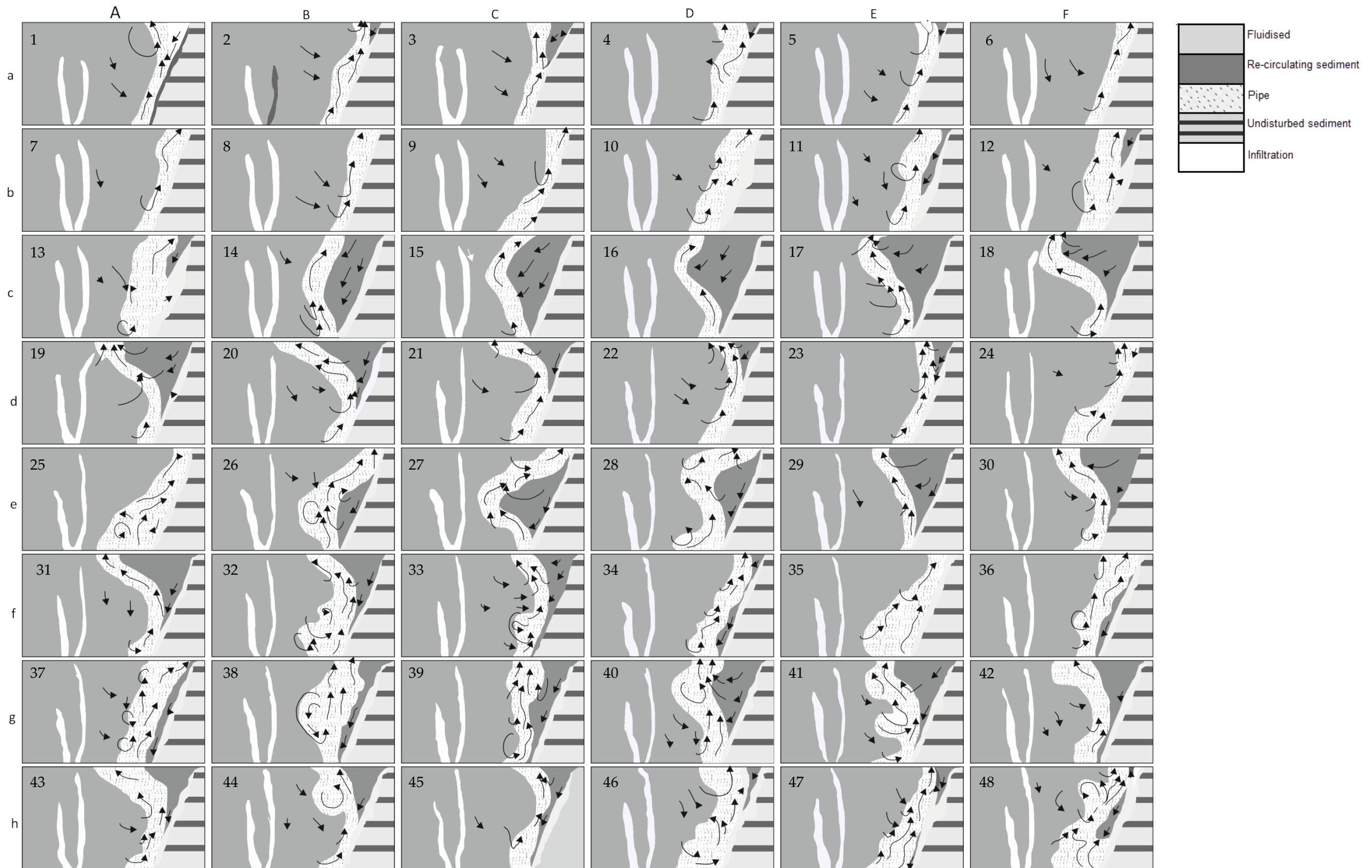


Figure 6.12. From experiment 5. Time-series of interpreted video frames over a 20 s period (every 10th frame) demonstrating particle trajectories and the variety of morphologies at any given time. Frames run from top left to bottom right. Frames are 16 mm wide.

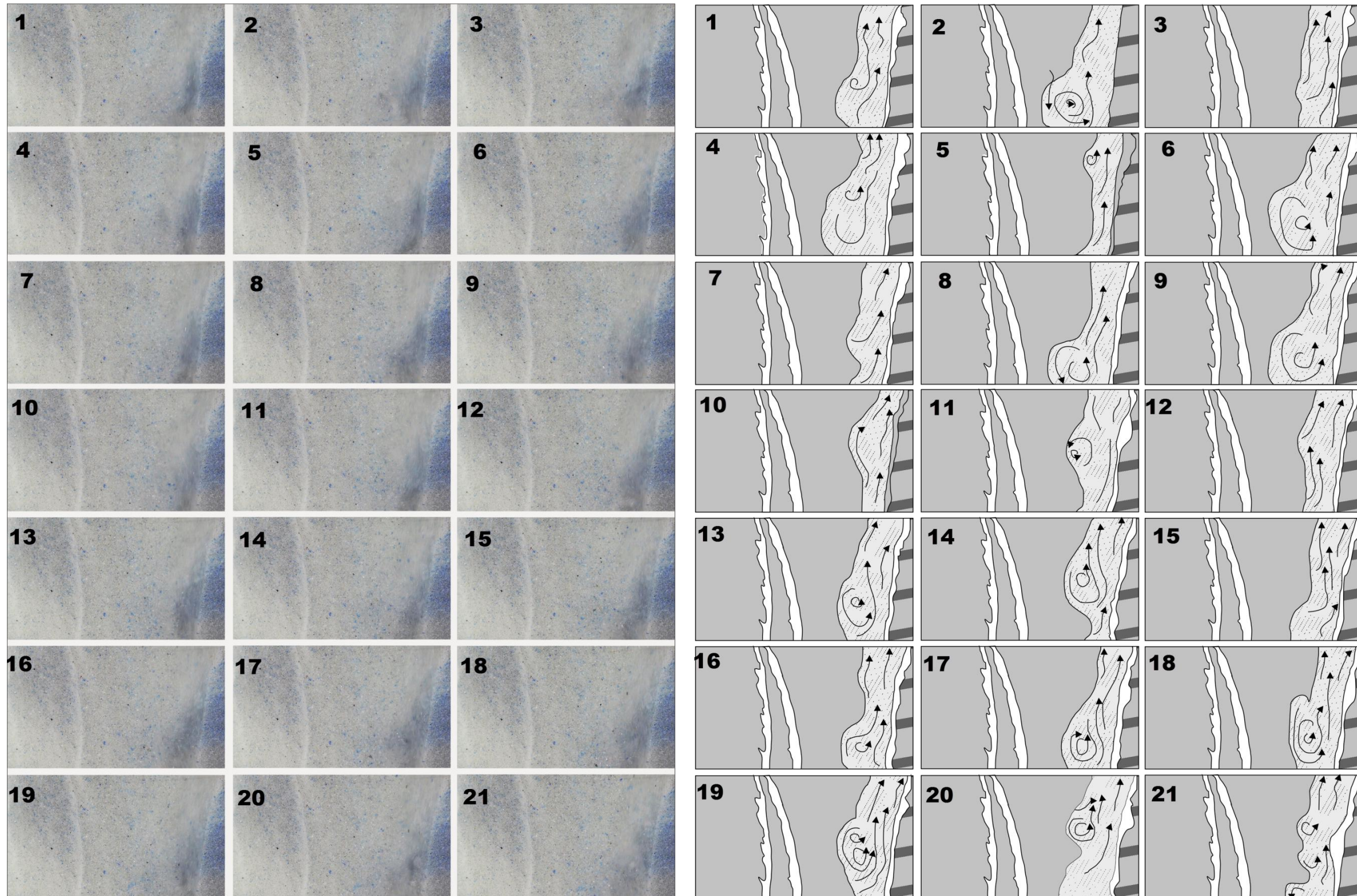


Figure 6.13. (Left) From Experiment 4, showing every-other frame extracted over 2 seconds of video (left) to demonstrate the spatial and temporal variation in pipe morphology. (Right) Interpretation of the video frames showing particle trajectories (arrows) and flow zones. The pipe is migrating from left to right. Frames are 16 mm wide. Key is the same as Figure 6.12.

6.4.6. PTV of fluidisation pipes

The velocity vectors obtained through PTV compare well with the direction of flow within the fluidisation pipes as observed visually. Local velocities show the particles moving in both the x and y axis as demonstrated in Figure 6.14. There is a wide spread of horizontal and vertical flow components with dominant flow being from bottom right to top left. Such a spread in velocity magnitudes and trajectories is attributed to the velocity data being obtained from the full field of view, therefore particle motion from the slumping sediment behind a pipe is recorded, as well as particles entrained within the fluidisation pipe. The maximum velocity recorded by the PTV processing is 5 cm s^{-1} although this is an underestimate as the fastest particles are unable to be tracked by the code. The original frames and an animation of the velocity vectors is provided on the accompanying DVD at a reduced frame rate of 10fps (6PTV.avi).

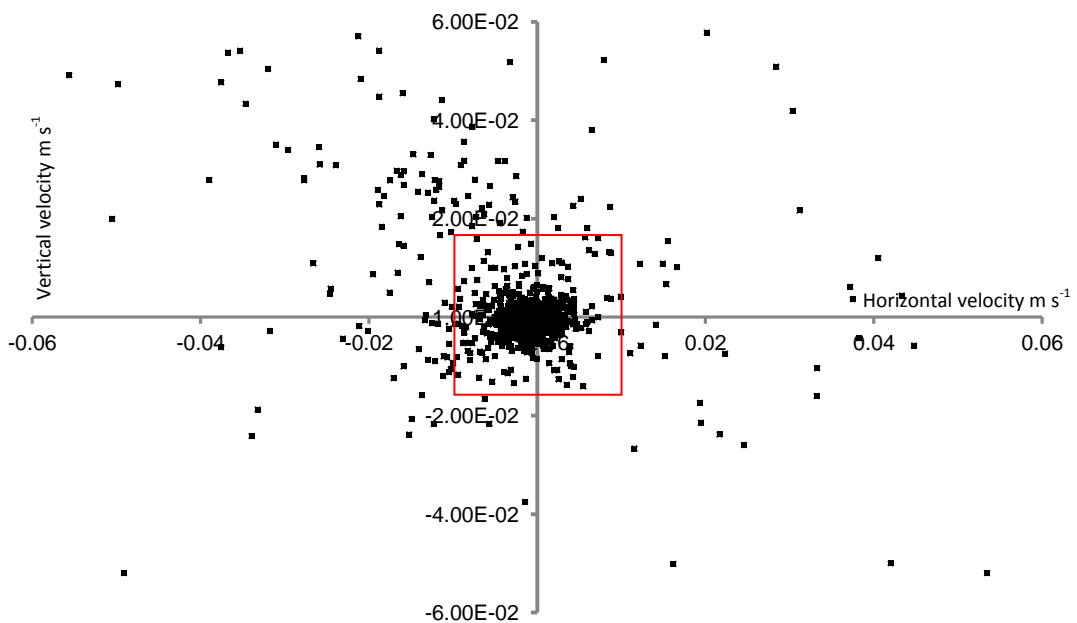


Figure 6.14. The horizontal and vertical components of the flow across the whole field of view, as derived by the PTV code. Red box denotes area shown in Figure 6.15.

In order to improve visualisation, velocity vectors below $1 \times 10^{-2} \text{ ms}^{-1}$ are plotted in Figure 6.15.

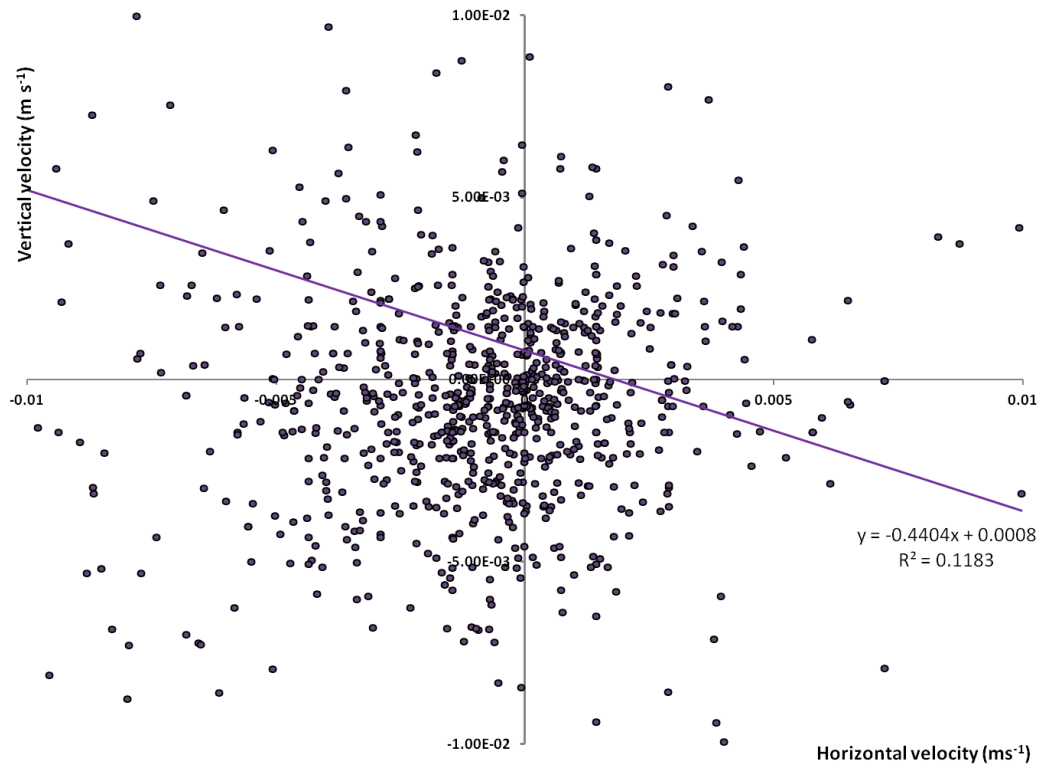


Figure 6.15. Horizontal and vertical velocity vectors below $1 \times 10^{-2} \text{ ms}^{-1}$.

The strong vertical component of flow that is clear from video and manual analysis of the data is missing from Figure 6.15, suggesting that the code is not identifying the full suite of velocity data available in the images.

A variety of flow components are highlighted by the PTV technique. Firstly, the infiltration of fine grains away from the pipe (highlighted by the green circle on Figure 6.16) appears similar to the trajectories tracked manually in Figure 6.9. In this case, the particles are infiltrating into the slumped zone behind the migrating pipe whereas in Figure 6.9 the infiltration is occurring in the same direction as pipe migration. It can also be seen that velocities are lowest at the leading (bottom) edge of the pipe (Fig. 6.16, blue highlight), where particles are being rolled up the pipe

edge, as opposed to those entrained in the pipe flow (Fig. 6.16, red highlight). Example vectors generated by the PTV software are shown in Figure 6.17.

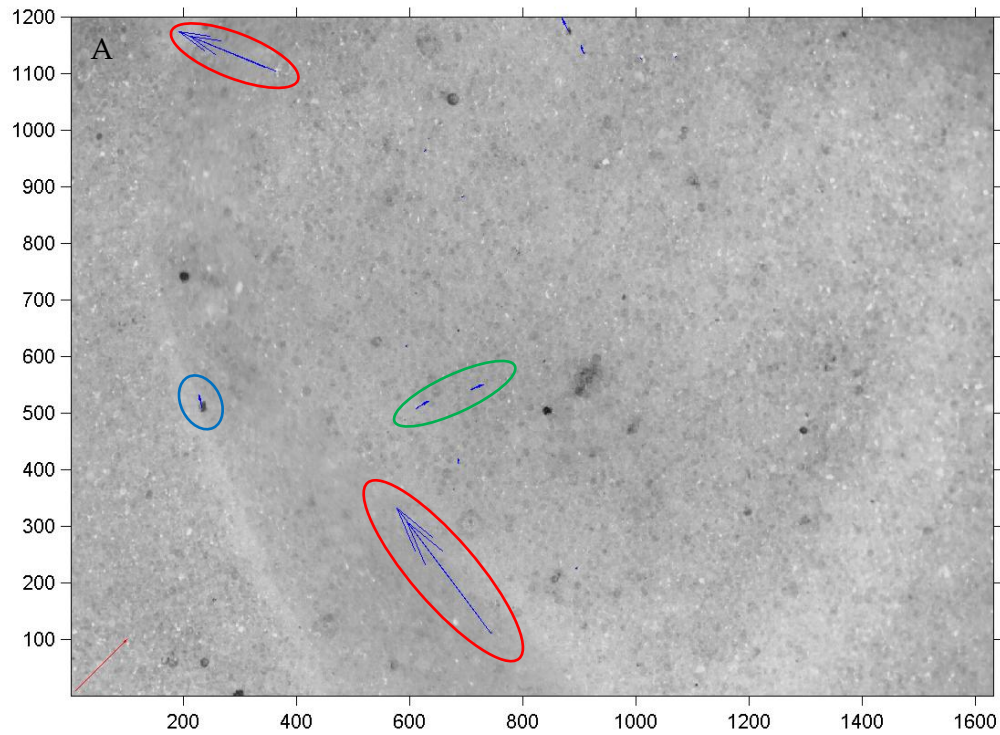
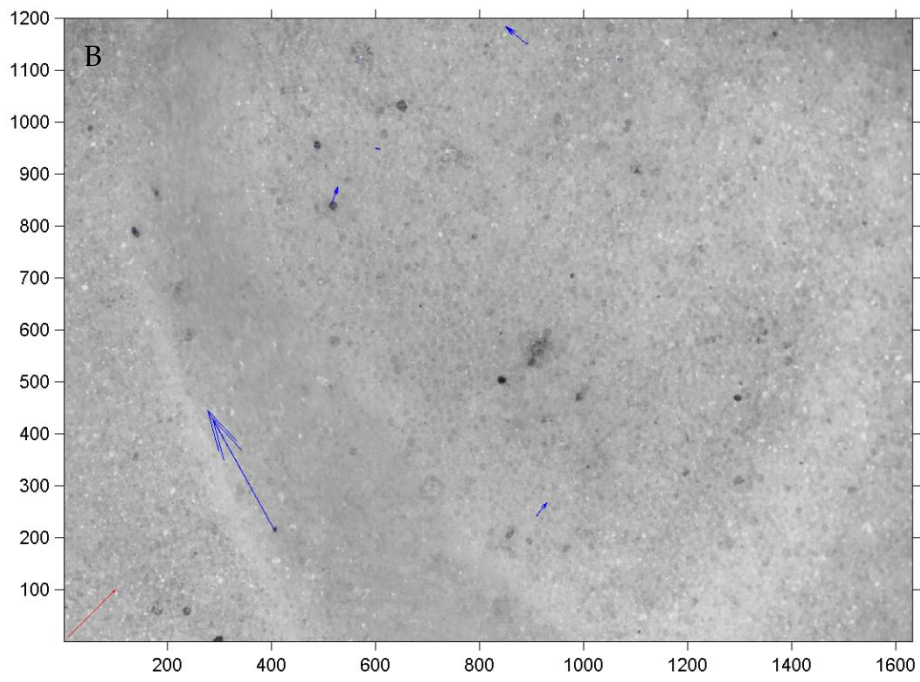
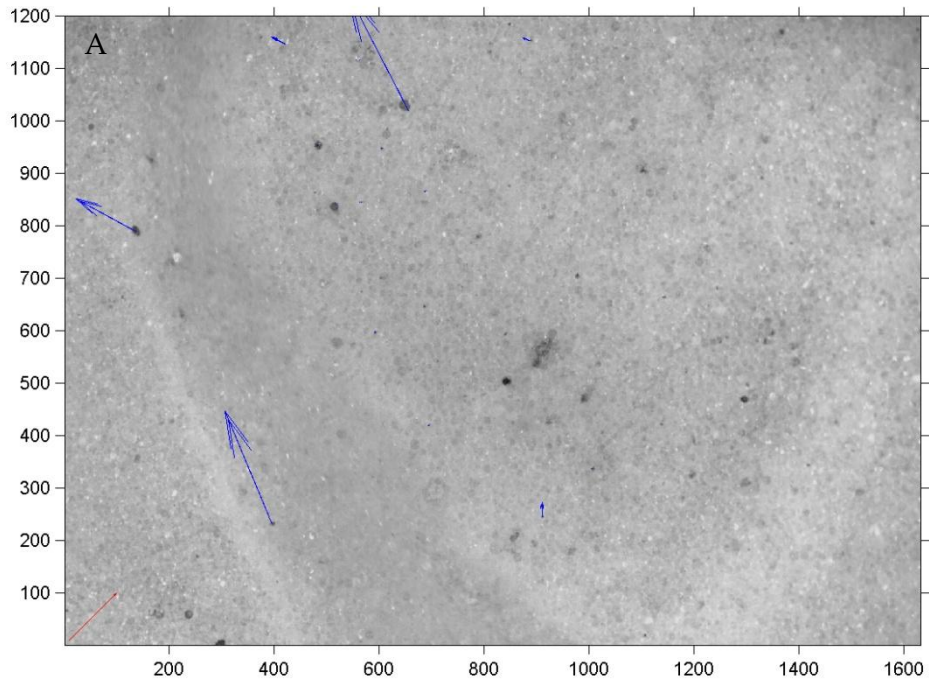


Figure 6.16. Full-field view with flow velocity vectors from experiment 3. Red vector at bottom left provide 100 pixel scale. Pipe migration is from right to left of the image. Red circles highlight maximum flow velocities, blue circle highlights particle trajectory on the pipe leading edge and the green circle highlights small particles infiltrating away from the pipe. Horizontal and vertical scales are in pixels, scale factor is 1.256.



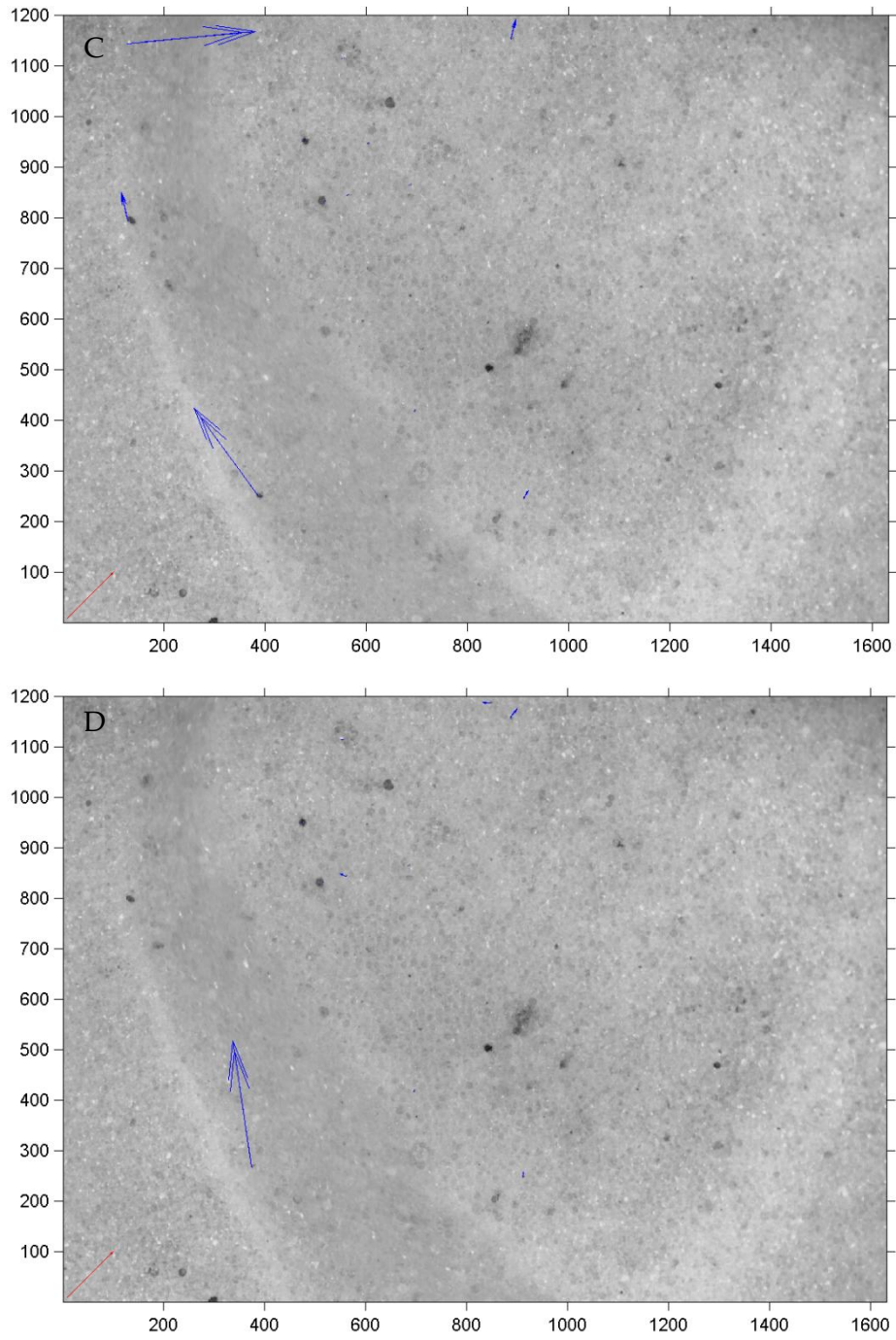


Figure. 6.17. Series of consecutive images demonstrating the trajectory of a particle suspended in the main flow over 40 milliseconds. Image is 23.57 x 17.33 mm.

6.5. Discussion

The experiments documented here have shown that particle movement in fluidisation pipes is more complex than previously thought. Although some studies have suggested that flow conditions in a pipe may be highly variable along its length and at any point in time (Scott *et al.*, 2009) no previous study has tested this hypothesis.

6.5.1. Pressure

The pressure data presented in section 6.4.1. suggests that there is no inherent link between the style of rupture and the associated pressure-drop in the system. The pressure drop marks the moment of rupture and the onset of fluidisation and piping. The secondary rupture recorded in the pressure data (Fig. 6.9) shows that fluidisation does not always occur as a single pipe. Multiple rupture zones are common and one pipe typically becomes dominant, resulting in shut-down of other fluidisation pipes. This shut-down will cause a brief pressure increase (Figure 6.9B') as water is re-directed towards the dominant pipe. The initial increase in pressure occurs as water flows through the lower coarse bed by Darcy flow and pools beneath the fine-grained horizon. Flow discharge is not constant in any given experiment but varies, as a function of pressure and even with the calculation of pressure gradients, the estimation of the minimum fluidisation velocity of the grains would not be appropriate due to the variation in sediment grain-size (section 5.3.1).

6.5.2. Particle concentration

It is not possible to calculate the particle concentration in the fluidisation pipes due to the narrow depth of field in the images, although Figure 6.12 demonstrates that concentration does vary considerably within a pipe; the dark areas represented low particle concentrations as considerably less light is reflected back towards the lens.

The maximum theoretical grain concentration for fluidisation is 54% (Leva, 1959), however, consideration of the frames presented in Figure 6.17 shows high grain concentration, probably close to this theoretical maximum, at the leading edge of the pipe indicating the influence of other factors on grain behaviour in the pipes. The areas of minimum concentration are coincident with the eddies that migrate vertically along the pipe margins. This is a common feature of particle-laden turbulent flows, with those particles denser than the fluid being heterogeneously distributed in the fluid and migrating away from eddies. This preferential concentration occurs due to the centrifugation of the inertial particles away from the turbulent vortices, themselves exhibiting low particle concentrations (Monchaux *et al.*, 2012). There is considerable evidence from numerical modelling for a high correlation between regions of high strain in a flow and regions of low vorticity and high concentration of heavy particles (e.g. Squires and Eaton, 1990; 1991; Tanaka *et al.*, 2002). This effect is enhanced by the boundary layer between the fluid and the wall of the pipe creating a region of high strain owing to the steep velocity gradient, further increased by the frictional resistance of the grains at the wall. Enhanced entrainment of particles into the fluidisation pipes at the base of eddies, as demonstrated in Figure 6.13 may well be linked to the development of turbulence in the pipes. Particle interactions with turbulent structures greatly enhance the settling velocity of these particles and falling particles are systematically swept toward the downward side of turbulent eddies (Wang and Maxey, 1993), thus increasing the rate at which overlying particles will slump towards the base of the pipe.

6.5.3. Calculation of flow regime in experimental pipes

In order to calculate the Reynolds number of the flow, a range of kinematic viscosities must be utilised due to the spatial variation in concentration (ϕ 0.1 to 0.54). These values are calculated according to Equations 6.7 and 6.8 and presented in Table 6.3.

ϕ	ρ_{pf} (kg m ³)	μ_{pf} (Pa s)
0.1	1150	0.0013
0.32	1480	0.0029
0.54	1810	0.0088

Table 6.3. Calculated pseudo-fluid density (ρ_{pf}) and viscosities (μ_{pf}) from experimental observations.

It is now possible to calculate a range of flow Reynolds numbers for the range of velocities calculated in Table 6.2

. All values are based on a measured pipe aperture of 2.38 mm.

Point in flow	Velocity (cms ⁻¹)	Re at ϕ 0.1	Re at ϕ 0.32	Re at ϕ 0.54
Leading edge	3	63	36	14
Centre	11.23	236	136	54
Trailing edge	8.05	168	97	39
Mean	7	147	85	34

Table 6.4. Calculated maximum and minimum flow Reynolds numbers for measured velocities in an active fluidisation pipe (experiment 3) based on psuedofluid values.

The values calculated above appear uncharacteristically low when turbulent eddies can clearly be seen migrating vertically, and extensive recirculation of sediment is occurring in the pipes. This suggests that either the effect of pipe roughness needs to be accounted for or the calculated values of fluid viscosity, density or velocity are affecting the calculated Reynolds value. However, re-calculation of the Re values with the density and dynamic viscosity of pure water as utilised in the experiments (1000 kg m³ and 0.001 Pa s respectively) suggests that these parameters have no impact on the calculated Re values (Table 6.5).

Point in flow	Velocity (cms ⁻¹)	Re
Leading edge	3	71
Centre	11.23	261
Trailing edge	8	190

Table 6.5. Calculated flow Reynolds numbers with density and dynamic viscosity values for pure water.

Flow regime and particle motion in experimental pipes

The flow visible in the experimental pipes may be considered as a plane Poiseuille flow where flow is driven by a pressure gradient and confined by stationary walls (Fitzgerald, 2004). In this case, flow adjacent to the walls has the same velocity as the wall, resulting in a laminar parabolic velocity distribution across the channel. However, when considering the 3D cylindrical geometry of the pipe, the flow is more accurately termed Hagen-Poiseuille flow (Fitzgerald, 2004). The unstable flow in the pipe may be transitional if the full diameter of the pipe is not in view, or that particles that can be seen are strongly affected by friction at the wall of the tank and are not representing maximum fluid velocities. A 22 mm wide pipe is required to ensure the onset of turbulent flow at a velocity of 11 cms⁻¹. It is unlikely that turbulent Reynolds numbers are reached in the fluidisation pipes from these experiments and that the recorded Reynolds numbers are not an artefact of a 2-D measurement field. The manual tracking of individual particles remains representative of true particle velocities. An average of many particle velocities at a range of points across the pipe diameter would be the preferred method to ascertain particle velocity. However, the visualisation technique does not provide images of sufficient sharpness to track multiple particles, nor do particles follow straight or predictable trajectories in 2 dimensions. Finally, due to the variation in flow direction relative to the pipe wall, particles appear and disappear at the pipe wall, thus tracking an individual particle can become unreliable at distances larger than 10 mm.

The effect of roughness on the Reynolds number will be higher than is considered in the current literature due to the scale of the experimental process, with grain diameters of up to 0.3 mm creating a mean roughness on the pipe wall equivalent to 10% of the total pipe diameter with a high wavelength. This is a parameter bound to generate instability as fluid moves to fill troughs in what would normally be the boundary layer in pipe flow (Allen *et al.*, 2007). Flow past a spherical particle has been shown to result in vortex shedding at low Reynolds number ($Re \sim 30$) with Re values of 300 resulting in organised periodic flow dominated by vortex shedding (Johnson and Patel, 1999). Toroidal vortices in the wake of spheres occur at Reynolds numbers as low as $Re = 25$ however axial symmetry in the wake of the sphere breaks down at $Re \sim 210$ (Johnson and Patel, 1999). Therefore, as each particle in the flow generates its own boundary and Kármán vortex street, the flow will be unsteady even at low Reynolds numbers. These instabilities are, in turn, superimposed on the primary perturbations introduced to the flow by variations in pressure and flow velocity through a pipe thus making a low Reynolds number flow appear unsteady. Localised “puffs” of disturbance are common in transitional flow and “slugs” of turbulence are typical at $Re > 4000$ (Hof *et al.*, 2003). Perturbations or, puffs, can persist for many tens of pipe diameters at $2000 \leq Re \leq 5500$ but do not cause the pressure variations associated with slugs of turbulence (Hof *et al.*, 2003). The turbulence transition in pipe flow is of interest to many industries as flow in the transitional regime, although more efficient, results in large pressure and flow variations. Therefore flows are frequently run inefficiently in the turbulent regime in order to reduce these effects (Hoff *et al.*, 2003; Fitzgerald, 2004).

6.5.4. Flow structures

The observed slumping at the trailing edge of pipes produces lamination at high angles to the pipe walls as the grains roll over each other at concentrations equal or close to the packing concentration. The seemingly random development and destruction of pipe margins points to vast temporal changes in flow rate during experimental fluidisation. This can be attributed to the shed vortices, which enhance

particle plucking from the pipe walls at their base and, due to turbophoresis, encourage deposition at the leading pipe edge concurrently. The erosive structures described in Section 6.1.3 may be the product of either individual eddies or other inflectional instabilities expected in shear flows; fundamental sinusoidal or sub-harmonic sinuous instabilities (Waleffe, 1997) or travelling waves (Wedin and Kerswell, 2004). These instabilities are created by a self-sustaining process that maintains structure in flows down to $Re \sim 120$ and consists of distinct phases: (i) streamwise rolls decouple from the streamwise velocity, redistributing the streamwise momentum, (ii) creating large fluctuations in the streamwise velocity and, (iii) these lateral or radial inflections then lead to 3-dimensional wake-like instabilities which, in turn, energise the streamwise rolls (Waleffe, 1997). These instabilities create fluctuations in pressure at the pipe wall (Figure 6.18) resulting in enhanced particle entrainment in regions of low pressure associated with eddies, and instabilities and net flow away from the pipe wall (Figure 6.19) in experiments with low cohesion sediments.

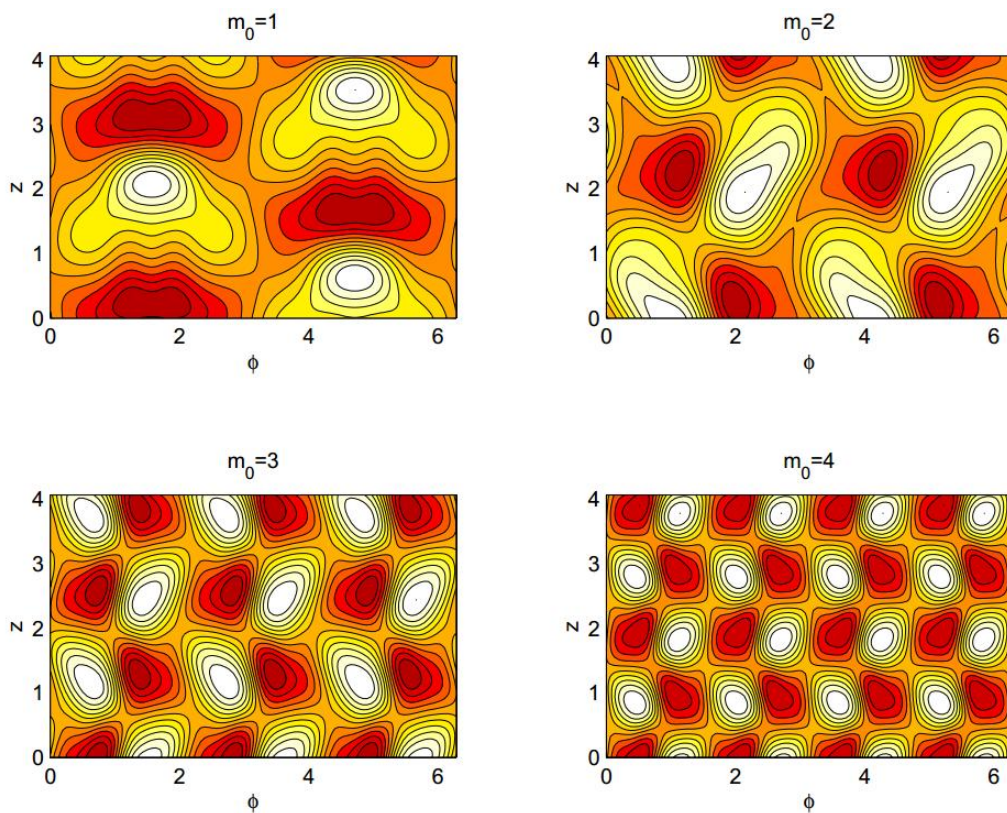


Figure 6.18. The pressure field at the pipe wall associated with travelling waves. m_0 = number of eigenvalues in the plane. Dark red corresponds to negative values, white to positive values. From Wedin and Kerswell (2004).

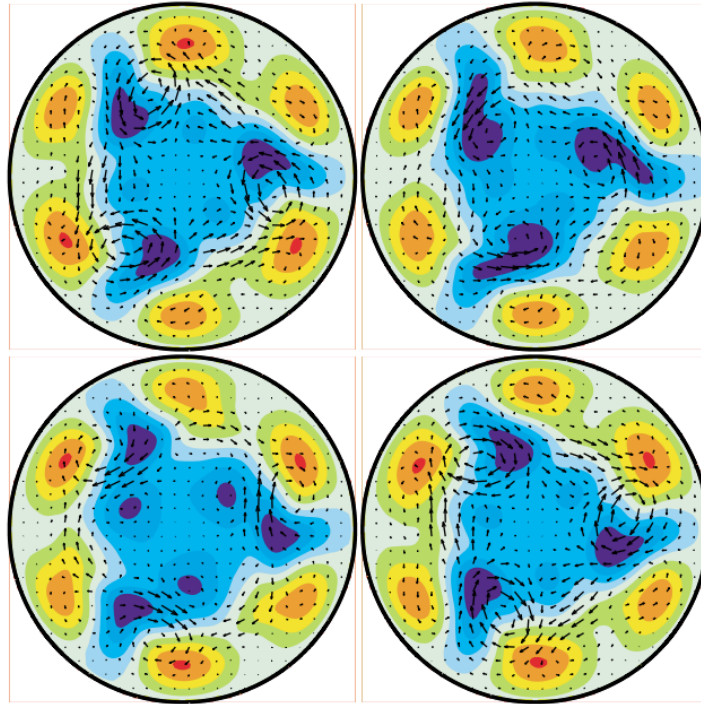


Figure 6.19. Axial section of a pipe at different downstream positions showing three-fold azimuthal symmetry in a travelling wave at $Re = 1250$. High speed streaks in the downstream flow component at the pipe wall (red) are more stable than low speed streaks (blue) near the centre of the pipe. Velocity components are shown by arrows, negative values are red and positive values are blue. From Faisst and Eckhardt (2003).

Laminations are produced at the pipe margins through rolling of particles in a zone of high shear and pressure. Increased lateral pressure gradients at the leading edge of pipes are shown by the tangential infiltration of fine-grained particles and may be influenced by cells of increased pressure caused by travelling waves (Figure

6.18). This suggests that lateral fluid escape driven by both the overall pressure gradient between the pipe and host sediment, and instabilities generated within the pipe, can be more dominant than previously thought and extend significantly further than the immediate infiltration horizon. Based on observations in these experiments, laminations parallel to pipe margins in geological examples are proposed to form either from grains being rolled up a pipe margin, or by impact into the pipe wall from turbophoresis, either from shed eddies or travelling wave-induced pressure gradients. Laminations at high angles to the pipe margins are shown to form through slumping of sediment towards the base of the pipe, either through brittle fracture on cohesive sediments or grain avalanching in non-cohesive sediments.

The present experiments have been undertaken at a small scale, one that as demonstrated is well within the laminar flow field. None-the-less even at these low flow Reynolds numbers a variety of mechanisms provide a range of instabilities enabling the influence of these velocity and concentration fluctuations to be at least qualitatively assessed. It is noted, that theoretical considerations and mathematical modelling of instabilities at low Re (e.g. Waleffe, 1997; Faisst and Eckhart, 2003; Wedin and Kerswell, 2004) suggest that axial and streamwise flow is considerably more complex than the linear parabolic velocity gradient implied by Hagen-Poiseuille flow. Consequently, the experiments do not strictly scale to fully turbulent systems. However, as with a wide range of physical models, these analogue experiments are capable of revealing much information about process dynamics (e.g., Peakall et al., 1996; Malverti et al., 2008; Paola et al., 2009). Critically, direct observations of the flow suggest that at any one time, the flow shows multiple states, in the present experiments from quiescent areas to dynamic areas with active flow structures. This is in agreement with the suggestion of Gallo and Woods (2004), based on observations of geological fluidisation pipes that flow regime is variable and frictional factors at pipe walls cause flow retardation. These

variations in flow structure are allied to large spatial and temporal variations in concentration within the flow, as has been previously postulated (Zhou *et al.* 2011).

6.5.5. Future work

Further consideration of the flow conditions in vertical pipes has shown that pipe edges are likely to be shaped by factors other than erosion, such as travelling waves and pressure fluctuations due to eddy-shedding in low Reynolds number regimes. Therefore, reassessment of non-linear margins of sandstone intrusions interpreted to be the product of turbulent flow acting upon the injection wall (*sensu* Scott *et al.*, 2009) may be necessary to improve understanding of their genesis. The flow structures and instabilities described in *Section 6.4.4.* suggest for the first time that, at any given time during sand injection, erosion can be both suppressed and enhanced by pressure and velocity perturbations even at low Re.

6.6. Conclusions

These experiments reveal for the first time that active sand injections show marked spatial and temporal variations in both flow velocity and concentration. Whilst pressure was not directly measured, these variations would lead to changes in the pressure field. Variations in flow parameters can induce erosion on the pipe walls since these are at the critical point of liquefaction, and small pressure fluctuations can trigger this. Repeated failure of pipe walls can lead to particles being reworked many times, with particles showing both downward and upward trajectories in different parts of the same pipe. In particular, large particles are frequently recirculated near the pipe-surface interface.

There has been much debate on the formation of laminations within injected pipes and sills. Here we show that laminations at high angles to pipe walls can form outside pipes by slumping and avalanching of grains, and lamination parallel to

pipe walls form at zones of high shear and/or pressure by rolling or impact into the pipe wall.

The experiments show that it is possible to get very dramatic flow variations across a pipe diameter with slower flows likely at the leading edge, maximum velocity in the centre of a pipe and significant downward movement of sediment at the trailing edge of pipes, this may help to explain the observed variations in sedimentary structures across many pipes in outcrop.

The present debate as to whether pipes are laminar or turbulent appears to be too simplistic in many cases. Large pipes may always be turbulent except immediately adjacent to the side-walls, however, smaller pipes, or pipes that don't reach the surface and therefore have lower pressure gradients driving them, and therefore smaller velocities, are likely to show spatial and temporal variations between laminar and turbulent flow.

6.7. Appendix: PTV code

```

pname = pwd;

[fname,newpname] = uigetfile('*.txt','Click on first data file');

cd(newpname)

%%%%%%%%%%%%%%%%%%%%%%%%%%%%%%%%%%%%%%%%%%%%%%%%%%%%%%%%%%%%%%%%%%%%%%%%%%
%%%%%%%%%%%%%%%%%%%%%%%%%%%%%%%%%%%%%%%%%%%%%%%%%%%%%%%%%%%%%%%%%%%%%%%%%% Read files and record file length to
allow padding

txt_files = length(dir('*.txt'));

bmp_files = length(dir('*.bmp'))/2;

n = txt_files;

n_bmp = bmp_files;

file_1 = fname(1:end-10);

%file_1 = 'Export.3d0eg44y.';

%file_1 = 'Export.3d07fisv.';

file_4 = '.txt';

Lengths = 0;

for x = 1:n

    if x<11

        file_2 = '00000';

    elseif x<101

        file_2 = '0000';

    else

```

```

        file_2 = '000';

        end

    file_3 = num2str(x-1);

    tempfilename = [file_1 file_2 file_3 file_4];

    miss=9;

    temp_data=dlmread(tempfilename,'\t',miss,0);

    temp_len = length(temp_data);

    Lengths = [Lengths temp_len];

end

Lengths = Lengths(2:end);

Max_len = max(Lengths);

clear temp*

%%%%%%%%%%%%%%%%%%%%%%%%%%%%%%%%%%%%%%%%%%%%%%%%%%%%%%%%%%%%%%%%%%%%%%%%%%%%%%
%%%%%%%%%%%%%%%%%%%%%%%%%%%%%%%%%%%%%%%%%%%%%%%%%%%%%%%%%%%%%%%%%%%%%%%%%%%%%% Load files pad to length of longest
file and concatenate into volume

Output = zeros(Max_len,7);

for y = 1:n

    if y<11

        file_2 = '00000';

    elseif y<101

        file_2 = '0000';

    else

        file_2 = '000';

```

```

        end

        file_3 = num2str(y-1);

        filename = [file_1 file_2 file_3 file_4];

        miss=9;

        PIV_data=dlmread(filename,'\t',miss,0);

        pad = zeros(1,7);

        pad_length = Max_len - Lengths(y);

        PAD = repmat(pad,pad_length,1);

        Padded = [PIV_data; PAD;];

        Output = cat(3,Output,Padded);

end

clear file*

Output = Output(:,2:end);

PIV_X = squeeze(Output(:,2,:));

PIV_Y = squeeze(Output(:,3,:));

PIV_U = squeeze(Output(:,5,:));

PIV_V = squeeze(Output(:,6,:));

%%%%%%%%%%%%%%%%%%%%%%%%%%%%%%%%%%%%%%%%%%%%%%%%%%%%%%%%%%%%%%%%%%%%%%%%%%%%%%
%%%%%%%%%%%%%%%%%%%%%%%%%%%%%%%%%%%%%%%%%%%%%%%%%%%%%%%%%%%%%%%%%%%%%%%%%%%%%% Animation of PIV vectors
%%%%%%%%%%%%%%%%%%%%%%%%%%%%%%%%%%%%%%%%%%%%%%%%%%%%%%%%%%%%%%%%%%%%%%%%%%%%%%

%figure(1)

%for z = 1:n

%    quiver(Output(:,2,z),Output(:,3,z),Output(:,5,z),Output(:,6,z))

%    xlim([0 1632]), ylim([0 1200])

```

```

%      M(z) = getframe;

%end

%movie2avi(M, 'myPeaks.avi', 'compression', 'None');

%movie(M,1)

%%%%%%%%%%%%%%%%%%%%%%%%%%%%%%%%%%%%%%%%%%%%%%%%%%%%%%%%%%%%%%%%%%%%%%%%%%%%%%
%%%%%%%%%%%%%%%%%%%%%%%%%%%%%%%%%%%%%%%%%%%%%%%%%%%%%%%%%%%%%%%%%%%%%%%%%%%%%% Collapsed vector plots
%%%%%%%%%%%%%%%%%%%%%%%%%%%%%%%%%%%%%%%%%%%%%%%%%%%%%%%%%%%%%%%%%%%%%%%%%%%%%%

figure(1002)

for z = 1:n

    quiver(Output(:,2,z),Output(:,3,z),Output(:,5,z),Output(:,6,z))

    hold on

    xlim([0 1632]), ylim([0 1200])

    title('Collapse of total vector population')

    xlabel('Pixels'), ylabel('Pixels')

end

%print -f2 -dpng % -depsc2

%%%%%%%%%%%%%%%%%%%%%%%%%%%%%%%%%%%%%%%%%%%%%%%%%%%%%%%%%%%%%%%%%%%%%%%%%%%%%%
%%%%%%%%%%%%%%%%%%%%%%%%%%%%%%%%%%%%%%%%%%%%%%%%%%%%%%%%%%%%%%%%%%%%%%%%%%%%%% Interpolation of PIV vectors into
regular grid

step = 50;

xlimt = 1632;

xstep = xlimt/step;

ylimt = 1200;

ystep = ylimt/step;

```

```
[x,y] = meshgrid(1:xstep:xlim, 1:ystep:ylim);  
  
xy_size = size(x);  
  
empty = zeros(xy_size);  
  
X_vol = empty;  
  
Y_vol = empty;  
  
U_vol = empty;  
  
V_vol = empty;  
  
for zz = 1:n  
  
    X = Output(:,2,zz);  
  
    Y = Output(:,3,zz);  
  
    U = Output(:,5,zz);  
  
    V = Output(:,6,zz);  
  
    [Xu,Yu,Uu] = griddata(X,Y,U,x,y);  
  
    [Xv,Yv,Vv] = griddata(X,Y,V,x,y);  
  
    U_vol = cat(3,U_vol,Uu);  
  
    V_vol = cat(3,V_vol,Vv);  
  
end  
  
U_vol = U_vol(:,:,2:end);  
  
V_vol = V_vol(:,:,2:end);  
  
U_mean = mean(U_vol,3);  
  
V_mean = mean(V_vol,3);  
  
clear empty
```



```
%piccy = imread('Export.3d07cluz.000000a.bmp');

Output = zeros(Max_len,7);

[fname,newpname] = uigetfile('*.bmp','Click on first data file');

file_1 = fname(1:end-11);

file_2_3 = '000000';

file_4 = 'a.bmp';

temp_filename = [file_1 file_2_3 file_4];

temp_file = imread(temp_filename);

temp_size = size(temp_file);

empty = zeros(temp_size);

Image_vol = empty;

clear temp

for p = 1:n_bmp

    if p<11

        file_2 = '00000';

    elseif p<101

        file_2 = '0000';

    else

        file_2 = '000';

    end

    file_3 = num2str(p-1);

    filename = [file_1 file_2 file_3 file_4];

    piccy = imread(filename);
```

```

        Image_vol = cat(3,Image_vol,piccy);

end

Image_vol = Image_vol(:,:,2:end);

clear file

%%%%%%%%%%%%%%%%%%%%%%%%%%%%%%%%%%%%%%%%%%%%%%%%%%%%%%%%%%%%%%%%%%%%%%%%%%%%%%
%%%%%%%%%%%%%%%%%%%%%%%%%%%%%%%%%%%%%%%%%%%%%%%%%%%%%%%%%%%%%%%%%%%%%%%%%%%%%% Plot of each frame overlain with
PIV and interpolated vectors

for frame = 1:n_bmp-1

    figure()

    imshow(flipud(Image_vol(:,:,frame)));

    hold on

    quiver(PIV_X(:,frame),PIV_Y(:,frame),PIV_U(:,frame),PIV_V(:,frame),'b'
)

    hold on

    quiver(Xv,Yv,U_vol(:,:,frame),V_vol(:,:,frame),'r')

    xlim([1 1632]), ylim([1 1200])

    set(gca, 'YDir', 'normal');

    print -f -dpng % -depsc2

end

close all

cd(pname)

```

7. Sub-aqueous sand extrusion dynamics

7.1. Introduction

Sand extrusions, referred to as extrudites, form when a sand injection breaches overburden to intersect with the sediment-water surface. Fluidised sand is then vented, resulting in the deposition of either discrete features such as sand volcanoes, or more areally extensive features termed sand sheets. Many systems exhibit combinations of these features (Boehm and Moore 2002; Jonk et al. 2007; Løseth et al. 2012). Extrudites have been described from a range of deposits, including; (i) deep water turbidites (Gill and Kuenen 1957; Gill 1979; Strachan 2002; Strachan and Alsop 2006; Pringle *et al.*, 2007; Jonk *et al.*, 2007; Vigorito *et al.*, 2008; Andresen *et al.*, 2009; Bouroullec and Pyles 2010; Løseth *et al.*, 2012); (ii) shallow marine (Boehm and Moore 2002); (iii) deltaic environments (Gill and Kuenen 1957; Nevill 1957; Johnson 1977; Okada and Whitaker 1979; Pisarska-Jamroży and Weckwerth 2013); (iv) fluvial (e.g. Allen 1961; Williams and Rust 1969); (v) lacustrine (van Loon and Maulik 2011); and, (vi) aeolian (Netoff 2002). The significance of extruded sandstones forming stratigraphic traps for hydrocarbon accumulations is also being recognised as their architecture is studied in more detail (Hurst *et al.* 2006; Andresen et al. 2009; Løseth et al. 2012). Furthermore, existing oil fields may in fact, be producing from extruded sand (e.g. the Eocene Chestnut Reservoir in the North Sea, Huuse et al. 2005a). However, due to the similarity between sheet-like extrusions and turbiditic or open-channel deposited sandbodies, their identification in many cases, remains speculative. Understanding of their formative mechanisms remains limited, in part because many of the studies are based on seismic data where geometries are well imaged, but process mechanics are hard to explain. As a consequence, outcrop examples of extruded sand must be examined. Key issues that are central to understanding these features are: 1), how

do sand sheets form from a point source(s), and, 2), what processes control the spatial distribution of extruded sand and determine whether point sourced (e.g. sand volcanoes, mounds, etc.) or areally extensive features (e.g. sheet) are produced? This study addresses these questions through field data collected from a well-exposed sand volcano field, enabling a process-based model of sand extrudite formation to be proposed for the first time.

7.1.1. Sand volcanoes and mounds

The most well recognised form of extrudite is the sandstone volcano, which often displays a sub-circular planform geometry and cone-shape in cross section, with low-angle ($0 - 15^\circ$) internal laminations dipping radially away from the vent (Gill and Kuenen 1957; Nevill 1957; Okada and Whitaker 1979; Jonk *et al.* 2007; Pringle *et al.* 2007; Hurst *et al.* 2011). The largest reported submarine sand-prone mounds are in the North Sea and these have a volume of up to 0.053 km^3 (Andresen *et al.* 2009), diameters of 700 – 1000 m and a thickness of up to 100 m (Løseth *et al.* 2012). Lateral transport of sediment over these distances is attributed to gravity flows from the vent sites (Ross *et al.* 2011; Løseth *et al.* 2012). These large-scale examples (Andresen *et al.* 2009; Løseth *et al.* 2012) have similarities, in that the deposits are asymmetric and display dipping, planar internal reflections. Furthermore, in both cases it is suggested that discrete phases of extrusion resulted in interbeds of clay or silt within the extruded sand mounds (Andresen *et al.* 2009; Løseth *et al.* 2012). Despite the impressive scale of the above examples, observations and associated interpretation are from seismic data sets that have limited well data control on lithology and sedimentary structure; detailed sedimentological analysis is therefore not possible.

7.1.2. Sand sheets

Sand sheets have been reported from both outcrop and seismic data, with clear relationships between the extruded sheet and feeder vents (Hildebrandt and

Egenhoff 2007) and mounds (Løseth *et al.* 2012). Outcrop observations and seismic data indicate that extruded sheets are bedding-parallel and extend up to 8 km laterally away from the vent sites (Hurst *et al.* 2011; Løseth *et al.* 2012). There is no consensus as to the internal geometry of sand sheets, some being described as homogeneous with no internal bedding (Hildebrandt and Egenhoff 2007), and others as heterogeneous with either internal lithological variations, low angle laminations (Boehm and Moore 2002; Jonk *et al.* 2007), and / or repeated abrupt grain size variations (Jonk *et al.* 2007). Whilst sub-aqueous sand volcanoes and mounds can be interpreted in terms of radial spreading of extruded material and deceleration away from a single point source (Ross *et al.* 2011; Løseth *et al.* 2012), extruded sheets (areally extensive, bedding parallel sandbodies that thin gradually and are often non-radial in shape; *sensu* Løseth *et al.* 2012) are conceptually more difficult to explain. Furthermore, it is unclear what controls point-sourced versus areally extensive deposition. Previous work has either not addressed this enigma (Boehm and Moore 2002; Løseth *et al.* 2012), or has linked sheets to the interfingering of sand volcanoes (Hurst *et al.* 2006; Jonk *et al.* 2007), or fissure-style venting (Hurst *et al.* 2006). Ross *et al.* (2011) used physical models to illustrate, for the first time, lateral gravity currents transporting extruded sediment from a sub-aqueous sand volcano vent. Although the physical experiments were spatially constrained, this mechanism could, at least conceptually, enable the transport of sediment over large areas. Løseth *et al.* (2012) invoke gravity currents as a sediment transport mechanism but do not explain why mounds are formed in some places and sheets elsewhere.

In order to address these questions on sub-aqueous extrudite dynamics, a well-exposed sandstone sheet is examined from the Carboniferous Shannon Basin, County Clare, Ireland. In doing so, this study aims to further the understanding of sand extrudite processes, enabling generic models of sand extrudite dynamics to be proposed. A previous study of this outcrop proposed that multiple extrusion events contributed to the formation of a single sandstone sheet (Jonk *et al.* 2007). The model proposed herein confirms some of the observations of Jonk *et al.* (2007), but provides an alternative interpretation and a process-based context, whereby we

demonstrate that sediment transport following extrusion was by gravity currents that were continuously active for the duration of sand sheet accumulation. We also reinterpret the triggering mechanism for deformation and remobilisation.

In addition, we contribute towards building paradigms for successful extrudite identification in the geological record, core and seismic data. Here we provide the sedimentological context and a detailed description of the sand sheet.

7.2. Geological Setting

The Shannon Basin formed during the Carboniferous in a foreland basin setting (Wignall and Best 2000, 2002; Martinsen and Collinson 2002; Martinsen *et al.* 2003; Pyles 2007, 2008; Tanner *et al.* 2011). The basin was filled by a series of upward-shallowing clastic sequences, which passed vertically from deep-water black shale, turbidites (Ross Formation), slope systems (Gull Island Formation) and deltaic cyclothems (Tullig, Kilkee, Doonlicky and higher cyclothems). Extensive synsedimentary deformation within this succession is attributed to incremental deformation front advancement, which was associated with orogenic shortening (Tanner *et al.* 2011). The study area comprises sediments of the Kilkee Cyclothem, exposed at Freagh Point, south of Liscannor Bay (Fig. 7.1). The lower Kilkee Cyclothem documents a net increase in accommodation, with fluvial elements (the Kilkee sandstone), overlying delta front strata, which include mouth-bars and distributary channels (Pulham 1989; Hampson *et al.* 1997; Wignall and Best 2004).

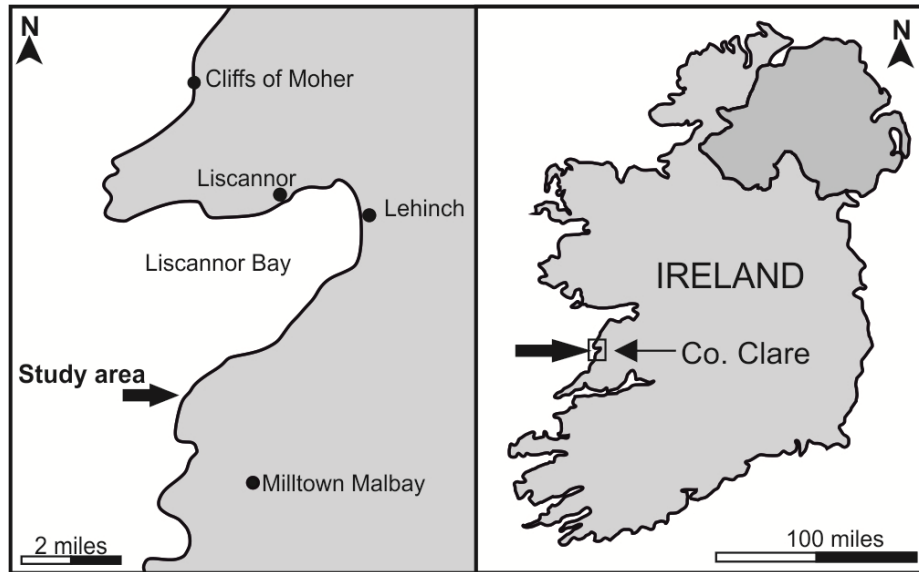


Figure 7.1. Location map of the study area.

7.2.1. Soft-sediment deformation in the Shannon Basin

The lower units of the Shannon Basin fill record extensive slope failure in the Gull Island and Ross Formations as slumps and slides up to 35 m thick (Martinsen 1989; Martinsen and Bakken 1990). These slumps display internal faults and folds that demonstrate lateral translation of sediment (Martinsen 1989; Martinsen and Bakken 1990; Strachan 2002; Strachan and Alsop 2006). Syn-sedimentary listric growth faults are described from both the Gull Island Formation (Martinsen 1989) and the lowest deltaic cyclothems (Wignall and Best, 2004; Martinsen and Bakken 1990). Mud diapirs up to 25 m in diameter are present at the Tullig - Kilkee cyclothem transition (Gill 1979; Wignall and Best 2000) and in the Gull Island Formation (Martinsen 1989). Sandstone injections and extrusions have been reported as sitting directly above slumps contained within the turbiditic sandstones, slope siltstones, and deltaic cyclothems of the Shannon Basin fill (Gill and Kuenen 1957; Gill 1979; Martinsen 1989; Strachan 2002; Strachan and Alsop 2006; Jonk *et al.* 2007; Pringle *et al.* 2007). Where a trigger mechanism for fluidisation of sediment and subsequent injection has been proposed, the sole theory is the terminal arrest of slumps and resulting compression of translated sediment (Strachan 2002; Jonk *et al.* 2007). Although soft-sediment deformation is prevalent in many units of the Shannon

Basin fill, the initiation of deformation in the Gull Island Formation and overlying deltaic cyclothem is attributed to a “generally unstable” delta slope, without the influence of biogenic methane but with possible intermittent seismicity (Martinsen 1989). No trigger mechanism for the soft-sediment deformation in the Ross Formation turbidites has been offered. Therefore no particular investigation into triggering mechanisms for the extensive soft-sediment deformation in the Shannon Basin fill has been undertaken.

7.2.3. Methods

Herein, an extensive sand volcano field exposed as an extruded sandstone sheet was studied, along with its relationship with the under and overlying sediments. The Freagh Point section is a 2600 m² coastal wave-cut platform with minor additional exposure at low tide (latitude 52°52'48.43"N: longitude 9°26'2.84"W). Exposure is limited to the South and West by the sea and to the east by cliffs to the East and overlying strata to the North. The step-like exposure accessible at low tide provides good three-dimensional control of the deformation features described. Sedimentary logging was undertaken; however, due to the spatial limitations of the outcrop any lateral changes in facies along strike could not be captured. Here we focus on the relationship between individual sand volcanoes, and how they merge to form the sand sheet. Figure 7.2 shows the spatial distribution of sand volcano vents, growth fault planes and facies present. Stratigraphic descriptions of the Kilkee Cyclothem can be found in: Pulham (1989), Hampson *et al.* (1997), and Wignall and Best (2004) amongst others. The geometrical parameters of 20 sand volcanoes were collected along with samples for microtextural analysis. The extruded units are bisected by a series of growth fault planes, providing natural cross-sections for detailed observations of laminations between individual sand volcanoes edifices. A total of 369 individual sand volcano vents were observed in the lower extruded unit.

7.3. Results – Facies

The sediments exposed at Freagh Point represent an overall mouth-bar dominated delta-top setting (Wignall and Best 2004) with strongly laminated, very fine grained sandstones, which erode with a distinctly flaggy character. Bioturbation is abundant in the form of sinuous *Scolicia* trace fossils, which represent efficient sub-sediment feeding traces as a response to slow or sporadic nutrient accumulation (Bromley *et al.* 1995). The Kilkee Cyclothem has undergone extensive soft-sediment deformation at the study locality, with beds of strongly liquefied siltstones, mud diapirs, extensive growth faulting, an extruded sand sheet and discrete sand volcanoes. Seven stratigraphic units are present in a 5 m thick section with three undeformed units, two deformed units and two extruded units (Figure 7.3). This assemblage is split into six lithofacies, those which retain their original depositional features (A), those which have been deformed (B), or have been remobilised (C). These lithofacies are described below and represented in a sedimentary log and photographs (Figs. 7.3 and 7.4) and their spatial relationships shown in Figures 7.2 and 7.5.

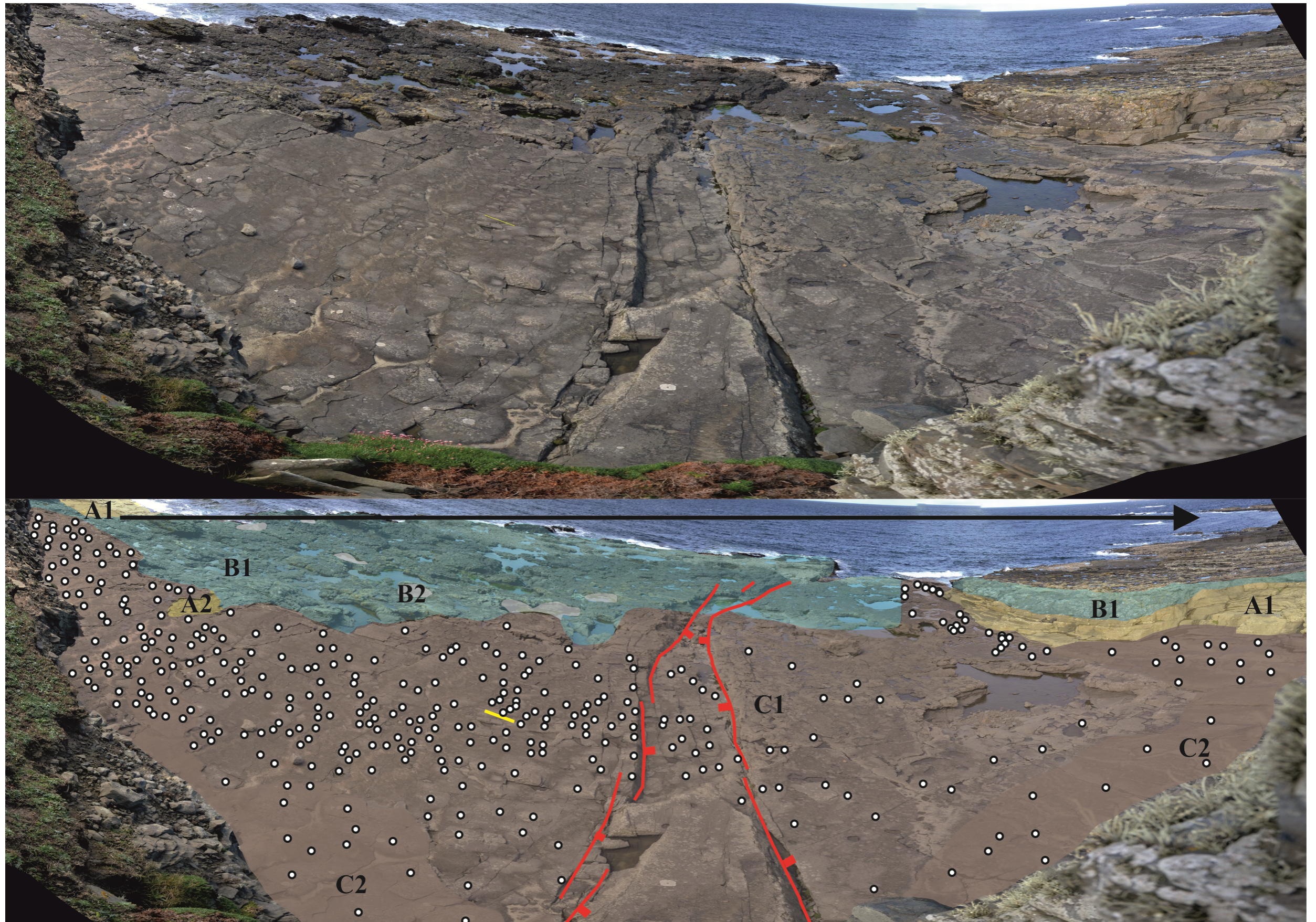
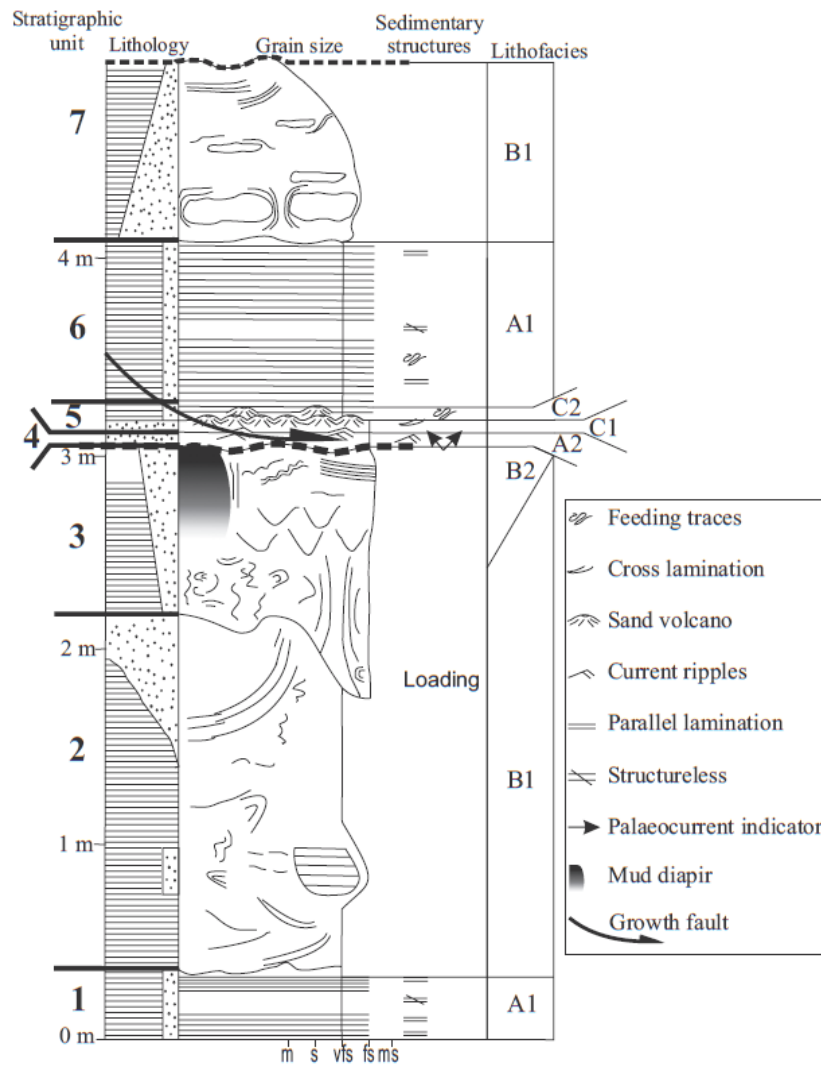


Figure 7.2. Photomontage of the outcrop at Freagh Point, facing West. Faults are marked and sand volcano vents are shown by white dots along with facies distribution in the underlying interpretation. Yellow 1 m scale bar to centre-left. See text for facies codes

Figure 7.3. Detailed sedimentary log of the study area with units and facies codes.



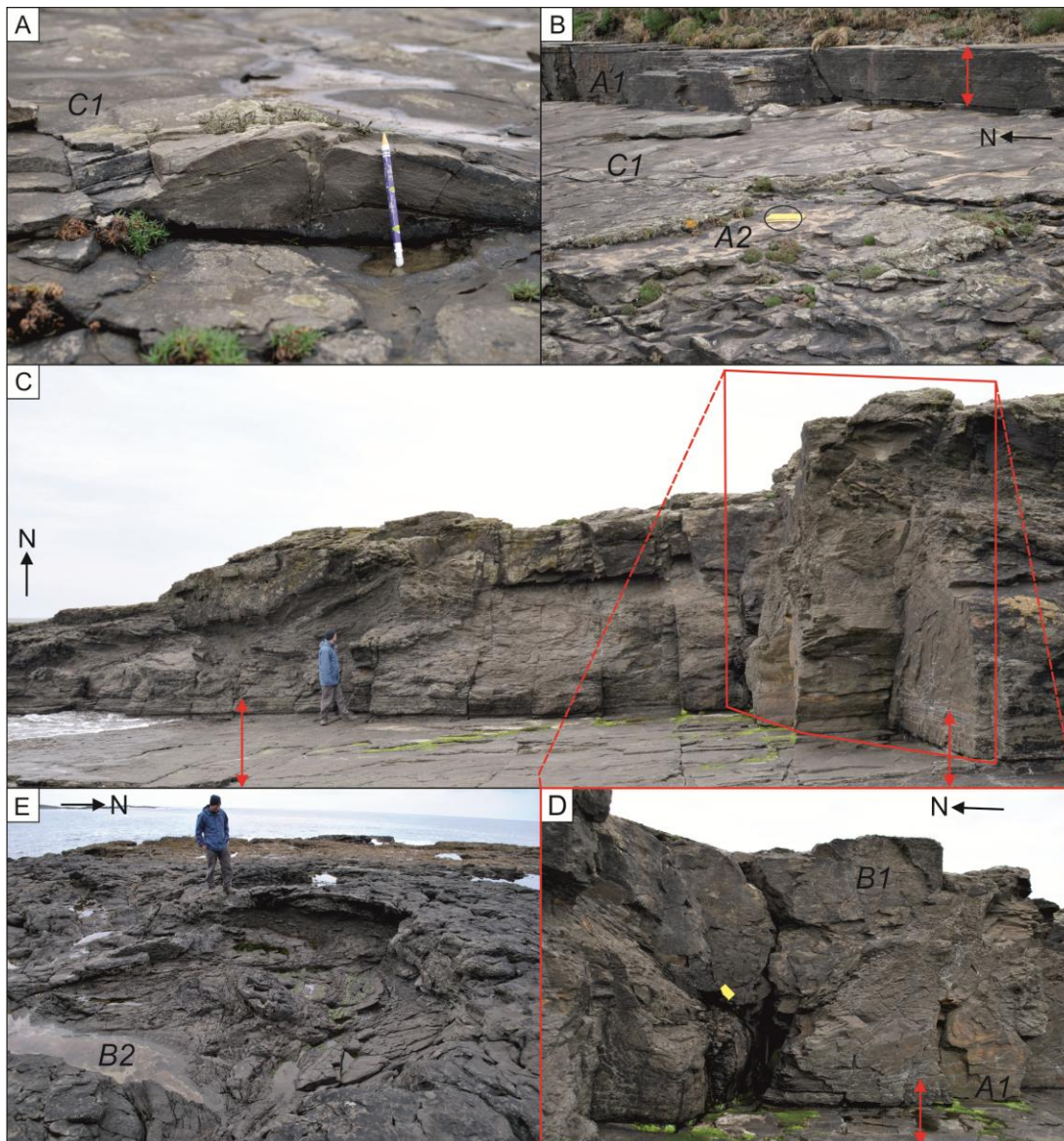


Figure 7.4. Photographs demonstrating the facies present (A) sand volcanoes with sandstone sheet comprising facies C1. (B) View facing NE, of units 4, 5 and 6. Yellow notebook sits on unit 4. Red arrow denotes thickness of facies A1. (C) Photomontage of units 1 and 2 showing deformation in facies B1. (D) View perpendicular to (E) to demonstrate large-scale dewatering structures and lack of directional indicators within this facies. Red arrow denotes extent of facies A1. (E) Bedding plane view of top of unit 3, showing mud diapir (B2) within B1. Person is standing above one edge of diapir.

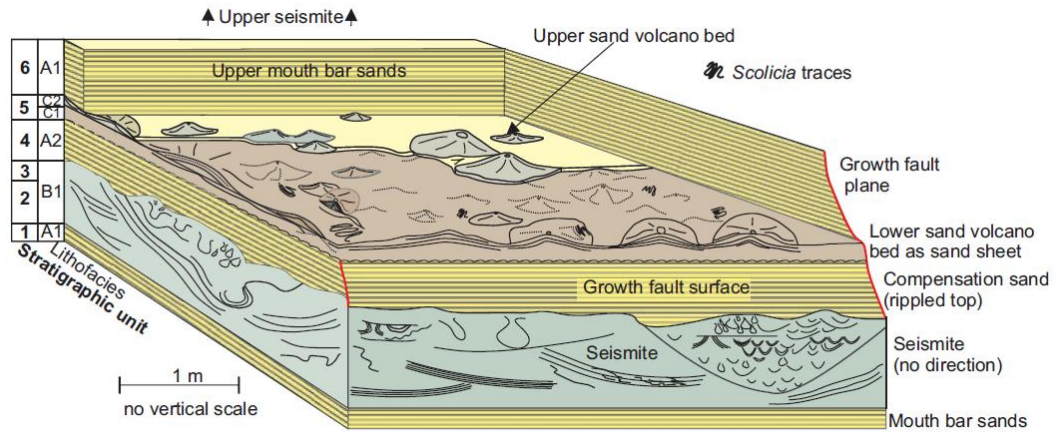


Figure 7.5. 3D schematic model of Freagh Point idealised along the plane of a major growth fault which cross-cuts the outcrop, demonstrating the relationships between and within the facies present. Facies labels and stratigraphic units are shown on the left of the figure.

7.3.1. A – Undisturbed facies

Two lithofacies in the study area are undeformed: (A1) strongly laminated sandstones and (A2) rippled sandstones. Both lithofacies are cut by growth faults; however these do not disrupt depositional textures within the beds.

7.3.1.1. A1 Laminated sandstones

The thin-bedded sandstones split readily into sheets 15-30 mm thick (flags) and are typically planar laminated with sharp bedding surfaces. This lithofacies comprises units 1 (Fig. 7. 4D red arrow) and 6 (Fig. 7.4B and 7.5). This facies is 40 cm thick in unit 1 with a sharp upper transition into highly deformed facies (lithofacies B1). The upper termination of this facies in unit 6 is again marked by an abrupt transition to heavily deformed facies (B1) that contain long wavelength load structures. These are the “Liscannor Flagstones” of Wignall and Best (2004).

Interpretation

Coeval outcrops of this facies are present along the County Clare coastline and are described and interpreted in Pulham (1989), Hampson *et al.* (1997) and Wignall and Best (2000, 2002, 2004). *A1* is believed to represent cretal mouth bar sands, deposited in pulses when the prograding fluvial system was in flood. This provides quiescent interludes, allowing burrowing organisms to colonise the area, accounting for the prevalence of *Scolicia* trace fossils.

7.3.1.2. **A2 Rippled sandstone**

This lithofacies (unit 4) has restricted outcrop covering 200 x 50 cm where the overlying facies has been eroded as shown in Figures 7.2 and 7.4B. It is formed by very fine grained sandstone and occurs as a 5-15 cm thick bed with an undulating basal contact with deformed facies (*B1*) in unit 3 (Fig. 7.5). The upper surface displays unidirectional ripples; palaeocurrents between 300° and 40° indicate dominant flow to the north. There is no internal bedding in this lithofacies.

Interpretation

A2 represents a period of seafloor compensation following formation of the seismite (facies *B1*). The undulating lower contact is attributed to influxes of sand infilling the topography generated on top of the seismite due to loading and other gravity instabilities. The rippled upper surface, in conjunction with the under and overlying beds suggests a period of fluvial influence at the delta front.

7.3.2. B - Deformed facies

Present in units 2, 3 and 7, these lithofacies show extensive liquefaction and density instability related deformation features: (B1) siltstones with pervasive soft-sediment deformation and dewatering, and (B2) mud diapirs.

7.3.2.1. B1 Heavily dewatered siltstones and sandstones

This facies is highly disturbed and contains abundant dewatering features, which increase in frequency towards the top of the exposure (Figure 7.4C and D). Features include sandstone rafts, dish structures and dewatering columns. The basal contact with facies A1 is loaded, with ~1 m lateral spacing between sandstone load structures. Above this, isolated sandstone rafts up to 70 cm diameter occur within 2 – 3 m of siltstones with well-defined fabrics. These fabrics do not provide any sense of movement and possible directions of movement are contradictory in 3-dimensional exposure. Pockets of heavily dewatered sand are loaded into the siltstones; pockets vary in diameter and vertical relief, but are typically up to 2 m deep and 4 m wide (Fig. 7.4D). Dewatering structures show intense, upwards water escape in the form of dish structures; pillars are mostly absent in the upper part of unit 3. Rafts of deformed and undeformed facies A1 are present in all occurrences of B1 (units 2, 3 and 7) where they have completely detached from their overlying parent unit. No basal shear zone or mud horizon is present at the base of this facies as it transitions sharply from A1.

Interpretation

This lithofacies has not previously been described in the Kilkee Cyclothem. The lack of a basal shear surface or décollement immediately precludes any interpretation that this unit represents a slump. In addition, the lack of a definitive directional fabric such as verging folds within the siltstones suggests no downslope movement occurred. The prevalence of dish structures and “bowls” of heavily dewatered sandstone, sandstone pillows that have clearly detached from the overlying units

and an overall chaotic fabric with no sense of vergence are indicative of *in-situ* deformation, which, when triggered by an earthquake is termed a seismite (Moretti *et al.* 1999; Montenat *et al.* 2007; Alfaro *et al.* 2010). Seismites are formed due to seismic shock and require a specific set of parameters: (i) waterlogged or saturated sediments, (ii) homogenous fine-grained sediment, (iii) very low local slope, the existence of a significant slope may result in seismites moving laterally and transitioning into slumps or slides, especially if an underlying lubricating lithology is present, and, (iv) an earthquake of sufficient proximity and magnitude (Montenat *et al.* 2007; Moretti and Sabato 2007). Minor changes in the vertical distribution of sediment rheology or grain size can determine which beds are most susceptible to seismic shock and previous studies have shown that deformation can be localised in coarser-grained packages isolated within finer-grained beds (Moretti *et al.* 1999). The repetition of facies *B1* further up section in unit 6, again showing no direction of movement further suggests seismic shock is responsible for deforming these horizons.

7.3.2.2. B2 Mud diapirs

Five mud diapirs up to 3 m in diameter were observed in unit 3 puncturing through the top of *B2* and deforming the surrounding siltstone (Fig. 7.4E). One diapir showed a roughly circular planform geometry, others are elliptical, although no preferred orientation was observed. In one case, shown in Figure 7.4E, remnant mud is still visible in the base of an eroded hollow and shows a chaotic internal fabric with concentric vertical laminations delineating the edge of the diapir. Surrounding lithofacies *B1* exhibits a concentric fabric up to 30 cm from the diapir margin. The bases of the mud diapirs are not visible and therefore their stratigraphic origin could not be established.

Interpretation

Mud diapirs are observed cutting up through the seismite. Interaction with the overlying unit 4 was not observed (facies *A2*), but they are not observed to cut

through the extrudites (unit 5 and above). Mud diapirs form due to the buoyancy difference between less dense buried mud and overlying denser saturated sand. Due to this gravitational instability, the mud deforms plastically and punctures up through the overlying seismite, deforming the surrounding strata into vertical, concentric laminations. Such mud diapirs are frequently associated with delta front environments (Morgan *et al.* 1968).

7.3.3. C – Remobilised facies

These are the extruded elements of the study locality (units 5 and 6) and can be assigned into two units: (C1) an extruded sandstone sheet and, (C2) discrete sand volcanoes. 369 individual sandstone volcano craters were identified. Their relationships are demonstrated in Figure 7.5.

7.3.3.1. C1 Tabular sandstone

This facies consists of a laterally extensive, tabular sheet of very fine-grained sandstone (unit 5), which conformably overlies facies A2 (Figs. 7.4A, B and 7.6). The upper surface of this facies is covered with sandstone volcanoes and vents, some of which are deeply eroded. It is up to 30 cm thick and displays dipping laminations in a 15 m long cross-section exposed by a growth fault plane. Laminations originate at sand volcano vents and dip away at approximately 15-20° in close proximity to the vent; dip angles decrease to ~5° up to 40 cm from vents (Fig. 7.7) with some flanks being flat-lying.

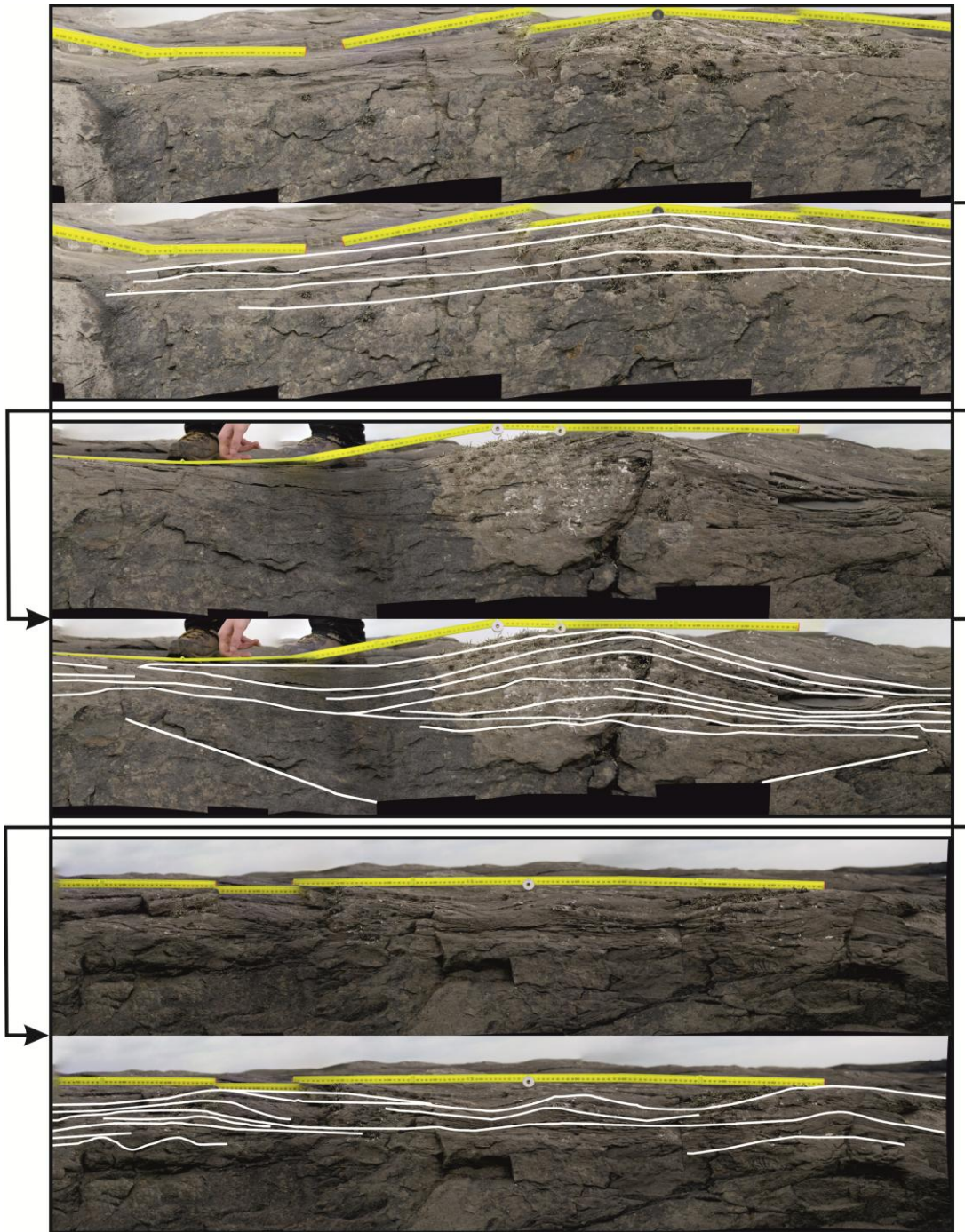


Figure 7.6. Photomontage of facies *C1* where it is cross-cut by a major growth fault. Continuous laminations within the sand-sheet are well preserved and have been interpreted (white lines) for clarity. Images flow from top-left to bottom-right.

SEM (scanning electron microscope) analysis shows that: proximal to the vents, grain size distribution is bimodal, with quartz grains ranging from 40 – 120 μm

(very fine sand) and well aligned sheets of primary chlorite and micas up to 200 μm long (Figs. 7.8A and B).

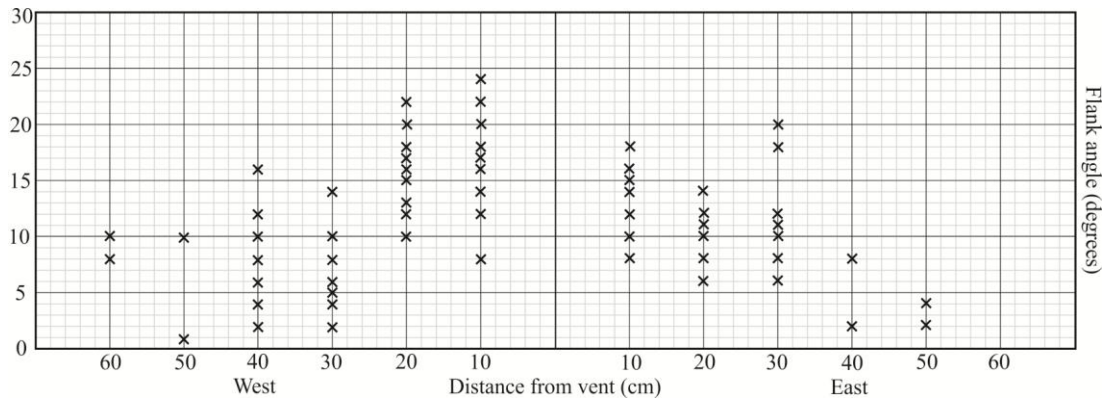


Figure 7.7. Scatter diagram of flank angles from representative sand volcanoes. The data demonstrates the decrease in sand volcano flank angles with increased distance from vent, up to 30 cm. A minor increase in flank angle is seen at 40 cm, or equidistant between vents.

No grain-size variation is present within individual laminations. Laterally, the sheet has a rather more chaotic internal organisation with a lower clay content (phengitic mica and chlorite) but better sorting, with grains between 25 – 100 μm (Fig. 7.8C). Note that the grain size data are likely to underestimate true grain size due to the effect of random cuts through ellipsoidal or spherical grains in a 2D plane (Johnson 1994). Some laminations can be traced laterally between sand volcanoes; others become difficult to identify mid-way between vents or appear to coalesce (Fig. 7.6). In plan view, the sand volcanoes are elliptical to circular with well-defined craters from which sediment was extruded. The original areal extent of this facies is difficult to identify as the outcrop is limited by erosion by the sea to the South and West, cliffs to the East and overlying strata to the North. This facies is overlain by occurrences of C2.

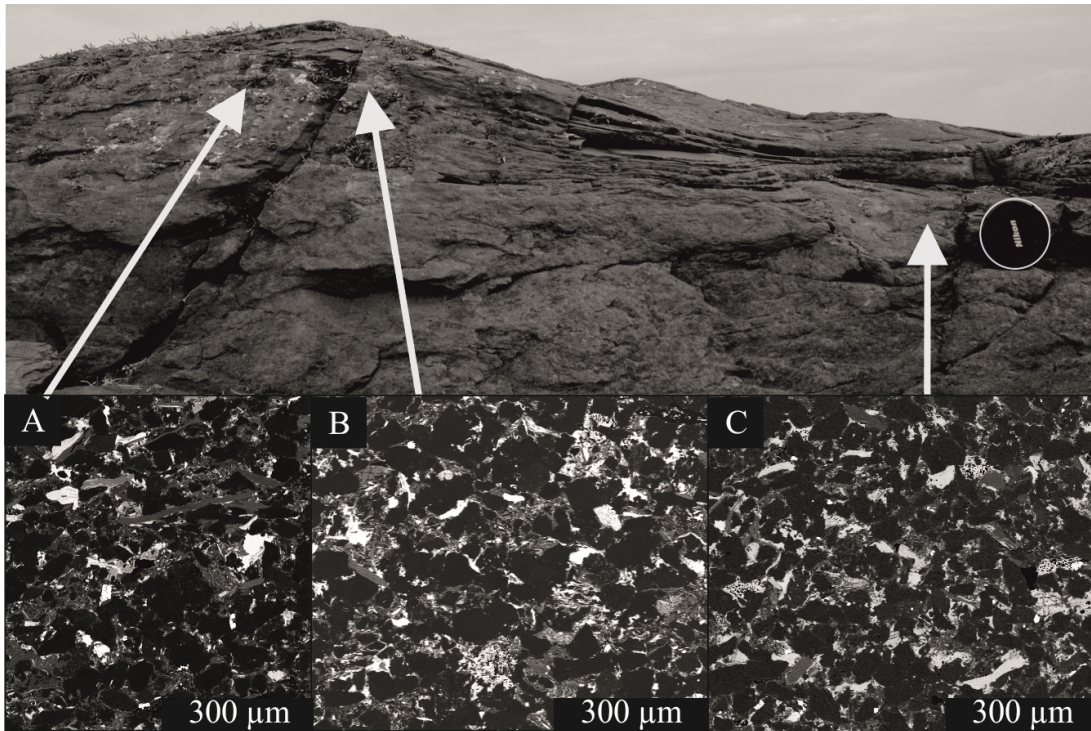


Figure 7.8. Cross-sectional view through the extruded sandstone sheet highlighting a sand volcano and positions of back-scattered electron diffraction images of the sandstone sheet demonstrating the decrease in grain-size away from vents. Quartz grains are black. Lens-cap for scale in upper image.

7.3.3.2. C2 Sand volcano bed

This lithofacies has been separated from the underlying facies *C1* owing to its interaction with overlying facies *A1* and a lack of overlap between nearby sand volcanoes. It is assigned to the lower part of a separate unit (6) in outcrop (Fig. 7.9). Discrete sand volcanoes up to 40 cm in diameter with well-defined craters and dipping laminations crop out around the edge of the study area. Grain size is silt to very fine sand. The low angle distal laminations originating from these sand volcanoes were observed grading laterally into facies *A1*, becoming indistinguishable from each other. Due to the interaction with the flaggy facies *A1*, this facies is easily erodible and would otherwise have covered the underlying *C1*.

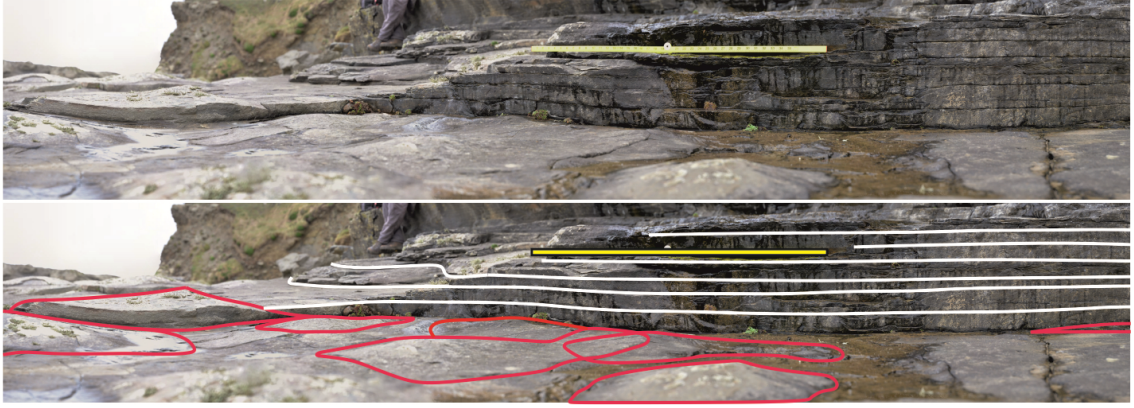


Figure 7.9. Photomontage demonstrating the relationship between facies C2 (individual sand volcanoes outlined in red) and A1 (white laminations). Scale bar (yellow) 1 m.

Interpretation

C1 and C2 represent sediment extrusions onto the seafloor as shown by the presence of hundreds of sandstone volcanoes on the present-day wave-cut surface. In facies C1 these sand volcanoes coalesce to form an extruded sheet whereas, in contrast, the sand volcanoes remain isolated in facies C2.

7.4. Discussion

The occurrence of two, distinct extruded layers (facies C1 and C2) with 3 cm of deltaic flood deposits between them, suggests sediment incursion into the area was periodic. This is supported by the presence of *Scolicia* burrows in the sandstone sheet and sandstone volcanoes, which indicate prolonged periods of quiescence to allow colonisation. Flank angles appear slightly lower to the east (Fig. 7.7) however, this is due to the local tectonic dip of 5° west.

A cross-section of the sand sheet (C1) is shown in Figure 7.6. Where flanks coalesce equidistant between vents, flank angles are low (0 – 5°) and are rarely above 15° proximal to vents. Continuous laminations, as highlighted in Figure 7.6, suggest the vents were active contemporaneously and the extruded material was mixing between vents, where the laminations can become difficult to define. Grain size ranges within the extruded sheet are small (silt to very fine sand) and clay, heavy mineral content, and grain size decrease with increasing distance away from vents. SEM analysis of samples from both the sand volcano flanks (proximal) and the sheet (distal) shows that individual laminations are internally structureless (Fig. 7.8). There is no evidence of erosion within the sand sheet; laminations are continuous with no cross-cutting relationships or fine-grained interbeds. These observations show that the sand volcanoes were contemporaneous with the sheet. The laminae do not thicken, nor is their interfingering between sand volcano flanks that might be expected if there were differences in timing between sand volcanoes or from relative flow rates between sand volcanoes erupting synchronously. These features suggest that flank flows are combining and sediment is transported between and downslope from the sand volcanoes.

7.4.1. Depositional mechanism

The evidence presented above, namely; low slope gradients, proximal deposition of the coarsest fraction and coalescing of flanks within the sheet is indicative of

deposition by gravity currents. The grain size data (Fig. 7.8) show that the coarsest and heaviest sediment load is deposited proximal to vents, and that the clay has been preferentially transported, subsequently settling at a later date. Additionally, low slope angles, far below the angle of repose of sand in water ((25 – 40°) (Carrigy 1970)), are indicative of a flow adding an applied shear stress to the sediment interface. These observations can be explained in terms of standard gravity currents dynamics where flows enhance basal shear stress, and where finer-grained sediments are preferentially bypassed, whilst the coarsest grains are deposited proximally (Middleton 1993). Such flows occur because particulate-laden fluid extruded from an active sub-aqueous vent is denser than the surrounding ambient fluid, and consequently flows radially away from the crater as a gravity current. Transport of sediment may be further aided by a halo of fluid flow through the flanks of the sand volcanoes at a velocity below that required to liquefy and fluidise the coarsest sediment, as demonstrated by Ross *et al.* (2011) (see Chapter 6). This additional seepage contributes to vertical velocities at the base of gravity flows, enhancing sediment transport. Interaction and mixing of gravity currents between vents will result in a cloud of extruded sediment inundating the seafloor and flowing around the active sand volcanoes. Slope gradients will change as extrusion becomes established due to deposition of the coarsest fraction and building of topography proximal to the vents, leading to increasing lateral confinement of the gravity currents as sediment accumulates on neighbouring sand volcanoes. Thus the fluid dynamics of gravity current interactions are considerably more complex than the literature addresses. Seafloor currents may theoretically have contributed as an additional sediment transport mechanism, however the circular planform geometry of the sand volcanoes preclude this medium as seafloor currents would be expected to create asymmetric vent geometries strongly aligned in a single direction.

7.4.2. Preservation of the sandstone sheet

The lack of asymmetry in the sand volcanoes suggests they have not been re-shaped and thus precludes any sediment reworking by tides or waves. Although the sedimentological setting is fluvial-dominated shallow-marine deltaic, there is a lack of tidal signatures in the upper cyclothem of the Shannon Basin fill (Pulham, 1989). This is because the basin is small and had only a limited connection to the epicontinental seaway that covered much of Northwest Europe in the Upper Carboniferous, which had a small tidal range of 5 – 10 cm (Wells *et al.* 2005a, b). The river-mouth processes recorded in the Kilkee Cyclothem show that both frictional and buoyant processes defined the mouth-bar deposits (Pulham 1989). The mouth bar that comprises this study was likely constructed by buoyant process at a channel-mouth as the presence of *Scolicia* trace fossils suggest a marine environment (Pulham, 1989) which, when combined with a lack of significant tidal processes in the Shannon Basin (Pulham 1989), would suggest the presence of a salt-wedge at the channel-mouth. Mouth bars comprised of well-sorted sands that exhibit planar laminations with dominant unidirectional current indicators at the crest are also typical of highly-stratified river-mouths (Wright and Coleman 1974). Salt-induced flocculation from the fine-grained suspended sediment load (Pulham 1989) would increase sediment rates on bars, and rapidly settling flocs have been shown to overwhelm the erosive power of waves on the Po Delta (Fox *et al.* 2004). This mechanism may also account for the lack of sediment reworking and preservation of the extruded sands. Finally, larger-scale deltaic morphology could account for the quiescence: the irregular shoreline typical of river-dominated deltas (Olariu and Bhattacharya 2006) would provide multiple embayments and protruding river-mouth bars as recorded in the Kilkee Cyclothem (Pulham 1989). Thus an individual mouth bar such as that in this study would be protected from significant wave influence by this topography.

7.4.3. Existing models of sand sheet formation

It has been suggested previously that the flanks of sandstone volcanoes may interfinger (Boehm and Moore 2002; Hurst *et al.* 2011); based on our observations, this mechanism is considered unlikely, because deposition from coeval, interacting gravity currents would not result in the formation of interfingering geometries. However, interfingering of flanks and stacking of vents (Hurst *et al.* 2011) may occur if sand volcanoes erupt consecutively, thus precluding any gravity current interactions. In the current study, flow velocities are unlikely to be identical from all the sand volcanoes, flow velocities being dependent on conduit width for example, yet interfingering does not occur due to the mixing of gravity currents. The presence of many hundreds of preserved craters on top of the studied sand sheet, a lack of fine grained-interbeds (*sensu* Jonk *et al.* 2007; Andresen *et al.* 2009) and the clear relationship between each volcano via the continuous laminations shows the volcanoes were contemporaneous. The second sand volcano bed (facies C2) was then extruded, the discrete sand volcanoes suggesting short-lived extrusion (Fig. 7.9).

Løseth *et al.* (2012) use seismic data to interpret spatially extensive extruded sands, which are partially confined by forced-folds above laccolith-like injection complexes that created mounds and topography on the palaeo-seafloor. They suggest that the extruded sands were confined by local topography, but do not explain how such confinement might lead to large-scale sheets. Here we suggest that flows of extruded sediment built upon initial topographic forcing (force-folded mounds) to initiate and construct channels, thus enabling longer run-out distances for gravity currents. Sheets form at the end of the channels as a gravity flow rapidly becomes unconfined, dropping its load in the same way that turbidites produce sheets at the end of submarine channels (e.g. Mutti and Normark 1987; Macdonald *et al.* 2011). Evidence in support of this interpretation is provided by seismic cross-section D, (Løseth *et al.* 2012, supplementary information) showing extruded sand with a levee-like geometry, suggesting sustained overbank deposition from a channelized

flow, rather than from the intermittent, explosive extrusion events as proposed by the authors. Without this topographic forcing from channelization, it would be problematic to envisage the deposition of 260 km² of sheet-like, fine to medium-grained sands, with no primary clay, from radially-expanding flows unless there were multiple, closely spaced vents extruding coevally.

A previous study of the Freagh Point outcrop noted that laminations are continuous between sand volcanoes and concluded that they were coeval (Jonk *et al.* 2007). However, no mechanistic explanation for this observed relationship was provided, instead it was proposed that each lamination represented a separate extrusion pulse with only the coarsest grains from the underlying deformed unit being fluidised with the fine-grained and clay fraction left behind and that the fine-grained laminae were deposited during periods of quiescence between extrusion pulses. There is no evidence for this mechanism in any previous study of fluidisation as the fine fraction is always preferentially fluidised owing to the lower fluid velocities required to suspend and transport the smaller particles (Di Felice 1995). Additionally, pulsation is improbable given that: (i) the lack of an impermeable cap will preclude significant overpressure build-up and therefore explosive extrusion; and, (ii) repeated liquefaction will lead to progressive compaction and increased packing density of the source bed, increasing the resistance to subsequent liquefaction events (Obermeier 1996), resulting in very dense sands requiring exceptionally strong shaking to produce fluidisation features (Seed *et al.* 1983). Moreover, the position of the sandstone sheet on a mouth-bar crest, suggests there would be limited time for background settling of clay between extrusion events, and indeed repeated seismicity on a scale required to repeatedly liquefy sands whilst also both increasing their relative density and expelling pore-water. These caveats exist in the study of Jonk *et al.* (2007) in part because the analysis of the Freagh Point sandstone sheet was based on microtextural data from sand volcanoes in the underlying Ross Formation.

The model proposed herein confirms the observation of continuous laminations, but places this in a process-based context whereby we demonstrate that sediment transport following extrusion was by gravity currents that were continuously active for the duration of sand volcano accumulation. Laminations are ubiquitous in subaqueous sand extrusions (Gill and Kuenen 1957; Nevill 1957; Gill 1979; Okada and Whitaker 1979; Boehm and Moore 2002) and can be explained in the majority of cases including the present example, as a product of tractional transport of sediment under gravity currents (Arnott and Hand 1989; Leclair and Arnott 2005). Grain flows cascading down the flanks can also produce lamination for steep-sided isolated sand volcanoes (Strachan 2002).

7.4.4. A process-based model of extrudite formation

Here we propose a first process-based conceptual model of extrusion dynamics for sand sheets and sand volcanoes (Fig. 7.10). If multiple vents are present and extruding coevally, the radial gravity currents produced can be expected to interact, coalesce, and transport sediment downslope, ultimately depositing a sandstone sheet. At the other end of the spectrum, if fluid flow is concentrated into one vent, considerable topography can be expected to form as the coarsest fraction of extruded material is deposited close to the vent and a radial gravity current transports material away from the crater.

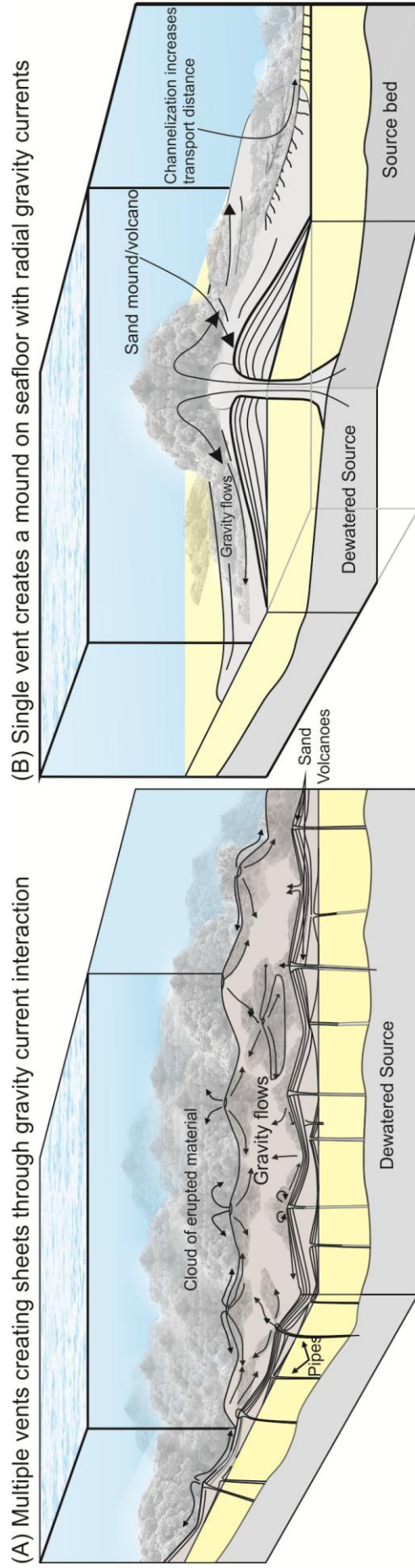


Figure 7.10. Process-based model of extrudite formation. (A) Where multiple, closely-spaced vents are present, the interaction of gravity currents will produce a sand-sheet with continuous laminations between vents. (B) A single vent will produce a discrete feature, such as a mound due to radial gravity flows. Long term extrusion events will result in channelling, redirecting the radial gravity flows, resulting in deposition away from the extrusion-site as shown to the right of the cartoon.

The present example is a small-scale sand sheet (2600 m² exposed) and the sand volcanoes are no larger than 2 m in diameter, with no evidence that the gravity flows emanating from them were erosive. However, if sand volcano vents, or vent fields are larger (*sensu* Løseth *et al.* 2012), then gravity currents are likely to be erosive, thus the mechanics become considerably more complex. Provided the gravity current is of sufficient size, erosion and a degree of channelization may occur, thus providing an additional method of transporting extruded material away from the craters. Once this transition into channelized flow occurs, the gravity currents can essentially be classified as turbidity currents and their deposits are likely to follow recognised turbidite depositional patterns such as the Bouma sequence, thus making their identification in core or outcrop problematic.

7.4.5. Identification of extruded sand sheets

Some parameters for the recognition of extruded sand sheets have been presented in the literature; namely a genetic relationship between the sheet and underlying sandstone dykes and sills, and low angle lamination and/or bedding (Hurst *et al.* 2006). However, localised disruption of underlying strata may not be present beneath the extruded sheet if the sediment has been transported away from vent sites, so such criteria will not be universal. This study has also shown that lamination angles can increase in proximity to vents, providing an additional identification mechanism. Hildebrandt and Egenhoff (2007) further suggested that key features of their extruded sands were i) the presence and lateral transport of semi-rigid, laminated sand-siltstone fragments preserved throughout the extrudites, and ii) the presence of steeply inclined conduits ('clastic dykes') that form between load structures. However, transport of semi-rigid sandstone-siltstone fragments as suspended load (Hildebrandt and Egenhoff 2007) in extruded gravity currents is improbable since their settling velocities would be orders of magnitude higher than the other grains, and they would be expected to be deposited in and close to the vents and at the base of the extruded sheet. Secondly, the proposed supply to the extrudites do not appear to be clastic dykes but are more akin to 'pillars' of

homogenous sediment which form between falling load structures. These characteristics fit with those observed in seismites (see earlier description) with the laminated siltstone-sandstone fragments examples of balls and pillows forming from collapse and descent of an overlying bed(s). Thus these units are not extrudites and such criteria cannot be applied to extrudites and care must be taken not to conflate extrudites and *in-situ* liquefied beds. Consistent bed- and core-scale paradigms for the recognition of extrudites may therefore not apply, and in some cases (especially in core) the deposits will be indistinguishable from those of turbidites. Sand volcanoes and sandstone sheets such as those in this study would be problematic to correctly identify in core, but will show laminations with dips directions between 0 – 360° whilst cross-laminations in turbidites will show alignment in a single direction. That said, the largest scale extruded channelized sheets are essentially turbidites with alignment in a single direction and are therefore synonymous at the bed and core scale. Therefore, correct identification of extruded sand sheets must incorporate regional evidence for sediment remobilization, such as the cross-cutting relationships commensurate with underlying injection complexes including identification of likely vent sites from which the sediment was erupted and careful consideration of the dynamics of sediment fluidisation and extrusion.

7.5. Conclusions

The outcrop at Freagh Point is an outstandingly exposed example of a seismically-induced sand sheet, formed through the coalescence of gravity currents. Here the combination of low sand volcano slope gradients, deposition of the coarsest fraction proximal to vents, and continuous laminations between sand volcanoes, demonstrate that the sand sheet formed from coalescing gravity currents emanating from hundreds of coevally erupting sand volcanoes. Here we propose a process-based mechanism for the generation of areally extensive sand sheets from point sources through sediment transport by gravity currents. Both discrete sand volcanoes and extruded sheets have formed in the same sedimentological setting, with the same trigger for fluidisation and the same source for extruded material, yet they display differing geometries. Sand sheets can form when multiple vents are extruding coevally, causing the gravity currents to coalesce and transport material downslope. If only a single vent is extruding, or coeval vents are spaced large distances apart, a sand volcano(es) or mound(s) will form unless topographic forcing (channelling or a local slope, for example) diverts and focuses the otherwise radial gravity currents resulting in sheet-like deposition of extruded material away from the extrusion site. The observations and mechanisms described in this study can be applied to future models of extrudite formation, facilitating the identification of extruded sand bodies and their differentiation from sands deposited by primary turbidity currents.

8. Facies and fluid flow of sandstone-hosted columnar intrusions.

8.1. Introduction

Large-scale sandstone intrusions have been documented in a wide variety of sedimentological settings. Predominantly described from deep-marine clastic settings as dykes (e.g. Parize and Friès, 2003; Hurst *et al.*, 2005; de Boer *et al.*, 2007; Jackson, 2007; Huuse, 2008), excellent examples also exist from, but are not limited to; shallow marine (e.g. Boehm and Moore, 2002; Thompson *et al.*, 2007; Scott *et al.*, 2009) and desert environments where they display a columnar or pipe-like morphology (e.g. Hannum, 1980; Netoff, 2002; Huuse *et al.*, 2005; Chan *et al.*, 2007; Glennie and Hurst, 2007; Hurst and Glennie, 2008). The recent recognition and description of large sandstone intrusion provinces (Cartwright, 2010) such as the ca. 40,000 km² North Sea Basin province, the 2000 km² Faeroe-Shetland basin intrusion province and the Panoche intrusion complex along a ~150 km lineament in California demonstrates the scale of some provinces. The sandstone intrusions hosted in the Jurassic strata of SE Utah could equally be classified as a large sandstone intrusion province, cropping out over 20,000 km². The intrusions occur in the Carmel Formation and the Gunsight Butte Member of the Entrada Sandstone and are spectacularly exposed at Kodachrome Basin State Park, over an area of ~4 km by 6 km (Fig. 8.1). Those large-sandstone intrusion provinces previously described in the literature are hosted in mudstone, often with associated polygonal and ring faulting (Huuse and Mickelson, 2004; Shoulders *et al.*, 2007; Vigorito *et al.*, 2008; Cartwright, 2010), whereas the intrusions described from the Colorado Plateau in SE Utah are hosted in aeolian sandstones and coastal strata (Hannum, 1980; Netoff, 2002; Huuse *et al.*, 2005; Chan *et al.*, 2007; Hurst *et al.*, 2011). Such sandstone-hosted sandstone intrusion and their flow processes are consequently less well understood, with relatively few studies undertaken (Jonk *et al.*, 2003; Glennie and Hurst, 2007; Hurst and Glennie, 2008; Moreau *et al.*, 2012).

Intrusions pose a challenge to petroleum exploration by acting as seal-bypass systems (Cartwright *et al.*, 2007) and can be difficult to image where sand-bodies are below seismic resolution or display high-angle geometries. However, no study has considered the inherent issues of sandstone intrusions hosted in sandstone-dominated successions and the drilling hazard they may pose. Despite their potential to affect petroleum reservoir character, breach top-seals and act as foci for basinal fluid flow, sandstone-hosted intrusions remain poorly understood in comparison to their mudstone-hosted counterparts in terms of their dynamics and morphologies. The current paradigm for sandstone intrusion formation requires; (i) unconsolidated sand encased in low-permeability mudstone (Huuse *et al.*, 2007); (ii) overpressure within these sands and; (iii) a triggering event, such as an earthquake (Hurst *et al.*, 2011). The intrusions in this study do not meet criteria (i) and therefore a new model for their emplacement is proposed.

By investigation of the SE Utah intrusions exposed in Kodachrome Basin State Park, Utah, this study aims to redress the balance by addressing the following questions: (i) what is the basal limit, or source bed for the intrusions; (ii) do the intrusions display any facies and morphological variation; (iii) what is the flow regime in a sand intrusion and, (iv) how do the intrusions impact fluid flow through the host strata? Intrusions in mudstone are known to act as conduits for basinal fluids which are geochemically and isotopically distinct, suggesting they remain fluid pathways long after emplacement (Hurst *et al.*, 2003; Jonk *et al.*, 2003), but can similar effects be expected in coarse-grained environments with higher overall permeabilities? This study highlights not only the wide variety of facies present in intrusions, but also emphasizes the importance of columnar intrusions as fluid flow conduits in aeolian strata.

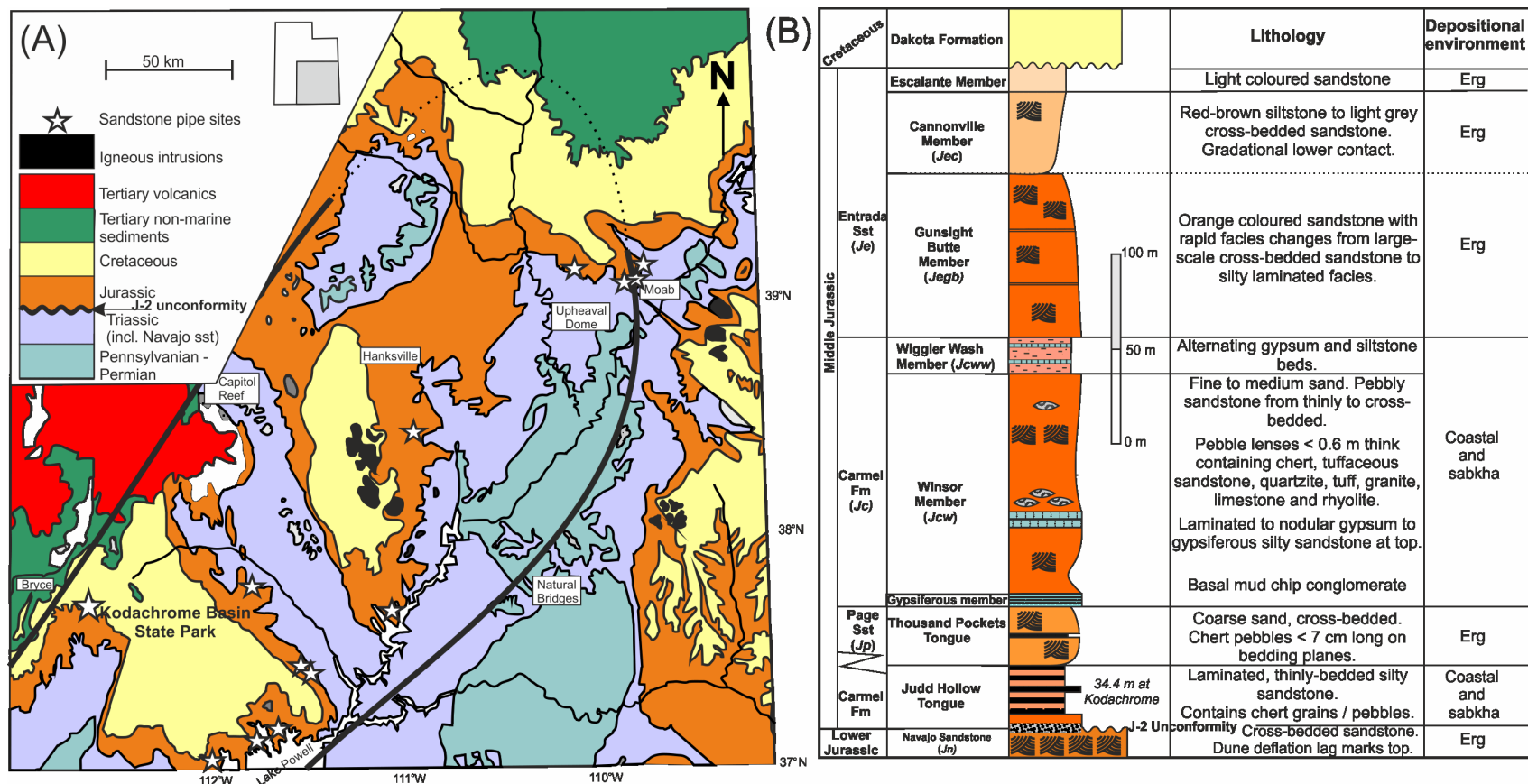


Figure 8.1. (A) Geological map of south-east Utah with sandstone pipe sites. (Modified from Huuse et al., 2005b). Heavy black line denotes the limits of Jurassic ergs (from Blakey, 1988). (B) Lithostratigraphy of the Middle Jurassic at Kodachrome Basin State Park, south central Utah. (Compiled from; Thompson and Stokes, 1970; Hannum, 1979; and Huuse et al., 2005b).

8.1.2. Intrusion Facies

A distinct set of sandstone facies which are intruded into muds has been recognised in core from the Alba Field (North Sea) (Duranti and Hurst, 2004). Facies that record fluidization and injection include; (i) giant pillars, that cut depositional bedding, are internally structureless, and have sharp to gradational boundaries; (ii) structureless sandstone; (iii) mudstone clast breccia, identified by the jigsaw arrangement of micro-fractured, angular mudstone clasts in a structureless sandstone matrix; (iv) sandstone dykes and sills, which are internally homogenous; and (v) dykes showing tabular geometry (Duranti and Hurst 2004). Similar facies are described from the Panoche Intrusion Complex including mudstone breccias and clasts with sandstone-filled microfractures (Scott *et al.*, 2009). Additionally, there is outcrop evidence for remobilisation and intrusion of conglomerates, sourced from deep-water submarine channel complexes and resulting in normally graded sills and dykes (Hubbard *et al.*, 2007).

Excellent 3-D exposure of 59 sandstone pipes in Kodachrome Basin State Park allows for the observation of lithofacies relationships and the geometric relationships between injected sands and the host strata, thus shedding light on sub-surface fluid flow behaviour. This study aims to provide data pertinent to the interpretation of sand hosted injectites and details of their flow processes with comparison to previous models. Detailed descriptions of these pipes have already been provided by Hannum (1980) and additional interpretations by Huuse *et al.* (2005).

8.1.3. Methods

This study is based on mapping of 59 intrusions in Kodachrome Basin State Park and detailed field observations including lithological descriptions, sketches and photographs of the pipes which are either eroded as pinnacles or exposed in cliff faces (**Figure 8.2**). In order to ascertain the diagenetic history of the intrusions., a

Quanta 650 FES scanning electron microscope at the University of Leeds was utilized for microscopic analysis of samples. Representative samples from 3 distinct facies, the host rock and the boundary between an intrusion and the host were analysed under a back-scattered electron microscope (BSE) and scanning-electron microscope (SEM). BSE images and energy-dispersive X-ray spectroscopy (EDS) are utilized to identify mineralogy of grains and cements. Fractured samples of the pipe and boundary facies were stub mounted and coated in 3 gold layers under vacuum for optimal imaging and analysis of pore-filling cements carried out under SEM. Blocks with sufficient competence were mounted in resin and carbon-coated for BSE analysis and calculation of porosity. Minimum flow velocities, flow Reynolds numbers and the energy release required to cause the intrusion are explored by building on existing theoretical approaches.

8.2. Geological Background

Units exposed in Kodachrome Basin State Park are Jurassic erg and sabkha deposits, namely the Carmel Formation (*Jc*) and Entrada Sandstone (*Je*). The Lower Jurassic Navajo Sandstone (*Jn*) is present as regionally extensive subcrop (Peterson and Pipiringos 1979; Blakey *et al.*, 1988; Blakey 1989) and is overlain by the Page Sandstone (*Jp*) (erg) and the Carmel Formation (sabkha, shallow-marine and floodplain deposits) which interfinger in the subsurface below the study area (Fig. 1B, Fig. 2). Separating the Navajo Sandstone and the Middle Jurassic deposits is the regionally extensive J-2 unconformity, defined by a carbonate-cemented chert pebble lag, sometimes reworked into the overlying strata (Thompson and Stokes, 1970; Peterson and Pipiringos, 1979; Blakey, 1989).

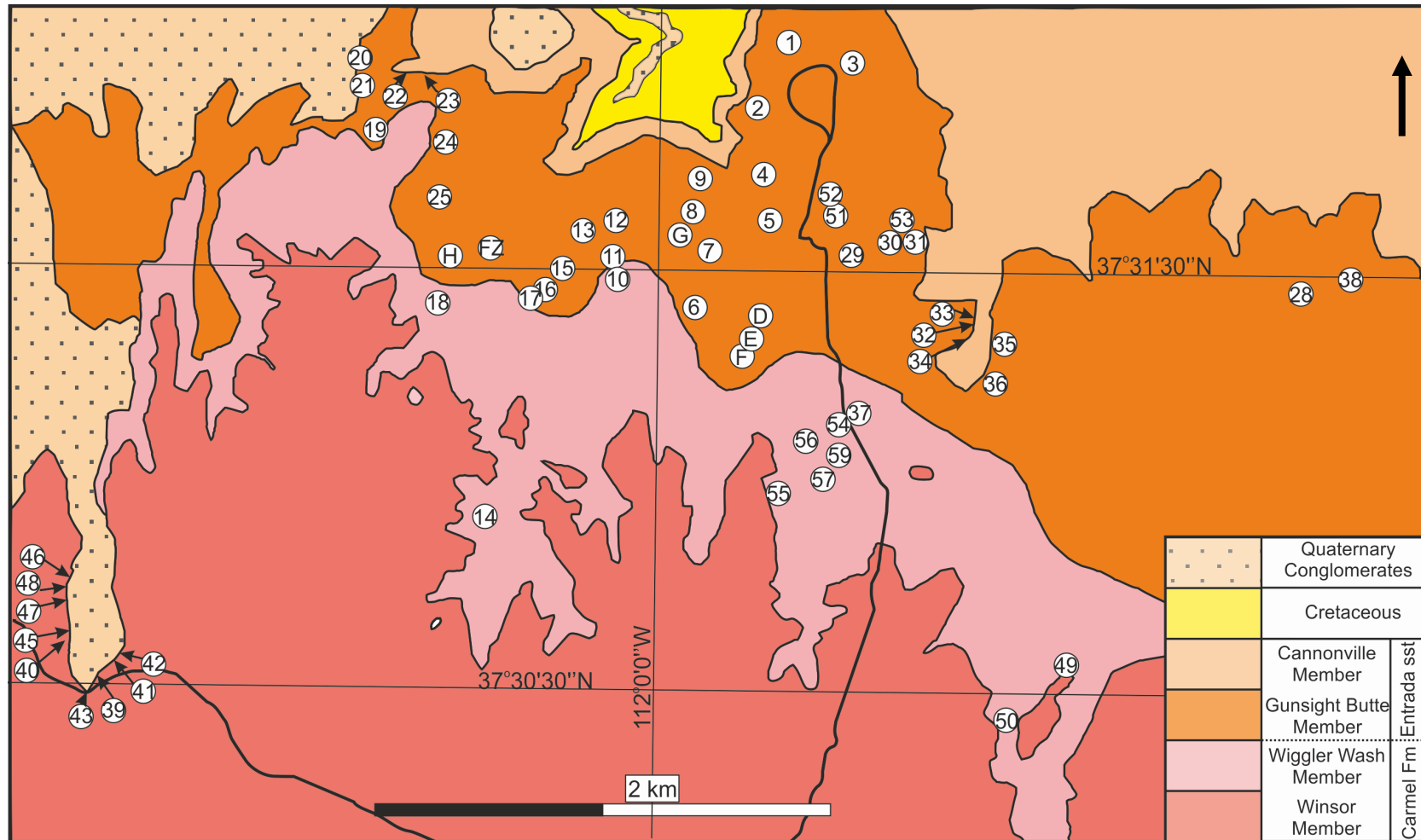


Figure 8.2. Geological Map of the study area with pipes. All pipes occur within the Carmel Formation or Gunsight Butte Member of the Entrada Sandstone. Modified after Doelling *et al.* (2000).

8.2.1. Stratigraphy

Page Sandstone

Page Sandstone

The Thousand Pockets Tongue (*Jptp*) of the Page Sandstone is lithologically similar to the cross-bedded main body of the erg Page Sandstone and interfingers with the Carmel Formation in the study area. The Page Sandstone contains angular pebbles of chert (0.5 to 7 cm long), even where it does not rest directly on the J-2 unconformity. Pebbles generally occur on bedding planes but are most abundant at the base of the formation (Peterson and Pipiringos, 1979).

Carmel Formation

The Carmel Fm is up to 185 m thick (Thompson and Stokes, 1970) and consists of 4 facies. Where the Judd Hollow Tongue (*Jcjh*) of the Carmel Fm lies directly on the Navajo Sandstone it contains scattered to locally concentrated coarse, very coarse and pebbles of sub-angular to angular orange to grey chert (Peterson and Pipiringos, 1979). The Judd Hollow Tongue is laterally equivalent to the western Limestone Member but consists of laminated to thin-bedded silty sandstone (Peterson and Pipiringos, 1979). The Gypsiferous Member (*Jcg*) of the Carmel Fm is made up of laminated to nodular gypsum with intercalated thin limestone beds grading to gypsiferous silty sandstone towards the top of the member. The base is delineated by a localised mud-chip conglomerate (Peterson and Pipiringos, 1979). The Winsor Member (*Jcw*) includes fine to medium grained sandstone, and pebbly sandstone varying from thinly bedded to cross-bedded. Pebble lenses up to 0.6 m thick are found throughout the Winsor Fm and include; rounded to sub-rounded chert; red to light purple tuffaceous sandstone; grey to green quartzite; silicified tuff; porphyritic granite; limestone and rhyolite (Peterson and Pipiringos, 1979; Blakey, 1989). The Wiggler Wash Member (*Jcww*) of the Carmel Fm is 17 m thick in the Kodachrome Basin area and consists of alternating beds of gypsum and siltstone with a limestone cap (Thompson and Stokes, 1970)

Entrada Sandstone

The Entrada is a complicated erg sandstone body which has a large spatial extent. It can be split into three members, the Gunsight Butte, Cannonville and Escalante Members from base to top. These are all exposed in the Kodachrome Basin study area below the pre-Cretaceous unconformity. The distinctly orange coloured Gunsight Butte Member (*Jegb*) averages 100 m thick and has rapid facies changes between large-scale cross bedded sandstone (lower 66.5 m) to silty parallel bedded facies. It contains minor beds of purple coloured shale throughout higher levels (Thompson and Stokes, 1970; Hannum, 1980). The Cannonville Member (*Jec*) has a gradational contact with the underlying *Jegb* and has characteristic red and grey striped banding. Facies range from dark red-brown siltstone to light grey, cross-bedded sandstone with variably coloured friable sandstone (Thompson and Stokes, 1970). The Escalante Member (*Jee*) consists of a light coloured sandstone overlying the medial Entrada unconformity.

Previous work on the large-scale sandstone intrusion of SE Utah has included; description of intrusion elements and the proposition of a cold spring related origin to columnar intrusions in Kodachrome Basin State park (Fig. 1) (Hannum, 1980); studies of large-scale deformation features not limited to, but including intrusive bodies (Chan *et al.*, 2007); discussion of their trigger mechanism (Alvarez *et al.*, 1998; Huuse *et al.*, 2005); and description of pipe outcrop patterns around Glen Canyon (Netoff and Shroba, 2001; Netoff, 2002) (Fig. 1). An extrusive sandstone body covering over 10,000 m² has been recognised in the Entrada Sandstone (Netoff, 2002), showing that at least some of these intrusions did breach the sediment surface. It has largely been agreed that fluidization and injection were likely triggered by seismicity in the late middle Jurassic (Alvarez *et al.*, 1998; Netoff, 2002; Huuse *et al.*, 2005).

8.3. Results

This section describes the major intrusive elements and their lithofacies. Subsequently the relationship between the intrusive architecture and the host strata is examined. Finally microtextural data and evidence for fluid migration through the intrusive facies are described from back-scattered electron (BSE) and scanning electron microscope (SEM) analysis. The intrusion complex is dominated by sandstone columns and pipes and minor small scale dykes, the distribution of which are shown in Figure 8.2. Most pipes occur in the Gunsight Butte Member (*Jegb*) of the Entrada Sandstone with some in the Winsor (*Jcw*) and Wiggler Wash (*Jcww*) members of the Carmel Formation.

8.3.1. Intrusion Facies

Five intrusive facies have been identified: (i) pipe rock (Fig. 8.3 C) which can be subdivided into (a) pipe-rock unassociated with any other facies; (b) mixed with conglomerate; (c) mixed with host or country rock, or (d) comprising the matrix of the clast breccia; (ii) rind rock (Fig 8.4); (iii) cobble and pebble conglomerates (Fig 8.5); (iv) clast breccias with country rock clasts up to 3 m in diameter (Fig 8.6) and (v) homogenised sandstone occurring in discrete zones. These are presented in **Table 8.1**; however, due to the internal variation in the facies and complex association, definite lithofacies associations are not appropriate.

Facies	Description	Occurrence
Pipe Rock	Friable, coarse-grained. Pale grey to cream in colour. Common red to orange chert grains and quartz, volcanoclastic fragments and minor limestone, quartz and gypsum. Some horizontal laminations.	Present in all pipes either as single facies comprising matrix.
Rind rock	Resistant, fine-grained cream in colour. Laminations are parallel to pipe-wall (concentric). Vertical streaking present on outside of pipes.	Forms 30 – 50 mm thick smooth outer wall or rind, of pipes.
Conglomerate <i>Granule (C1)</i> <i>Pebble (C2)</i> <i>Cobble (C3)</i>	C1 – sub-rounded to angular 2-4 mm grains of chert in pipe rock matrix. C2 – sub-rounded 4-64 mm clasts of chert with minor limestone, volcanoclastic and sandstone clasts. Either clast or matrix supported. C3 – well rounded cobbles of varying lithology, volcanoclastics, sandstone and chert are dominant. Clast concentration varies from matrix to clast supported.	Conglomerates occur as bands and streaks in pipes. Clast alignment is common.
Clast Breccia	5 cm to 3 m clasts of underlying lithologies (<i>Jegb</i> , <i>Jcw</i> and pale, bedded sandstone). Clast boundaries are sub-angular to rounded, some show ductile deformation at clast boundaries. Matrix comprises <i>pipe rock</i> .	Two distinct occurrences as; (i) “jig-saw” texture with <i>in situ</i> clasts and pipe rock matrix in close proximity to pipes. Occurs only in silty facies of <i>Jegb</i> and (ii), chaotic breccia in pipes with clearly rotated clasts of varying lithologies.
Homogenous zones	Light pink in colour, fine to medium grained sandstone. Typically massive although dewatering mottling sometimes present.	As metre-scale discrete, funnel-shape zones present in cliffs.

Table 8.1. Facies present within the intrusions.

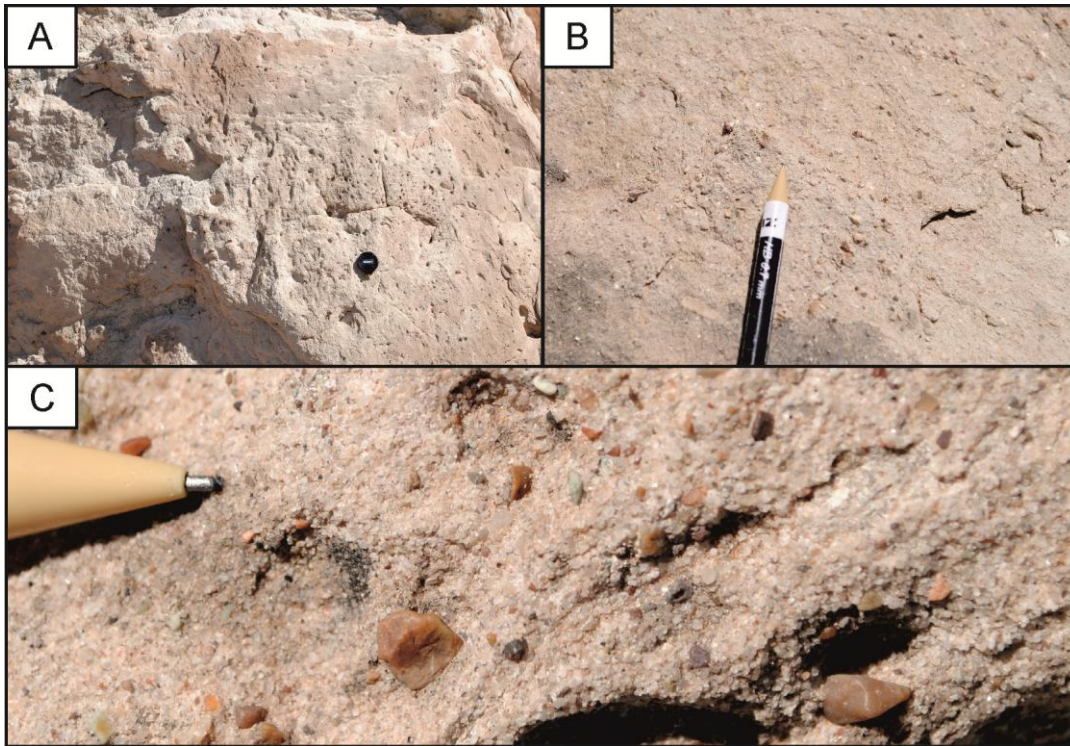


Figure 8.3. Representative photographs of the pipe rock showing (A) homogenous pipe rock, (B) pipe rock with chert grains and (C) chert grains in pipe rock. Lens cap is 5 cm.

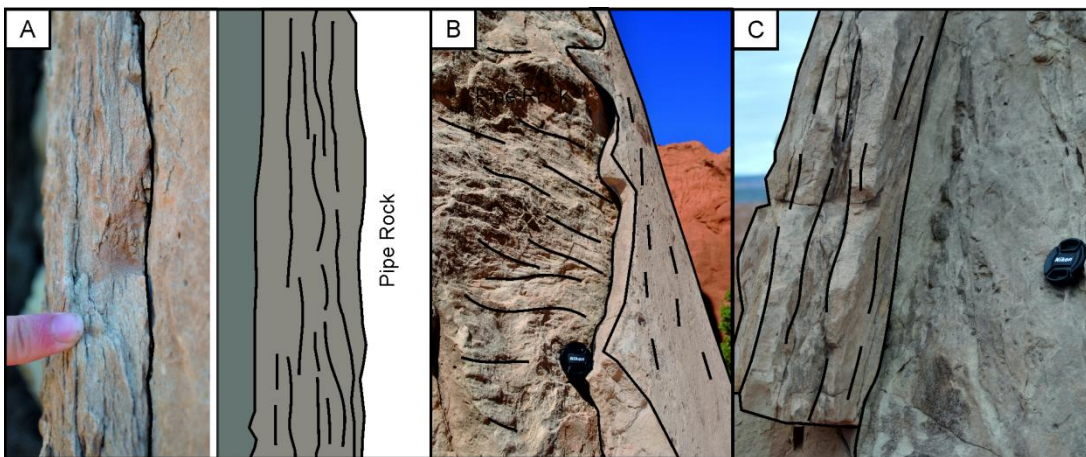


Figure 8.4. Rind Rock (A) Cross-sectional photograph and line interpretation of the rind rock at pipe7 with vertical layering highlighted. (B) Oblique view of resistant rind rock (highlighted) encasing pipe rock at 29. (C) Vertical laminations in rind rock (highlighted) at pipe 53.

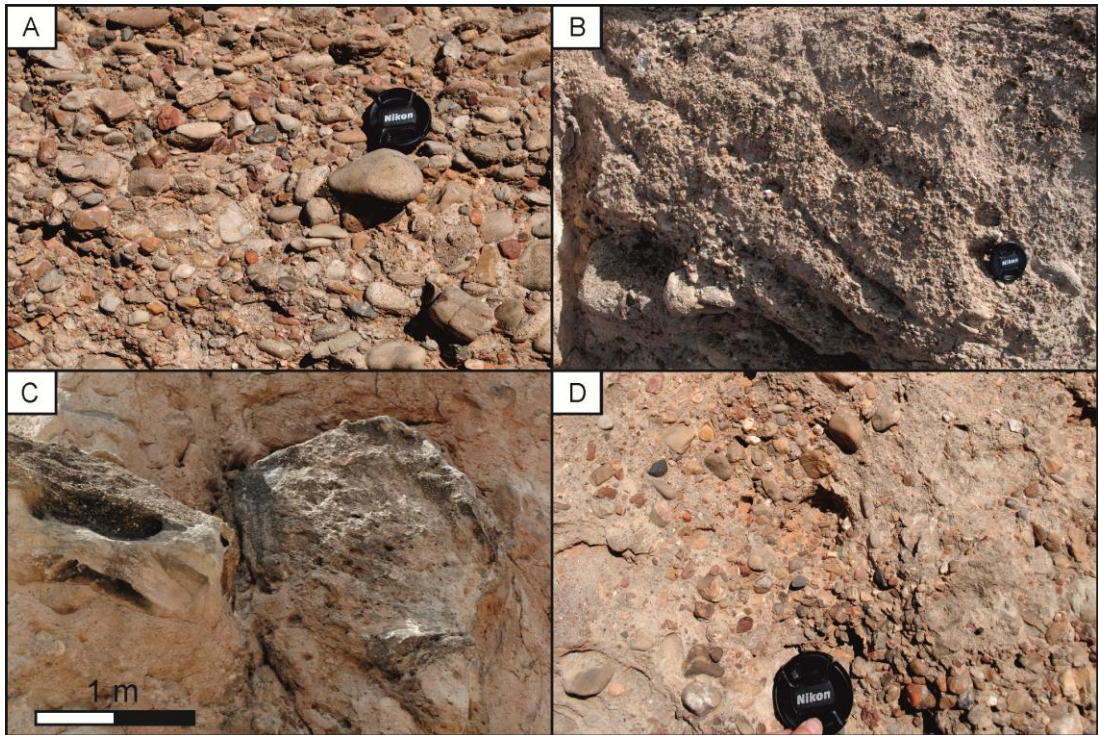


Figure 8.5. (A) Cobble conglomerate in pipe 2. Note imbrication of cobbles. (B) granule conglomerate in pipe 18, (C) “Floating clasts” of conglomerate suspended 8 m above present ground level in pipe rock matrix at pipe 14. (D) Sub-vertical band of pebble conglomerate in pipe 12. Lens cap is 5 cm.

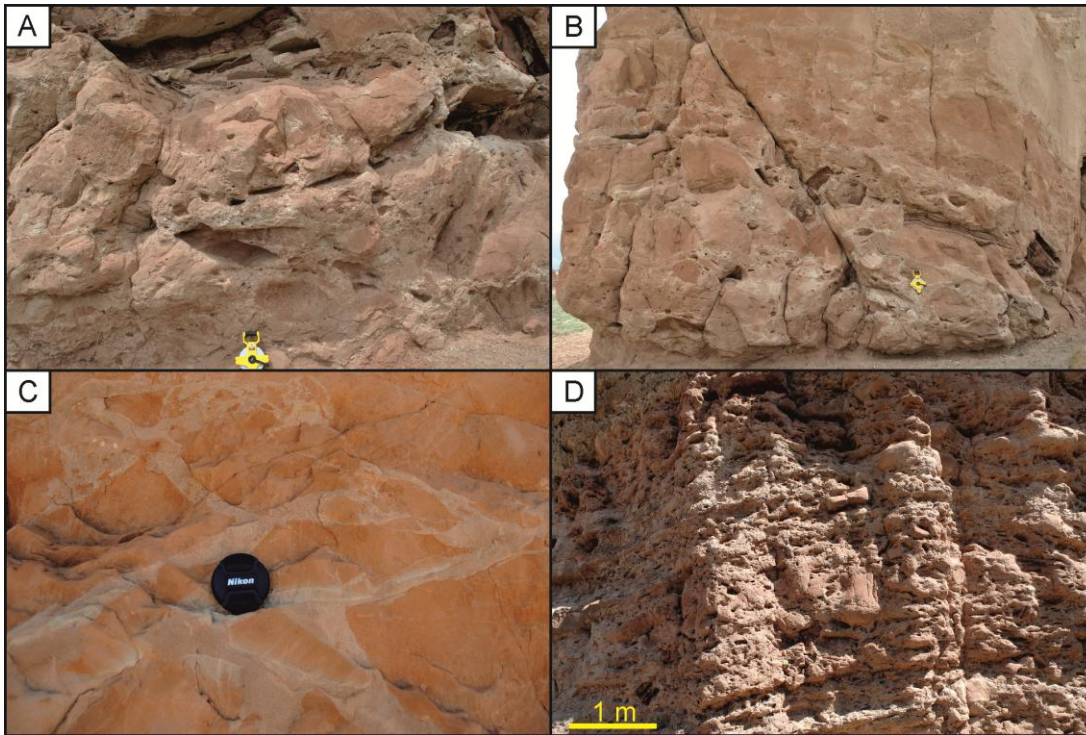


Figure 8.6. (A) Clast breccia in pipe 28 featured 3 m clasts of Carmel Formation (dark brown with desiccation cracks). Tape measure is 30 cm wide. (B) Clast breccia at the present base of pipe 28, (C) Microfractured host Gunsight Butte Member of Entrada Sandstone (orange) at pipe 4. Pipe rock (cream) fills fractures between host clasts, Lens cap is 5 cm. (D) Sub-horizontal alignment of clasts in pipe 18.

8.3.1.1. Other Facies

As the main facies types described in Table 8.1 are in themselves so variable, their end-members often overlap. For example the pipe rock can contain minor clasts of conglomerate or conglomerate clasts, or isolated clasts of country rock, without being classified as a matrix-supported conglomerate or clast breccia respectively. Homogenous *Jegb* containing isolated pockets of pipe rock is common, often occurring in close proximity to large pipes, but also occurring in discrete spires and resistant zones of cliffs. Lastly, isolated clasts of carbonized wood were present in one pipe.

8.3.2. Intrusion Morphology

The intrusions in the study area are far more complex than a simple concentration of fluidization pipes, and the relationship between the pipes and the host strata may allow additional information about the emplacement mechanism of the pipes to be ascertained. The intrusion complex, although dominated by pipes (Figs. 8.7 and 8.8), also contains; i) metre scale sills which are often strongly associated with a pipe (occurring within 10 m of, and often verging towards a pipe (Fig. 8.7D); ii) networks of anastomosing centimetre scale sills which are observed in cliff faces and the *Jegb* surrounding a pipe; iii) cross-over structures, which have both horizontal and vertical flow indicators suggesting a transition between sill and pipe behaviour; and iv) fluidization zones (Fig. 8.7E). This latter expression of fluidization in sandstone intrusions has not previously been described from outcrop.

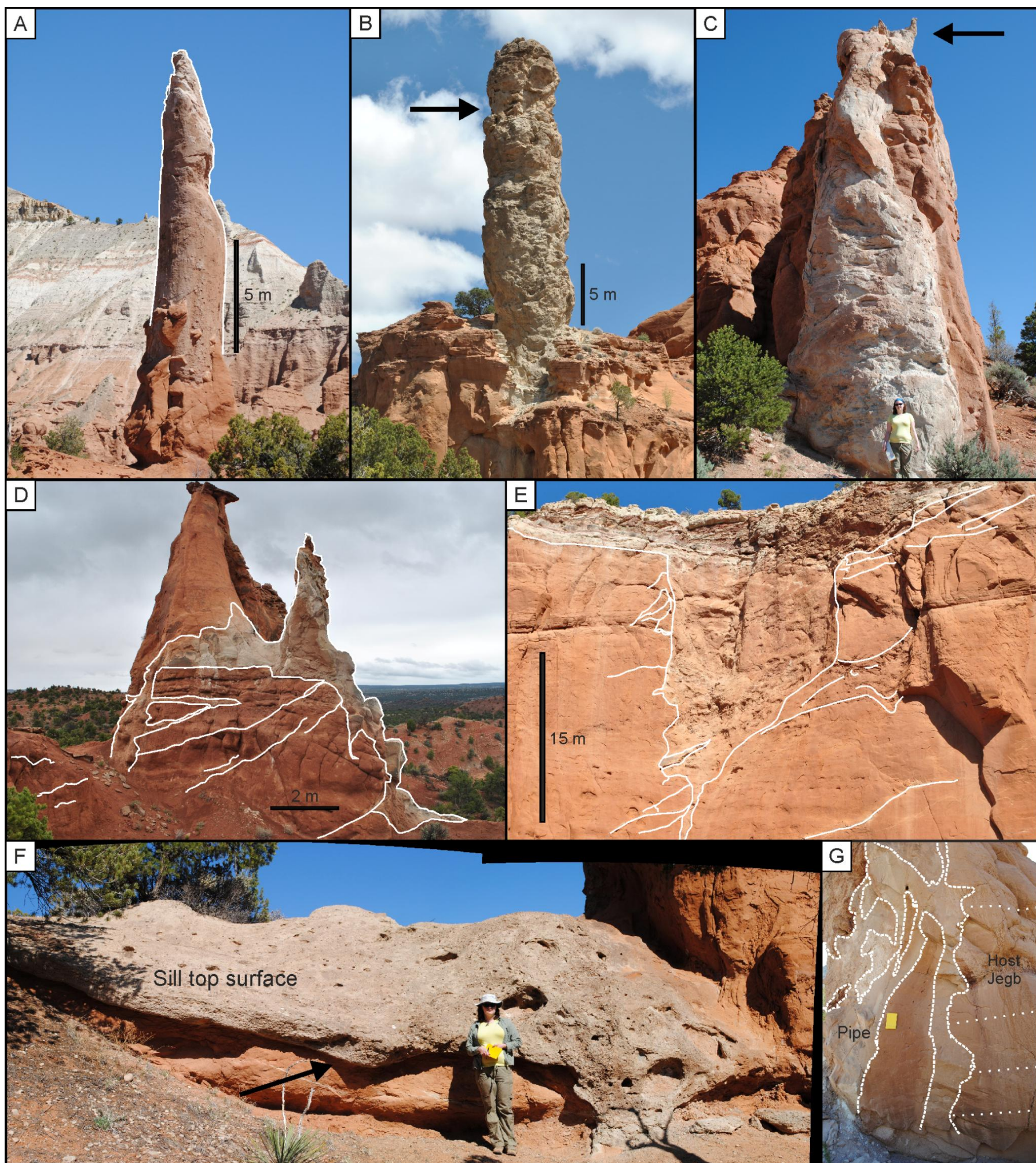


Figure 8.7. Morphologies of the intrusions. (A) Pipe 8, a columnar intrusion with host *Jegb* present at the base of the pipe. (B) Pipe 37 as a columnar intrusion with host *Jegb* at the base. Note feathered edge. Clasts of *Jc* are present at the top of the pipe (arrowed). (C) Pipe 6 showing upward-tapering. Arrow denotes flow becoming horizontal at the top. (D) Pipe 56. Complex intrusion geometry comprising 3 pipes and a connecting sill. Numerous minor injections (highlighted) verge towards the main intrusion. (E) Fluidisation zone (FZ on Fig. 2) in *Jegb*, minor sills verge towards the feature (highlighted). (F) Sill 12. Sill top is inclined towards the viewer. Basal contact undulates and cuts down <30 cm into *Jegb*. Feeder pipe to right of person. (G) Pipe 2. Remnant *Jegb* is present at the base of this pipe, upward bending of the bedding is apparent close to the boundary of the intrusion. Some internal structure within the pipe is visible. A small dyke is associated with this pipe (seen as an elongate ridge), which has a L-shaped geometry in plan view.

8.3.2.1. Fluidisation zones

Fluidization zones were observed only in cliff faces at three localities, 53, 30 and 59 (Fig. 7E) and show a funnel-shaped geometry. Two of these structures are accessible in outcrop and show considerable variation between them. At 30, the fluidized zone is highlighted by the deformation of the surrounding *Jegb*. The surrounding dune cross-stratified beds down-warp towards the 8 m wide fluidization zone, which displays chaotic internal organisation. A minor colour difference between the fluidization zones and surrounding strata enables identification, the fluidized zones appearing lighter in colour with larger grains (< 4 mm) than the surrounding strata. At 53 (Fig. 8.7E) the fluidization zone is at least 15 m from top to base and distinguished by a clear colour contrast with the host *Jegb*. Slumped structures are present and, although inaccessible, breccia clasts are observed in the base of the fluidized zone. Networks of small-scale sills (highlighted in white on Figure 8.7E) verge towards the fluidization zone. The internal organisation of fluidized zones is heterogeneous, with rotational features and a lack of bedding. Networks of cm-scale sills verge towards these features (Figure 8.7E).

8.3.3. Internal Structures

The internal architecture of the intrusions is highly complex with preservation of some flow structures and possible post-fluidization settling structures. Large-scale internal structures are presented in Figure 8.8 and include flow indicators as bed-like structures that are inclined relative to the pipe wall (Fig. 8.8A, C and 8.9 C) and internal slumping (Fig 8.8 D). Pipe 14 (Fig. 8.8A) is a 15 m high structure which is elongate in plan view. The southern limit of the intrusion (right hand side of image) is clast-breccia dominated. The internal structure has five main components from north to south; i) a pipe core at the northern edge composed of pipe rock; ii) multiple bands of alternating conglomerate and homogenous pipe rock which dip towards the pipe core; iii) a sub-vertical zone of conglomerate with floating conglomerate clasts (Fig. 8.5C); iv) a sinuous zone of clast breccia with a sill to pipe

geometry; and v) a relatively homogenous zone of fluidized intruded material and host *Jegb*.

In pipe 28, the basal clast breccia (Fig 8.6B) is unevenly distributed and has an inclined contact with the overlying conglomerate. Clasts of conglomerate suspended in a pipe rock matrix, above layers of conglomerate and pipe rock were observed (Fig. 8.8B). Metre-scale bands of pipe rock that are inclined at 20-60° relative to the pipe-wall may represent an element of vortex-like flow in pipe 29 (Fig. 8.8C). Other features observed in pipes include; i) composite “pipe in pipe” structures where a central core is present within a larger intrusion (Fig. 8.8D), the inner pipe shows possible slumping or flow-relaxation structures; and, ii) the surrounding pipe rock shows vertical to sub-horizontal laminations similar to the rind facies. *In-situ* brecciation of the host *Jegb* is present within 2 m of the pipe boundary at this locality. Smaller scale internal structures as horizontal and inclined bands also record flow structures within the pipes (Figs. 8.8 and 9). The rheological behaviour of the conglomerate appears to be variable between pipes, occurring as coherent clasts (Fig. 8.5C) or zones of strung-out conglomerate (Fig. 8.5D and 8.9A and B), where flow structures have been highlighted) with an apparently ductile response to flow. Figure 8.9C highlights the complex relationship between an intrusion (with internal flow structures) and the fractured host strata.



Figure 8.8. Internal structures of the intrusions. (A) Intrusion 14. A large-scale elongate intrusion. Facing NE. Internal structures suggest flow was from right to left with a sub-vertical component. A pipe core, comprised of Pipe Rock is present to the far left of the intrusion. Alternating bands of conglomerates and clast breccia are present, with a concentration of clast breccia to the right. Homogenous zone of intruded material and host *Jegb* present at top right of intrusion. Other internal structures are highlighted by sub horizontal banding. Person in foreground for scale. (B) Pipe 28, facing SW (left) and NW (right). Clast breccia is present at pipe base, inclined boundary with overlying facies. Upper facies consists of pipe rock with pseudo-banded conglomerates. Large clasts of conglomerate appear to float in the matrix high up in the pipe. There is a suggestion of sub-horizontal clast alignment in the clast breccia; however the dune-bedded sandstone clast on the right highlights the lack of conformity. Person for scale. (C) Pipe 29, facing N, internal structures suggest climbing flow. Flow appears to have been from right to left with a vortex-like component based on the 3D structure of this intrusion. (D) Pipe 51, 5 m wide at base and thins to 2 m at the top. Displays “sagged” laminations in the centre.

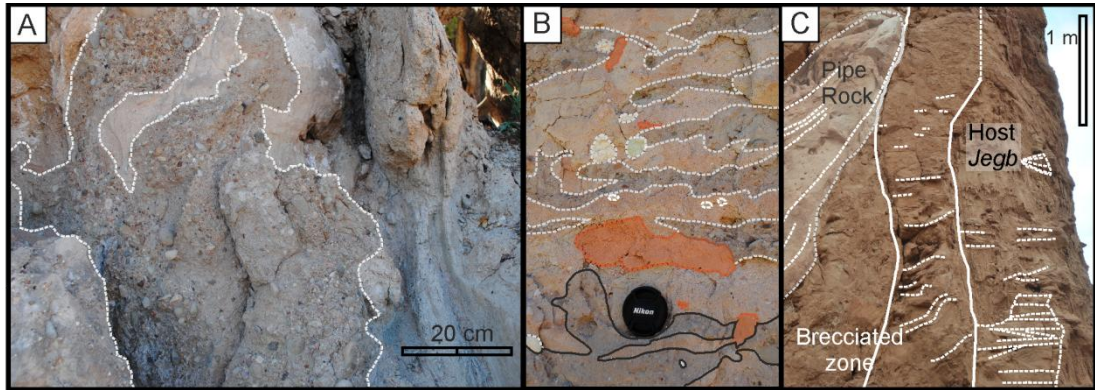


Figure 8.9. (A) Sub-vertical zone of conglomerate (grey) at locality 14, occurring at the transition from sill to pipe. Sub-vertical lamination can be seen in the cream coloured pipe rock to the right of the conglomerate. (B) Sub-horizontal bands of conglomerate (grey) and pipe rock at locality 43. Clasts of limestone (green), and *Jegb* (orange) are present. (C) Complex pipe boundary at locality 30. Bands on pipe rock and brecciated *Jegb* inclined against the pipe wall. The host *Jegb* is also brecciated and dips down towards the pipe boundary.

8.3.4. Intrusion and host relationships

Boundaries between the intrusive facies and the host material vary considerably and can be classified into the following types; linear, non-linear and gradational. Each of the relationships between injected and host material can then be subdivided to demonstrate the variety. It should be noted that pipes do not have vertically consistent diameters, some thinning vertically when cropping-out as pinnacles or in cliff-faces.

8.3.4.1. Linear

Typically, when a pipe is exposed in 3 dimensions as a spire, one side of the pipe will have a linear boundary, whereas the opposing side will be non-linear (Fig. 8.7A). Linear boundaries are characterised by resistant rind-rock or bleaching into

the host *Jegb*. In some cases, alignment of pebble or clasts axes parallel to the pipe wall highlight the contact.

8.2.4.2. Non-linear

Many intrusions have stepped or non-linear boundaries. Morphologies range from an irregular contact with the host rock, where host is incorporated into the pipe, and pipe material is present in the host rock at the boundary, or more organised “stepped” boundaries (Fig. 8.7B). The stepped boundaries display either a repeated inclined-horizontal or feathered geometry. A feathered contact is often associated with the presence of rind-rock, where the concentric laminations parallel to the pipe wall have weathered to produce a steeply inclined stepped morphology (e.g. pipe 37). Some non-linear boundaries are curvilinear, although this boundary type is uncommon. The contacts of sills and low-angle dykes are typically curvilinear; for example, the lower boundary of pipe 14 has an undulating basal contact with 30 cm relief, similar to an erosive scour without associated clast alignment or lamination, and a 20 mm fine-grained horizon at the base of the sill (Fig.8. 7F).

8.3.4.3. Gradational

An uncommon boundary type defined by a lack of discernible contact between intruded and host material such as in pipe 3 (Fig. 8.7G). Here there are multiple vertical bands of pipe rock intercalated with *Jegb*. Colour variations from cream to orange away from the main pipe track the decrease in concentration of pipe rock and concurrent increase in host rock.

8.3.5. SEM data

Table 8.2 presents calculated porosities prior to and including the calcite cement in 3 injected facies, the host *Jegb*, and the boundary zone between a pipe and the *Jegb*. Representative examples from the major facies; pipe rock; rind rock; granule

conglomerate; host *Jegb*, and a gradational boundary are shown in Figure 8.10. Microcrystalline quartz cement is present in the pipe rock, rind rock and boundary samples. Calcite is a late stage as it overgrows the microcrystalline quartz (e.g. Fig 8.10D). The injected facies do not show any clay mineral cementation and only rare ~5 μm detrital clays are observed among pore fillings. The majority of injected grains are quartz and chert, although minor albite grains are scattered throughout. The injected conglomerate (Fig. 8.10E and F) contains oversized pores filled with calcite cement; these are unlikely to have formed post-emplacement as the fluid pressure acting on the grains during transport results in tight packing and therefore we suggest that the pores were cemented by calcite prior to remobilisation of the conglomerate.

Facies	Final porosity (%)	Porosity minus calcite cement (%)
Pipe Rock	5.3	17
Rind	5.6	23
Granule conglomerate	3	-
Boundary	5.2	10
<i>Jegb</i> (host)	7.2	-

Table 8.2. Mean porosities for each facies averaged over 5 samples. Porosity calculated by point counting.

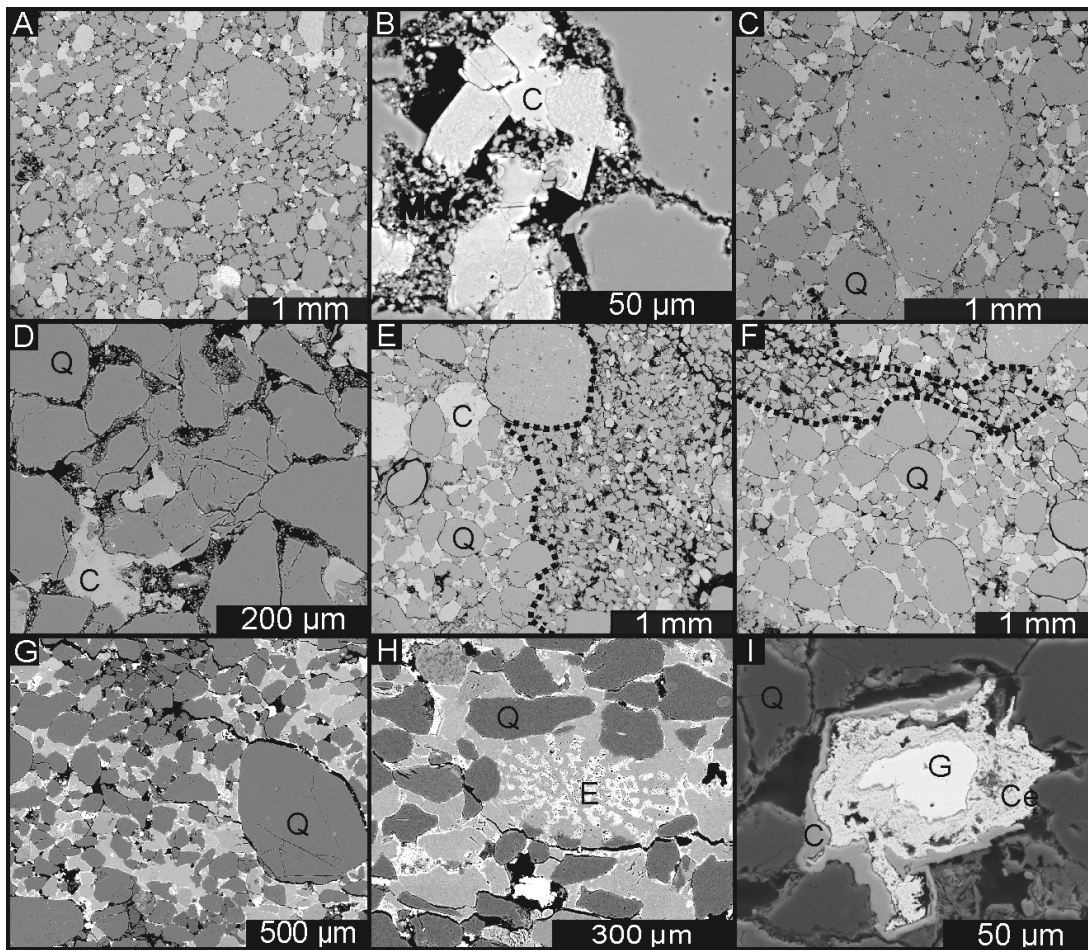


Figure 8.10. Backscattered electron microscope images. (A) Boundary zone between pipe and host. Note bimodal grain size distribution and crude lamination (bottom left to top right). Cement is microcrystalline quartz, MQ, and calcite, C. (B) Late calcite cement overgrowing microcrystalline quartz (MQ) in pore space. (C) Pipe rock. Chert grain in centre. MQ and calcite cement. (D) MQ surrounding quartz, Q, grains and late calcite cement. (E & F) Boundary between granule conglomerate and *Jegb*. Conglomerate is poorly sorted and shows oversized pores filled with calcite cement (pre-transport). Host *Jegb* is poorly cemented with clay minerals. (G) Rind rock. Cement is calcite (light grey) and cerussite (white). Cerussite (PbCO_3) is concentrated in bedding parallel bands. (H) - Echinoid spine, E, in rind facies with calcite and cerussite replacement. (I) Mixed BSE and SE image of detrital galena, G, in the rind facies, with zoned cerussite halo, Ce, which grades into calcite.

Representative examples from the major facies; pipe rock; rind rock; granule conglomerate; host *Jegb*, and a gradational boundary are shown in Figure 10. Microcrystalline quartz cement is present in the pipe rock, rind rock and boundary samples. Calcite is a late stage as it overgrows the microcrystalline quartz (e.g. Fig 8.10D). The injected facies do not show any clay mineral cementation and only rare ~5 µm detrital clays are observed among pore fillings. The majority of injected grains are quartz and chert, although minor albite grains are scattered throughout. The injected conglomerate (Fig. 8.10E and F) contains oversized pores filled with calcite cement; these are unlikely to have formed post-emplacment as the fluid pressure acting on the grains during transport results in tight packing and therefore we suggest that the pores were cemented by calcite prior to remobilisation of the conglomerate.

In Figures 8.10G and H macro-crystalline cerussite (PbCO_3) lines the pore rims of the rind facies, with pore spaces occupied by calcite, suggesting the fluids responsible for precipitating these phases may not have been coeval. Grains of detrital galena < 70 µm diameter are common (e.g., Fig. 8.10I) in the rind facies as a placer-style concentration of the heavy mineral fraction in the fluidized sediment load. The host *Jegb* (Fig. 8.10E and F) is friable in outcrop and hand specimen. SEM analysis shows it is poorly cemented by clay minerals and provides an exemplary juxtaposition with the heavily carbonate-cemented intruded facies.

to be a product of very early diagenesis (Aase *et al.*, 1996). The presence of microcrystalline quartz (1 – 5 µm) as cement was confirmed. The microcrystalline quartz coats the sand grains effectively (Fig. 8.11C and E) and fills pores; it is observed bridging pore-throats between grains (Fig. 8.11A).

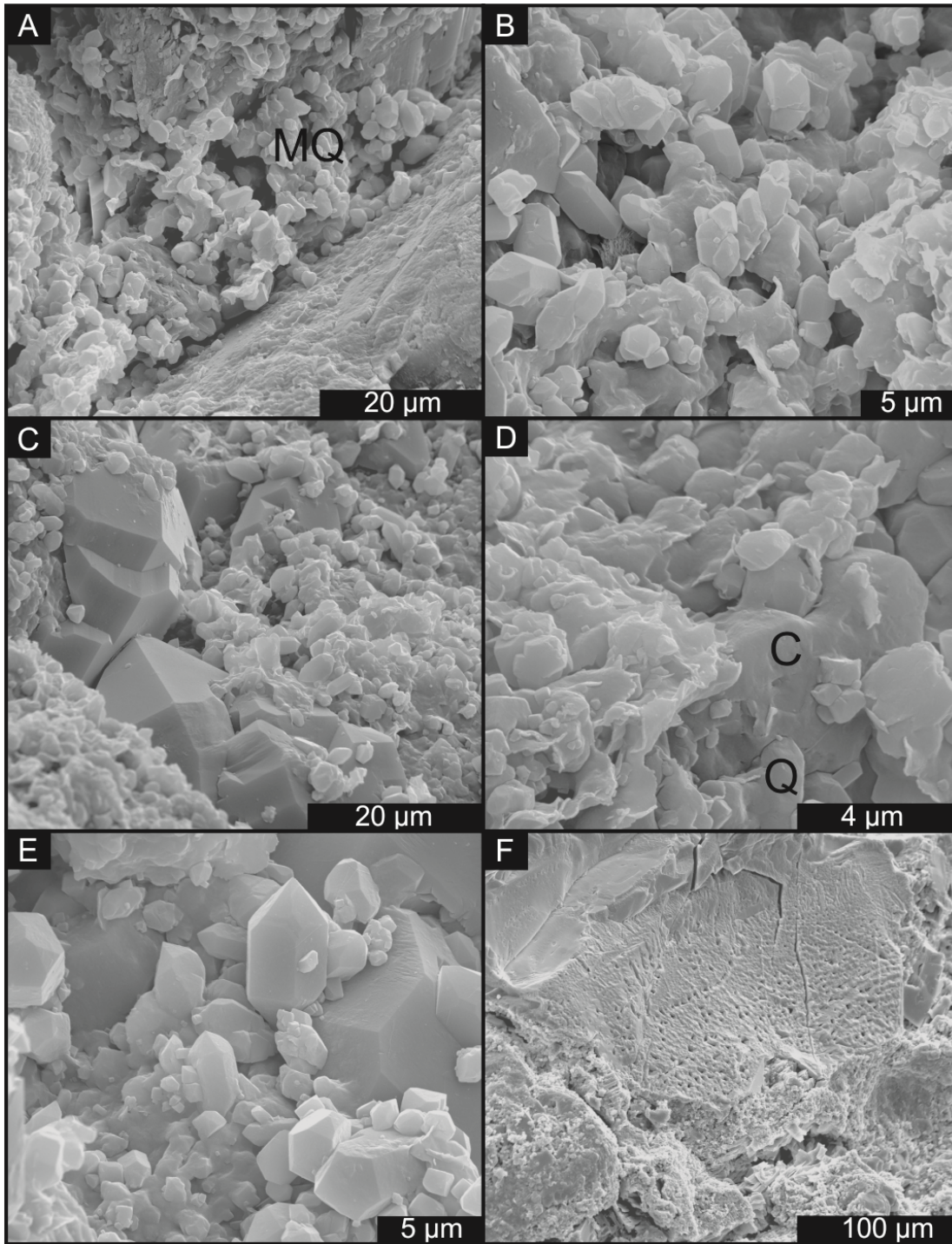


Figure 8.11. Scanning electron microscope images. (A, B & C) Pipe rock at pipe boundary. Shows microcrystalline quartz, MQ, in pore space (A), euhedral 5 μm quartz crystals (B), and MQ overgrowths (C). (D & E) Pipe rock. (D) Calcite shown overgrowing microcrystalline quartz. (E), MQ on grain surface, (F) Grain contact, dissolution of microquartz overgrowths has caused pitting on the grain edge.

Due to sample distribution limitations, it is not possible to confirm the presence of microcrystalline quartz cement in all intruded material. An occurrence of amorphous quartz overgrowing euhedral microcrystalline quartz is shown in Figure 8.11B (centre) suggesting more than one phase of quartz cementation may have occurred. Very minor amounts of detrital clays are present in the samples. Figure 8.11D shows calcite overgrowing microcrystalline quartz although no relationship between amorphous quartz and calcite was observed.

8.4. Discussion

The Jurassic sandstone intrusions exposed in Kodachrome Basin State Park contain an array of lithologies that cannot have been sourced from the Entrada Sandstone, ranging from clean-sandstone and fine-grained rinds to conglomerates and breccias containing exotic lithologies. As the basal extremities of the intrusion complex are unknown, it is necessary to link the facies identified within the pipes to the underlying strata in order to unravel their origin.

8.4.1. Palaeogeography

The Entrada Sandstone overlies a complex and laterally variable coastal dune system and as sedimentary architecture has been suggested to exert a control on the distribution of soft-sediment deformation (Bryant and Miall 2010), the palaeogeography of the Kodachrome region may shed light on the occurrence of large-scale sand intrusions in the area. In the middle Jurassic, the study area lay on the western limit of the Entrada erg, which stretched from NW Arizona to NW Colorado, across Utah (Blakey *et al.*, 1988, Fig. 8.1A). The Western Interior Seaway, also known as the Carmel Seaway episodically flooded the area from the NW (resulting in the deposition of the marine-sabkha Carmel Formation) and ensured a high-water table in the coastal regions of the Entrada erg. Prior to deposition of the Carmel and Entrada Sandstones, the J-2 surface (Fig. 8.1B) had topographic relief of > 10 m due to heterogeneous cementation of the Navajo Sandstone in relation to

perched water tables (Bromley, 1992). Here we suggest these palaeohills and perched aquifers may have acted as loci and fluid sources for the intrusions in the study area, as illustrated in Figure 8.12, and possibly other intrusion sites throughout SE Utah (Huuse *et al.*, 2005b). Horizons of impermeable limestone and evaporitic horizons in the Carmel formation may have provided effective barriers to natural dewatering during consolidation and burial as the overlying Entrada Sandstone was deposited.

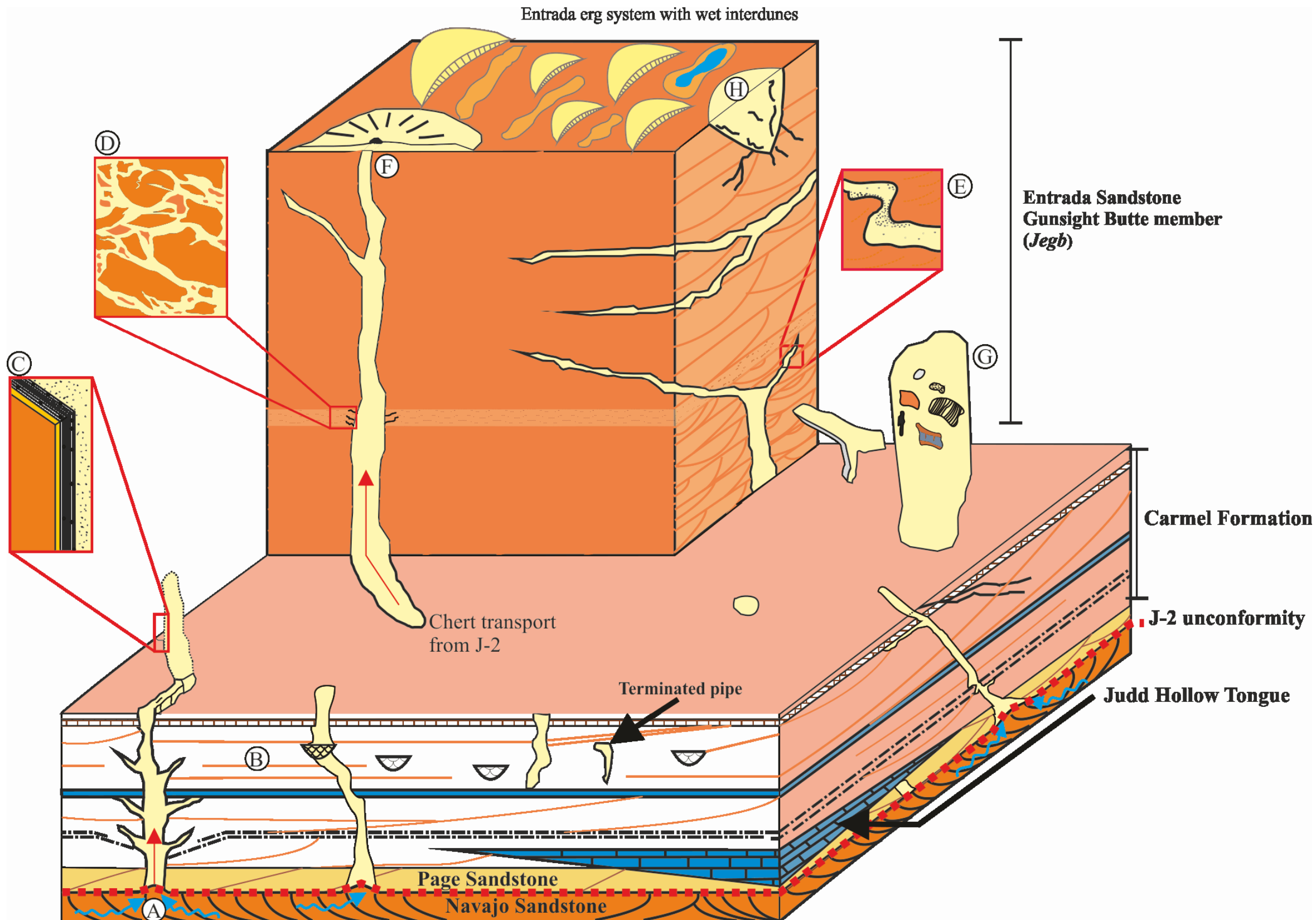


Figure 8.12. Model depicting injection complex architecture and processes. (A) Fluid Flow from Navajo sandstone. (B) Fluidisation and pipe intrusion with preferential exploitation of conglomeratic channels in Carmel Formation. (C) Laminated Rind facies with placer-style accumulation of heavy minerals in concentric laminations. (D) Hydro-fractured clast breccia in silty facies of the Gunsight Butte Member. (E) Normal and reverse grading in sills. (F) - Extrusion (max. pressure gradient). (G) Exotic lithologies suspended in pipes (Page Sandstone, Carmel Formation, chert pebbles from J-2 unconformity). (H) Fluidisation zones possibly representing vents at the palaeosurface.

8.4.2. Origin of the intruded material & timing

Previous studies have not attempted to link the Kodachrome intrusions with a source body (Hannum, 1980; Huuse *et al.*, 2005) as the bases of the intrusions are not fully exposed. However, the internal lithology of the intrusions can be used to reveal how much vertical transport of sediment occurred. The predominant mineralogy of the intrusions is quartz arkose, with limited (<10%) detrital feldspar and lithic fragments. It is however, the occurrence of chert grains and granules in the pipe rock that is crucial to understanding the source of the intruded material. The stratigraphy underlying the study area (Fig. 1A) contains no indication of considerable chert accumulation apart from the regionally extensive J-2 unconformity, a dune-deflation lag some 250 m stratigraphically below the studied horizons (Thompson and Stokes, 1970; Peterson and Pipiringos, 1979; Blakey, 1989). The chert-pebble lag is cemented by carbonate, with oversized pores between grains (O'Sullivan and Pipiringos, 1998); this type of cementation was observed in BSE images (Fig. 10). The chert grains found scattered through the pipe rock are a likely result of disaggregation of J-2 clasts during fluidization and transport as a component of a slurry. Figure 13 demonstrates the range of chert types found in the pipes, which is representative of the chert described from the J-2 unconformity such as; (i) yellow and grey banded chert likely sourced from erosion of the Upper Triassic Chinle Formation (Fig. 13A) (Pipiringos and O'Sullivan, 1975); (ii) red fluted and pitted angular chert from the Navajo Sandstone (Fig. 13B) (Pipiringos and O'Sullivan, 1975) and; (iii) chert with black desert varnish (Fig. 13C) (Pipiringos and O'Sullivan, 1975) indicative of long exposure on the J-2 surface. As no other significant concentration of chert pebbles is present in the subcrop (only locally reworked J2 unconformity chert is present in the Carmel Formation) and given the striking similarity of the chert-pebble lag to the granule conglomerates found in the pipes, it would be reasonable to assume the two are linked, with the J-2 unconformity providing not only barriers to flow and possible generation of overpressure, but an accumulation of chert grains.

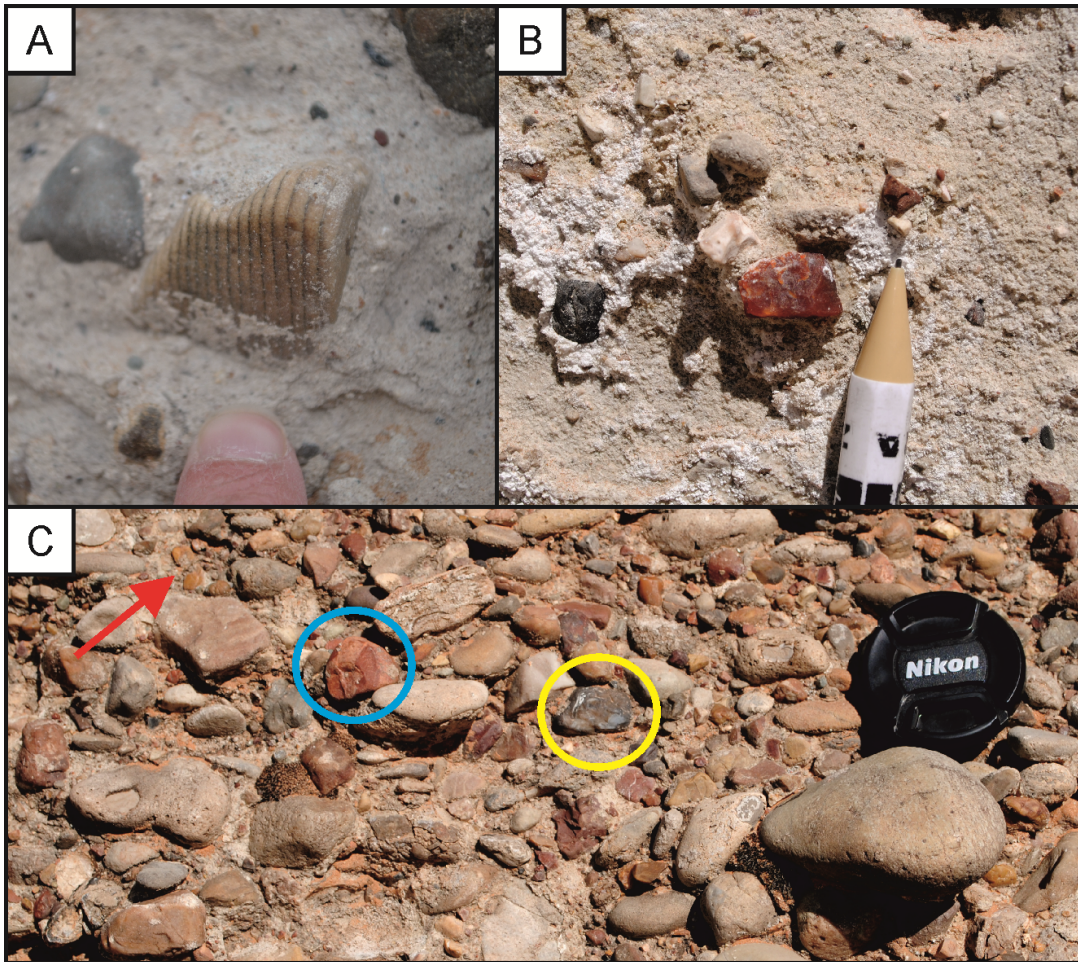


Figure 8.13. Chert types found in the pipes. (A) yellow and grey banded chert in pipe 3. (B) red angular chert in pipe 3. (C) red angular chert (blue circle) rounded chert with black desert varnish (yellow circle) and tan chert (red arrow). Lens cap is 5 cm.

Additionally, fossiliferous material is rare to absent in the Entrada Sandstone, therefore the echinoid spine in Figure 8.10H is likely to be sourced from the underlying Carmel Formation where echinoids and other marine fossils are found (Gillette and Hayden 1997). Clasts of the *Jcw* (Carmel Formation), also reported by Huuse *et al.* (2005), and dune-bedded clean sandstone, presumably from the aeolian Page Sandstone are present within the clast breccia facies; these provide strong evidence for the upwards transport of material in the pipes. Additional evidence for the vertical transport of material from underlying units lies within the cobble

conglomerates found in some pipes and sills (Fig. 8.3). The cobbles in Figure 3A are sub-rounded to rounded, show a wide grain size distribution and are imbricated. Cobbles of this size, roundness and lithological variation would require fluvial conditions for transport. The only evidence for fluvial conditions in the underlying stratigraphy are pebbly isolated channels within the Carmel Formation (Peterson and Pippingos 1979; Blakey 1989) and Page Sandstone, thought to be ephemeral and carrying volcanoclastic remnants as pebbles in a muddy matrix (Jones and Blakey 1997). Additionally, fragments of carbonized wood (coal) found in pipe 22 suggest upwards transport of material from the Carmel Formation as coal is reported from the lower Winsor Member (Doelling and Davis, 1989). Therefore, we suggest that actively intruding, fluidized slurry may have preferentially exploited conglomeratic channels for their higher permeability and porosity than the surrounding aeolian or sabkha facies and thus incorporated the pebbles into the slurry (Fig. 8.12).

Fluidization zones have been shown to occur near a palaeosurface as an expression of venting (Ross *et al.*, 2011) and recycle fluidized sediment in a wide zone of fluidization. The upper limit of the fluidization zones was not observable in the field, although they appear in the upper *Jegb*. Critically, a mega-sand blow has been identified at the top of the Gunsight Butte Member of the Entrada Sandstone (Netoff, 2002) just below the upper Jurassic unconformity between the *Jegb* and *Jec*. As no pipes were observed in the younger Cannonville or Escalante Members of the Entrada, it can be assumed that intrusion occurred before deposition of the Cannonville Member. Decompacted thickness profiles across southern Utah suggest the maximum thickness of the Navajo to Entrada succession was 1.1 km during deposition of the Entrada Sandstone (Bjerrum and Dorsey, 1995). This is in agreement with Jonk (2010) in that sand remobilization and injection is likely at shallow burial depths, < 1 km. When combined with other recent studies of the Jurassic sandstone pipes of southern Utah (Netoff, 2002; Huuse *et al.*, 2005) we can unequivocally state that upwards transport of material occurred during large-scale

fluidization of erg sands. This is in contrast with previous studies which suggest that the pipes are collapse and breccia pipes (Hannum, 1980; Doelling and Davis, 1989).

8.4.3. Particle segregation in fluidization pipes

Although the rind facies is broadly similar to the pipe rock, the concentric laminations and differential cementation suggest differing emplacement conditions. Similar features have been reported surrounding fluidization pipes and termed “fluidization haloes” (Mount, 1993) and have been modelled in physical experiments as a fine-grained lining on pipe edges (Ross *et al.*, 2011). Fine-grained margins are common in sandstone dykes where they are thought to form due to the shear between the dyke wall and the flow (Diggs, 2007; Kazerouni *et al.*, 2011). The similarity between the characteristics of the rind on the pipes and features modelled by Ross *et al.* (2011) suggest similar formation processes. Therefore, we suggest the fine-grained rind forms not only due to shear, but also due to the difference in flow velocity, turbulence and pressure between the pipe and the surrounding country rock, which forces finer grains in the pipe into the pore-spaces of the host rock. This accretion style will produce the concentric lamination seen in outcrop and is thought to stabilise pipes and may also account for the placer-style concentration of heavy minerals in this facies. The development and preservation of placers requires long-term sediment aggradation in sustained flow, such as a stream and the small, dense heavy minerals are concentrated in the viscous sub-layer (Carling and Breakspear, 2006). This concentration of galena in the rind, and the complexity and lack of understanding of shear-zone sorting across density gradients (Kazerouni *et al.*, 2011), leads us to propose turbophoresis to be a dominant factor in heavy mineral sorting at the pipe walls. Turbophoresis is a common phenomenon in vertical fluidization pipes observed in chemical engineering, which results in fluidized particles migrating in the direction of decreasing turbulence, towards the viscous sub-layer at pipe walls (Picano *et al.*, 2009). Turbophoresis is dependent on particle inertia (Reeks, 1983), therefore, galena grains having higher inertia than the

surrounding quartz of equal grain size (Fig. 8.10I), are more susceptible to turbophoresis and thus accumulation at the pipe walls. Consequently, the concentric accretion of the rind facies and incorporation of heavy minerals by hydraulic separation into the rind, suggests the pipes were stable, and venting fluidized material for an appreciable duration before flow waned.

8.4.4. Initial intrusion and microfracturing

Microfracturing, “jigsaw” fabric, and *in situ* brecciation of host rocks has been reported from other studies of intrusion facies, but only in mudstone hosts where it has been attributed to *in-situ* hydraulic fracturing of the host rock, with fluidized sand infilling the induced fractures and isolating host rock clasts (Duranti and Hurst 2004). The differing styles of incorporation of the host rock into the intrusions from microfractured *Jegb* to being fully assimilated into the pipe rock may be related to the complex facies within the Entrada Sandstone. The *Jegb* is predominantly aeolian, with minor silty facies and distinctive bands of shale. One occurrence of transported Entrada Sandstone showed intense deformation of the bedding with upturned clast margins and corresponding internal bedding, suggesting the Entrada Sandstone was not fully consolidated at the time of intrusion and subsequent clast transport. This is in contrast with some clasts that contain considerable amounts of cream coloured pipe rock in a network of microfractures (Fig. 8.6C). As the permeability of the host significantly affects how sand injectites intrude (Baer, 1991; Jonk, 2010), where the host rock is highly permeable (> 1 Darcy, (Bear, 1972)) an intruding slurry is likely to fluidize the host and create a mixed slurry of host and intruded sediment. Studies of igneous dyke propagation into poorly cemented porous sandstone have demonstrated that significant fluidization of the host rock by hydrothermal fluids occurs at the fracture tip (Baer, 1991). In contrast, where permeability is less, microfracturing occurs, leading to brecciation. Therefore, the rapid vertical and lateral facies changes in the *Jegb* account for both the microfractured *Jegb* clasts arranged in a jigsaw texture

(silty facies) and fully assimilated zones of homogenous pink mixed *Jegb* and pipe facies (cross bedded facies).

This mechanism however, does not explain the presence of 3 m clasts of *Jcw* (Fig. 8.6A) and dune-bedded clean sandstone clasts, presumably sourced from the aeolian Page Sandstone, in concentrated zones of breccia where the clasts have no preferred orientation. These differing occurrences of breccia suggest two formation mechanisms; (i) *in-situ* hydraulic fracturing of silty *Jegb*, resulting in brecciation and representing early-stages of intrusion with no discernible vertical transport, and; (ii) transport of clasts in fluidized slurry which are preserved as layers of breccias in the pipes due to batch sedimentation processes and grain jamming as the overpressure is released and vertical transport ceases (Corwin *et al.*, 2005; Di Felice, 2010).

8.4.5. Flow regimes in pipes

The preservation of dynamic fluidization flow structures and settling related slumping in pipe cores must first be distinguished as they record very different sediment transport processes. This discussion will focus on the dynamic structures. Figure 8.8A shows progressive stages of pipe emplacement and stabilisation in an elongate intrusion. In experimental fluidization, sand through sand fluidization pipes have been shown to migrate laterally through unconsolidated strata by erosion on the leading edge of pipes (Ross *et al.*, 2011), in contrast to the hydrofracturing and subsequent slurry emplacement mechanism suggested for mudstones (Hurst *et al.*, 2011). The internal architecture of intrusion 14 (Fig. 8.8A) records the temporal evolution of the intrusions, suggesting progressive emplacement from right to left in the figure, with a pipe core representing the stabilised pipe, possibly venting the slurry out onto a palaeosurface. The bed-scale lineations at angles up to 30° relative to the pipe walls, which comprise the internal structure of some pipes (Figs. 8.8C and 8.9C), can be traced in 3 dimensions spiralling up the pipe. These may represent vortex-like flow in the slurry, whereas

laminar flow would be expected to form vertical laminations parallel to pipe walls, such as in the pipe rock facies. The smaller, metre-scale structures composed of strung-out conglomerates and vertically laminated pipe rock found inside the pipes may also point toward highly turbulent flow which disaggregates the semi-consolidated conglomerates and incorporates the matrix and chert pebbles into the pipe rock (Fig. 8.9A and B). The sub-horizontally banded conglomerate and pipe rock may be interpreted as a settling structure, formed during waning flow (Fig. 8.9B), however, fluidization pipes may transport sediment as plugs of clast-rich slurry, interspersed with fluid or less concentrated slurry (Di Felice, 2010) and therefore, this process mechanism may also account for the layered appearance of some pipes (Fig. 8.8B). The clast-supported nature and imbrication of the intruded conglomerates (Fig. 8.5A) suggests traction was an important factor in governing clast deposition and settling. As the velocity of the slurry decreased during emplacement, the grains and clasts entrained will transition from a flowing slurry to a critical threshold where the fluid can no longer support the grains in the flow and they will geometrically lock (*sensu* Corwin *et al.*, 2005; Sherry *et al.*, 2012). This jamming threshold will be reached for the large clasts before the sand grains and may be responsible for the clast-supported nature of the breccias. Where internal structures indicate downward movement of sediment in the pipe (e.g. Fig. 8.8D), significant downward movement of the slurry may have occurred before the jamming threshold was reached. Pipes composed entirely of the pipe rock facies display these downwarped structures, indicating that the presence of large clasts and conglomerates may initiate jamming at an early point in slurry deceleration, preventing significant downward movement of the slurry before the grains lock. The large tabular breccia clasts in the pipes are typically orientated with the long-axis approximately perpendicular to the expected vertical flow direction (Figs. 8.6A and D). Fluidization experiments and computational fluid dynamics combined with discrete element modelling show that prolate spheroids (*i.e.* tabulate blocks) tend to be orientated with their maximum projection area perpendicular to the direction of transport (Zhou *et al.*, 2011). Alternative explanations for the orientation and clustering of tabulate clasts such as *in situ* hydraulic fracturing are untenable given

the evidence from exotic clasts for long-distance sediment transport. This suggests that the clasts of *Jegb* and *Jcw* have been entrained in a fluidised slurry (Fig. 8.6A, B and D). This sub-horizontal layering of clasts perpendicular to flow direction has not been described from mudstone-hosted sandstone intrusions, perhaps due to the sub-vertical or inclined nature of many of these intrusions and associated flow, or due to the absence of more tabulate clasts.

Appreciable (< 20 m) funnel-shaped areas of cliff faces appear to be structureless near some pipes (11 and 10) suggesting fluidization of these areas has occurred and the sediment homogenised. Figure 8.7E shows where stratigraphy has been erased by fluidization in such an area. Similar features were produced in analogue experiments by Ross *et al.* (2011) and may be representative of pipes intersecting with the sediment surface. In these zones, discharge rates from fluidization pipes were not high enough to carry sediment above the pipe-surface interface and recirculation of sediment occurred in a wide zone. The chaotic organisation of the interior of fluidization zones (Fig. 8.7E) bears a strong resemblance to the cone-shaped vents of Ross *et al.* (2011) that recorded a fluidization pipe breaching the sediment surface, but did not produce surface expressions of extrusion. Analogue experiment investigations into the genesis of maar diatremes produced similar, funnel-shape structures with chaotic internal organisation (*e.g.* Woolsey *et al.*, 1975; Walters *et al.*, 2006). Sub-aqueous sand extrusions often have good preservation potential (Ross *et al.*, 2013) whereas sub-aerial extrusions, especially those in desert environments are either uniquely preserved (Loope *et al.* 2013) or removed by wind erosion (Bryant and Miall, 2010).

8.4.6. Flow regime and velocity during sand injection

The internal structures preserved in the pipes demonstrate considerable spatial and temporal variation in flow during intrusion. Estimates of the flow regime in active intrusions range from viscous laminar (Taylor, 1982) to fully turbulent, with

estimates of Reynolds numbers up to 89×10^6 (Duranti and Hurst, 2004; Scott *et al.*, 2009; Sherry *et al.*, 2012). The velocity of the rising suspension can be estimated as it must be equal to, or greater than, the terminal fall velocity of the largest clast in the system. Stokes' law is inappropriate in this situation as it is only valid for particles up to $100 \mu\text{m}$ (Allen, 1985) and vastly overestimates settling velocities for larger particles; by a factor of more than 10 for particles $> 1 \text{ mm}$ diameter (Gregory, 2006). Duranti and Hurst (2004), followed by Scott *et al.* (2009) and Sherry *et al.* (2012) provide a theoretical basis for calculations where flow velocity is calculated using the terminal settling velocity of the largest clast in the system, which must be at least equivalent to the fluid velocity and is derived from the square root law of Allen (1985):

$$U = k \left(\frac{\rho_s - \rho_f}{\rho_f} g D \right)^{0.5} \quad (8.1)$$

where ρ_f is the ambient fluid density, ρ_s is the particle density, g is gravity, D is the particle diameter, and k is given by:

$$k = \frac{4}{3} C_{D,0} \quad (8.2)$$

where $C_{D,0}$ is the drag coefficient for a solitary sphere in a fluid with a particulate concentration of zero, taken as a constant of 0.45 (Allen, 1985), and ρ_f is taken as the density of the ambient fluid, in this case that of the pseudo-fluid; the average fluid-particulate density (Duranti and Hurst, 2004; Scott *et al.*, 2009; Sherry *et al.*, 2012). The pseudo-fluid density (ρ_{pf}) of the suspension of sand and water, in this case, the fluid and the smaller (sand-grade or finer) particles, is calculated herein using the approach of Di Felice (2010).

$$\rho_{pf} = \varphi_s^* \rho_s + (1 - \varphi_s^*) \rho_f \quad (8.3)$$

And:

$$\varphi_s^* = \frac{\varphi_s}{1 - \varphi_L} \quad (8.4)$$

For a homogenous fluidising suspension with a φ_s of 20%, φ_L of 0.01%, sand density of 2500 kg m⁻³, and water density of 1000 kg m⁻³, the pseudo-fluid density is therefore 1300 kg m⁻³.

Equation 8.1 is only valid for single, spherical particles settling in a stagnant fluid, a fundamental limitation when considering particles in a fluidised system. Furthermore, as noted above, the value of k in *Equation 8.2* (Duranti and Hurst, 2004; Scott *et al.*, 2009; Sherry *et al.*, 2012) is calculated using a drag coefficient based on a particulate concentration of zero ($C_{D,0}$) rather than that of the pseudo-fluid itself. In the limiting case of a particle free fluid, the value of 0.45 for $C_{D,0}$ is only valid for small spheres, whereas $C_{D,0}$ for coarse, natural particles is approximately 1.4 (Gregory, 2006). Therefore we propose the implementation of *Equation 8.5* (Allen, 1985) which incorporates the effects of a particle settling through a fluid of a given particle concentration:

$$U = \left(\frac{4(1-\varphi)^{2n}(\rho_L - \rho_{pf})gD}{3 C_D \rho_{pf}} \right)^{0.5} \quad (8.5)$$

Where φ is the solid volume concentration, and C_D in the fluidised system is given by (Allen, 1985):

$$C_D = C_{D,0}/(1 - \varphi_s)^{2n-2} \quad (8.6)$$

The exponent n is a function of particle shape (Richardson and Zaki, 1954):

$$n = 2.7k_s^{0.16} \quad (8.7)$$

Where k_s is a volumetric shape factor which must be calculated from the particle dimensions (Richardson and Zaki, 1954):

$$k_s = \left(\frac{\pi}{6} \right) \left(\frac{D_s^3}{D_c^3} \right) \quad (8.8)$$

Where D_s is the diameter of a sphere with the same volume as the particle and D_c is the diameter of a circle of the same area as the projected profile of the particle in its most stable orientation (Richardson and Zaki, 1954).

It is now possible to recalculate the flow velocity estimates of Scott *et al.* (2009) using their 3 models of varying particle concentration with C_D calculated from measurements of their largest clast (section 8.6 *Appendix*) and recalculation of the fluid density using the approach of Di Felice (2010) (*Equations 8.3 and 8.4*) and subsequently, the flow velocity (*Equation 8.5*). This reveals that the previous calculations of Scott *et al.* (2009) have overestimated the minimum flow velocity by up to two orders of magnitude (Table 8.3).

Parameter	Values of Scott et al.			Values calculated		
	(2009)			herein		
Clast diameter (m)	0.7	0.7	0.7	0.7	0.7	0.7
Clast density (kg m ⁻³)	2298	2298	2298	2298	2298	2298
Grain concentration (%)	54	30	15	54	30	15
Fluid density (kg m ⁻³)	1891	1495	1247.5	1864	1480	1240
n	-	-	-	3.58	3.58	3.58
C_D	0.45	0.45	0.45	76.96	8.81	3.23
Minimum velocity (m s ⁻¹)	2.41	6.01	9.43	0.01	0.21	0.87

Table 8.3. Minimum settling velocities for a clast diameter of 0.7 m as a function of grain concentration in the pseudo-fluid, for the example in Scott *et al.* (2009).

Sherry *et al.* (2012) also test the flow velocities provided by Scott *et al.* (2009) who employed the equations of Duranti & Hurst (2004) as it is recognized therein that the fluid viscosities provided by Scott *et al.* (2009) are incorrect, leading Sherry *et al.* (2012) to calculate terminal settling velocities of clasts to be 2-4 ms⁻¹ based upon unspecified fluid densities. However, using the approach adopted herein with an equation based upon a grain falling through a fluid of a given concentration,

terminal fall velocities are still reduced by up to two orders of magnitude over the estimates of Sherry *et al.* (2012).

Using the new approach outlined above, minimum flow velocities for the largest observed clast (3 m, Fig. 6A) in an injectite pipe in the Kodachrome Basin complex can be calculated (*Appendix III*) and are presented in **Table 8.4**.

Parameter	Grain concentration	Grain concentration	Grain concentration
	54%	30%	15%
Clast diameter (m)	3	3	3
Clast density (kg m⁻³)	1875	1875	1875
Pseudofluid density (kg m⁻³)	1864	1480	1240
n	2.26	2.26	2.26
C_D	9.91	3.44	2.11
Minimum velocity (m s⁻¹)	0.026	0.78	2.14

Table 8.4. Minimum settling velocities for a clast diameter of 3 m through a pseudo-fluid of varying particle concentrations, for a pipe in the Kodachrome Basin.

8.4.7. Flow Reynolds numbers

Fluid velocities will decrease as particle concentrations in the pseudo-fluid increase, due to increased drag, hence the need to calculate C_D according to the particle concentration and not assume an arbitrary value based on Re values for drag on a solitary particle in a stagnant fluid. Using the particle concentration in the fluidised flow, we can calculate the density and viscosity of the fluid responsible for

transporting the large clast, using the approach of Di Felice (2010) and thus the Reynolds number (Re) of the flow. Previous estimates of Re by Scott *et al.* (2009) show highly turbulent flow ($Re = 2.1 \times 10^6$ to 89.8×10^6) at grain concentrations (ϕ) of 0.54 and 0.15 respectively. Flow Reynolds numbers (Equation 8.9) for the example in Scott *et al.*, (2009) are recalculated using this approach and presented in **Table 8.5** (section 8.6 Appendix).

$$Re = \frac{(U \cdot A \cdot \rho_{pf})}{\mu_{pf}} \quad (8.9)$$

Where A is the pipe aperture and μ_{pf} is the dynamic viscosity of the pseudo fluid.

$$\mu_{pf} = \mu_f * (1 - \phi_s^*)^{-2.8} \quad (8.10)$$

Parameter	Values of Scott <i>et al.</i> (2009)			Values calculated herein		
Fracture aperture (m)	6.25	6.25	6.25	6.25	6.25	6.25
Grain concentration (%)	54	30	15	54	30	15
Fluid density (kg m ⁻³)	1891	1495	1247.5	1864	1480	1240
Fluid viscosity (Pa·S)	0.026	0.003	0.001	0.008	0.0024	0.0014
Minimum velocity (m s ⁻¹)	2.41	6.01	9.43	0.01	0.21	0.87
Re	2.1×10^6	3.68×10^7	8.98×10^7	1.54×10^4	8.09×10^5	4.80×10^6

Table 8.5. Recalculated minimum flow velocities and flow Reynolds numbers for the data in Scott *et al.* (2009) showing that values have dropped by up to 2 orders of magnitude.

At high grain concentrations (ϕ 0.54) the flow Reynolds number of Scott *et al.* (2009) is reduced by 2 orders of magnitude and is not as overwhelmingly turbulent as originally proposed, but is still turbulent rather than laminar supporting the field observations. This drastic reduction in flow Reynolds numbers is primarily due to the increased drag coefficient. Solid-solid interactions in a fluidized flow are negligible up to volume fractions ϕ 0.5, above which solid-solid interactions are likely to become dominant (Di Felice, 2010). However, an order of magnitude difference is still present at the lowest volume fraction, thus demonstrating the impact of fluid viscosity on the calculated Reynolds number. Moreover, the Re values calculated are all for examples where the injection has been shown or assumed to have breached the surface (Duranti and Hurst, 2004; Scott *et al.*, 2009), thus providing the maximum potential pressure gradient between the source and surface. For examples where the surface is not breached during injection, velocities may be lower and the correlative Re values may slip into the laminar flow regime. This is in broad agreement with the conclusion drawn by Sherry *et al.* (2012) that Reynolds numbers will decrease and possibly reflect a laminar flow regime as the fluid velocity decreases in the waning stages of injection. However, the deductions in the study of Sherry *et al.* (2012) were based upon velocities calculated using a range of viscosities from 1-30 Pa·s, unstated fluid densities, and the square root law of Allen (1985) as first implemented by Duranti and Hurst (2004), our *Equation 8.1*, which we have shown to be an inappropriate realization of the problem. Hence, although it was recognized that the fluid viscosity values required more accurate determination, the highest fluid viscosity calculated herein is 8 Pa·s, significantly lower than the highest estimate of 30 Pa·s (Sherry *et al.*, 2012) and therefore we are unable to confirm the Reynolds numbers calculated therein.

Using the approach outlined above, flow Reynolds numbers for the flow regime in the Kodachrome Basin pipes can be calculated (**Table 8.6**) (*section 8.6 Appendix*).

Parameter			
Fracture aperture (m)	5	5	5
Grain concentration (%)	54	30	15
Fluid density (kg m ⁻³)	1864	1480	1240
Fluid viscosity (Pa·S)	0.0078	0.0024	0.0014
Minimum velocity (m s ⁻¹)	0.03	0.78	2.14
Re	3.13×10^4	2.39×10^6	9.45×10^6

Table 8.6. Calculated Reynolds numbers (Re) for grain concentrations of $\phi_s = 0.54$, $\phi_s = 0.30$ and $\phi_s = 0.15$ for a pipe in the Kodachrome Basin.

8.4.8. Energy release and triggering mechanism

An extrusive element to the intrusions of SE Utah as described by Netoff (2002) generates the maximum possible pressure gradient between the overpressured fluid source and the surface. This enables calculation of the total volumetric flow rate through the injections and a step towards comprehending how much sediment may have been transported. If average pipe radius is 3.5 m and total length is 250 m, the total volume of the Kodachrome intrusion complex = volume of 1 pipe \times 59 = $9625 \times 59 = 5.67 \times 10^5$ m³. Assuming 20% porosity in the injected sandstone (**Table 8.2**) the volume of sand in the intrusion is 4.54×10^5 m³. At the maximum calculated flow rate (1.38 ms⁻¹) it would take ~90 seconds to emplace all the sand in the intrusion complex as currently exposed. This estimate of time taken to intrude the sand is a minimum as the upper termini of the pipes are not observed and many may have been eroded, or did not breach the surface. It is now possible to calculate the energy

required to uplift this mass of sand using the elegant approach of Duranti (2007) where the potential energy ($E_{pot(e)}$) is the buoyant lift acting on the sand grains, given by:

$$E_{pot(e)} = V_d(1 - \varphi)\rho_q g h_{(c)} \quad (8.11)$$

Where V_d is the volume of the injected sand grains, ρ_q is the density of quartz and $h_{(c)}$ is $H/3$ and H the height of the pipe. Therefore the total energy required to uplift $4.54 \times 10^5 \text{ m}^3$ of sand is $8.3 \times 10^{12} \text{ J}$. This estimate is conservative considering the modest estimate of volume.

Huuse *et al.* (2005b) considered the distribution of sandstone pipes in the Entrada Sandstone across the Colorado Plateau and determined that they formed due to a regionally synchronous event rather than individual responses to localized triggers. It is known that the heterogeneous facies distribution in wet ergs (Mountney, 2012) can impact their style of soft-sediment deformation (Bryant and Miall, 2010) and Huuse *et al.* (2005b) suggest that pipes were emplaced as a response to a seismic trigger, and that an earthquake of at least $M_w \geq 7$ would be required to trigger liquefaction in susceptible sediments over the areal extent of the Colorado Plateau intrusion complex. The amount of energy calculated to emplace the sandstone intrusions in Kodachrome Basin State Park is equivalent to an earthquake $M_w = 5.4$ if 100% of the energy is imparted into the injection process. If only 1/1000th of the total energy of an earthquake was required to emplace the Kodachrome Basin complex the earthquake responsible would be $M_w = 7.4$, with the fluidisation event lasting at least 90 seconds once the surface had been breached. Three earthquakes of M_w 7-8 triggered liquefaction over 10,000 km^2 along a 100 km lineament in the New Madrid seismic zone (Obermeier, 1996), demonstrating that large-scale sediment remobilization can be triggered by earthquakes of the magnitude calculated. Deformation and sandstone intrusions associated with Upheaval Dome in Utah may have been triggered by bolide-impact (Alvarez *et al.*, 1998), for which estimates of energy range from 0.7 to $25 \times 10^{16} \text{ J}$ (Melosh, 1989). Therefore we can add validity

to the suggestion of Huuse *et al.* (2005b) who showed that the injection could have been triggered by seismicity in the late Middle Jurassic and suggest that similar estimates could be provided for other clusters of sandstone intrusions elsewhere in the intrusion complex.

8.4.9. Post Intrusion Fluid Flow

From **Table 8.2**, it is clear that late stage precipitation of calcite cement has greatly reduced the porosities of the injected facies. For example the pipe rock had a mean initial porosity of 17%, including the microcrystalline cement. Microcrystalline cements are unusual and are thought to be important in preserving porosity of sandstones during burial as they inhibit growth of authigenic quartz cements (Aase *et al.*, 1996; Weibel *et al.*, 2010). Their precipitation in the pore spaces of the intruded facies is possibly related to the elutriation of clay minerals from the system, as phyllosilicate dissolution and overgrowths and grain-coatings of clay minerals do not occur. Where microcrystalline quartz has previously been described, it occurs in close association with biogenic silica such as sponge spicules and is thought to originate from their dissolution (Fisher *et al.*, 2000). Sponge spicule dissolution releases water, resulting in sandstone with oversized pores and, due to the microcrystalline quartz coating the grains, increased resistance to compaction (Fisher *et al.*, 1999).

The presence of an echinoid spine made of calcite in the Rind facies (Fig. 8.10H); likely sourced from the underlying shallow-marine Carmel Formation (Davidson, 1967) suggests other marine fossils may have been transported. The microcrystalline quartz may have originated *in-situ* from silcretes, a common duricrust in arid environments and known to occur in the Navajo Sandstone palaeohills (Bromley, 1992) however, the euhedral nature of the microcrystalline quartz crystals (Fig. 8.11) implies they are authigenic and have not been transported in a fluidisation pipe, and thus the microcrystalline quartz cement post-dates intrusion emplacement.

Oversized pores in the calcite-cemented granule conglomerate facies must have been present prior to transport. The presence of placer-style deposition of detrital galena grains in the vertically laminated rind-rock shows later remobilization of Pb by oxidising fluids. A carbonate bearing fluid has leached Pb from galena to form cerussite (PbCO_3) both *in situ* and through pore spaces. The overgrowth relationships of the cements in the injected facies suggest the following fluid history:

- Precipitation of microcrystalline quartz (MQ) cement
- Precipitation of amorphous silica overgrowing MQ (Fig. 8.11B)
- Leaching of detrital galena to precipitate cerussite in rind facies (requires low pH)
- Precipitation of calcite cement (requires a slightly higher pH than cerussite).

The precipitation of cerussite and calcite consecutively suggests extraformational fluids were exploiting the pipes themselves, rather than the host *Jegb* or any ring faults or internal deformation bands (Jonk *et al.*, 2005).

Previous investigations into the effect of sandstone intrusions on post-intrusion fluid flow have been limited to mudstone-hosted examples (Mazzini *et al.*, 2003; Jonk *et al.*, 2005; Scott *et al.*, 2009; Sherry *et al.*, 2012) with the exception of Jonk *et al.* (2005) which studied sandstone hosted intrusions. Post-intrusion fluid flow has been shown to alter not only the granular texture of the intruded sand (Scott *et al.*, 2009; Sherry *et al.*, 2012), but also exerts control on the porosity and permeability of the intrusion through precipitation of multiphase cements (Jonk *et al.*, 2005). Sandstone intrusions will have an inherently higher porosity and permeability than the mudstone in which they are encased; therefore it is not unexpected that they become preferential conduits for the migration of hydrocarbon and basinal fluids long after their emplacement (Huuse *et al.*, 2005; Jonk *et al.*, 2005). However, only the study of Jonk *et al.* (2003) addresses the effect of sandstone-hosted intrusions on

basinal-fluid flow and found that; although the injection process was driven by geochemically distinct hot fluids, the host and injected sandstones displayed the same diagenetic sequence following emplacement. Therefore, this study is the first to report geochemically distinct fluids exploiting sandstone intrusions in a sand-dominated succession; however, detailed geochemical analysis is beyond the scope of this chapter.

8.4.10. Implications for petroleum exploration

If a series of pipes of comparable internal complexity were to be cored in the subsurface, identification of the facies and subsequent determination of their origin may prove a recondite task. For identification of sandstone-hosted clastic intrusions in core and spatially limited outcrop, the recognition of associations of facies is a key factor in their correct interpretation. Transitions between host sandstone and a vertically laminated fine-grained facies may indicate the presence of an intrusion. Although the remobilised sediment within the pipe may appear lithologically similar to the host, a sudden change in fabric may indicate fault-induced juxtaposition, or remobilisation and injection of fluidised sediment. Sandstone-hosted intrusions will not act as stratigraphic traps for hydrocarbon accumulations in the same way as their mudstone-hosted counterparts due to the porous and permeable host rock, but their presence significantly increases uncertainty regarding seal-integrity, fluid migration and drilling safety. However, they can also enhance inter- and intra- reservoir connectivity; the intrusions in this study provide a direct and highly porous and permeable pathway between the Navajo and Entrada Sandstones.

8.5. Conclusions

The sandstone intrusions studied herein record injection of an unsteady turbulent sediment-water mixture which transported material from the Page Sandstone, Carmel Formation and Entrada Sandstone in excess of 200 m towards the palaeosurface. The flow velocities during injection are estimated to be between $0.026 - 2.138 \text{ ms}^{-1}$ and calculated flow Reynolds numbers show that flow was turbulent. During fluidization, heavy minerals were separated and sorted to the pipe margins, resulting in placer-style concentrations encased in fine-grained sand. Petrographic data reveal multiple stages of cementation with microcrystalline quartz precipitating early and at low temperatures, preserving porosity in the intrusions until extraformational fluids exploited the pipes as preferential flow pathways despite the relatively high porosity and permeability of the host sandstone. Sandstone intrusions hosted in sand-dominated successions remain largely unrecognised compared to their mudstone-hosted counterparts, in part because they are problematic to image in seismic data, however, this study shows they may play a key role in the fluid history of continental successions. The internal facies of such sandstone-hosted intrusions can be extremely varied, depending on the nature of the underlying and host stratigraphy making their identification a significant challenge from well and core data.

8.6. Appendix

Assuming that the clast is a trapezoid prism; $n = 3.58$ can be calculated from

Equations 7-8 using the following parameters:

Parameter	Value
H (cm)	39
B1(cm)	20
B2(cm)	70
L (cm)	20
Partial H (cm)	35
Volume (cm ³)	103967
Surface area (cm ²)	7690
D _s	58.33
D _c	78.98
K _s	5.91

Calculation of pseudofluid viscosity and density from Scott *et al.* (2009) using Equations 3, 4 and 10.

Small particle concentration (ϕ_s)	0.54	0.3	0.15
Large particle concentration (ϕ_L)	0.0001	0.0001	0.0001
Large particle density (kg m ⁻³)	2298	2298	2298
Small particle density (kg m ⁻³)	2600	2600	2600
Pseudofluid density (kg m ⁻³)	1864	1480	1240
Pseudofluid viscosity (Pa·sec)	0.0078	0.0024	0.0014

These values are then used to calculate the Reynolds number

$$Re = (U * A * \rho_{pf}) / \mu_{pf}$$

Parameter	Values of Scott <i>et al.</i> (2009)			Values calculated herein		
Clast diameter (m)	0.7	0.7	0.7	0.7	0.7	0.7
Pipe Aperture (m)	6.25	6.25	6.25	6.25	6.25	6.25
Large particle density (kg m ⁻³)	2298	2298	2298	2298	2298	2298
Small particle density (kg m ⁻³)	-	-	-	2600	2600	2600
Grain concentration (%)	54	30	15	54	30	15
Pseudofluid density (kg m ⁻³)	1891	1495	1247.5	1864	1480	1240
Pseudofluid viscosity (Pa Sec)	0.026	0.003	0.001	0.008	0.0024	0.0014
<i>N</i>	-	-	-	3.58	3.58	3.58
<i>C_{D,0}</i>	-	-	-	1.4	1.4	1.4
<i>C_D</i>	0.45	0.45	0.45	76.96	8.81	3.23
Velocity (m sec ⁻¹)	2.41	6.01	9.43	0.01	0.21	0.87
Re	2.1 x 10 ⁶	3.68 x 10 ⁷	8.98 x 10 ⁷	1.54 x 10 ⁴	8.09 x 10 ⁵	4.80 x 10 ⁶

Parameters used to calculate flow velocity and Reynolds numbers for the Kodachrome Basin intrusion complex.

Bulk density of an oblong Carmel Formation clast based on 25% porosity and sabkha facies = 1875 kg m⁻³.

Height (cm)	100
Length (cm)	300
Depth (cm)	150
Volume (cm ³)	4500000
Surface area (cm ²)	45000
D _s	204
D _c	239
K _s	0.32
<i>n</i>	2.25

Parameter			
φ _s	0.54	0.3	0.15
φ _L	0.0001	0.0001	0.0001
Q _L (kg m ⁻³)	1875	1875	1875
Q _s (kg m ⁻³)	2600	2600	2600
Aperture (m)	5	5	5
C _{D,0}	1.4	1.4	1.4
C _D	9.91	3.44	2.11
Q _{pf}	1864	1480	1240
μ _{pf}	0.0078	0.0024	0.0014
D (m)	3	3	3
Velocity (m sec ⁻¹)	0.026	0.779	2.138
Re	3.13 × 10 ⁴	2.39 × 10 ⁶	9.45 × 10 ⁶

9. Sandstone- and mudstone-hosted intrusions, a comparative analysis: geometry, facies, processes, and fluid flow.

9.1. Introduction

The research presented in this thesis incorporates a multidisciplinary approach towards understanding the underlying processes of the formation, dynamics and sedimentology of shallow sand injections in sub-aqueous environments and sand injection into coarse-grained sequences. Four investigative approaches were employed and were presented in Chapters 5-8:

- (i) Experimental modelling of shallow clastic injection in cohesionless sediments.
- (ii) Application of particle-imaging-velocimetry techniques to fluidisation pipes.
- (iii) The analysis of extruded sandstone volcanoes and sheets on an ancient seafloor.
- (iv) The analysis of a large-scale sandstone intrusion complex hosted in coarse-grained strata.

This thesis has not attempted to cover the process of sand injection in all depositional environments, but instead has made advances in determining the flow regime during sand injection and how that impacts grain entrainment and subsequently, the interaction between an injection and the host sediment on a range of scales. The chapters herein cover; (i) an introduction to mudstone-hosted sandstone intrusions; (ii) experimental sand injection in shallow, cohesionless sands; (iii) experimental sand extrusion; (iv) ancient sandstone extrusions resulting from shallow sand injection in fine-grained sand and; (v) sandstone-hosted

sandstone intrusions. Other scenarios, such as shallow sand injection in unconsolidated muds have not been examined (e.g. Strachan, 2002) and others have not been described, for instance sub-aqueous examples of sandstone-hosted sandstone intrusion complexes. This synthesis will integrate the findings of this thesis with the current understanding of sandstone intrusions in order to place this research in a wider context and highlight the advances made herein. **Figure 9.1** demonstrates some of the key differences and similarities in intrusions in sub-aqueous mudstone-hosted, sub-aqueous sandstone-hosted and sub-aerial sandstone-hosted sandstone intrusions.

9.2. Architectural elements of clastic intrusions.

The four elements of a mudstone-hosted sandstone intrusion complex: parent sand bodies, dikes, sills and extrudites are well defined and can be distinguished. This concept was introduced in Chapter 2 (Figure 9.2).

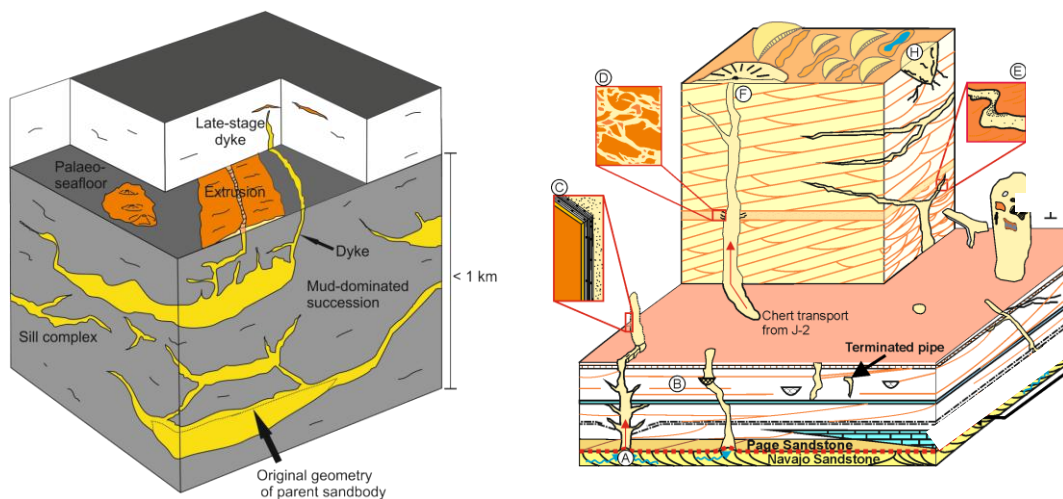


Figure 9.2. Tripartite architecture of mudstone-hosted intrusions (left, from Hurst *et al.*, 2011) and bipartite architecture of sandstone-hosted intrusions.

The elements of sandstone-hosted intrusions are somewhat more difficult to assign architectural elements. Parent sandbodies have not been defined in any previous study and cannot be definitively identified in Chapter 8. In the Kodachrome examples the base of the injection complex may be at the level of the J-2 unconformity, but a lack of observable basal pipe contacts means parent sand bodies cannot be identified. The base of pipes described from aeolian strata by Loope *et al.*, (2013) are associated with broken laminations and up-warped strata, and there is no indication of wholesale remobilization and injection of the parent sand which is associated with mudstone-hosted intrusions. Due to the highly erosive nature of injection in cohesionless sediments, a large proportion of the sediment in the intrusion is sourced from the host material, hence why translation of a large volume of sediment from a parent sand body is not required to emplace the sediment in the pipes of Loope *et al.*, (2013) or the intrusion in Kodachrome Basin.

There are some similarities between sandstone-hosted sandstone intrusions and hydrothermal vent complexes, which are often cylindrical and associated hydrofracturing of the host rock results in increased brecciation of the host which is incorporated into the conduit (Svenson *et al.*, 2006). This is a similar mechanism to that developed in Chapter 8 (**Figure 9.2**) to explain angular clasts of the Carmel Formation that have been brecciated by hydrofracturing and uplifted to younger stratigraphic levels by fluidisation pipes. The model proposed in Chapter 5 outlines the basic architecture of intrusions in coarse-grained hosts, comprising a pipe with a sharp basal contact and a vent, which represents the intersection between the pipe and the sediment-water or sediment-air interface. The geometry of the vent is dependent on the nature of that interface which in turn, controls the behaviour of the extruded material. Thus, without identifiable parent sand bodies, sandstone-hosted intrusions can be described as having a bipartite architecture with an intrusive and an extrusive element.

9.3. Distribution of sandstone intrusions

The model of shallow sand injection in non-cohesive sediments developed in Chapter 5 suggests that breaching of the impermeable horizon by migrating fluids results in a self-organising system of dewatering pipes that entrain and fluidise grains from the host strata. A similar model, albeit on a larger scale is proposed for the intrusions in SE Utah where overpressure was released by upwards injection of sediment and occurred as clusters of pipes (Netoff, 2002; Huuse *et al.*, 2005; Chan *et al.*, 2007). Mudstone-hosted sandstone intrusions have been used to determine the palaeostress regime at the time of emplacement by examining their preferred orientation (Boehm and Moore, 2002). Vertical distribution of the intrusive elements of mudstone-hosted intrusions (Vigorito and Hurst, 2008; Vetel and Cartwright, 2010), are using the geometry of an injection (sill or dyke) to predict the stratigraphic level of the injection at the time of emplacement (**Figure 9.3**) although the significance of these relationships has not been tested in other sandstone-hosted sandstone intrusion complexes. The base of the “sill zone” of the Panoche Giant Injection Complex (PGIC), a mudstone-hosted sandstone intrusion complex where sills are the dominant intrusion type, is thought to be related to the thickness of the overburden (Vigorito and Hurst, 2010).

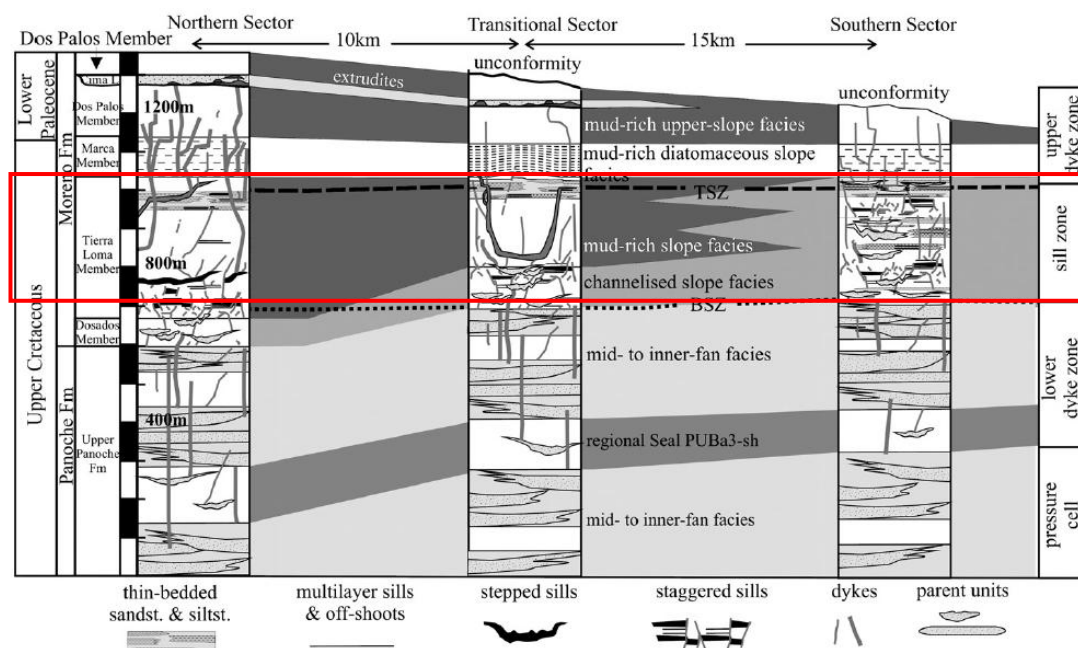


Figure 9.3. Summary of the relationship between host strata and the architecture of sandstone intrusions in the Panoche Giant Injectite Complex. The “sill zone” is marked by the red box. From Hurst *et al.* (2011) based on Vigorito and Hurst (2010).

At present, no such system exists for coarse-grained hosted systems. Such a scheme is unlikely to be developed due to the dissimilarity of the initial emplacement mechanism. The orientation of fracture networks that control the emplacement of mudstone-hosted intrusions are influenced by factors such as regional stress regimes, pre-existing joints and faults, and the nature of the host setting (Jolly and Lonergan, 2002; Vetel and Cartwright, 2010; Levi *et al.*, 2011). The few studies into sandstone-hosted intrusions have found no relationship between intrusion distribution and regional jointing (Hannum, 1980) but have suggested that the distribution of pipe clusters is related to palaeogeography and thus proximity to the water table (Netoff, 2002). Man-made perturbations to earthquake-induced sand blow activity, by coring through overburden towards a liquefiable layer, has revealed that weaknesses in an otherwise low permeability overburden exert a first-order control on the distribution of sand blow vents, regardless of underlying fracture orientation (Quigley *et al.*, 2013).

Proximity to the water table is a parameter unique to continental and perhaps some coastal environments, but is not applicable to injection in buried marine mudstones or shallow subaqueous injection such as that described in Chapter 7 or modelled in Chapters 5 & 6. Examples of a water table control include the regionally extensive remobilisation of aeolian sandstones in the Weissliegend (Permian Rotliegend Group) which have been linked to water table fluctuations and periodic flooding of dunes (Strömbäck and Howell, 2002). Similarly, a temporarily high water table may have increased the liquefaction potential or overpressure in the sand blow event associated with the Christchurch earthquake in 2010 (Quigley *et al.*, 2013).

The base of the “sill zone” of the Panoche Giant Injection Complex (PGIC), where sills are the dominant intrusion type, is thought to be equal to the depth at which the pressure of the injecting fluids was approximately equal to the lithostatic pressure. Therefore, as the thickness of the overburden is roughly consistent across the PGIC, the sills are confined to a window of equal depth across the area. (Vigorito and Hurst, 2010). The vertical distribution of sills was not explored in Kodachrome Basin due to the limited vertical extent of the outcrop relative to the total height of the intrusions, however a supra-lithostatic zone may have existed during injection and controlled the occurrence of sills. The evidence presented thus far suggests that sills are more likely to occur in only the fine-grained strata in continental sandstone-hosted successions. An intimation of this behaviour was seen in Chapter 5 where sill-like geometries were seen in a bimodal host (see **Figure 5.6**), suggesting that fine-grained horizons can cause lateral injection. The “upper dyke zone” of the PGIC was injected into the shallow (< 450 m burial) Marca Shale Member, a diatomaceous ooze at the time of injection whose mechanical properties were unlikely to influence the style of injection, therefore sill formation did not occur (Vigorito and Hurst, 2010). Any retardation of vertical injection by an impermeable horizon will result in pressure build-up in the injection until supra-lithostatic pressure is achieved and lateral injection occurs. This suggests two possible prerequisites for sill formation are; (i) a bedding-parallel weakness or heterogeneity to exploit, or; (ii) injection from sufficient depth that a supra-lithostatic pressure is reached before the injection breaches the sediment surface.

9.4. Extrudites

Chapter 7 (Ross *et al.*, 2013) showed that a sandstone sheet formed during a single, prolonged eruption event with the interaction of radial gravity currents from the hundreds of vents exerting control on the internal architecture of the extrudite. These field observations were developed into a model of extrudite formation, the first time such a process-based model has been developed and it was demonstrated that for a sandstone sheet to form, multiple vents must be extruding coevally in a

subaqueous environment, wherein the gravity currents which flow radially from the vents, interact with each other and coalesce to form a spatially extensive sheet. It is suggested that long-term or large vents (*sensu* Løseth *et al.* 2012) will produce gravity currents of sufficient magnitude to erode underlying substrate and the flanks of the sand volcano field and initiate channelization of the gravity current. This would in turn, vastly increase the transport distance of the extruded sediment and produce deposits akin to turbidite sequences. This concept is reinforced by observations of post-depositional channelisation on the flanks of recent sand volcanoes created by the flowing, extruded sediment and water (Quigley *et al.*, 2013). This phenomenon occurs despite the sediment-water interface causing faster deposition of the suspended sediment load than if extrusion occurs in a subaqueous setting. Based on the observations in this thesis, shallow mudstone-hosted intrusions will produce multiple vents, regardless of the host material (Gill and Kuenen, 1957; Okada and Whitaker 1979; Obermeier, 1989; Oliveira *et al.*, 2009; Loope *et al.*, 2013; Ross *et al.* 2013), whereas those sourced from depth appear to be prone to forming single vents (Andresen *et al.*, 2009) (**Figure 9.1**). However, few studies exist on ancient extruded sandstone mounds, which have only been described from seismic data (Andresen *et al.*, 2009; Løseth *et al.* 2012).

Distinguishing between extruded sandstones sheets and turbidites is likely to be problematic, especially in spatially restricted data such as core, and data presented in Chapter 7 add to the current paradigms for their recognition. These criteria include; local and regional evidence for sediment remobilisation, identification of vent sites and, identification of laminations sloping away from the vents that dip at orientations of between 0-360°. The study of Hildebrandt and Egenhoff (2007) proposed transported clasts of extruded material (up to 3 cm long) as a criterion for recognising extrudites, however extruded sediment which is flowing away from a vent as gravity currents is unlikely to be able to support clasts of extruded material. The experiments in Chapters 5 and 6 suggest that large clasts are rarely extruded and instead circulate in the vent zone with only the smaller particles being extruded

onto the surface. If the fluid velocity is sufficient to carry large clasts onto the surface, it is unlikely that such clasts will be transported by a gravity flow and thus they will be deposited very close to the vent. In fact, it is likely that these clasts will not be extruded and will increase in concentration until they block the vent and new intrusions will be triggered elsewhere.

Some studies have undertaken physical modelling of sand injectites using air as the fluidising medium (Rodrigues *et al.*, 2009; Løseth *et al.* 2012). Although the geometry of the injected component of the system may be analogous to clastic intrusions, the extruded integrant of these experiments is not comparable to subaqueous extrusion of a sediment-water slurry as the extrudite forms through air-fall of the vented material as opposed to transport by gravity currents away from a vent. Therefore the sand volcanoes produced experimentally in Chapter 5 are comparable to those described in Chapter 7.

At present, no description of a large-scale (10s of metres) sediment extrusion in a sub-aerial setting exists, although detailed descriptions of metre-scale sand blows exist from recent earthquakes (Quigley *et al.*, 2013) and Jurassic examples from aeolian deposits (Loope *et al.*, 2013). Features of the modern deposits of consecutive extrusion events include, capping silt-drapes, post-depositional channels, rills, ripples and “microdunes” (Quigley *et al.*, 2013) although detailed descriptions of their internal architecture do not, as yet, exist. The study of Loope *et al.* (2013) suggests that sand blows may be constrained around the vent in such a setting and unless the water table is close to the sediment surface extruded water would be expected to percolate back into the permeable sediment, immediately depositing extruded material adjacent to the vent. The description of funnel-shaped “wide fluidisation-zones” in Chapter 5 underpinned the interpretation of funnel-shaped intrusions in Kodachrome Basin as palaeo-vents, or zones where the intrusions breached the unconsolidated sediment-air interface. Their geometry is in agreement

with Jurassic sand-blows described from aeolian strata in Zion National Park, Utah (Loope *et al.*, 2013) which display a broad, funnel-shaped geometry. The interpretation of Loope *et al.*, (2013) is that accumulations of extruded sediment progressively depresses the sediment surface leaving a flat-topped, bowl-shaped vent, however, based on the observations in Chapters 5 and 6, it is possible that this sediment was never erupted but recirculated in the vent, progressively eroding the surrounding strata. Any sediment which was extruded would be rapidly deposited as water percolated back into permeable sand, thus limiting any expression of venting to a zone immediately surrounding the pipe/surface interface.

9.5. Intrusion and host rock relationships.

The experimental observations of Chapters 5 and 6 and the field study of Chapter 8 suggest the margins of sandstone-hosted intrusions are more susceptible to modification during the injection process, in part due to the relatively high irregularity of the inner wall (due to the ratio of grain size to pipe aperture) and, in the case of the Kodachrome Basin intrusions (Chapter 8) perhaps a lack of sufficient cement to prevent grains being eroded from the sidewalls and entrained in the fluidised slurry. It is therefore suggested that the contacts of mudstone-hosted and sandstone-hosted columnar intrusions are dominated by the initial intrusion mechanism: a columnar intrusion forming in non-cohesive or coarse-grained strata by erosion, and tabular sills and dykes as a result of hydrofracturing a fine-grained host (Taylor, 1982; Duranti and Hurst 2004; Scott *et al.*, 2009; Hurst *et al.*, 2011) (Section 3.5.3.). **Figure 9.4** demonstrates the nature of boundaries at a range of scales and in different environments.

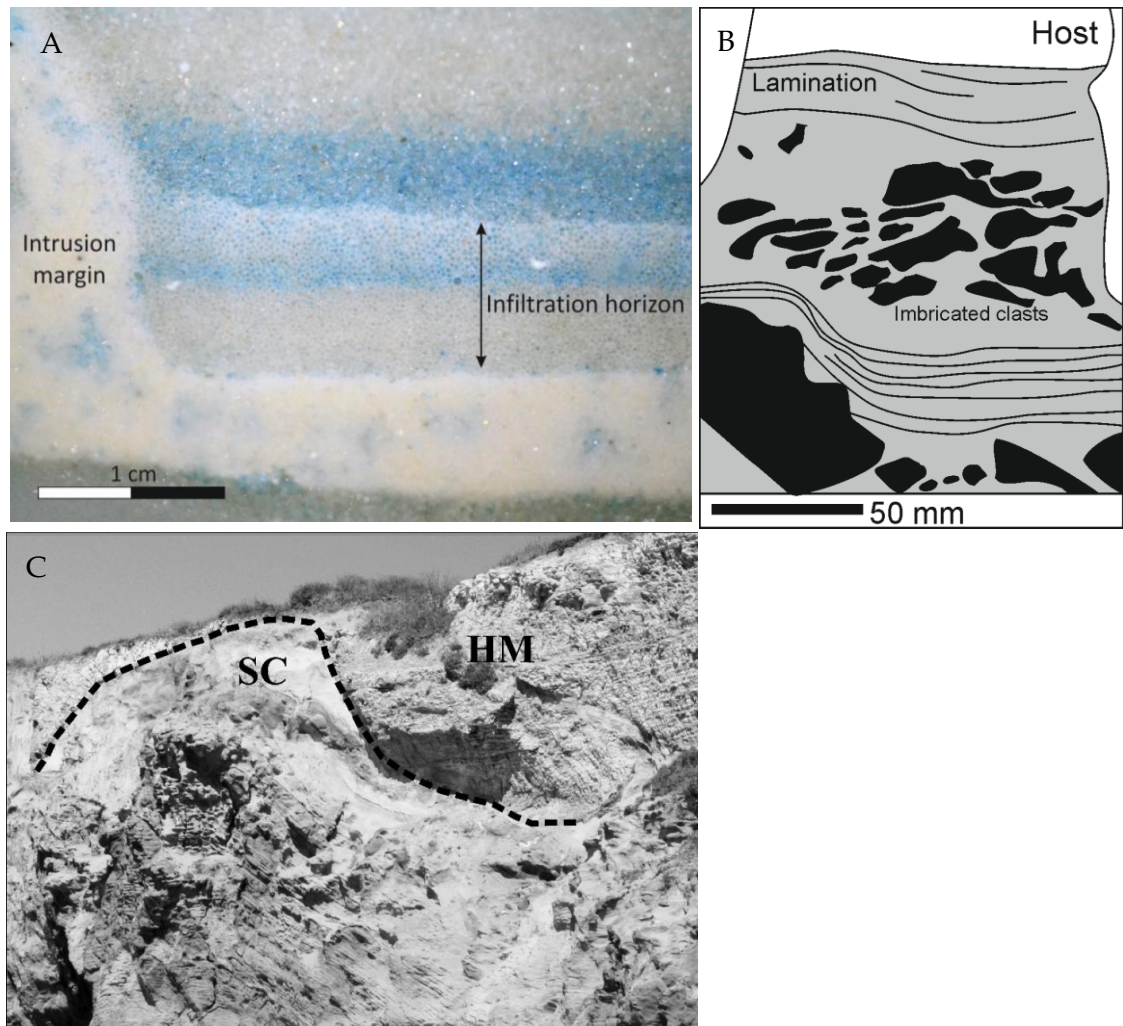


Figure 9.4. Intrusion margins at a range of scales. Curvilinear intrusion margins with thick, fine-grained lining. From experiments in Chapter 7. **B.** Interpreted sketch of a sandstone sill, host rock is white and margin is curvilinear. Flow is from left to right in image. Adapted from Kawakami and Kawamura (2002). **C.** Undulous margin between injected banded sandstone (SC) and host mudstone (HM) interpreted as a scallop. Adapted from Scott *et al.* (2009).

These fundamental differences ensure that comparison between the macro-scale architecture of mudstone-hosted sandstone intrusions, as described in *Chapter 2*, and those hosted in coarse-grained strata can be problematic. However, the boundaries between an intrusion and the host rock regardless of grain size appear broadly similar, for example often irregular with curvilinear geometries. Erosion of

the host will occur more easily in cohesionless sandstones (Chapter 8) or sequences deposited shortly before injection occurs (Chapter 7), however erosional structures are reported from systems where the overburden was thick and cohesive (Scott *et al.*, 2009) (**Figure 9.4**).

Shallow sand injections or injections into unconsolidated sediment have been shown to display itinerant behaviour, the velocity and pressure instabilities in the flow exerting a control on the stability of the active injection. An uneven distribution of stresses on the host sediment results in increased erosion of sediment on one side of the pipe and migration is initiated with sediment on the trailing edge of the pipe avalanching back into the conduit provided the fluid velocity is below that required to fluidise the grains. This mechanism is unlikely to occur in host sediments which are cohesive or consolidated.

9.6. Internal processes in injectites.

Grain plucking and avalanching of grains in active injections has been described for the first time from experiments in Chapter 6, however, the generation of a fine-grained rim on the inside of intrusions, as described from various intrusions (Peterson 1968; Taylor, 1982; Mount, 1993) and Chapter 5 can act as a barrier to this process. It is a common factor in intrusion, both on small scales as produced experimentally, and likely occurs in cm-scale intrusions that source extrudites as investigated in Chapter 7. Embedding of fine-sediment in the walls of the pipe is likely to occur in an injection regardless of conduit length (depth of parent sand body or fluid source) and concentric laminations are reported from small-scale intrusions in sandstone-hosted injections (Loope *et al.*, 2013). Shallow sand intrusions often have a smaller conduit diameter than those which originate at depth, therefore the flow is likely to be in the transitional or perhaps laminar regime. This may however depend on the solid volume concentration in the injecting slurry and the velocity of the flow. It may be an oversimplification to

assume that flow in shallow sand injections is laminar or transitional and those originating at depth are turbulent, however, in either scenario they may have surprisingly high initial flow rates which are not reflected in the make-up of the final intrusion, leading to underestimations of the peak flow parameters. This is the first study to name turbophoresis as a dominant processes in the formation of laminations at the margins of pipes and the same mechanism may also be responsible for the laminations on the margins of tabular intrusions in fine-grained hosts although modelling of fluidised flow in planar channels is lacking.

In Chapter 7, the volume of sediment extruded and the internal architecture of the extruded sandstone sheet suggests that the injections may have been active long enough to generate fine-grained linings and further study of such outcrops to determine the presence of such features is therefore warranted. Concentrations of heavy minerals on intrusion margins have only been reported from one study prior to the observations in Chapter 8 (Kazerouni *et al.*, 2007), however petrographic investigations of intrusions margins are not commonplace and many more examples may exist.

9.7. Facies in clastic intrusions.

Breccias and large clasts of host rock are unlikely to found in shallow intrusions due to the likely unconsolidated nature of the host and likely lack of a sufficient upwards driving force to support large clasts in the flow. Structureless sandstones, sandstones with wavy laminae, and mudstone-clast breccias are the predominant facies described from mudstone-hosted sand intrusions (Duranti and Hurst, 2004; Scott *et al.*, 2009, Sherry *et al.*, 2012) whereas 5 facies have been described from a single sandstone-hosted intrusion complex in Chapter 9, even without consideration of the internal structures within the pipe rock facies. This disparity exists merely because continental successions are more heterogeneous than deep-marine mudstones that so many intrusions are described from. The Kodachrome

Basin intrusions are likely to have transported material from aeolian, evaporitic, sabkha and fluvial deposits resulting in the array of facies they contain. Additionally, recycling of large clasts at the vent creates concentrations of large clasts which are preserved as breccias, whereas breccias in mudstone-hosted intrusions will always consist of mudstone clasts unless some heterogeneity exists in the overburden. Provenance of injected sandstones can be difficult to distinguish due to the lack of variation in the injected sediment.

However, recent work by Morton *et al.* (2014) has shown that the heavy mineral assemblage can be utilised to identify the parent sand body of the mudstone-hosted sandstone intrusions in the Maule Field, where seismic data was not sufficient to identify the parent sandstone. Two possible parent bodies for the intrusions were identified (the Forties and Brimmond depositional sandstones) and are shown to have distinct heavy mineral and garnet geochemistry, allowing correlation of the assemblage of the intruded Maule reservoir with the Brimmond sandstone. If the mineralogical variation in mudstone-hosted sandstone intrusions can be used to identify the source for the injected sediment, the distribution of heavy minerals in the injected sandstone could also be used to identify facies in much the same way as in Chapter 8. Lateral and vertical variation in heavy mineral-associated facies or heavy mineral concentration could also reveal additional information about the flow regime in sandstone intrusions.

9.8. Intrusions as long-term fluid conduits.

Without early cementation, sandstone intrusions at any scale may act as conduits through which fluids may later migrate. Intrusions have been recognised as pathways for fluids in many studies (Jenkins, 1930; Dixon *et al.*, 1995; Jonk *et al.*, 2003; Mazzini *et al.*, 2003; Huuse and Mickleson, 2004) and provided the intrusion is of higher porosity and permeability than the host sediment, post-emplacement fluids will preferentially migrate through the intrusion. Some sandstone intrusions

acted as conduits for a single fluid phase post-emplacment (Mazzini *et al.*, 2003) and others have been shown to be conduits for hydrocarbons (Jonk *et al.*, 2005). Sandstone-hosted intrusions have been shown to act as foci for migrating fluids post-emplacment in much the same way, as they act as vertical permeable pathways. That sandstone-hosted sandstone intrusions act as fluid foci, despite the high permeability of the host strata, was unanticipated and the first description of such a phenomenon. Despite the high permeability of the host strata, the intrusions in Kodachrome Basin remained as open permeability pathways for enough time to be exploited by geochemically distinct fluids from those that drove the injection process, a novel finding.

9.9. Ease of recognition in core and seismic data.

Sandstone sills in particular may only display localized discordance with bedding and thus may be broadly similar to depositional sandstones; especially parent sand bodies which have been extensively remobilised and so display fluidisation structures. In a similar vein, identification of extrudites in outcrop may not be conclusive (*Section 7.4.5.*). One criterion for the recognition of an extrudite is associated disruption of underlying sediment related to the presence of a feeder, however, if sediment has been transported away from a vent, this criterion is invalid. As stated in Chapter 7, extrudite identification must include consideration of likely vents sites from which the sediment was extruded and any regional evidence for remobilisation. However, definitive identification in core is unlikely unless a vent (sand volcano) is cross-cut and small enough to be recognised within the diameter of the core. Mudstone clast breccias can be confused with debrites and other mass transport deposits and homogeneous sandstones can resemble those formed by rapid deposition of high to medium density turbidites (e.g. Bouma A deposits).

The recognition of sandstone intrusions in reflection seismic data is reliant on their discordant geometry and high amplitude response relative to the host rock. Mudstone-hosted sandstone intrusions are likely to have a “soft” response in seismic as their acoustic impedance is likely to be less than that of mudstone. Relative acoustic impedance may be difficult to discern in sandstone-hosted intrusions, but if the intrusion has been pervasively cemented and thus has a higher acoustic impedance than the host sandstone, it may be recognised by a hard response. The wireline log character of mudstone-hosted intrusions is well known (Newman *et al.*, 1993; Dixon *et al.*, 1995; Duranti and Hurst, 2004) and log calibration is often sufficient to confirm the presence of an intrusion, especially where remobilisation has been proven locally. In contrast, positive confirmation of the presence of a sandstone-hosted intrusion would likely require observation of fluidisation structures from core.

9.10. Suggestions for future work

This thesis has provided an understanding of the formation and dynamics of sand injections on a variety of scales and in both laboratory and geological settings. However, new questions now remain to be answered:

In Chapter 3, grain size distribution is shown to exert control on the liquefaction potential of a sediment, therefore further experimental work is required to ascertain the effect on grain-size distribution on the susceptibility of natural sediments to fluidisation. Future field studies of sandstone injections should incorporate sedimentological analysis of the parent bed to compliment analysis of the injected material and investigate any inherent link between injection style and parent sand-body nature. Identification of new field locations and perhaps a thorough review of data available from aeolian systems may lead to increased recognition of sandstone-hosted intrusions. As many studies are focussed on the timing of sand injection, especially with the regard to later hydrocarbon migration and potential seal bypass,

identification and mapping of sandstone extrusion will aid understanding of not just the timing of injection, but the spatial distribution of extrudites and perhaps their identification as potential reservoir units.

The experimental aspects of this investigation have provided a new array of laboratory-produced injection features but under a stringent set of parameters. Further experimental work utilising a range of bed thicknesses, grain size(s) range(s) and cohesiveness, hydrostatic pressures and possibly fluid types to emulate natural conditions is now required to further define the formative mechanisms of a range of fluidisation features.

Although advances have been made in analysing flow process in active injections in this thesis, development of a more sophisticated technique to automatically track particles will produce accurate PTV plots and further the understanding of flow in active sand injections. Proper dissemination and application of established chemical engineering knowledge of fluidisation behaviour in pipes and pipe flow processes to the geological community will result in a vastly improved understanding of processes in sand injections.

As this is first time that the velocity of fluidised particles in sand injections has been measured directly, and the first time that flow has been quantified using PTV, areas where the technique can be improved are clear:

- Implementation of a strobe light linked to the high-speed camera to produce frames with no motion-blur.
- Improved particle-seeding practices to increase particle visualisation.
- Improved seeding will result in more velocity vectors being produced with the aim of producing a velocity map.

- This will require a stable pipe than does not migrate across the frame or complex image masking and stacking techniques to remove any lateral pipe movement.
- Greater consideration of scaling, utilizing sediment with a smaller grain-size or production of pipes with higher diameters will greatly reduce the friction factor at pipe boundaries.

Despite the increasing recognition of sandstone extrusions in field studies, the criteria for their recognition are under-recognised and care must be taken when interpreting remobilised sands so as not to confuse *in-situ* liquefied and fluidised sediments. Extrudites are not yet widely recognised in the subsurface and this study goes some way to providing core-scale paradigms along with a scalable overall architecture to aid their recognition in seismic data.

It is clear from Chapter 8 that sandstone-hosted clastic injection can not only have an effect on basinal fluid-flow in a similar manner to those hosted in mudstone, but the array of facies described suggests that greater scrutiny should be applied when assessing the heterogeneity of sand-dominated successions. Additional studies are required on the sandstone injections of the Entrada Sandstone to verify the origin of the injected material and through sedimentological analysis, ascertain whether the injections were contemporaneous, or occurred as discrete events. A thorough investigation of sill occurrence will confirm whether they occur in a supra-lithostatic zone or are simply controlled by bedding-parallel heterogeneities. The impact of sandstone injection in sand-dominated successions on fluid flow certainly warrants further investigation as their impact on seal integrity and hydrocarbon charge although clearly apparent, is under-recognised.

10. References

- Aase, N.E., Bjorkum, P.A., and Nadeau, P.H. (1996) The effect of grain-coating microquartz on preservation of reservoir porosity. *AAPG Bulletin*, **80**, 1654-1673.
- Alfaro, P., Gibert, L., Moretti, M., García-Tortosa, F.J., Sanz de Galdeano, C., Galindo-Zaldívar, J. and López-Garrido, A.C. (2010) The significance of giant seismites in the Plio-Pleistocene Baza palaeo-lake (Spain). *Terra Nova*, **22**, 172-179
- Allen, J.R.L., (1961) Sandstone plugged pipes in the Lower Old Red Sandstone of Shropshire, England. *Journal of Sedimentary Petrology*, **31**, 325-335.
- Allen, J.R.L. (1985) *Principles of Physical Sedimentology*: Caldwell, The Blackburn Press, 272.
- Alvarez, W., Staley, E., O'Connor, D., and Chan, M.A. (1998) Synsedimentary deformation in the Jurassic of southeastern Utah - A case of impact shaking? *Geology*, **26**, 579-582.
- Amos, K., Peakall, J., Bradbury, P.W., Roberts, M., Keevil, G. and Gupta, S. (2010) The influence of bend amplitude and planform morphology on flow and sedimentation in submarine channels. *Marine and Petroleum Geology*, **27**, 1431-1447.
- Andresen, J.K., Clausen, O.R. and Huuse, M. (2009) Giant ($5.3 \times 10^7 \text{ M}^3$) Middle Miocene (c. 15 Ma) sediment mound (M1) above the Siri Canyon, Norwegian–Danish Basin: origin and significance. *Marine and Petroleum Geology*, **26**, 1640-1655.
- Arnott, R.W.C. and Hand, B.M. (1989) Bedforms, primary structures and grain fabric in the presence of suspended sediment rain. *Journal of Sedimentary Research*, **59**, 1062 – 1069.
- Asif, M., (2004) The complete segregation model for a liquid fluidized bed: formulation and related issues. *Powder Technology*, **140**, 21–29.
- Asif, M., Kalogerakis, N. and Behie, L.A. (1992) Hydrodynamics of liquid fluidized beds including the distributor region. *Chemical Engineering Science*, **47**, 4155-4166

- Audemard M, F.A., Gómez, J.C., Tavera, H.J. and Orihuela G.N.** (2005) Soil liquefaction during the Arequipa Mw 8.4, June 23, 2001 earthquake, southern coastal Peru. *Engineering Geology*, **78**, 237-255.
- Baas, J.H., Best, J.L., Peakall, J, and Wang, M.** (2009) A phase diagram for turbulent, transitional, and laminar clay suspension flows. *Journal of Sedimentary Research*, **79**, 162-183.
- Baer, G.** (1991) Mechanisms of dike propagation in layered rocks and in massive, porous sedimentary rocks. *Journal of Geophysical Research: Solid Earth*, **96**, 11911-11929.
- Batchelor, G. K.,** (1982), Sedimentation in a dilute polydisperse system of interacting spheres. Part 1. General theory. *Journal of Fluid Mechanics*. **119**, 379-408.
- Bear, J.** (1972) *Dynamics of Fluids in Porous Media*: Elsevier, New York, 764.
- Beard, D.C. and Weyl, P.K.** (1973) Influence of texture on porosity and permeability of unconsolidated sand. *AAPG Bulletin*, **57**, 349-369.
- Bezerra, F.H.R., da Fonseca, V.P., Vita-Finzi, C., Lima-Filho, F.P. and Saadi, A.** (2005) Liquefaction-induced structures in Quaternary alluvial gravels and gravelly sediments, NE Brazil. *Engineering Geology*, **76**, 191-208.
- Bhattacharya, S., and Dutta, B.K.,** (2002) Effective voidage model of a binary solid-liquid fluidized bed: application to solid layer inversion. *Industrial and Engineering Chemistry Research*, **41**, 5098-5108.
- Birchfield, S.** (1997) Derivation of Kanade-Lucas-Tomasi Tracking Equation. <http://www.ces.clemson.edu/~stb/klt/birchfield-klt-derivation.pdf> (accessed July 1st 2013).
- Blakey, R.C.** (1988) Basin tectonics and erg response. *Sedimentary Geology*, **56**, 127-151.
- Blakey, R.C.** (1989) Triassic and Jurassic geology of the southern Colorado Plateau, In: *Geologic Evolution of Arizona* (Eds J.P. Jenny, and S.J. Reynolds) Arizona Geological Society, 369-396.
- Blakey, R.C., Peterson, F., and Kocurek, G.** (1988) Synthesis of late Paleozoic and Mesozoic eolian deposits of the western interior of the United States. *Sedimentary Geology*, **56**, 3-125.
- Boehm, A. and Moore, J.C.** (2002) Fluidized sandstone intrusions as an indicator of Paleostress orientation, Santa Cruz, California. *Geofluids*, **2**, 147-161.
- Bouroullec, R.A. and Pyles., D.R.** (2010) Sandstone extrusions and slope channel architecture and evolution: Mio-Pliocene Monterey and Capistrano Formations, Dana Point Harbor, Orange County, California, U.S.A. *Journal of Sedimentary Research*, **80**, 376-392.

- Briedis, N.A., Bergslien, D., Hjellbakk, A., Hill, R.E. and Moir, G.J.** (2007) Recognition criteria, significance to field performance, and reservoir modelling of sand injections in the Balder field, North Sea. In: *Sand Injectites: Implications for Hydrocarbon Exploration and Production*. (Eds A. Hurst and J. Cartwright), *AAPG Mem.*, **87**, 91-102.
- Bromley, M.** (1992) Topographic inversion of early interdune deposits, Navajo Sandstone (Lower Jurassic), Colorado Plateau, USA. *Sedimentary Geology*, **80**, 1-25.
- Bromley, R.G.** (1996) Trace fossil assemblages, diversity and facies. In: *Trace Fossils: Biology, Taxonomy and Applications*. Chapman and Hall, 208-253.
- Bryant, G., and Miall, A.** (2010) Diverse products of near-surface sediment mobilization in an ancient eolianite: outcrop features of the early Jurassic Navajo Sandstone. *Basin Research*, **22**, 578-590.
- Burne, R. V.** (1970) The origin and significance of sand volcanoes in the Bude Formation (Cornwall). *Sedimentology*, **15**, 211-218.
- Carling, P.A. and Breakspear, R.M.D.** (2006) Placer formation in gravel-bedded rivers: A review. *Ore Geology Reviews*, **28**, 377-401.
- Carrigy, M.** (1970) Experiments on the angles of repose of granular materials, *Sedimentology*, **14**, 147-158.
- Cartwright, J.** (2010) Regionally extensive emplacement of sandstone intrusions: a brief review. *Basin Research*, **22**, 502-516.
- Cartwright, J.A., James, D.M.D, and Bolton, A.J.** (2003) The genesis of polygonal fault systems: A review. In: *Subsurface sediment mobilization*. (Eds Van Rensbergen, P., Hillis, R., Maltman, A. and Morley, C.) *Geological Society of London Special Publication*, **216**, 223-242.
- Cartwright, J., Huuse, M., and Aplin, A.,** (2007) Seal bypass systems. *AAPG Bulletin*, **91**, 1141-1166.
- Cartwright, J.A., Huuse, M., James, D.M.D., Vetel, W. and Hurst, A.** (2008) The geometry and emplacement of conical sandstone intrusions. *Journal of Structural Geology*, **30**, 854-868.
- Chan, M., Netoff, D. Blakey, Kocurek, G. and Alvarez, W.** (2007) Clastic-injection pipes and syndepositional deformation structures in Jurassic eolian deposits: Examples from the Colorado Plateau. In: *Sand Injectites: Implications for Hydrocarbon Exploration and Production*. (Eds A. Hurst and J. Cartwright), *AAPG Memoir*, **87**, 233 – 244.
- Collinson, J.** (1994) Sedimentary deformation structures. In: *The Geological Deformation of Sediments* (Ed. A. Maltman), Chapman and Hall, 95-125.

- Cosgrove, J.W.** (1995) The expression of hydraulic fracturing in rocks and sediments. In: *Fractography: Fracture Topography as a Tool in Fracture Mechanics and Stress Analysis* (Ed., M.S. Ameen), *Geological Society of London Special Publications*, **92**, 187-196.
- Cosgrove, J.W.** (2001) Hydraulic fracturing during the formation and deformation of a basin: A factor in the dewatering of low-permeability sediments. *AAPG Bulletin*, **85**, 737-748.
- Couderc, J.P.** (1985) Incipient fluidisation and particulate systems. In: *Fluidization* (Eds J.F. Davidson, R. Clift and D. Harrison) 2nd edition. Academic Press.
- Craig, R.F.** (2004) *Soil Mechanics*, Spon Press, 7th Edition. 83.
- de Boer, W., Rawlinson, P.B. and Hurst, A.** (2007) Successful exploration of a sand injectite complex: Hamsun prospect, Norway Block 24/9. In: *Sand Injectites: Implications for Hydrocarbon Exploration and Production*. (Eds A. Hurst and J. Cartwright), *AAPG Memoir.*, **87**, 65-68.
- Davidson, E.S.** (1967) Geology of the Circle Cliffs area, Garfield and Jane Counties, Utah. *US Geological Survey Bulletin*, **1249**, 1-149.
- Davies, R.J.** (2003) Kilometre-scale fluidization structures formed during early burial of a deep-water slope channel on the Niger Delta. *Geology*, **31**, 949-952.
- Davies, R.J., Huuse, M., Hirst, P., Cartwright, J. and Yang, Y.** (2006) Giant clastic intrusions primed by silica diagenesis. *Geology*, **34**, 917-920.
- Didwania, A.K. and Homsy, G.M.** (1981) Flow regimes and flow transitions in liquid fluidized beds. *International Journal of Multiphase Flow*, **7**, 563-580.
- Di Felice, R.** (1995) Hydrodynamics of liquid fluidisation. *Chemical Engineering Science*, **50**, 1213-1245.
- Di Felice, R.** (2010) Liquid–solid suspension theory with reference to possible applications in geology. *Basin Research*, **22**, 591-602.
- Di Felice, R. and Kehlenbeck., R.** (2000) Sedimentation velocity of solids in finite size vessels. *Chemical Engineering Technology*, **23**, 1123-1126
- Diggs, T.N.** (2007) An outcrop study of clastic injection structures in the Carboniferous Tesnus Formation, Marathon Basin, Trans-Pecos Texas. In: *Sand Injectites: Implications for Hydrocarbon Exploration and Production*. (Eds A. Hurst and J. Cartwright), *AAPG Memoir*, **87**, 37-48.
- Dixon, R.J., Schofield, K., Anderton, R., Reynolds, A.D., Alexander, R.W.S., Williams, M.C. and Davies, K.G.** (1995) Sandstone diapirism and clastic intrusion in the Tertiary Submarine fans of the Bruce-Beryl Embayment, Quadrant 9, UKCS. In: *Characterisation of Deep Marine Clastic Systems* (Eds

A.J. Hartley and D.J. Prosser), *Geological Society of London Special Publication*, **94**, 77-94.

- Doelling, H.H., and Davis, F.D.** (1989) The geology of Kane County, Utah, geology, mineral resources, geologic hazards. *Utah Geological and Mineral Survey Bulletin*, **124**, 1-192.
- Doelling, H.H. Blackett, R.E., Hamblin, A.H., Powell J.D. and Pollock, G.L.** (2000) Geology of Grand Staircase-Escalante National Monument, Utah. In: *Geology of Utah's Parks and Monuments* (Eds D.A. Sprinkel, T.C. Chidsey, Jr and P.B. Anderson), *Utah Geological Association Publication*, **28**, 1-43.
- Dott, R.H.** (1966) Cohesion and flow phenomena in clastic intrusions. *American Association of Petroleum Geologists Bulletin*, **50**, 610-611
- Dragantis, E. And Janda, C.** (2003) Subaqueous artesian springs and associated spring pits in a Himalayan pond. *Boreas*, **32**, 436-442.
- Draganits, E., Grasmann, B. and Schmid, H.P.** (2003) Fluidization pipes and spring pits in a Gondwanan barrier-island environment: groundwater phenomenon, palaeo-seismicity or a combination of both? In: *Subsurface Sediment Mobilization* (Eds P. van Rensbergen., R.R. Hillis, A.J. Maltman and C.K. Morley), *Geological Society of London Special Publication*, **216**, 109-121.
- Duranti, D.** (2007) Large-scale sand injection in the Paleogene of the North Sea: Modeling of energy and flow velocities. In: *Sand Injectites: Implications for Hydrocarbon Exploration and Production*. (Eds A. Hurst and J. Cartwright), *AAPG Memoir*, **87**, 129-139.
- Duranti, D. and Hurst, A.** (2004) Fluidization and injection in the deep-water sandstones of the Eocene Alba Formation (UK North Sea). *Sedimentology*, **51**, 503-529.
- Duranti, D. and Mazzini, A.** (2005) Large-scale hydrocarbon-driven sand injection in the Paleogene of the North Sea. *Earth and Planetary Science Letters*, **239**, 327- 335.
- Duranti, D., Hurst, A., Bell, C., Groves, S. and Hanson, R.** (2002) Injected and remobilized Eocene sandstones from the Alba Field, UKCS: core and wireline log characteristics. *Petroleum Geoscience*, **8**, 99-107.
- Epstein, N., and LeClair, B.P.**, (1985) Liquid fluidization of binary particle mixtures—II. Bed inversion. *Chemical Engineering Science* **40**, 1517-1526.
- Eschner, T.B. and Kocurek, G.** (1986) Marine destruction of eolian sand seas: Origin of mass flows. *Journal of Sedimentary Petrology*, **56**, 401-411.

- Escudié, R., Epstein, N., Grace, J.R. and Bi, H.T.** (2006) Layer inversion phenomenon in binary-solid liquid-fluidized beds: Prediction of the inversion velocity. *Chemical Engineering Science*, **61**, 6667-6690.
- Fasisst, H. And Eckharalt, B.** (2003) Travelling waves in pipe flow. *Physical Review Letters*, **91**, 224502-224506.
- Fernandes, L.A., Bonatto de Castro, A. and Basilici, G.** (2007) Seismites in continental sand sea deposits of the Late Cretaceous Caivá Desert, Bauru Basin, Brazil. *Sedimentary Geology*, **199**, 51-64.
- Fisher, Q.J., Casey, M., Clennell, M.B., and Knipe, R.J.** (1999) Mechanical compaction of deeply buried sandstones of the North Sea. *Marine and Petroleum Geology*, **16**, 605-618.
- Fisher Q.J., Knipe R.J., and Worden R.H.** (2000) Microstructures of deformed and non-deformed sandstones from the North Sea: implications for the origins of quartz cement in sandstones, In: *Quartz Cementation in Sandstones* (Ed R. Worden), 129-146.
- Fitzgerald, R.** (2004) New experiments set the scale for the onset of turbulence in pipe flow. *Physics Today*, **57**, 21-24.
- Frey, S.E., Gingras, M.K. and Dashtgard, S.E.** (2009) Experimental studies of gas-escape and water-escape structures: Mechanisms and morphologies. *Journal of Sedimentary Research*, **79**, 808-816.
- Fox, J.M., Hill, P.S., Milligan, T.G., and Boldrin, A.,** (2004) Flocculation and sedimentation on the Po River Delta. *Marine Geology*, **203**, 95-107.
- Funamizu, N. and Takakuwa. T** (1995) An improved Richardson-Zaki formula for computing mixed layer composition in binary solid-liquid fluidized beds. *Chemical engineering science*, **50**, 3025-3032.
- Gallo, F. and Woods, A.W.** (2004) On steady homogeneous sand-water flows in a vertical conduit. *Sedimentology*, **51**, 195-210.
- Gibilaro, L.G., Di Felice, R. and Foscolo, P.U.,** (1990) Added mass effect in fluidised beds: application of the Guerst-Wallis analysis of inertial coupling in two-phase flow. *Chemical Engineering Science*, **45**, pp. 1561-1565.
- Gill, W.D** (1979) Syndepositional sliding and slumping in the West Clare Namurian Basin, Ireland. *Geological Survey of Ireland, Special Paper*, **4**, 1- 31.
- Gill, W.D. and Kuenen, P.H.** (1957) Sand volcanoes on slumps in the Carboniferous of County Clare, Ireland. *Quarterly Journal of the Geological Society London*, **113**, 441-460.

- Gillette, D.D., and Hayden, M.C.** (1997) A preliminary inventory of paleontological resources within the Grand Staircase-Escalante National Monument, Utah, *Utah Geological Survey Professional Paper*, **164**, 2-39
- Glennie, K.W. and Hurst, A.** (2007) Fluidisation and associated soft-sediment deformation in aeolian sandstones: Hopeman Sandstone (Permian), Scotland, and Rotliegend, North Sea. In: *Sand Injectites: Implications for Hydrocarbon Exploration and Production*. (Eds A. Hurst and J. Cartwright), *AAPG Memoir*, **87**, 221-226.
- Gluyas, J.G.** (2005) Ardmore Field: rebirth of the first offshore oil fields, UKCS. *Petroleum Geology Conference Series*, **6**, 367-388.
- González de Vallejo, L.I., Tsigé, M. and Cabrera, L.** (2005) Paleoliquefaction features on Tenerife (Canary Islands) in Holocene sand deposits. *Engineering Geology*, **76**, 179-190.
- Gregory, J.** (2006) *Particles in Water: Properties and Processes*. Taylor & Francis Group. pp188.
- Guhman, A.I. and Pederson, D.T.** (1992) Boiling Sand Springs, Dismal River, Nebraska - Agents for formation of vertical cylindrical structures and geomorphic change. *Geology*, **20**, 8-10.
- Hamberg, L., Jepsen, A.M., Borch, N.T., Dam, G., Engkilde, M.K., and Svendsen, J.B.**, (2007) Mounded Structures of Injected Sandstones in Deep-marine Paleocene Reservoirs, Cecile Field, Denmark.. In: *Sand Injectites: Implications for Hydrocarbon Exploration and Production*. (Eds A. Hurst and J. Cartwright), *AAPG Memoir*, **87**, 69-79.
- Hampson, G.J., Elliott, T. and Davies, S.J.** (1997) The application of sequence stratigraphy to upper Carboniferous fluvio-deltaic strata of the onshore UK and Ireland: Implications for the Southern North Sea. *Journal of the Geological Society of London*, **154**, 719-733.
- Handley, D., Doraisamy, A., Butcher, K. L., and Franklin, N. L.**, (1966) A study of fluid and particle mechanics in liquid-fluidised beds. *Transactions of the Institution of Chemical Engineers and the Chemical Engineer*. **44**, 260 - 273.
- Hannum, C.** (1980) Sandstone and conglomerate-breccia pipes and dikes of the Kodachrome Basin area, Kane County, Utah. *Brigham Young University Geology Studies Special Publication 7*, 31-50.
- Harrison, D., Davidson, J.F. and de Kock, J.W.**, (1961.) On the nature of aggregative and particulate fluidisation. *Transactions of the Institution of Chemical Engineers and the Chemical Engineer*. **39**, 202-211.
- Hasset, N.J.** (1961) The mechanism of fluidization. *British Chemical Engineering*, **6**, 777 - 780.

- Hesse, R. and Reading, H.G.** (1978) Subaqueous clastic fissure eruptions and other examples of sedimentary transposition in the lacustrine Horton Bluff Formation (Mississippian), Nova Scotia, Canada. In: *Modern and Ancient Lake Sediments* (Eds A. Matter and M.E. Tucker), *International Association of Sedimentologists, Special Publication*, **2**, 241-257.
- Higgs, R.**, (1998) Return of 'The Fan That Never Was': Westphalian turbidite systems in the Variscan Culm Basin: Bude Formation (south-west England). *Sedimentology*, **45**, 961-975.
- Hildebrandt, C. and Egenhoff, S.** (2007) Shallow-marine massive sandstone sheets as indicators of palaeoseismic liquefaction — an example from the Ordovician Shelf of Central Bolivia. *Sedimentary Geology*, **202**, 581-595.
- Hillier, R.D. and Cosgrove, J.W.** (2002) Core and seismic observations of overpressurerelated deformation within Eocene sediments of the Outer Moray Firth, UKCS. *Petroleum Geoscience*, **8**, 141-149.
- Hird, C.C. and Hassona, F.A.K.** (1990) Some factors affecting the liquefaction and flow of saturated sands in laboratory tests. *Engineering Geology*, **28**, 149-170.
- Hiscott, R.N.** (1979) Clastic sills and dikes associated with deep-water sandstones, Tourelle Formation, Ordovician, Quebec. *Journal of Sedimentary Petrology*, **49**, 1-10.
- Hof, B., Juel, A. and Mullin, T.** (2003) Scaling of the turbulence transition threshold in a pipe. *Physical Review Letters*, **91**, 244502 1-4.
- Hooke, R.** (1968) Model geology; prototype and laboratory streams: discussion. *Geological Society of America, Bulletin*, **79**, 391-393.
- Hubbard, S.M., Romans, B.W. and Graham, S.A.** (2007) An outcrop example of large-scale conglomeratic intrusions sourced from deep-water channel deposits, Cerro Toro Formation, Magallanes basin, southern Chile. In: *Sand Injectites: Implications for Hydrocarbon Exploration and Production*. (Eds A. Hurst and J. Cartwright), *AAPG Memoir*, **87**, 199-207.
- Hu, X.**, (2002) The segregation in the binary-solid liquid fluidized bed. *Chemical Engineering and Technology* **25**, 911-915.
- Hurst, A. and Cartwright, J.** (2007) Relevance of sand injectites to hydrocarbon exploration and production. In: *Sand Injectites: Implications for Hydrocarbon Exploration and Production*. (Eds A. Hurst and J. Cartwright), *AAPG Memoir*, **87**, 1-21.
- Hurst, A. and Glennie, K.W.** (2008) Mass-wasting of ancient aeolian dunes and sand fluidization during a period of global warming and inferred brief high precipitation: the Hopeman Sandstone (Late Permian), Scotland. *Terra Nova*, **20**, 274-279.

- Hurst, A., Cartwright, J., Huuse, M., Jonk, R., Schwab, A., Duranti, D. and Cronin, B.** (2003) Significance of large scale sand injectites as long-term fluid conduits: Evidence from seismic data. *Geofluids*, **3**, 263–274.
- Hurst, A., Cartwright, J., Duranti, D., Huuse, M. and Nelson, M.** (2005) Sand injectites: An emerging global play in deep-water clastic environments. In: *North-west Europe and global perspectives - Proceedings of the 6th Petroleum Geology Conference* (Eds A., Dore and B., Vining), *Geological Society of London*, 133–144.
- Hurst, A., Cartwright, J., Huuse, M. and Duranti, D.** (2006) Extrusive sandstones (extrudites): A new class of stratigraphic trap? In: *The Deliberate Search for Stratigraphic Traps: Where are they now?* (Eds M.R. Allen, G.P. Goffey, R.K. Morgan and I.M. Walker), *Geological Society of London Special Publications*, **254**, 289–299.
- Hurst, A., Scott, A. and Vigorito, M.** (2011) Physical characteristics of sand injectites. *Earth-Science Reviews*, **106**, 215–246.
- Huuse, M.** (2008) Sandstone intrusions: Implications for exploration and production. *World Oil*, **229**, issue 6, 9–9.
- Huuse, M. and Mickelson, M.** (2004) Eocene sandstone intrusions in the Tampen Spur area (Norwegian North Sea Quad 34) imaged by 3D seismic data. *Marine and Petroleum Geology*, **21**, 141–155.
- Huuse, M., Duranti, D., Steinsland, N., Guargena, C.G., Prat, P., Holm, K., Cartwright, J. and Hurst, A.** (2004) Seismic characteristics of large-scale sandstone intrusions in the Paleogene of the South Viking Graben, UK and Norwegian North Sea. In: *3D Seismic Technology: Application to the Exploration of Sedimentary Basins* (Eds R.J. Davies, J. Cartwright, S.A. Stewart, M. Lappin and J.R. Underhill), *Geological Society of London, Memoirs*, **29**, 263–277.
- Huuse, M., Cartwright, J. A., Gras, R., and Hurst, A.** (2005a) Kilometre-scale sandstone intrusions. In: Dore, A.G. & Vining, B.A. (eds) *Petroleum Geology: North-West Europe and Global Perspectives - Proceedings of the 6th Petroleum Geology Conference*, 1577–1594.
- Huuse, M., Shoulders, S., Netoff, D. and Cartwright, J.** (2005b) Giant sandstone pipes record basin-scale liquefaction of buried dune sands in the Middle Jurassic of SE Utah. *Terra Nova*, **17**, 80–85.
- Huuse, M., Cartwright, J., Hurst, A. and Steinsland, N.** (2007) Seismic characterization of large-scale sandstone intrusions. In: *Sand Injectites: Implications for Hydrocarbon Exploration and Production*. (Eds A. Hurst and J. Cartwright), *AAPG Memoir*, **87**, 21–35.
- Jackson, C.A.** (2007) The geometry, distribution, and development of clastic injections in slope systems: Seismic examples from the Upper Cretaceous

Kyrre Formation, Måløy slope, Norwegian margin. In: *Sand Injectites: Implications for Hydrocarbon Exploration and Production*. (Eds A. Hurst and J. Cartwright), *AAPG Memoir*, **87**, p. 37-48.

- James, D.M.D., Jolly, R.J.H. and Lonergan, L.** (2003) Discussion on the mechanisms and controls on the formation of sand intrusions. *Journal of the Geological Society of London*, **160**, 495-496.
- Jenkins, O. P.** (1930) Sandstone dykes as conduits for oil migration through shales: *AAPG Bulletin*, **14**, 411-421.
- Johnson, H.D.** (1977) Sedimentation and water escape structures in some late Precambrian shallow marine sandstones from Finnmark, North Norway. *Sedimentology*, **24**, 389-411.
- Johnson, M.R.** (1994) Thin section grain size analysis revisited. *Sedimentology*, **41**, 985-999.
- Johnson, T.A.** (1999) Flow past a sphere up to a Reynolds number of 300. *Journal of Fluid Mechanics*, **378**, 19-70.
- Jolly, R.J.H. and Lonergan, L.** (2002) Mechanisms and controls on the formation of sand intrusions. *Journal of the Geological Society of London*, **159**, 605-617.
- Jones, L.S., and Blakey, R.C.** (1997) Erosional remnants and adjacent unconformities along an eolian-marine boundary of the Page Sandstone and Carmel Formation, Middle Jurassic, south-central Utah. *Journal of Sedimentary Petrology*, **63**, 852-859.
- Jonk, R.** (2010) Sand-rich injectites in the context of short-lived and long-lived fluid flow. *Basin Research*, **22**, 603-621.
- Jonk, R., Duranti, D., Parnell, J., Hurst, A. and Fallick, A.** (2003) The structural and diagenetic evolution of injected sandstones: Examples from the Kimmeridgian of NE Scotland. *Journal of the Geological Society of London*, **160**, 881-894.
- Jonk, R., Parnell, J. and Hurst, A.** (2005) Aqueous and petroleum fluid flow associated with sand injectites. *Basin Research*, **17**, 241-257.
- Jonk, R., Cronin, B.T. and Hurst, A.** (2007) Variations in sediment extrusion in basin-floor, slope, and delta-front settings: Sand volcanoes and extruded sand sheets from the Namurian of County Clare, Ireland. In: *Sand Injectites: Implications for Hydrocarbon Exploration and Production*. (Eds A. Hurst and J. Cartwright), *AAPG Memoir*, **87**, 221-226.
- Kane, I.A.** (2010) Development and flow structures of sand injectites: The Hind Sandstone Member injectite complex, Carboniferous, UK. *Marine and Petroleum Geology*, **27**, 1200-1215.

- Kawakami, G. and Kawamura, M.** (2002) Sediment flow and deformation (sfd) layers: evidence for intrastratal flow in laminated muddy sediments of the Triassic Osawa Formation, northeast Japan. *Journal of Sedimentary Research*, **72**, 181-181.
- Kazerouni, A.M., Friis, H., Svendsen, J.B. and Weibel, R.** (2011) Heavy mineral sorting in downwards injected Palaeocene sandstone, Siri Canyon, Danish North Sea. *Sedimentary Geology*, **236**, 279-285,
- Keevil, G.M., Peakall, J. and Best J.L.** (2007) The influence of scale, slope and channel geometry on the flow dynamics of submarine channels. *Marine and Petroleum Geology*, **24**, 487-503.
- Keighley, D.G. and Pickerill, R.K.** (1994) Flute-like marks and associated structures from the Carboniferous Port Hood formation of eastern Canada: Evidence of secondary origin in association with sediment intrusion. *Journal of Sedimentary Research*, **64**, 253–263.
- Kennedy, S. C. and Bretton, R. H.,** (1966), Axial dispersion of spheres fluidized with liquids. *American Association of Chemical Engineers Journal*, **12**, 24-30.
- Leclair, S.F, and Arnott, R.W.C.** (2005) Parallel lamination formed by high-density turbidity currents. *Journal of Sedimentary Research*, **75**, 1-5.
- Le Roux, J.P., Nielsen, S.N., Kemnitz, H. and Henriquez, A.** (2008) A Pliocene mega-tsunami deposit and associated features in the Ranquil Formation, southern Chile. *Sedimentary Geology*, **203**, 164-180.
- Leva, B.** (1959) *Fluidization*: New York, McGraw-Hill, 327.
- Levi, T., Weinberger, R. and Eyal, Y.** (2011) A coupled fluid-fracture approach to propagation of clastic dykes during earthquakes. *Tectonophysics*, **498**, 35-44.
- Li, Y., Craven, J., Schweig, E.S. and Obermeier, S.F.** (1996) Sand boils induced by the 1993 Mississippi River Flood: Could they one day be misinterpreted as earthquake-induced liquefaction? *Geology*, **24**, 171-174.
- Limas-Ballesteros, R., Riba, J P. and Couderc, J. P.,** (1982), Expansion characteristics of non-spherical particles in a liquid. *Entropie*, **106**, 37-45
- Lockett, M. J. and Al-Habbooby, H. M.,** (1973), Differential settling by size of two particle species in a liquid. *Transactions of the Institution of Chemical Engineers*, **51**, 281-292.
- Lockett, M. J. and Al-Habbooby, H. M.,** (1974), Relative particle velocities in two-species settling. *Powder Technology*, **10**, 67-71.
- Loeffler, A. L. and Ruth, B. F.,** (1959), Particulate fluidization and sedimentation of spheres. *American Association of Chemical Engineers Journal*,. **5**, 310-314.

- Lonergan, L., Borlandelli, C., Taylor, A., Quine, M. and Flanagan, K.** (2007) The three dimensional geometry of sandstone injection complexes in the Gryphon Field, United Kingdom North Sea. In: *Sand Injectites: Implications for Hydrocarbon Exploration and Production*. (Eds A. Hurst and J. Cartwright), *AAPG Memoir*, **87**, 103–112.
- van Loon, A.J. and Maulik, P.** (2011) Abraded sand volcanoes as a tool for recognizing paleo-earthquakes, with examples from the Cisuralian Talchir Formation near Angul (Orissa, Eastern India). *Sedimentary Geology*, **238**, 145-155.
- Loope, D.B., Elder, J.F., Zlotnik, V.A., Kettler, R.M., and Pederson, D.T.** (2013) Jurassic earthquake sequence recorded by multiple generations of sand blows, Zion National Park, Utah. *Geology*, **41**, 1131-1134.
- Løseth, H., Rodrigues, N. and Cobbold, P.R.** (2012) World's largest extrusive body of sand? *Geology*, **40**, 467-470.
- Lovell, J.P.B.** (1974) Sand volcanoes in the Silurian rocks of Kirkcudbrightshire. *Scottish Journal of Geology*, **10**, 161-162.
- Lowe, D.R.** (1975) Water escape structures in coarse-grained sediments. *Sedimentology*, Relative particle velocities in two-species settling., 157-204.
- Macdonald, H.A., Peakall, J., Wignall, P.B., and Best, J.** (2011) Sedimentation in deep-sea lobe-elements: implications for the origin of thickening-upward sequences. *Journal of the Geological Society of London*, **168**, 319-332.
- Mahaney, W.C., Milner, M.W., Netoff, D.I., Malloch, D., Dohm, J.M., Baker, V.R., Miyamoto, H., Hare, T.M. and Komatsu, G.** (2004) Ancient wet aeolian environments on Earth: clues to presence of fossil / live microorganisms on Mars. *Icarus*, **171**, 39-53.
- Major, J. J., and T. C. Pierson** (1992) Debris flow rheology: Experimental analysis of fine-grained slurries, *Water Resource Research*, **28**(3), 841–857.
- Makse, H.A., Havlin, S., King, P.R. and Stanley, H.E.** (1997) Spontaneous stratification in granular mixtures. *Nature*, **386**, 379-382.
- Maltman, A.** (1994) Causes of deformation. In: *The Geological Deformation of Sediments*, (Ed., A. Maltman), Chapman & Hall, 16-33.
- Malverti, L., Lajeunesse, E. and Metivier, F.** (2008) Small is beautiful: Upscaling from microscale laminar to natural turbulent rivers. *Journal of Geophysical Research*, **113**, F04004.
- Martin, M.E. and Bourgeois, J.** (2012) Vented sediments and tsunami deposits in the Puget Lowland, Washington – differentiating sedimentary processes. *Sedimentology*, **59**, 419–444.

- Martinsen, O.J. and Bakken, B.** (1990) Extensional and compressional zones in slumps and slides and examples from the Namurian of County Clare, Ireland. *Journal of the Geological Society*, **147**, 153-164.
- Martinsen, O.J. and Collinson, J.D.** (2002) The Western Irish Namurian Basin reassessed—a discussion. *Basin Research*, **14**, 523–542.
- Martinsen, O.J., Lien, T., Walker, R.G. and Collinson, J.D.** (2003) Facies and sequential organisation of a mudstone-dominated slope and basin floor succession: the Gull Island Formation, Shannon Basin, Western Ireland. *Marine and Petroleum Geology*, **20**, 789–807.
- Masliyah, J. H.**, (1979), Hindered settling in a multi-species particle system. *Chemical Engineering Science*, **34**, 1166-1168.
- Massari, F., Ghibaudo, G., D'Alessandro, A. and Davaud, E.** (2001) Water-upwelling pipes and soft-sediment-deformation structures in lower Pleistocene calcarenites (Salento, southern Italy). *Geological Society of America Bulletin*, **113**, 545-560.
- Mazzini, A., Duranti, D., Jonk, R., Parnell, J., Cronin, B.T., Hurst, A. and Quine, M.** (2003) Palaeo-carbonate seep structures above an oil reservoir, Gryphon Field, Tertiary, North Sea. *Geo-Marine Letters*, **23**, 323–339.
- van der Meer, J.J.M., Kjaer, K.H. and Krüger, J.** (1999) Subglacial water-escape structures and till structures, Sléttjökull Iceland. *Quaternary Science Reviews*, **14**, 191-205.
- van der Meer, J.J.M., Kjaer, K.H., Krüger, J., Rabassa, J. and Kilfeather, A.A.** (2009) Under pressure: clastic dykes in glacial settings. *Quaternary Science Reviews*, **28**, 708-720.
- Melosh, H. J.** (1989) Impact cratering: A geologic process: New York, Oxford University Press.
- Middleton, G.V.** (1993) Sediment deposition from turbidity currents. *Annual Review of Earth and Planetary Sciences*, **21**, 89–114.
- Monchaux, R., Bourgoïn, M. and Cartellier, A.** (2012) Analyzing preferential concentration and clustering of inertial particles in turbulence. *International Journal of Multiphase Flow*, **20**, 1-18.
- Monkul, M.M. and Ozden, G.**, (2007) Compressional behavior of clayey sand and transition fines content, *Engineering Geology*, **8**, 195-205.
- Monkul, M.M. and Yamamuro, J.A.**, (2011) Influence of silt size and content on liquefaction behavior of sands, *Canadian Geotechnical Journal*, **48**, 931-942.
- Montenat, C., Barrier, P., Ott D'estevou, P. and Hibsich, C.** (2007) Seismites: An attempt at critical analysis and classification. *Sedimentary Geology*, **196**, 5-30.

- Moody, L. F.** (1944) Friction factors for pipe flow. *Transactions of the American Society of Mechanical Engineers*, **66** (8), 671–684.
- Moreau, J., Ghienne, J.F. and Hurst, A.** (2011) Kilometre-scale sand injectites in the intracratonic Murzuq Basin (South-west Libya): an igneous trigger? *Sedimentology*, **59**, 1321-1344.
- Moretti, M.** (2000) Soft-sediment deformation structures interpreted as seismites in middle-late Pleistocene Aeolian deposits (Apulian foreland, southern Italy). *Sedimentary Geology*, **135**, 167–179.
- Moretti, M. and Sabato, L.** (2007) Recognition of trigger mechanisms for soft-sediment deformation in the Pleistocene lacustrine deposits of the Sant'Arcangelo Basin (Southern Italy): seismic shock vs. overloading. *Sedimentary Geology*, **196**, 31-45.
- Moretti, M. Alfaro, P., Caselles, O. and Canas, J.A.** (1999) Modelling seismites with a digital shaking table. *Tectonophysics*, **304**, 369-383.
- Morgan, J.P., Coleman, J.M., and Gaglino, S.M.,** (1968) Mudlumps: Diapiric structures in the Mississippi delta. In: *Diapirism and Diapirs*. (Eds. Braunstein, J. & O'Brien, G.D.) *AAPG Memoir*, **8**, 145-161.
- Moritomi, H., Yamagishi, T. and Chiba, T.,** (1986), Prediction of complete mixing of liquid-fluidized binary solid particles. *Chemical Engineering Science*, **41**, 297-305.
- Morton, A., McFayden, S., Hurst, A., Pyle, J and Rose, P.** (2014) Constraining the origin of reservoirs formed by sandstone intrusions: Insights from heavy mineral studies of the Eocene in the Forties area, United Kingdom central North Sea. *AAPG Bulletin*, **98**, 545-561.
- Mörz, T., Karlik, E.A., Kreiter, S. and Kopf, A.** (2007) An experimental setup for fluid venting in unconsolidated sediments: New insights to fluid mechanics and structures. *Sedimentary Geology*, **196**, 251–267.
- Mount, J.F.** (1993) Formation of fluidization pipes during liquefaction: examples from the Uratanna Formation (Lower Cambrian), South Australia. *Sedimentology*, **40**, 1027-1037.
- Mountney, N. P.** (2012) A stratigraphic model to account for complexity in aeolian dune and interdune successions. *Sedimentology*, **59**, 964-989.
- Murchison, R.I.,** (1827) On the coal field of Bora in Sutherlandshire and some other stratified deposits in the North of Scotland. *Geological Society of London*, **2**, 293–326.
- Mutti, E. and Normark, W.R.** (1987) Comparing examples of modern and ancient turbidite systems: problems and concepts. In: *Marine Clastic Sedimentology:*

Concepts and Case Studies. (Eds. Legget, J. K. & Zuffa, G.G.) Graham and Trotman, London, 1-38.

- Naeini, S.A. and Baziar, M. H.** (2004) Effect of fines content on steady-state strength of mixed and layered samples of a sand, *Soil Dynamics and Earthquake Engineering*, **24**, 181-187.
- Nagtegaal, P.J.C.** (1978) Sandstone-framework instability as a function of burial diagenesis. *Journal of the Geological Society of London*, **135**, 101-105.
- Netoff, D.** (2002) Seismogenically induced fluidization of Jurassic erg sands, south-central Utah. *Sedimentology*, **49**, 64-80.
- Netoff, D.I. and Shroba, R.R.** (2001) Conical sandstone landforms cored with clastic pipes in Glen Canyon National Recreation Area, southeastern Utah. *Geomorphology*, **39**, 99-110.
- Neumann-Mahlkau, P.** (1976) Recent sand volcanoes in the sand of a dike under construction. *Sedimentology*, **23**, 421-425.
- Nevill, W.E.** (1957) Sand volcanoes, sheet slumps and stratigraphy of part of the Slieverdagh Coalfield, County Tipperary. *Royal Society of Dublin Scientific Proceedings*, **27**, 313-324.
- Newman, S. J., Reeder, M. L., Woodruff, A. H. W. and Hatton, I.R.** (1993) The geology of the Gryphon oil field. In: *Petroleum geology of Northwest Europe; Proceedings of the 4th conference* (Ed. J. R. Parker), *Petroleum geology of northwest Europe*, **4**, 123-133.
- Nichols, R.J.** (1995) The liquefaction and remobilization of sandy sediments. In: *Characterization of Deep Marine Clastic Systems* (Eds A.J. Hartley and D.J. Prosser), *Geological Society of London Special Publication*, **94**, 63-76.
- Nichols, R.J., Sparks, R.S.J. and Wilson, C.J.N.** (1994) Experimental Studies of the fluidization of layered sediments and the formation of fluid escape structures. *Sedimentology*, **41**, 233-253.
- Obermeier, S.F.** (1996) Use of liquefaction-induced features for paleoseismic analysis - An overview of how seismic liquefaction features can be distinguished from other features and how their regional distribution and properties of source sediment can be used to infer the location and strength of Holocene paleo-earthquakes. *Engineering Geology*, **44**, 1-76.
- Obermeier, S.F., Olson, S.M. and Green, R.A.** (2005) Field occurrences of liquefaction-induced features: a primer for engineering analysis of paleoseismic shaking. *Engineering Geology*, **76**, 209-234.
- Okada, H. and Whitaker, J.H.M.** (1979) Sand volcanoes of the Palaeogene Kumage Group, Tanegashima, Southwest Japan. *Journal of the Geological Society of Japan*, **85**, 187-196.

- Olariu, U. C. and Bhattacharya, J.P.** (2006) Terminal distributary channels and delta front architecture of river-dominated delta systems. *Journal of Sedimentary Research*, **76**, 212-233.
- Oliveira, C.M.M., Hodgson, D.M. and Flint, S.S.** (2009) Aseismic controls on in situ soft-sediment deformation processes and products in submarine slope deposits of the Karoo Basin, South Africa. *Sedimentology*, **56**, 1201–1225.
- Oliveira, C.M.M., Hodgson, D.M. and Flint, S.S.** (2011) Distribution of soft-sediment deformation structures in clinoform successions of the Permian Ecca Group, Karoo Basin, South Africa. *Sedimentary Geology*, **235**, 324-330.
- Osborne, M.J. and Swarbrick, R.E.,** 1997, Mechanism for generating overpressure in sedimentary basins: A re-evaluation. *American Association of Petroleum Geologists*, **81**, 1023-1041.
- O'Sullivan, R.B., and Pipiringos, G.N.** (1998) Maps showing distribution of erosional clasts on the Middle Jurassic J-2 unconformity in the western interior of the United States. In: *Geologic Investigations Series I-2622*. U.S. Department of the Interior, U.S. Geological Survey.
- Owen, G.** (1996) Experimental soft-sediment deformation: Structures formed by the liquefaction of unconsolidated sands and some ancient examples. *Sedimentology*, **43**, 279-293.
- Paola, C., Straub, K., Mohrig, D. and Reinhardt, L.** (2009) The "unreasonable effectiveness" of stratigraphic and geomorphic experiments. *Earth-Science Reviews*, **97**, 1-43.
- Parize, O. and Friès, G.** (2003) The Vocontian clastic dykes and sills: a geometric model. In: *Subsurface Sediment Mobilization* (Eds P. van Rensbergen., R.R. Hillis, A.J. Maltman and C.K. Morley), *Geological Society of London Special Publication*, **16**, 51-71.
- Patwardhan, V.S., and Tien, C.,** (1985) Sedimentation and liquid fluidization of solid particles of different sizes and densities. *Chemical Engineering Science* **40**, 1051–1060.
- Peakall, J., Ashworth, P. and Best, J.** (1996) Physical modelling in fluvial geomorphology: principles, applications and unresolved issues. In: *The Scientific Nature of Geomorphology* (Eds B.L. Rhoads and C.E. Thorn), Wiley, Chichester. 221–253.
- Peakall, J., Amos, K.J., Keevil, G.M., Bradbury, P.W. and Gupta, S.** (2007) Flow processes and sedimentation in submarine channel bends. *Marine and Petroleum Geology*, **24**, 470-486.
- Peterson, G.L.** (1986) Flow structures in sandstone dikes. *Sedimentary Geology*, **2**, 177-190.

- Peterson, F., and Pipiringos, G.N.** (1979) Stratigraphic relationships of the Navajo Sandstone to Middle Jurassic formations in parts of southern Utah and northern Arizona. *U.S. Geological Survey Professional Paper*. **1035**, 1-43.
- Plint, A.G.** (1983) Liquefaction, fluidization and erosional structures associated with bituminous sands of the Bracklesham Formation (Middle Eocene) of Dorset, England. *Sedimentology*, **30**, 525-535.
- Picano, F., Sardina, G. and Casciola, C.M.** (2009) Spatial development of particle-laden turbulent pipe flow. *Physics of Fluids*, **21**, 21-36.
- Pipiringos, G.N., and O'Sullivan, R.B.** (1975) Chert pebble unconformity at the top of the Navajo Sandstone. In *southeastern Utah, Four Corners Geological Society Guidebook, 8th Field Conference, Canyonlands, Four Corners Geological Society*, 149-156.
- Pisarska-Jamroży, M. and Weckwerth, P.** (2013) Soft-sediment deformation structures in a Pleistocene glaciolacustrine delta and their implications for the recognition of subenvironments in delta deposits. *Sedimentology*. **60**, 637–665.
- Pralle, N., Kulzer, M. and Gudehus, G.** (2003) Experimental evidence on the role of gas in sediment liquefaction and mud volcanism. In: *Subsurface Sediment Mobilization* (Eds P. van Rensbergen., R.R. Hillis, A.J. Maltman and C.K. Morley), *Geological Society of London Special Publication*, **216**, 159-171.
- Pringle, J.K., Westerman, A.R., Stanbrook, D.A., Tatum, D.I. and Gardiner, A.R.** (2007) Sand volcanoes of the Carboniferous Ross Formation, County Clare, western Ireland: 3-D internal sedimentary structure and formation. In: *Sand Injectites: Implications for Hydrocarbon Exploration and Production*. (Eds A. Hurst and J. Cartwright), *AAPG Memoir*, **87**, 227– 231.
- Pulham, A.J.** (1989) Controls on internal structure and architecture of sandstone bodies within Upper Carboniferous fluvial-dominated deltas, County Clare, Western Ireland. In: *Deltas: Sites and traps for fossil fuels*. (Eds Whateley, M. K. G. & Pickering, K. T.) *Geological Society, London, Special Publication*, **41**, 179-203.
- Purvis, K., Kao, J., Flanagan, K., Henderson, J. and Duranti, D.** (2002) Complex reservoir geometries in a deep water clastic sequence, Gryphon Field, UKCS: injection structures, geological modelling and reservoir simulation. *Marine and Petroleum Geology*, **19**, 161–179.
- Pyles, D. R.** (2007) Architectural elements in a ponded submarine fan, Carboniferous Ross Sandstone, Western Ireland. In: *Atlas of Deep-Water Outcrops*, (Eds T.H. Nilsen, R.D. Shew, G.S. Steffens, & J. Studlick) *AAPG Studies in Geology*, **56**, 206-209.

- Pyles, D.R.** (2008) Multiscale stratigraphic analysis of a structurally confined submarine fan: Carboniferous Ross Sandstone, Ireland. *American Association of Petroleum Geologists Bulletin*, **92**, 557–587.
- Quigley, M.C., Bastin, S. and Bradley, B.A.** (2013) Recurrent liquefaction in Christchurch, New Zealand, during the Canterbury earthquake sequence. *Geology*, **41**, 419-422.
- Reddy, D.V., Nagabhushanan, P., Kumar, D., Sukhija, B.S., Thomas, P.J., Pandey, A.K., Sahoo, R.N., Ravi Prasad, G.V. and Datta, K.** (2009) The great 1950 Assam Earthquake revisited: field evidences of liquefaction and search for palaeoseismic events. *Tectonophysics*, **474**, 463-472.
- Reeks, M.W.** (1983) The transport of discrete particles in inhomogeneous turbulence. *Journal of Aerosol Science*, **14**, 729-739.
- van Rensbergen, P., Hillis, R.R., Maltman, A.J. and Morley, C.K.** (2003) Subsurface sediment mobilization: introduction. In: *Subsurface Sediment Mobilization* (Eds. P. van Rensbergen, R.R. Hillis, A.J. Maltman and C.K. Morley). *Geological Society of London Special Publication*, **216**, 1-8.
- Richardson, J.F. and Shabi, F.A.**, (1960), The determination of concentration distribution in a sedimenting suspension using radio-active solids. *Transactions of the Institute of Chemical Engineers*, **38**, 33-42.
- Richardson, J.F. and Zaki, W.N.**, (1954), Sedimentation and fluidisation. Part I. *Transactions of the Institute of Chemical Engineers*, **32**, 35-53.
- Rodrigues, N., Cobbold, P.R. and Løseth, H.** (2009) Physical modelling of sand injectites. *Tectonophysics*, **474**, 610-632.
- Ross, J.A., Peakall, J. and Keevil, G.M.** (2011) An integrated model of extrusive sand injectites in cohesionless sediments. *Sedimentology*, **58**, 1693-1715.
- Ross, J.A., Peakall, J. and Keevil, G.M.** (2013) Sub-aqueous sand extrusion dynamics, *Journal of the Geological Society*, **170**, 593-602.
- Rowe, C.** (2013) Shaking Loose: Sand volcanoes and Jurassic earthquakes. *Geology*, **41**, 1135-1136.
- Satur, N., and Hurst, A.** (2007) Sand-injection structures in deep-water sandstones from the Ty formation (Paleocene), Sleipner Øst Field, Norwegian North Sea.. In: *Sand Injectites: Implications for Hydrocarbon Exploration and Production*. (Eds A. Hurst and J. Cartwright), *AAPG Memoir*, **87**, 113-117.
- Saucier, R.T.** (1989) Evidence for episodic sand-blow activity during the 1811-1812 New Madrid (Missouri) earthquake series. *Geology*, **17**, 103-106.
- Schumm, S.A., Mosley, M.P. and Weaver, W.E.**, (1987) *Experimental Fluvial Geomorphology*. John Wiley and Sons, New York, 413.

- Scott, A., Vigorito, M. and Hurst, A.** (2009) The process of sand injection: internal structures and relationships with host strata (Yellowbank Creek Injectite Complex, California, U.S.A.). *Journal of Sedimentary Research*, **79**, 568-583.
- Seed, H.B., Idriss, I.M. and Arango, I.** (1983) Evaluation of liquefaction potential using field performance data. *Journal of Geotechnical Engineering*, **109**, 458-482.
- Selim, M. S., Kothari, A. C. and Turian, R. M.,** (1983) Sedimentation of multisized particles in concentrated suspensions. *American Association of Chemical Engineers Journal*, **29**, 1029-1038.
- Shapiro, S. and Yamamuro, J. A.** (2003) Effects of Silt on Three-Dimensional Stress–Strain Behavior of Loose Sand. *Journal of Geotechnical and Geoenvironmental Engineering*, **129**, 1-11
- Sherry, T.J., Rowe, C.D., Kirkpatrick, J.D. and Brodsky, E.E.** (2012) Emplacement and dewatering of the world's largest exposed sand injectite complex. *Geochemistry Geophysics Geosystems*, **13**, Q08008.
- Shi, J., and Tomasi, C.** (1994) Good features to track. *IEEE Conference on computer vision and pattern recognition*, Seattle WA, 21-34 June.
- Shoulders, S.J., Cartwright, J. and Huuse, M.** (2007) Large-scale conical sandstone intrusions and polygonal fault systems in Tranche 6, Faroe-Shetland Basin. *Marine and Petroleum Geology*, **24**, 173-188.
- Sinclair, A.R. and Robins, A. W.** (1952) Method for the Determination of the Time Lag in Pressure Measuring Systems Incorporating Capillaries, *National Advisory Committee for Aeronautics*, **2793**, 4.
- Singh, P and Jospheh, D. D.,** (1991) Finite size effects in fluidized beds in liquid-solid flows. FED 118. (Eds, M. C. Roco and Mayasuma, T.) *American Society of Mechanical Engineers*, 77-86.
- Singh, V.P., Ojha, C.S.P., Adrian, D.D., Ozkan, S. and Sills, G.E.** (2001) Role of sand boil formation in levee failure. In: *Forecasting and Mitigation of Water-Related Disasters, Theme C, Proceedings - 21st Century: The New Era for Hydraulic Research and Its Applications* (Ed G. Li), Tsinghua University Press, Beijing, 226-231.
- Squires, K.D., and Eaton, J.K.** (1990) Particle response and turbulence modification in isotropic turbulence. *Physics of Fluids*, **2**, 1191 -1203.
- Squires, K.D., and Eaton, J.K.** (1991) Preferential concentration of particles by turbulence. *Physics of Fluids*, **3**, 1169–1178.
- Stanley-Wood, N.G., Obata, E., Takahashi, H. and Ando, K.** (1990) Liquid fluidisation curves. *Powder Technology*, **60**, 61-70.

- Strachan, L.J.** (2002) Slump-initiated and controlled syndepositional sandstone remobilization: an example from the Namurian of County Clare, Ireland. *Sedimentology*, **49**, 25-41.
- Strachan, L. J. and Alsop, G.I.** (2006) Slump folds as estimators of palaeoslope: a case study from the Fisherstreet slump of County Clare, Ireland. *Basin Research*, **18**, 451-470.
- Surlyk, F. and Noe-Nygaard, N.** (2001) Sand remobilisation and intrusion in the Upper Jurassic Hareelv Formation of East Greenland. *Geological Society of Denmark Bulletin*, **48**, 169-188.
- Strömbäck, A. C. and Howell, J. A.** (2002) Predicting distribution of remobilized aeolian facies using sub-surface data: the Weissliegendes of the UK Southern North Sea. *Petroleum Geoscience*, **8**, 237-249.
- Svensen, H., Jamtveit, B., Planke, S., and Chevallier, L.** (2006). Structure and evolution of hydrothermal vent complexes in the Karoo Basin, South Africa. *Journal of the Geological Society*, **163**, **4**, 671-682.
- Tanaka, M., Maeda, Y., and Hagiwara, Y.** (2002) Turbulence modification on a homogeneous turbulent shear flow laden with small heavy particles. *International Journal of Heat and Fluid Flow*, **23**, 615-626.
- Tanner, D.C., Bense, F.A. and Ertl, G.** (2011) Kinematic retro-modelling of a cross-section through a thrust-and-fold belt: The Western Irish Namurian Basin. In: *Kinematic evolution and structural styles of fold-and-thrust belts*. (Eds. J. Poblet, & R.J. Lisle) *Geological Society, London, Special Publication*, **349**, 61-76.
- Taylor, B.J.** (1982) Sedimentary dykes, pipes and related structures in the Mesozoic sediments of south-eastern Alexander Island. *British Antarctic Survey Bulletin*, **51**, 1-42.
- Thompson, A.E., and Stokes, W.L.** (1970) Stratigraphy of the San Rafael Group, southwest and south central Utah. *Utah Geological and Mineral Survey Bulletin*, **87**, 1-53.
- Thompson, B.J., Garrison, R.E. and Moore, C.J.** (1999) A late Cenozoic sandstone intrusion west of Santa Cruz, California: Fluidised flow of water and hydrocarbon saturated sediments. In: *Late Cenozoic Fluid Seeps and Tectonics along the San Gregorio Fault Zone in the Monterey Bay region, California* (Eds R.E. Garrison, I.W. Aiello and C.J. Moore), *AAPG Pacific Section volume and guidebook*, **GB-76**, 53-74.
- Thompson, B.J., Garrison, R.E. and Moore, J.C.** (2007) A reservoir-scale Miocene injectite near Santa Cruz, California. In: *Sand Injectites: Implications for Hydrocarbon Exploration and Production*. (Eds A. Hurst and J. Cartwright), *AAPG Memoir*, **87**, 151-162.

- Tomasi, C.** and **Kanade, T.** (1991) Detection and tracking of Point Features. *Carnegie Mellon University Technical Report*, **91**, 1-20.
- van Heijst, M.W.I.M., Postma, G., Meijer, X.D., Snow, J.N.** and **Anderson, J.B.** (2001) Quantitative analogue flume-model study of river-shelf systems: principles and verification exemplified by the late Quaternary Colorado River-delta evolution. *Basin Research*, **13**, 243-268.
- Vigorito, M., Hurst, A., Cartwright, J.** and **Scott, A.** (2008) Regional-scale subsurface sand remobilization: geometry and architecture. *Journal of the Geological Society of London*, **165**, 609-612.
- Vigorito, M.** and **Hurst, A.** (2010) Regional sand injectite architecture as a record of pore-pressure evolution and sand redistribution in the shallow crust: insights from the Panoche Giant Injection Complex, California. *Journal of the Geological Society*, **167**, 889-904.
- Volpicelli, G., Massimilla, L.** and **Zenz, F.A.**, (1960) Non-homogeneities in solid-liquid fluidization. *Chemical Engineering Progress Symposium Series*, **62**, 42–50.
- Waleffe, F.** (1997) On a self-sustaining process in shear flow. *Physics of Fluids*, **9**, 883-900.
- Wang, L.P.** and **Maxey, M.R.** (1993) Settling velocity and concentration distribution of heavy particles in homogeneous isotropic turbulence. *Journal of Fluid Mechanics*, **256**, 27–68.
- Wedin, H.** and **Kerswell, R.** (2004) Exact coherent structures in pipe flow: travelling wave solutions. Online at <http://www.maths.bris.ac.uk/~marrk/WK.pdf>. accessed 14th September 2013.
- Weibel, R., Friis, H., Kazerouni, A.M., Svendsen, J.B., Stokkendal, J.** and **Poulsen, M.L.K.** (2010) Development of early diagenetic silica and quartz morphologies – Examples from the Siri Canyon, Danish North Sea. *Sedimentary Geology*, **228**, 151-170.
- Wells, M.R., Allison, P.A., Hampson, G.J., Piggott, M.D.** and **Pain, C.C.** (2005a). Modelling ancient tides: the Upper Carboniferous epi-continental seaway of Northwest Europe. *Sedimentology*, **52**, 715-735.
- Wells, M.R., Allison, P.A., Piggott, M.D., Pain, C.C., Hampson, G.J.** and **de Oliveira, C.R.E.** (2005b) Large sea, small tides: the late Carboniferous seaway of northwest Europe. *Journal of the Geological Society of London*, **162**, 417–420.
- Wignall, P.B.** and **Best, J.L.** (2000) The Western Irish Namurian Basin reassessed, *Basin Research*, **12**, 59-78.

- Wignall, P.B. and Best, J.L.** (2002) Reply to comment on The Western Irish Namurian Basin reassessed: by O.J. Martinsen & J.D. Collinson, *Basin Research*, **14**, 531-542.
- Wignall, P.B. and Best, J.L.** (2004) Sedimentology and kinematics of a large, retrogressive growth-fault system in Upper Carboniferous deltaic sediments, Western Ireland. *Sedimentology*, **51**, 1343-1358.
- Wild, J. and Briedis, N.** (2010), Structural and stratigraphic relationships of the Palaeocene mounds of the Utsira High. *Basin Research*, **22**, 533-547.
- Wilhelm, T. and Wilmański, K.** (2002) On the onset of flow in granular media due to porosity inhomogeneities, *International Journal of Multiphase Flow*, **28**, 1929-1944.
- Williams, P.F., and Rust, B.R.,** (1969) The sedimentology of a braided river. *Journal of Sedimentary Petrology*, **39**, 649-679.
- Wright, L.D.** (1977) Sediment transport and deposition at river mouths: A synthesis: *Geological Society of America Bulletin*, **88**, 857-868.
- Wright, L.D. and Coleman, J.M.,** (1974) Mississippi river mouth processes: effluent dynamics and morphologic development. *The Journal of Geology*, **82**, 751-778.
- Xenaki, V.C. and Athanasopoulos, G.A.,** (2003) Liquefaction resistance of sand-silt mixtures: an experimental investigation of the effect of fines, *Soil Dynamics and Earthquake Engineering*, **23**, 1-12.
- Yamamuro, J.A. and Lade, P.V.** (1999) Experiments and modelling of silty sands susceptible to static liquefaction. *Mechanics of Cohesive-Frictional Materials*, **4**, 545-564.
- Zhou, Z.Y., Pinson, D., Zou, R.P. and Yu, A.B.** (2011) Discrete particle simulation of gas fluidization of ellipsoidal particles. *Chemical Engineering Science*, **66**, 6128-6145.